

**TURBULENT FLAME PROPAGATION CHARACTERISTICS OF  
HIGH HYDROGEN CONTENT FUELS**

A Thesis  
Presented to  
The Academic Faculty

by

Andrew Marshall

In Partial Fulfillment  
of the Requirements for the Degree  
Doctor of Philosophy in the  
School of Mechanical Engineering

Georgia Institute of Technology  
August 2015

Copyright © 2015 by Andrew Marshall

**TURBULENT FLAME PROPAGATION CHARACTERISTICS OF  
HIGH HYDROGEN CONTENT FUELS**

Approved by:

Dr. Tim C. Lieuwen, Advisor  
School of Aerospace Engineering  
*Georgia Institute of Technology*

Dr. Ben T. Zinn  
School of Aerospace Engineering  
*Georgia Institute of Technology*

Dr. Caroline Genzale  
School of Mechanical Engineering  
*Georgia Institute of Technology*

Dr. Jerry Seitzman  
School of Aerospace Engineering  
*Georgia Institute of Technology*

Dr. Suresh Menon  
School of Aerospace Engineering  
*Georgia Institute of Technology*

Date Approved: 2 May 2015

*To my amazing wife Hillary.*

## ACKNOWLEDGEMENTS

It was a long and arduous journey to get here, but completing this PhD has increased my patience and perseverance, made me more thoughtful and critical when faced with new information, and has helped me become much more adept at communicating ideas and information in both written and oral forms. The whole process was filled with ups and downs, triumphs and setbacks. From losing an entire hard drive of data, to a hydrogen detonation that left my experimental facility in pieces, it has not been an easy path. But I overcame these obstacles with help from some of the best people I've ever known. This thesis would not have been possible without the help and support, both emotionally and intellectually, of numerous individuals along the way.

I'd like to start by thanking my parents, Robert and Georgia Marshall, for their love, support, and guidance. They worked very hard to raise me right and provided me with every opportunity to succeed. I couldn't ask for better parents. I'd also like to thank my two older siblings, Laura and Taylor, for everything they have done for me. When times are hard, my family has always been there for me.

My advisor, Tim Lieuwen, has guided and supported me through this process. He has always pushed me hard to succeed, and has molded me to think critically and to become a better scientist and engineer. His wealth of knowledge and experience was critical to my success. I have always appreciated that, though he expects hard work and dedication from all of his students, he treats us with respect and shows his appreciation for the hard work we do. Some of my fondest memories from graduate school have been formed on trips to his cabin in North Georgia, where there has always been plenty of fun activities, eating, drinking and spending time with friends.

Jerry Seitzman's mentorship throughout the years is also very much appreciated. His contributions to this work are numerous. He was a regular attendee and active participant in our weekly turbulent flame group meeting, offering advice and critical feedback on the

results I presented. Jerry is never afraid to ask why, even if he already knows the answer, in order to make sure you understand it thoroughly. These regular question and answer sessions with Jerry helped prepare me for handling and responding to feedback from audiences when presenting my work.

I'd also like to thank the rest of my committee members for their contributions to this work: Doctors Ben Zinn, Caroline Genzale, and Suresh Menon. Their feedback on my proposal offered fresh ideas and helped guide the framework of this thesis.

For my first five and a half years of graduate school I was partnered on this research with Prabhakar Venkateswaran (now Prof. Prabhakar Venkateswaran, visiting assistant professor at Trinity College). A lot of the work presented in this thesis is directly related to the hard work and dedication that he spent on his own thesis material. Prabhakar became a very close friend of mine while we worked on our PhDs together under the advisement of Tim. We spent long hours at the lab working on our experiment, collecting data, or trying to make project deadlines. Prabhakar's excellent sense of humor, hearty laugh, and down-to-earth personality always made time spent in the lab much more enjoyable. His laughter and good spirit were contagious throughout the entire combustion lab; even people who didn't know him well would recognize his booming laugh as it echoed throughout the front offices of the Ben T. Zinn Combustion Lab. Outside of the lab, Prabhakar and I spent a great deal of time on our bicycles, pounding out 100 miles on the Silver Comet Trail one Saturday. Cycling is often said to be a sport for masochists, which I guess makes sense why a bunch of the graduate students in the combustion lab would be so into it.

When Prabhakar was getting ready to graduate, Tim put graduate student Julia Lundrigan onto our project to be his successor. Those are some big shoes to fill, but Julia was definitely up to the task (and not just because she actually has big feet). I have a theory that Tim thought I was too quiet and so he paired me with the loudest members of the combustion lab throughout my graduate school tenure in order for us to average out to a normal volume. Julia excelled quickly on our research team. I am very thankful for her help and contributions over the past 3+ years. We became very close friends over the years, and Julia was supportive and encouraging even during some of the most trying and frustrating

portions of my PhD. She spent months helping me rebuild my experimental facility after we had a detonation occur at high pressure. Julia also got back into cycling in graduate school (maybe it's contagious), so in addition to getting a new research partner, I also got a new cycling (and triathlon) buddy. She also helped me improve my swimming, which started out pretty ghastly, in order to not drown during that portion of a triathlon. I thank her for that, because drowning probably would not have helped get this PhD finished.

During the whole time that Prabhakar, Julia, and I were working on the experimental side, Alberto Amato was our computational and numerical counterpart. His contributions, especially towards the development of advanced analytical tools and analysis of DNS data, were vital towards the understanding of this research topic. Alberto truly deserved his title of "The Converger."

Chris Foley is another Lieuwenite that I'd like to acknowledge. He came to the combustion lab only a semester after me, and we became friends quickly, probably due to our strangely similar senses of humor. In addition, as the first and second Tim Lieuwen mechanical engineering PhD students, we suffered through a lot of classes together. I think that part of the reason we develop close friendships in graduate school is that mutual suffering is one of the best forms of bonding. Of course, wild nights out until the early morning in places like Princeton, New Jersey and Copenhagen, Denmark can also be an excellent form of bonding. We shared an office during the later portion of our PhDs, and he was an excellent person to bounce ideas off of or to chat with while taking a break from work.

To Jackie O'Connor (now Prof. O'Connor at Pennsylvania State University), who is always willing to engage in thoughtful discussions, whether intellectual or personal. She constantly strove to better both the Lieuwen group and the combustion lab as a whole through organization of numerous technical working groups from seminars on laser diagnostics, to in-depth investigations of sources of experimental uncertainties, to discussions on how to be an effective mentor to undergraduate researchers. Her constant efforts towards betterment of herself and the lab inspired the rest of us to work to achieve that same standard of excellence.

I'd like to thank Ben Wilde and Matt Quinlan, who resided in the same office with Chris

Foley and me during the later portions of our PhDs. All of us were working on writing our theses during most of the time that we occupied that office, and they were both excellent people to commiserate with over the struggles of writing. They also helped to keep that office focused and productive, which made for a very conducive writing environment. I also appreciate their assistance when it came to discussion on experimental methods and post-processing techniques or when we would bounce ideas back and forth on possible methods to solve programming issues. I will also never forget White Russian Night at the Wilde's or hanging out at bars (and golf courses) around Princeton University with Matt.

There were numerous graduate students at the combustion lab who helped me when I started and I had very little idea of what I was doing. My sincere gratitude goes out to Karthik Periagaram, Jack Crawford, Santosh Hemchandra, Yash Kochar, Sai Kumar Thumuluru, Dong-Hyuk Shin, and Shreekrishna for their invaluable assistance and wealth of knowledge. I'd also like to thank Ben Emerson, Brandon Sforzo, Ianko Chtereve, Michael Malanoski, Michael Aguilar, Nick Magina, Nishant Jain, Sampath Adusumilli, Vishal Acharya, Luke Humphrey, Gina Magnotti, Ben Knox, and Travis Smith for help and support along the way. My heartfelt gratitude goes out to the entirety of the Ben T. Zinn Combustion Laboratory, for being one of the best groups I've ever had the pleasure to work with.

This work would not have been possible without the help of numerous undergraduate researchers along the way. Their efforts, big and small, brought the turbulent flame speed rig to life, and kept the gears turning over the years. Special thanks to the hard work and dedication of Jose Antezana, Juan Camilo Pedroza, Edouard Bahous, and Andrew Irby. I'd also like to give a huge thank you to Ramon Romero, who came to work with Prabhakar and I as part of a high school internship class, got accepted to Georgia Tech, and, despite spending four months with us as an impressionable young high school student, decided to come back to the lab and work with us again as an undergraduate. Ramon worked with me on this research project until he graduated from Georgia Tech, and over the course of that time, became quite the CHEMKIN expert.

The research engineers and staff of the Ben T. Zinn Combustion Laboratory have been

an integral part of this PhD. I'd like to thank Bobby Noble, Brad Ochs, Dr. Sasha Bibik, and Dr. David Scarborough for their invaluable assistance, thoughtful discussions, and expertise in experimental research. In addition, Shane Getchell and Seth Hutchins both helped me in numerous ways in the development of my experimental facility. I'd also like to thank the machinists at the Daniel Guggenheim School of Aerospace Engineering machine shop, Scott Elliott, Scott Moseley, and Henry "Red" Russell, for turning my designs and ideas into reality and offering numerous suggestions for ways to improve them.

Finally, I would like to thank my wife, Hillary, for her love, patience, and support through this entire process. It has not always been easy, and at times it has been very stressful, but she has always been there to encourage me and keep my spirits up. She is the most important person in my life, and I couldn't imagine getting here without her.

# TABLE OF CONTENTS

<b>DEDICATION</b> . . . . .	<b>iii</b>
<b>ACKNOWLEDGEMENTS</b> . . . . .	<b>iv</b>
<b>LIST OF TABLES</b> . . . . .	<b>xii</b>
<b>LIST OF FIGURES</b> . . . . .	<b>xiii</b>
<b>NOMENCLATURE</b> . . . . .	<b>xxiv</b>
<b>SUMMARY</b> . . . . .	<b>xxix</b>
<b>I INTRODUCTION</b> . . . . .	<b>1</b>
1.1 Motivation . . . . .	1
1.2 Theoretical Background . . . . .	2
1.2.1 Turbulent Premixed Flames . . . . .	2
1.2.2 Flame Stretch . . . . .	13
1.3 Literature Review . . . . .	22
1.4 Thesis Overview . . . . .	27
<b>II METHODS</b> . . . . .	<b>29</b>
2.1 Experimental Facility . . . . .	29
2.1.1 Flow Facility . . . . .	30
2.1.2 Turbulence Generator . . . . .	35
2.1.3 Low Swirl Burner . . . . .	42
2.1.4 High Pressure Capabilities . . . . .	48
2.2 Flow Field Measurements . . . . .	55
2.2.1 Single Point Measurements . . . . .	55
2.2.2 Velocity Field Measurements . . . . .	57
2.3 Flame Measurements . . . . .	62
2.3.1 Chemical Kinetic Calculations . . . . .	62
2.3.2 Flame Front Topology . . . . .	63
2.3.3 Turbulent Flame Speed . . . . .	70

<b>III FLOW FIELD CHARACTERIZATION</b>	<b>73</b>
3.1 Turbulence Generator Characterization	73
3.1.1 Mean and Turbulence Profiles	74
3.1.2 Flow Length and Time Scales	78
3.1.3 Power Spectra	80
3.1.4 Summary	81
3.2 Low Swirl Burner Velocity Field Characterization	82
3.2.1 Mean and Turbulence Profiles	82
3.2.2 Integral Length Scales	85
<b>IV TURBULENT FLAME SPEED MEASUREMENTS</b>	<b>87</b>
4.1 Turbulent Global Consumption Flame Speeds	88
4.1.1 Overview	88
4.1.2 Background	89
4.1.3 Methods	89
4.1.4 Results	90
4.1.5 Analysis	91
4.2 Turbulent Local Displacement Flame Speeds	98
4.2.1 Overview	98
4.2.2 Results	99
4.2.3 Analysis	101
4.3 Conclusions	104
<b>V FLAME FRONT TOPOLOGY AND STRETCH STATISTICS</b>	<b>106</b>
5.1 Introduction	107
5.2 Methods	113
5.3 Results and Discussion	114
5.3.1 Global (Unconditioned) Stretch Statistics	117
5.3.2 Instantaneous Leading Point Stretch Statistics	122
5.3.3 Flame Brush Leading Point Stretch Statistics	130
5.4 Concluding Remarks	142

<b>VI CONCLUSIONS AND RECOMMENDATIONS FOR FUTURE WORK</b>	<b>143</b>
6.1 Conclusions and Contributions . . . . .	143
6.1.1 Experimental Methodologies . . . . .	145
6.1.2 Turbulent Flame Speed Measurements . . . . .	147
6.1.3 Flame Topology and Stretch Statistics . . . . .	147
6.2 Recommendations for Future Work . . . . .	148
6.2.1 Advanced Leading Points Measurements and Analysis . . . . .	148
6.2.2 High Pressure and Temperature Flame Topology Measurements . .	150
6.2.3 Turbulent Flame Speed Measurements and Analysis . . . . .	151
<b>APPENDIX A — FLOW METERING AND CALIBRATION . . . . .</b>	<b>153</b>
<b>APPENDIX B — FLOW FIELD DATA . . . . .</b>	<b>163</b>
<b>REFERENCES . . . . .</b>	<b>209</b>

## LIST OF TABLES

1	Dependence of Lewis number on equivalence ratio and molecular weight of fuel. . . . .	17
2	Effect of flame stretch on the laminar flame speed for different Lewis number. . . . .	17
3	Instrument and valve list for Figure 16 . . . . .	51
4	Instrument and valve list for Figure 17 . . . . .	52
5	Equipment, instrument and valve list for Figure 18 . . . . .	53
6	Summary of literature investigations of fuel effects on the LSB. . . . .	54
7	Experimental parameters and conditions for the two datasets acquired using PIV . . . . .	58
8	Maximum values of normalized mean axial, radial, and azimuthal velocity at three different blockage ratios. . . . .	74
9	Investigated 12 mm burner data set . . . . .	91
10	Experimental parameters and conditions for the two datasets acquired using PIV . . . . .	114
11	Local displacement turbulent flame speeds, $S_{T,LD}/S_{L,0}$ , average curvature, $1/\mathcal{R}$ , and standard deviation of the curvature, $\sigma$ , at the instantaneous leading points (ILP) and at the flame brush leading points (FBLP). Uncertainties are for a 95% confidence interval. . . . .	115
12	Local displacement turbulent flame speeds, $S_{T,LD}/S_{L,0}$ , average tangential strain rate, $\overline{\kappa_s}$ , and standard deviation of the tangential strain rate, $\sigma$ , at the instantaneous leading points (ILP) and at the flame brush leading points (FBLP). Uncertainties are for a 95% confidence interval. . . . .	116
13	Instrument and valve list for Figure 17 . . . . .	156

## LIST OF FIGURES

1	Graphical depiction of the turbulent flame speed, $S_T$ . . . . .	4
2	Example dataset demonstrating the fuel effect on the turbulent flame speed [97]. . . . .	5
3	Example dataset demonstrating the “bending effect” on the turbulent flame speed [88]. . . . .	5
4	Example dataset that does not exhibit the “bending effect” on $S_T$ [90]. . . . .	6
5	Turbulent combustion regime diagram created by Borghi [13] with modifications from Peters [105] . . . . .	7
6	(a) Ensemble of flamelets that occupy a finite volume of space known as (b) the turbulent flame brush. Figure reproduced from Turns [131]. . . . .	10
7	Correlation of turbulent flame speed data developed by Bradley [14] from approximately 1650 turbulent flame speed measurements. . . . .	11
8	Definition of the turbulent local displacement speed, $S_{T,LD}$ . . . . .	12
9	Depictions of flame stretch from (a) non-unity Lewis number effects and (b) preferential diffusion effects. . . . .	14
10	Positively stretched stagnation flame model with $k = 0, 1$ for Cartesian and cylindrical coordinates, respectively. Figure reproduced from [79]. . . . .	15
11	Dependence of the laminar flame speed on Karlovitz number for $\text{CH}_4$ :air flames at different equivalence ratios. Figure reproduced from [129]. . . . .	20
12	Representation of the twin, premixed flames in an opposed jet burner configuration used in the OPPDIF software module. Figure reproduced from [67]. . . . .	21
13	Stretch sensitivity calculations of $\text{H}_2$ :CO fuel blends and $\text{CH}_4$ [133]. . . . .	21
14	Dependence of the laminar flame speed on Karlovitz number for steady and oscillating stretch rates for a $\text{H}_2$ :air flame at $\phi = 0.4$ . Figure reproduced from [62]. . . . .	22
15	(a) Measured dependence of the turbulent flame speed, $S_{T,GC}$ , upon turbulence intensity, $u'_{rms}$ , normalized by $S_{L,0}$ at various conditions for several $\text{H}_2$ :CO ratios and pure $\text{CH}_4$ . (b) $S_{T,GC}$ data from (a) normalized by $S_{L,max}$ . See Venkateswaran et al. [133] for details on experimental conditions. . . . .	26
16	Diagram of the experimental facility for control of fuel regulators. . . . .	31
17	Diagram of the experimental facility for metering and mixing of fuels. . . . .	33
18	Diagram of the experimental facility for fuel and air delivery to the burner. . . . .	34

19	Schematic of the experimental facility for characterization of the turbulence generator. Dimensions in mm. . . . .	39
20	Schematic of the turbulence generating plates: (a) fully open and (b) partially closed. . . . .	39
21	Flow characteristics (a) without and (b) with flow straighteners. . . . .	40
22	Detailed views of the turbulence generator plates and contoured nozzle (12 mm nozzle diameter shown) (a) with dimensions and (b) isometric cut-away. Dimensions in mm. . . . .	41
23	Detailed view of the pass-through assembly for the central shaft of the turbulence generator. . . . .	42
24	Schematic of the original LSB [25]. . . . .	43
25	Schematic of the LSB [10] with the turbulence generator of Videto and Santavicca [135]. . . . .	45
26	Detailed views of the (a) LSB nozzle and (b) swirler model. Dimensions in mm. . . . .	48
27	Schematic of the pressure vessel used to perform high pressure experiments. Pressure vessel is shown with the 20 mm Bunsen burner installed. . . . .	50
28	Illustration of direction and orientation of cuts and location of data points acquired in LDV characterization. . . . .	56
29	Illustration of direction and orientation of cuts performed in LDV velocity characterization relative to the turbulence generator top plate. . . . .	56
30	Particle kinetic energy normalized by fluid kinetic energy as a function of cutoff frequency $f_c$ for a range of relaxation frequencies $C$ [93]. . . . .	60
31	Particle velocity $v_P$ and fluid velocity $v_F$ versus axial distance in a $\text{CH}_4$ -air stagnation flame [122]. . . . .	61
32	Demonstration of the post-processing procedure used to identify the flame edge from PIV images. (a) raw image, (b) median-filtered image, (c) thresholded image used to identify reactants and products and find the flame edge, and (d) flame edge (green), fitted spline curve (red), instantaneous leading point (yellow x) and average progress variable, $\langle c \rangle$ , (white) overlaid onto raw image. Data presented are for a 50:50 $\text{H}_2$ :CO fuel mixture at STP for a swirl number of $S = 0.58$ , mean flow velocity $U_0 = 30$ m/s, and equivalence ratio $\phi = 0.55$ . . . . .	65
33	Comparison of curvature PDFs generated using two arc length intervals for a 50:50 $\text{H}_2$ :CO mixture at $U_0 = 30$ m/s. . . . .	67
34	Average progress variable $\langle c \rangle$ along the axial centerline of the burner. The red line is an error function fit to the data. Conditions are the same as in Figure 32. . . . .	69

35	PDF of locations of instantaneous leading points in $\langle c \rangle$ -space for three different fuel compositions. . . . .	70
36	Mean velocity normalized by $U_0$ in the axial direction along the burner centerline for a reacting (100% $\text{CH}_4$ , $\phi = 0.9$ ) case at STP. $U_0 = 20$ m/s, $S = 0.57$ , and $BR = 69\%$ . . . . .	71
37	LDV profiles for the 12 mm burner at (a,b) $BR = 69\%$ , (c,d) $BR = 81\%$ , and (e,f) $BR = 93\%$ . (left) Mean axial, radial and azimuthal velocities and (right) RMS of the fluctuating axial, radial, azimuthal and total velocities as a function of radial distance from the center of the burner for $U_0 = 30$ m/s. Dashed and solid lines correspond to pressures of 1 and 5 atm, respectively. . . . .	75
38	LDV profiles for the 20 mm burner at (a,b) $BR = 69\%$ , (c,d) $BR = 81\%$ , and (e,f) $BR = 93\%$ . (left) Mean axial, radial and azimuthal velocities and (right) RMS of the fluctuating axial, radial, azimuthal and total velocities as a function of radial distance from the center of the burner for $U_0 = 50$ m/s. Dashed and solid lines correspond to pressures of 1 and 5 atm, respectively. . . . .	76
39	Dependence of the burner centerline total turbulence intensity on blockage ratio for the (a) 12 mm and (b) 20 mm diameter burners. The solid line corresponds to the linear fit of the data, and the dashed lines correspond to the 95% confidence level. Slopes and $R^2$ values of the linear fits are displayed on the graphs . . . . .	78
40	Comparison of turbulence intensity in the shear layer to turbulence intensity along the nozzle centerline. . . . .	79
41	Autocorrelation function plotted against normalized lag time for the 20 mm diameter burner at $U_0 = 4$ m/s, $BR = 75\%$ . (a) Over one time constant and (b) zoomed in on initial roll-off region. . . . .	79
42	Comparison of characteristic longitudinal length scale, $l$ (normalized by burner diameter $d$ ) as a function of blockage ratio for the two burner diameters over a range of mean flow velocities. . . . .	80
43	Turbulent power spectra for the 20 mm burner at (a) $U_0 = 10$ m/s at three different blockage ratios and (b) $BR = 77\%$ at three different mean flow velocities. . . . .	81
44	Mean velocity normalized by $U_0$ for (a) non-reacting and (b) reacting (100% $\text{CH}_4$ , $\phi = 0.9$ ) cases at STP. $U_0 = 20$ m/s, $S = 0.57$ , and $BR = 69\%$ . . . . .	82
45	Mean velocity normalized by $U_0$ in the axial direction along the burner centerline for (a) non-reacting and (b) reacting (100% $\text{CH}_4$ , $\phi = 0.9$ ) cases at STP. $U_0 = 20$ m/s, $S = 0.57$ , and $BR = 69\%$ . . . . .	83
46	Mean axial velocity normalized by $U_0$ in the axial direction along the burner centerline for (a) 70:30 $\text{H}_2$ :CO ( $\phi = 0.51$ ) and (b) 100% $\text{H}_2$ ( $\phi = 0.46$ ) cases at STP for $U_0 = 30$ and 50 m/s. $S = 0.58$ and $BR = 69\%$ . . . . .	84

47	RMS velocity normalized by $U_0$ in the axial direction along the burner centerline for (a) non-reacting and (b) reacting (100% $\text{CH}_4$ , $\phi = 0.9$ ) cases at STP. $U_0 = 20$ m/s, $S = 0.57$ , and $BR = 69\%$ . . . . .	84
48	Integral length scale $l_0$ (normalized by burner diameter $d$ ) as a function of downstream distance $y/d$ for (a) low and high blockage ratios ( $S = 0.58$ , $U_0 = 30$ m/s, 70:30 $\text{H}_2$ :CO), (b) low and high bulk flow velocity ( $S = 0.58$ , 50:50 $\text{H}_2$ :CO, $BR = 69\%$ ), and (c) three different fuel compositions ( $S = 0.58$ , $U_0 = 30$ m/s, $BR = 69\%$ ). Errors bars are for the 95% confidence interval. . . . .	86
49	Borghi-Peters diagram showing location of 12 mm burner data points at 1, 5 and 10 atm. . . . .	92
50	$S_{T,GC}$ as a function of $u'_{rms}$ normalized by $S_{L,0}$ at various mean flow velocities, $\text{H}_2$ :CO ratios, and pressures for the 12 mm diameter burner (See Table 9 for the legend of mixture conditions, flow velocities and pressures). . . . .	92
51	Ratio of $S_{T,GC}$ at 5 and 10 atm to 1 atm across the range of turbulence intensities investigated. . . . .	93
52	Pressure effect on mixture stretch sensitivity for 70:30 $\text{H}_2$ :CO mixtures at constant $S_{L,0}$ . . . . .	93
53	$S_{T,GC}$ as a function of $u'_{rms}$ normalized by $S_{L,max}$ at various mean flow velocities, $\text{H}_2$ :CO ratios and pressures using the 12 mm diameter burner (See Table 9 for legend of mixture conditions, flow velocities and pressures). . . . .	94
54	Variation in $\tau_{S_{L,max}}$ as a function of $\text{H}_2$ content for the different mixtures and conditions investigated. 0% $\text{H}_2$ corresponds to the pure $\text{CH}_4$ mixture. . . . .	96
55	Dependence of $S_{T,GC}/S_{L,max}$ on $\tau_{S_{L,max}}/\tau_{flow}$ at two turbulence intensities $u'_{rms}/S_{L,max} = 7$ and 13.5 for the 12 mm diameter burner. Power law fits with the corresponding slopes are also included. . . . .	97
56	Dependence of $S_{T,GC}/S_{L,max}$ on $\tau_{S_{L,max}}/\tau_{flow}$ at two turbulence intensities $u'_{rms}/S_{L,max} = 12$ and 24 for the 20 mm diameter burner. Power law fits with the corresponding slopes are also included. . . . .	98
57	Borghi-Peters diagram showing location of LSB data points. See Figures 58 and 59 for legends. . . . .	99
58	$S_{T,LD}$ as a function of $u'_{ax}$ normalized by $S_{L,0}$ at various mean flow velocities and $\text{H}_2$ :CO ratios for the LSB. . . . .	100
59	$S_{T,LD}$ as a function of $u'_{ax}$ normalized by $S_{L,0}$ at various mean flow velocities and $\text{H}_2$ : $\text{CH}_4$ ratios for the LSB. . . . .	101
60	$S_{T,LD}$ as a function of $u'_{ax}$ normalized by $S_{L,0}$ at various mean flow velocities for $\text{H}_2$ :CO and $\text{H}_2$ : $\text{CH}_4$ mixtures obtained in the LSB. See Figures 58 and 59 for legends. . . . .	102
61	$S_{T,LD}$ as a function of $u'_{ax}$ normalized by $S_{L,max}$ at various mean flow velocities and $\text{H}_2$ :CO ratios for the LSB. . . . .	102

62	$S_{T,LD}$ as a function of $u'_{ax}$ normalized by $S_{L,max}$ at various mean flow velocities and H <sub>2</sub> :CH <sub>4</sub> ratios for the LSB. . . . .	103
63	$S_{T,LD}$ as a function of $u'_{ax}$ normalized by $S_{L,max}$ at various mean flow velocities for H <sub>2</sub> :CO and H <sub>2</sub> :CH <sub>4</sub> mixtures obtained in the LSB. See Figures 58 and 59 for legends. . . . .	104
64	Stretch sensitivity calculations of H <sub>2</sub> :CO fuel blends and CH <sub>4</sub> [133]. . . . .	108
65	(a) Measured dependence of the turbulent flame speed, $S_{T,GC}$ , upon turbulence intensity, $u'_{rms}$ , normalized by $S_{L,0}$ at various conditions for several H <sub>2</sub> :CO ratios and pure CH <sub>4</sub> . (b) $S_{T,GC}$ data from (a) normalized by $S_{L,max}$ . See Venkateswaran et al. [133] for details on experimental conditions. . . . .	112
66	Unconditioned ( $0 \leq \langle c \rangle \leq 1$ ) (a, b) curvature and (c, d) tangential strain rate PDFs for varying fuel compositions at (a, c) $U_0 = 30$ m/s and (b, d) $U_0 = 50$ m/s. Secondary top-axis in (b) shows curvature normalized by the unstretched flame thickness for the 100% H <sub>2</sub> case. . . . .	118
67	Normalized strain rates as a function of average progress variable along the burner center line at (a, c) $u'_{rms}/S_{L,0} \approx 5$ and (b, d) $u'_{rms}/S_{L,0} \approx 10$ for (a, b) 50:50 H <sub>2</sub> :CO and (c, d) 100% H <sub>2</sub> . . . . .	119
68	Unconditioned (a, b) curvature and (c, d) tangential strain rate PDFs for (a, c) 50:50 H <sub>2</sub> :CO and (b, d) 100% H <sub>2</sub> . . . . .	120
69	Unconditioned joint PDFs of curvature and tangential strain rate at (a, c, e) $u'_{rms}/S_{L,0} \approx 5$ and (b, d, f) $u'_{rms}/S_{L,0} \approx 10$ for (a, b) 50:50 H <sub>2</sub> :CO, (c, d) 70:30 H <sub>2</sub> :CO and (e, f) 100% H <sub>2</sub> . . . . .	123
70	Instantaneous leading point (a, b) curvature and (c, d) tangential strain rate PDFs for (a, c) $U_0 = 30$ m/s and (b, d) $U_0 = 50$ m/s. . . . .	124
71	Instantaneous leading point (a, b) curvature and (c, d) tangential strain rate PDFs for (a, c) 50:50 H <sub>2</sub> :CO and (b, d) 100% H <sub>2</sub> . . . . .	126
72	Instantaneous leading point average (a) curvature and (b) tangential strain rate vs. the critical stretch rate at $S_{L,max}$ for varying fuel compositions at various turbulence levels. . . . .	128
73	Instantaneous leading point average (a) curvature and (b) tangential strain rate vs. turbulence intensity normalized by the unstretched laminar flame speed for varying fuel compositions. . . . .	129
74	Comparison of curvature PDFs generated using two arc length intervals for a 50:50 H <sub>2</sub> :CO mixture at $U_0 = 30$ m/s. . . . .	130
75	Instantaneous leading point conditioned joint PDFs of curvature and tangential strain rate at (a, c, e) $u'_{rms}/S_{L,0} \approx 5$ and (b, d, f) $u'_{rms}/S_{L,0} \approx 10$ for (a, b) 50:50 H <sub>2</sub> :CO, (c, d) 70:30 H <sub>2</sub> :CO and (e, f) 100% H <sub>2</sub> . . . . .	131
76	Flame brush leading point ( $0 \leq \langle c \rangle \leq 0.01$ ) (a, b) curvature and (c, d) tangential strain rate PDFs for (a, c) $U_0 = 30$ m/s and (b, d) $U_0 = 50$ m/s. . . . .	132

77	Time-averaged (a, b) curvature and (c, d) tangential strain rate as a function of progress variable $\langle c \rangle$ for (a, c) $U_0 = 30$ m/s and (b, d) $U_0 = 50$ m/s. . .	134
78	Flame brush leading point ( $0 \leq \langle c \rangle \leq 0.01$ ) (a, b) curvature and (c, d) tangential strain rate PDFs for (a, c) 50:50 H <sub>2</sub> :CO and (b, d) 100% H <sub>2</sub> . . .	136
79	Flame brush leading point average (a) curvature and (b) tangential strain rate vs. the critical stretch rate at $S_{L,max}$ for varying fuel compositions at various turbulence levels. . . . .	137
80	Flame brush leading point average (a) curvature and (b) tangential strain rate vs. turbulence intensity normalized by the unstretched laminar flame speed for varying fuel compositions. . . . .	138
81	Flame brush leading point standard deviations of (a) curvature and (b) tangential strain rate vs. turbulence intensity normalized by the unstretched laminar flame speed for varying fuel compositions. . . . .	140
82	Flame brush leading point conditioned ( $0 \leq \langle c \rangle \leq 0.01$ ) joint PDFs of curvature and tangential strain rate at (a, c, e) $u'_{rms}/S_{L,0} \approx 5$ and (b, d, f) $u'_{rms}/S_{L,0} \approx 10$ for (a, b) 50:50 H <sub>2</sub> :CO, (c, d) 70:30 H <sub>2</sub> :CO and (e, f) 100% H <sub>2</sub> . . . . .	141
83	Diagram of the experimental facility for metering and mixing of fuels. . . .	154
84	Drum-type gas meter used to measure volume flow rates for critical orifice calibrations [49]. . . . .	157
85	Measurement error in the drum-type gas meter. . . . .	158
86	Measured mass flow rate as a function of theoretical mass flow rate calculated using measured pressure and temperature as inputs in Equation 47 for an orifice diameter of $d = 0.006$ in. . . . .	159
87	Measured mass flow rate as a function of theoretical mass flow rate calculated using measured pressure and temperature as inputs in Equation 47 for an orifice diameter of $d = 0.018$ in. . . . .	159
88	Measured mass flow rate as a function of theoretical mass flow rate calculated using measured pressure and temperature as inputs in Equation 47 for an orifice diameter of $d = 0.024$ in. . . . .	160
89	Measured mass flow rate as a function of theoretical mass flow rate calculated using measured pressure and temperature as inputs in Equation 47 for an orifice diameter of $d = 0.032$ in. . . . .	160
90	Measured mass flow rate as a function of theoretical mass flow rate calculated using measured pressure and temperature as inputs in Equation 47 for an orifice diameter of $d = 0.043$ in. . . . .	161
91	Measured mass flow rate as a function of theoretical mass flow rate calculated using measured pressure and temperature as inputs in Equation 47 for an orifice diameter of $d = 0.055$ in. . . . .	161

92	Measured mass flow rate as a function of theoretical mass flow rate calculated using measured pressure and temperature as inputs in Equation 47 for an orifice diameter of $d = 0.060$ in. . . . .	162
93	Measured mass flow rate as a function of theoretical mass flow rate calculated using measured pressure and temperature as inputs in Equation 47 for an orifice diameter of $d = 0.079$ in. . . . .	162
94	Mean and RMS velocity profiles for the 12 mm burner at $p = 1$ atm, $T = 300$ K, $U_0 = 30$ m/s, $BR = 69\%$ for the (a) $x$ and (b) $y$ traverses. . . . .	163
95	Mean and RMS velocity profiles for the 12 mm burner at $p = 1$ atm, $T = 300$ K, $U_0 = 30$ m/s, $BR = 73\%$ . . . . .	164
96	Mean and RMS velocity profiles for the 12 mm burner at $p = 1$ atm, $T = 300$ K, $U_0 = 30$ m/s, $BR = 77\%$ . . . . .	164
97	Mean and RMS velocity profiles for the 12 mm burner at $p = 1$ atm, $T = 300$ K, $U_0 = 30$ m/s, $BR = 81\%$ . . . . .	165
98	Mean and RMS velocity profiles for the 12 mm burner at $p = 1$ atm, $T = 300$ K, $U_0 = 30$ m/s, $BR = 85\%$ . . . . .	165
99	Mean and RMS velocity profiles for the 12 mm burner at $p = 1$ atm, $T = 300$ K, $U_0 = 30$ m/s, $BR = 87\%$ . . . . .	166
100	Mean and RMS velocity profiles for the 12 mm burner at $p = 1$ atm, $T = 300$ K, $U_0 = 30$ m/s, $BR = 89\%$ . . . . .	166
101	Mean and RMS velocity profiles for the 12 mm burner at $p = 1$ atm, $T = 300$ K, $U_0 = 30$ m/s, $BR = 91\%$ . . . . .	167
102	Mean and RMS velocity profiles for the 12 mm burner at $p = 1$ atm, $T = 300$ K, $U_0 = 30$ m/s, $BR = 93\%$ . . . . .	167
103	Mean and RMS velocity profiles for the 12 mm burner at $p = 1$ atm, $T = 300$ K, $U_0 = 50$ m/s, $BR = 69\%$ for the (a) $x$ and (b) $y$ traverses. . . . .	168
104	Mean and RMS velocity profiles for the 12 mm burner at $p = 1$ atm, $T = 300$ K, $U_0 = 50$ m/s, $BR = 73\%$ for the (a) $x$ and (b) $y$ traverses. . . . .	168
105	Mean and RMS velocity profiles for the 12 mm burner at $p = 1$ atm, $T = 300$ K, $U_0 = 50$ m/s, $BR = 77\%$ for the (a) $x$ and (b) $y$ traverses. . . . .	169
106	Mean and RMS velocity profiles for the 12 mm burner at $p = 1$ atm, $T = 300$ K, $U_0 = 50$ m/s, $BR = 81\%$ for the (a) $x$ and (b) $y$ traverses. . . . .	169
107	Mean and RMS velocity profiles for the 12 mm burner at $p = 1$ atm, $T = 300$ K, $U_0 = 50$ m/s, $BR = 85\%$ for the (a) $x$ and (b) $y$ traverses. . . . .	170
108	Mean and RMS velocity profiles for the 12 mm burner at $p = 1$ atm, $T = 300$ K, $U_0 = 50$ m/s, $BR = 87\%$ for the (a) $x$ and (b) $y$ traverses. . . . .	170
109	Mean and RMS velocity profiles for the 12 mm burner at $p = 1$ atm, $T = 300$ K, $U_0 = 50$ m/s, $BR = 89\%$ for the (a) $x$ and (b) $y$ traverses. . . . .	171

110	Mean and RMS velocity profiles for the 12 mm burner at $p = 1$ atm, $T = 300$ K, $U_0 = 50$ m/s, $BR = 91\%$ for the (a) $x$ and (b) $y$ traverses. . . . .	171
111	Mean and RMS velocity profiles for the 12 mm burner at $p = 1$ atm, $T = 300$ K, $U_0 = 50$ m/s, $BR = 93\%$ for the (a) $x$ and (b) $y$ traverses. . . . .	172
112	Mean and RMS velocity profiles for the 12 mm burner at $p = 5$ atm, $T = 300$ K, $U_0 = 10$ m/s, $BR = 69\%$ for the (a) $x$ and (b) $y$ traverses. . . . .	173
113	Mean and RMS velocity profiles for the 12 mm burner at $p = 5$ atm, $T = 300$ K, $U_0 = 10$ m/s, $BR = 75\%$ for the (a) $x$ and (b) $y$ traverses. . . . .	173
114	Mean and RMS velocity profiles for the 12 mm burner at $p = 5$ atm, $T = 300$ K, $U_0 = 10$ m/s, $BR = 81\%$ for the (a) $x$ and (b) $y$ traverses. . . . .	174
115	Mean and RMS velocity profiles for the 12 mm burner at $p = 5$ atm, $T = 300$ K, $U_0 = 10$ m/s, $BR = 87\%$ for the (a) $x$ and (b) $y$ traverses. . . . .	174
116	Mean and RMS velocity profiles for the 12 mm burner at $p = 5$ atm, $T = 300$ K, $U_0 = 10$ m/s, $BR = 93\%$ for the (a) $x$ and (b) $y$ traverses. . . . .	175
117	Mean and RMS velocity profiles for the 12 mm burner at $p = 5$ atm, $T = 300$ K, $U_0 = 30$ m/s, $BR = 69\%$ for the (a) $x$ and (b) $y$ traverses. . . . .	175
118	Mean and RMS velocity profiles for the 12 mm burner at $p = 5$ atm, $T = 300$ K, $U_0 = 30$ m/s, $BR = 75\%$ for the (a) $x$ and (b) $y$ traverses. . . . .	176
119	Mean and RMS velocity profiles for the 12 mm burner at $p = 5$ atm, $T = 300$ K, $U_0 = 30$ m/s, $BR = 81\%$ for the (a) $x$ and (b) $y$ traverses. . . . .	176
120	Mean and RMS velocity profiles for the 12 mm burner at $p = 5$ atm, $T = 300$ K, $U_0 = 30$ m/s, $BR = 87\%$ for the (a) $x$ and (b) $y$ traverses. . . . .	177
121	Mean and RMS velocity profiles for the 12 mm burner at $p = 5$ atm, $T = 300$ K, $U_0 = 30$ m/s, $BR = 93\%$ for the (a) $x$ and (b) $y$ traverses. . . . .	177
122	Mean and RMS velocity profiles for the 12 mm burner at $p = 5$ atm, $T = 300$ K, $U_0 = 30$ m/s, $BR = 95\%$ for the (a) $x$ and (b) $y$ traverses. . . . .	178
123	Mean and RMS velocity profiles for the 12 mm burner at $p = 5$ atm, $T = 300$ K, $U_0 = 50$ m/s, $BR = 69\%$ for the (a) $x$ and (b) $y$ traverses. . . . .	178
124	Mean and RMS velocity profiles for the 12 mm burner at $p = 5$ atm, $T = 300$ K, $U_0 = 50$ m/s, $BR = 75\%$ for the (a) $x$ and (b) $y$ traverses. . . . .	179
125	Mean and RMS velocity profiles for the 12 mm burner at $p = 5$ atm, $T = 300$ K, $U_0 = 50$ m/s, $BR = 81\%$ for the (a) $x$ and (b) $y$ traverses. . . . .	179
126	Mean and RMS velocity profiles for the 12 mm burner at $p = 5$ atm, $T = 300$ K, $U_0 = 50$ m/s, $BR = 87\%$ for the (a) $x$ and (b) $y$ traverses. . . . .	180
127	Mean and RMS velocity profiles for the 12 mm burner at $p = 5$ atm, $T = 300$ K, $U_0 = 50$ m/s, $BR = 93\%$ for the (a) $x$ and (b) $y$ traverses. . . . .	180
128	Mean and RMS velocity profiles for the 12 mm burner at $p = 5$ atm, $T = 427$ K, $U_0 = 50$ m/s, $BR = 69\%$ for the (a) $x$ and (b) $y$ traverses. . . . .	181

129	Mean and RMS velocity profiles for the 12 mm burner at $p = 5$ atm, $T = 427$ K, $U_0 = 50$ m/s, $BR = 81\%$ for the (a) $x$ and (b) $y$ traverses. . . . .	181
130	Mean and RMS velocity profiles for the 12 mm burner at $p = 5$ atm, $T = 427$ K, $U_0 = 50$ m/s, $BR = 93\%$ for the (a) $x$ and (b) $y$ traverses. . . . .	182
131	Mean and RMS velocity profiles for the 12 mm burner at $p = 5$ atm, $U_0 = 50$ m/s, for $T = 427$ K (solid lines) and $T = 300$ K (dashed lines) at (a) $BR = 69\%$ and (b) $BR = 93\%$ . . . . .	182
132	Mean and RMS velocity profiles for the 12 mm burner at $p = 10$ atm, $T = 300$ K, $U_0 = 10$ m/s, $BR = 69\%$ for the (a) $x$ and (b) $y$ traverses. . . . .	183
133	Mean and RMS velocity profiles for the 12 mm burner at $p = 10$ atm, $T = 300$ K, $U_0 = 10$ m/s, $BR = 75\%$ for the (a) $x$ and (b) $y$ traverses. . . . .	183
134	Mean and RMS velocity profiles for the 12 mm burner at $p = 10$ atm, $T = 300$ K, $U_0 = 10$ m/s, $BR = 81\%$ for the (a) $x$ and (b) $y$ traverses. . . . .	184
135	Mean and RMS velocity profiles for the 12 mm burner at $p = 10$ atm, $T = 300$ K, $U_0 = 10$ m/s, $BR = 87\%$ for the (a) $x$ and (b) $y$ traverses. . . . .	184
136	Mean and RMS velocity profiles for the 12 mm burner at $p = 10$ atm, $T = 300$ K, $U_0 = 10$ m/s, $BR = 93\%$ for the (a) $x$ and (b) $y$ traverses. . . . .	185
137	Mean and RMS velocity profiles for the 12 mm burner at $p = 10$ atm, $T = 300$ K, $U_0 = 27$ m/s, $BR = 69\%$ for the (a) $x$ and (b) $y$ traverses. . . . .	185
138	Mean and RMS velocity profiles for the 12 mm burner at $p = 10$ atm, $T = 300$ K, $U_0 = 27$ m/s, $BR = 75\%$ for the (a) $x$ and (b) $y$ traverses. . . . .	186
139	Mean and RMS velocity profiles for the 12 mm burner at $p = 10$ atm, $T = 300$ K, $U_0 = 27$ m/s, $BR = 81\%$ for the (a) $x$ and (b) $y$ traverses. . . . .	186
140	Mean and RMS velocity profiles for the 12 mm burner at $p = 10$ atm, $T = 300$ K, $U_0 = 27$ m/s, $BR = 87\%$ for the (a) $x$ and (b) $y$ traverses. . . . .	187
141	Mean and RMS velocity profiles for the 12 mm burner at $p = 10$ atm, $T = 300$ K, $U_0 = 27$ m/s, $BR = 93\%$ for the (a) $x$ and (b) $y$ traverses. . . . .	187
142	Mean and RMS velocity profiles for the 12 mm burner at $p = 20$ atm, $T = 300$ K, $U_0 = 10$ m/s, $BR = 69\%$ for the (a) $x$ and (b) $y$ traverses. . . . .	188
143	Mean and RMS velocity profiles for the 12 mm burner at $p = 20$ atm, $T = 300$ K, $U_0 = 10$ m/s, $BR = 81\%$ for the (a) $x$ and (b) $y$ traverses. . . . .	188
144	Mean and RMS velocity profiles for the 12 mm burner at $p = 20$ atm, $T = 300$ K, $U_0 = 10$ m/s, $BR = 93\%$ for the (a) $x$ and (b) $y$ traverses. . . . .	189
145	Mean and RMS velocity profiles for the 20 mm burner at $p = 1$ atm, $T = 300$ K, $U_0 = 4$ m/s, $BR = 69\%$ for the (a) $x$ and (b) $y$ traverses. . . . .	190
146	Mean and RMS velocity profiles for the 20 mm burner at $p = 1$ atm, $T = 300$ K, $U_0 = 4$ m/s, $BR = 73\%$ for the (a) $x$ and (b) $y$ traverses. . . . .	190

147	Mean and RMS velocity profiles for the 20 mm burner at $p = 1$ atm, $T = 300$ K, $U_0 = 4$ m/s, $BR = 75\%$ for the (a) $x$ and (b) $y$ traverses. . . . .	191
148	Mean and RMS velocity profiles for the 20 mm burner at $p = 1$ atm, $T = 300$ K, $U_0 = 4$ m/s, $BR = 77\%$ for the (a) $x$ and (b) $y$ traverses. . . . .	191
149	Mean and RMS velocity profiles for the 20 mm burner at $p = 1$ atm, $T = 300$ K, $U_0 = 4$ m/s, $BR = 81\%$ for the (a) $x$ and (b) $y$ traverses. . . . .	192
150	Mean and RMS velocity profiles for the 20 mm burner at $p = 1$ atm, $T = 300$ K, $U_0 = 4$ m/s, $BR = 83\%$ for the (a) $x$ and (b) $y$ traverses. . . . .	192
151	Mean and RMS velocity profiles for the 20 mm burner at $p = 1$ atm, $T = 300$ K, $U_0 = 4$ m/s, $BR = 85\%$ for the (a) $x$ and (b) $y$ traverses. . . . .	193
152	Mean and RMS velocity profiles for the 20 mm burner at $p = 1$ atm, $T = 300$ K, $U_0 = 4$ m/s, $BR = 89\%$ for the (a) $x$ and (b) $y$ traverses. . . . .	193
153	Mean and RMS velocity profiles for the 20 mm burner at $p = 1$ atm, $T = 300$ K, $U_0 = 4$ m/s, $BR = 91\%$ for the (a) $x$ and (b) $y$ traverses. . . . .	194
154	Mean and RMS velocity profiles for the 20 mm burner at $p = 1$ atm, $T = 300$ K, $U_0 = 4$ m/s, $BR = 93\%$ for the (a) $x$ and (b) $y$ traverses. . . . .	194
155	Mean and RMS velocity profiles for the 20 mm burner at $p = 1$ atm, $T = 300$ K, $U_0 = 30$ m/s, $BR = 69\%$ for the (a) $x$ and (b) $y$ traverses. . . . .	195
156	Mean and RMS velocity profiles for the 20 mm burner at $p = 1$ atm, $T = 300$ K, $U_0 = 30$ m/s, $BR = 75\%$ for the (a) $x$ and (b) $y$ traverses. . . . .	195
157	Mean and RMS velocity profiles for the 20 mm burner at $p = 1$ atm, $T = 300$ K, $U_0 = 30$ m/s, $BR = 81\%$ for the (a) $x$ and (b) $y$ traverses. . . . .	196
158	Mean and RMS velocity profiles for the 20 mm burner at $p = 1$ atm, $T = 300$ K, $U_0 = 30$ m/s, $BR = 87\%$ for the (a) $x$ and (b) $y$ traverses. . . . .	196
159	Mean and RMS velocity profiles for the 20 mm burner at $p = 1$ atm, $T = 300$ K, $U_0 = 30$ m/s, $BR = 93\%$ for the (a) $x$ and (b) $y$ traverses. . . . .	197
160	Mean and RMS velocity profiles for the 20 mm burner at $p = 1$ atm, $T = 300$ K, $U_0 = 50$ m/s, $BR = 69\%$ for the (a) $x$ and (b) $y$ traverses. . . . .	198
161	Mean and RMS velocity profiles for the 20 mm burner at $p = 1$ atm, $T = 300$ K, $U_0 = 50$ m/s, $BR = 75\%$ for the (a) $x$ and (b) $y$ traverses. . . . .	198
162	Mean and RMS velocity profiles for the 20 mm burner at $p = 1$ atm, $T = 300$ K, $U_0 = 50$ m/s, $BR = 81\%$ for the (a) $x$ and (b) $y$ traverses. . . . .	199
163	Mean and RMS velocity profiles for the 20 mm burner at $p = 1$ atm, $T = 300$ K, $U_0 = 50$ m/s, $BR = 87\%$ for the (a) $x$ and (b) $y$ traverses. . . . .	199
164	Mean and RMS velocity profiles for the 20 mm burner at $p = 1$ atm, $T = 300$ K, $U_0 = 50$ m/s, $BR = 93\%$ for the (a) $x$ and (b) $y$ traverses. . . . .	200
165	Mean and RMS velocity profiles for the 20 mm burner at $p = 5$ atm, $T = 339$ K, $U_0 = 50$ m/s, $BR = 69\%$ for the (a) $x$ and (b) $y$ traverses. . . . .	201

166	Mean and RMS velocity profiles for the 20 mm burner at $p = 5$ atm, $T = 339$ K, $U_0 = 50$ m/s, $BR = 75\%$ for the (a) $x$ and (b) $y$ traverses. . . . .	201
167	Mean and RMS velocity profiles for the 20 mm burner at $p = 5$ atm, $T = 339$ K, $U_0 = 50$ m/s, $BR = 81\%$ for the (a) $x$ and (b) $y$ traverses. . . . .	202
168	Mean and RMS velocity profiles for the 20 mm burner at $p = 5$ atm, $T = 339$ K, $U_0 = 50$ m/s, $BR = 87\%$ for the (a) $x$ and (b) $y$ traverses. . . . .	202
169	Mean and RMS velocity profiles for the 20 mm burner at $p = 5$ atm, $T = 339$ K, $U_0 = 50$ m/s, $BR = 93\%$ for the (a) $x$ and (b) $y$ traverses. . . . .	203
170	Mean and RMS velocity profiles for the 20 mm burner at $p = 5$ atm, $T = 515$ K, $U_0 = 50$ m/s, $BR = 69\%$ for the (a) $x$ and (b) $y$ traverses. . . . .	204
171	Mean and RMS velocity profiles for the 20 mm burner at $p = 5$ atm, $T = 515$ K, $U_0 = 50$ m/s, $BR = 75\%$ for the (a) $x$ and (b) $y$ traverses. . . . .	204
172	Mean and RMS velocity profiles for the 20 mm burner at $p = 5$ atm, $T = 515$ K, $U_0 = 50$ m/s, $BR = 81\%$ for the (a) $x$ and (b) $y$ traverses. . . . .	205
173	Mean and RMS velocity profiles for the 20 mm burner at $p = 5$ atm, $T = 515$ K, $U_0 = 50$ m/s, $BR = 87\%$ for the (a) $x$ and (b) $y$ traverses. . . . .	205
174	Mean and RMS velocity profiles for the 20 mm burner at $p = 5$ atm, $T = 515$ K, $U_0 = 50$ m/s, $BR = 93\%$ for the (a) $x$ and (b) $y$ traverses. . . . .	206
175	Mean and RMS velocity profiles for the 20 mm burner at $p = 10$ atm, $T = 330$ K, $U_0 = 50$ m/s, $BR = 69\%$ for the (a) $x$ and (b) $y$ traverses. . . . .	207
176	Mean and RMS velocity profiles for the 20 mm burner at $p = 10$ atm, $T = 330$ K, $U_0 = 50$ m/s, $BR = 75\%$ for the (a) $x$ and (b) $y$ traverses. . . . .	207
177	Mean and RMS velocity profiles for the 20 mm burner at $p = 10$ atm, $T = 330$ K, $U_0 = 50$ m/s, $BR = 81\%$ for the (a) $x$ and (b) $y$ traverses. . . . .	208

## NOMENCLATURE

$A$	Area.
$a_{ax}$	Normalized mean axial strain rate.
$a_c$	Confidence coefficient.
$A_f$	Average flame area.
$\alpha$	Thermal diffusivity.
$A_T$	Instantaneous flame area.
$\langle c \rangle$	Average progress variable.
$c$	Instantaneous progress variable.
$C_d$	Discharge coefficient.
<b>CTA</b>	Constant temperature (hotwire) anemometry.
$D$	Species diffusivity.
$d$	Burner diameter.
<b>DAQ</b>	Data acquisition.
$\delta_f$	Laminar flame thickness.
$\delta_{f,0}$	Unstretched laminar flame thickness.
$\delta_f _{S_{L,max}}$	Laminar flame thickness at $S_{L,max}$ .
$\Delta\tau$	Slot width for autocorrelation calculations.
<b>DLN</b>	Dry-Low-NO <sub>x</sub> .
<b>DNS</b>	Direct numerical simulations.
$\eta$	Progress variable normal coordinate.
<b>FBLP</b>	Flame brush leading point.
$\gamma$	Ratio of specific heats.
<b>HHC</b>	High hydrogen content.
$I_0$	Flame stretch factor.
<b>ICCD</b>	Intensified charge-coupled device.
<b>ILP</b>	Instantaneous leading point.
$K$	Proportionality constant.

$Ka$	Karlovitz number.
$\kappa$	Flame stretch rate.
$\kappa_c$	Flame curvature-induced stretch rate.
$\kappa_{crit}$	Flame critical stretch rate.
$\kappa_{ext}$	Flame extinction stretch rate.
$\kappa_s$	Flame tangential strain rate.
<b>KPP</b>	Kolmogorov-Petrovskii-Piskunov (theorem).
$l$	Characteristic length scale.
$l_0$	Integral length scale.
<b>LDV</b>	Laser Doppler velocimetry.
$Le$	Lewis number.
<b>LES</b>	Large eddy simulations.
$l_\eta$	Kolmogorov length scale.
$l_M$	Markstein length.
<b>LSB</b>	Low swirl burner.
$\dot{m}$	Mass flow rate.
$m$	Ratio of central channel to swirler mass flow rates.
$Ma$	Markstein number.
$\dot{m}_c$	Central channel mass flow rate.
$\dot{m}_s$	Swirler mass flow rate.
$\mu$	True mean value.
$MW$	Molecular weight.
$MW_{air}$	Molecular weight of air.
$MW_{fuel}$	Molecular weight of fuel.
$MW_{mix}$	Molecular weight of mixture.
$\vec{n}$	Unit normal vector.
$N$	number of samples.
<b>NO<sub>x</sub></b>	Nitrous Oxides.
$\nu$	Viscosity.

<b>OH-PLIF</b>	Hydroxyl radical planar laser-induced fluorescence.
$p$	Pressure.
<b>PDF</b>	Probability density function.
$\phi$	Equivalence ratio.
<b>PID</b>	Proportional-integral-derivative controller.
<b>PIV</b>	Particle image velocimetry.
<b>PLIF</b>	Planar laser-induced fluorescence.
$p_s$	Smoothing parameter for cubic smoothing splines.
$R$	Universal gas constant.
$\mathcal{R}$	Ratio of central channel to burner radii.
$\mathcal{R}$	Radius of curvature.
$\mathcal{R}_1$ <b>and</b> $\mathcal{R}_2$	Principal radii of curvature.
$R_b$	Burner radius.
$R_c$	Central channel radius.
$Re$	Reynolds number.
$Re_D$	Geometric Reynolds number.
$Re_{l_0}$	Turbulent Reynolds number.
$r_f$	Flame ball spatially-averaged radius.
$\rho$	Density.
$\rho_{ac}$	Autocorrelation function.
$\rho_u$	Density of the unburned reactant mixture.
$S$	Swirl number.
$s$	Arc length.
$SE_{\bar{x}}$	Standard error of the mean.
$\Sigma$	Flame surface density.
$S_L$	Laminar flame speed.
$S_{L,0}$	Unstretched laminar flame speed.
$S_{L,max}$	Maximum stretched laminar flame speed.
$S_T$	Turbulent flame speed.

$S_{T,GC}$	Turbulent global consumption speed.
$S_{T,GD}$	Turbulent global displacement speed.
$S_{T,LC}$	Turbulent local consumption speed.
$S_{T,LD}$	Turbulent local displacement speed.
<b>STP</b>	Standard temperature (300 K) and pressure (1 atm).
$s_x$	Sample standard deviation.
$T$	Temperature.
$\tau_c$	Flame chemical timescale.
$\tau_\eta$	Kolmogorov timescale.
$\tau_{flow}$	Bulk flow timescale.
$\tau_{int}$	Integral timescale.
$\tau_{max}$	Maximum lag time for autocorrelation calculation.
$\tau_{S_{L,max}}$	Chemical time scale associated with $S_{L,max}$ .
$\theta$	Swirler vane angle.
$T_p$	Product temperature.
$T_r$	Reactant temperature.
$u'$	Turbulence intensity.
$\vec{u}$	Reactant velocity.
$u$	Axial velocity.
$U_0$	Bulk flow velocity.
$u'_{ax}$	Axial turbulence intensity.
$u'_{azi}$	Azimuthal turbulence intensity.
$U_{azi}$	Mean azimuthal flow velocity.
$\vec{U}_f$	Mean flame brush velocity (lab referenced).
$u'_{LP}$	Leading point turbulence intensity.
$\vec{U}_r$	Mean reactant velocity (lab referenced).
$u'_{rad}$	Radial turbulence intensity.
$U_{rad}$	Mean radial flow velocity.
$u'_{rms}$	Total turbulence intensity.

$w$	Azimuthal velocity.
$\bar{x}$	Sample mean.
$y_0$	virtual origin of the low swirl burner.
$y_f$	axial location of flame brush leading edge.

## SUMMARY

Increasingly stringent pollution and emission controls have caused a rise in the use of combustors operating under lean, premixed conditions. Operating lean (excess air) lowers the level of nitrous oxides ( $\text{NO}_x$ ) emitted to the environment. In addition, concerns over climate change due to increased carbon dioxide ( $\text{CO}_2$ ) emissions and the need for energy independence have spurred interest in developing combustors capable of operating with a wide range of fuel compositions. One method to decrease the carbon footprint of modern combustors is the use of high hydrogen content (HHC) fuels.

The objective of this research is to develop tools to better understand the physics of turbulent flame propagation in highly stretch sensitive premixed flames in order to predict their behavior at conditions realistic to the environment of gas turbine combustors. The propagation rate of turbulent premixed flames into unburned reactants is characterized by a parameter known as the turbulent flame speed,  $S_T$ .  $S_T$  has a leading order impact on important combustor phenomena such as the life of hot section components, flashback and blowoff limits, and the operating limits before damaging combustion dynamics occur [85].

This thesis presents the results of an experimental study into the flame propagation characteristics of highly stretch-sensitive, turbulent premixed flames generated in a low swirl burner (LSB). This study uses a scaling law, developed in an earlier thesis [134] from leading point concepts for turbulent premixed flames, to collapse turbulent flame speed data over a wide range of conditions. The flow and flame structure are characterized using high speed particle image velocimetry (PIV) over a wide range of fuel compositions, mean flow velocities, and turbulence levels. The first part of this study looks at turbulent flame speeds for these mixtures and applies the previously developed leading points scaling model in order to test its validity in an alternate geometry. The model was found to collapse the turbulent flame speed data over a wide range of fuel compositions and turbulence levels, giving merit to the leading points model as a method that can produce meaningful results

with different geometries and turbulent flame speed definitions.

The second part of this thesis examines flame front topologies and stretch statistics of these highly stretch sensitive, turbulent premixed flames. Instantaneous flame front locations and local flow velocities are used to calculate flame curvatures and tangential strain rates. Statistics of these two quantities are calculated both over the entire flame surface and also conditioned at the leading points of the flames. Results presented do not support the arguments made that the leading points are critically stretched. Only minor effects of fuel composition are noted on curvature statistics, which are mostly dominated by the turbulence. There is a stronger sensitivity for tangential strain rate statistics, however, time-averaged values are still well below the values hypothesized from the leading points model. The results of this study emphasize the importance of local flame topology measurements towards the development of predictive models of the turbulent flame speed.

# CHAPTER I

## INTRODUCTION

### *1.1 Motivation*

For the past several decades, increasingly stringent pollution and emission controls have caused a rise in the use of combustors operating under lean, premixed conditions. Operating lean (excess air) lowers the level of nitrous oxides ( $\text{NO}_x$ ) emitted to the environment [38]. However, operating lean does not come without its disadvantages. Combustors operating under lean conditions are more susceptible to damaging combustion instabilities [35]. In addition, concerns over climate change due to increased carbon dioxide ( $\text{CO}_2$ ) emissions and the need for energy independence in the United States have spurred interest in developing combustors capable of operating with a wide range of fuel compositions [85]. One possible solution to decrease the carbon footprint of modern combustors is the use of high hydrogen content (HHC) fuels. While these fuels offer the opportunity to reduce pollutant and  $\text{CO}_2$  emissions, their burning characteristics are not currently well understood. One parameter that is particularly important to the understanding of turbulent burning characteristics is the turbulent flame speed. A large focus of this research is on developing better tools and models to measure and predict turbulent flame speeds over conditions realistic to the burning environment of gas turbine combustors.

The objective of this research is to improve the understanding of turbulent flame propagation characteristics of high stretch sensitivity, premixed flames. The propagation rate of turbulent flames into unburned reactants is characterized by a parameter known as the turbulent flame speed,  $S_T$ . The turbulent flame speed has a leading order impact on important combustor phenomena such as the life of hot section components, flashback and blowoff limits, and the operating limits before damaging combustion dynamics occur [85]. The life of components such as the combustor liner and fuel nozzle is determined by their thermal loading, which is affected by the proximity of the flame to the components. The

proximity of the flame to these components is directly related to the flame length; a parameter controlled by the turbulent flame speed and reactant flow rate. Flashback occurs when the flame propagates upstream of its attachment point into a region of the combustor not designed for high temperature operation, causing serious damage. Blowoff is the opposite of flashback. This phenomenon occurs when the flame detaches from its stabilization point and is blown out of the combustor. The propensity of a flame to flashback or blowoff is influenced by the incoming mass flow rate of reactants and the turbulent flame speed. The turbulent flame speed also exhibits a leading order influence on combustion dynamics, the coupling between pressure oscillations in the combustor and heat release oscillations in the flame, due to its effect on the flame shape [86].

The rest of this chapter presents an overview of the theoretical background for this research, a review of relevant literature, and an overview of the scope and organization of the thesis.

## ***1.2 Theoretical Background***

This section presents an overview of the main theoretical concepts used in this thesis. These include an overview of turbulent premixed flames and the concept of flame stretch and its effects on flame propagation. These sections will present the most important concepts for this thesis, however, numerous literature exists on these topics; see Poinso and Veynante [110], Law [79], and Peters [106] for more detailed coverage of the topics presented.

### **1.2.1 Turbulent Premixed Flames**

Turbulent premixed flames are of significant practical interest towards the development and understanding of modern, Dry-Low-NO<sub>x</sub> (DLN) burners for gas turbines and industrial burners. Operating under lean conditions does not come without side effects, however, with issues arising from flame stabilization and combustion instabilities. In addition, little is known about the effects of changing fuel compositions on these and other important combustor parameters. Therefore, an understanding of turbulent premixed flames and their properties is important for the continued development of fuel-flexible combustors generating lower emissions.

### 1.2.1.1 The Turbulent Flame Speed

In laminar premixed flames, mixing occurs through molecular diffusion processes only. The important scales are the flame thickness,  $\delta_{f,0}$ , and the flame speed,  $S_{L,0}$ . In turbulent premixed flames, however, the flame interacts with turbulent eddies, resulting in a wide range of length and time scales. The turbulence acts to wrinkle the laminar flame front, leading to an increase in the rate of consumption of reactants. To characterize this increase in reactant consumption, the concept of the turbulent flame speed,  $S_T$ , was introduced. The most basic definition of the turbulent flame speed is that it is the average flow velocity needed to keep a flame stationary in a fixed control volume [110]. This concept is illustrated in the graphic shown in Figure 1. In this figure,  $A_f$  is the inlet area of the control volume,  $A_T$  is the instantaneous flame area, and  $S_L$  is the local flame speed. For this simple representation, it is assumed that locally the flame is propagating at the laminar flame speed. Using this control volume and the continuity equation, the turbulent flame speed is defined as [110]:

$$S_T = \frac{A_T}{A_f} S_L \quad (1)$$

Since  $A_T > A_f$ , the turbulent flame speed is always larger than the laminar flame speed. Damköhler hypothesized that turbulent flames propagated locally at the unstretched laminar flame speed,  $S_{L,0}$ , and that the flame area increased linearly with turbulence intensity,  $u'$ , leading to the following simple correlation [40]:

$$\frac{S_T}{S_{L,0}} \approx 1 + \frac{u'}{S_{L,0}} \quad (2)$$

This simple model captures the basic physics of the problem, however, it misses some important physical mechanisms. First, the laminar flame speed,  $S_L$ , is not constant and will vary spatially and temporally as a function of the local flame stretch rate  $\kappa$ , discussed in more detail in Section 1.2.2. These stretch effects on  $S_T$  are generally observed when changing fuel composition and are commonly referred to as fuel effects on  $S_T$ . An example of these fuel effects is presented in Figure 2 from the work of Nakahara and Kido [97]. In this dataset, the unstretched laminar flame speed,  $S_{L,0}$ , was held constant by simultaneously

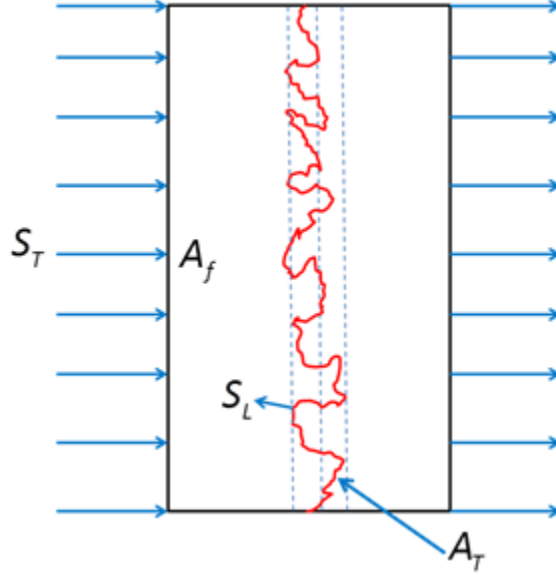


**Figure 1:** Graphical depiction of the turbulent flame speed,  $S_T$ .

adjusting both the equivalence ratio,  $\phi$ , and the fuel composition. According to Equation 2, all these mixtures should have the same  $S_T$ , however, they observed an approximate doubling of  $S_T$  at a given  $u'$  from the lowest  $S_T$  to the highest.

Second, a number of experimental datasets show that the turbulent flame speed does not continue to increase linearly with turbulence intensity at higher turbulence intensities [50]. Instead, as turbulence increases,  $S_T$  begins to flatten, commonly known as the “bending effect,” (and in some cases decreases) before finally quenching. This phenomenon is demonstrated in Figure 3, reproduced from Lipatnikov and Chomiak [88] with original data by Karpov and Severin [65]. While the bending effect is fairly common, it is not always observed in experimental data. For example, Littlejohn et al. [90] reported a linear increase in  $S_T$  over a very wide range of  $u'$ , as shown in Figure 4.

The phenomena discussed in the previous paragraphs and exemplified in Figures 2-4 show that  $S_T$  cannot be characterized solely by  $u'$  and  $S_{L,0}$ ; it is also affected by turbulent length scales [7, 78], experimental configuration [50, 28], and, as discussed in Section 1.1, fuel composition [88, 97, 70]. These factors will be discussed in further detail in the subsequent sections.

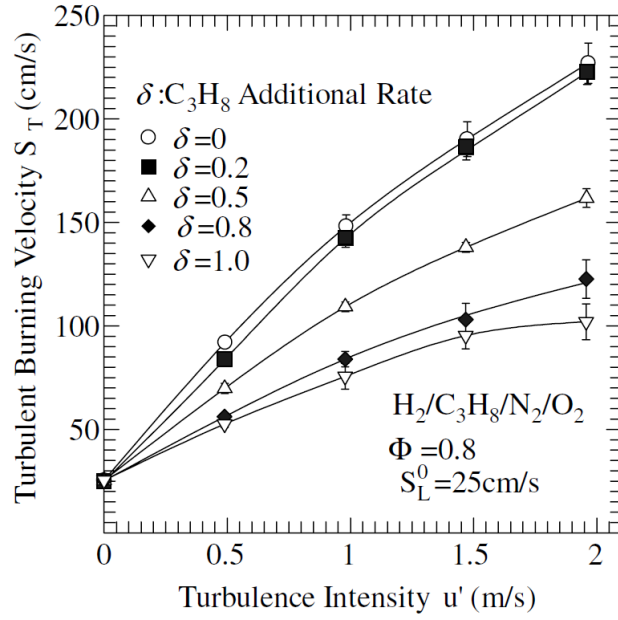


**Figure 2:** Example dataset demonstrating the fuel effect on the turbulent flame speed [97].

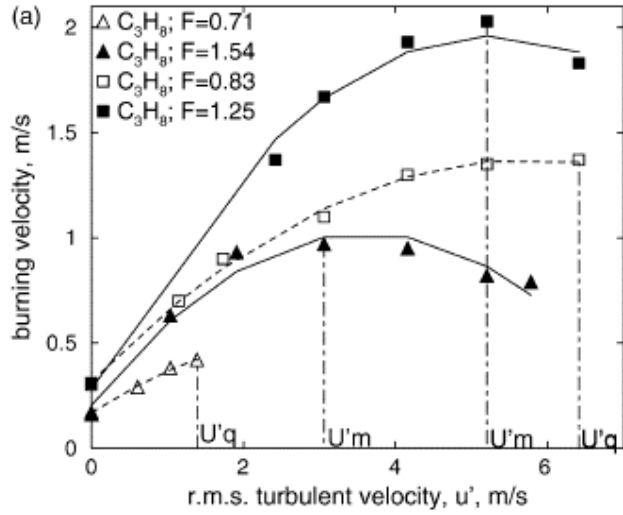


**Figure 3:** Example dataset demonstrating the “bending effect” on the turbulent flame speed [88].

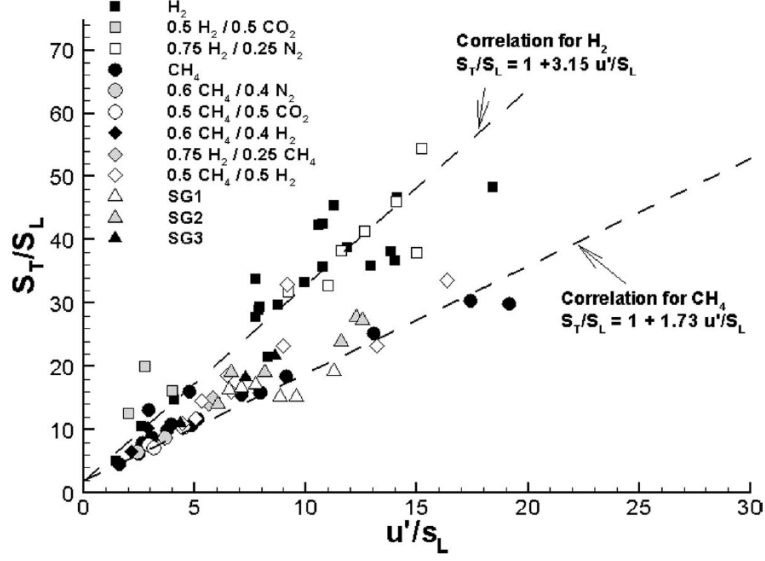


**Figure 4:** Example dataset that does not exhibit the “bending effect” on  $S_T$  [90].

### 1.2.1.2 The Regimes of Turbulent Combustion

The manner in which turbulence can modify the flame front is affected by the length and velocity scales of the turbulence in relation to the length and velocity scales of the laminar flame front. To compare these scales, a combustion regime diagram was created by Borghi [13], that plotted the ratio of the turbulence intensity,  $u'$ , and laminar flame speed,  $S_{L,0}$ , against the ratio of the turbulent integral length scale,  $l_0$ , and the laminar flame thickness,  $\delta_{f,0}$ . A version of this diagram with modifications proposed by Peters [105] is presented in Figure 5.

This diagram is divided into five regions separated by solid lines: laminar flames, wrinkled flamelets, corrugated flamelets, thin reaction zones, and broken reaction zones:

- The laminar flames region is characterized as laminar premixed combustion where  $Re_{l_0} < 1$ .  $Re_{l_0}$  is the turbulent Reynolds number and is defined as:

$$Re_{l_0} = \frac{u'l_0}{\nu} = \frac{u'}{S_{L,0}} \frac{l_0}{\delta_{f,0}} \quad (3)$$

where  $\nu$  is the viscosity and the relation  $\delta_{f,0} = \nu/S_{L,0}$  has been used.

- The flamelets region is where  $Ka < 1$ . The Karlovitz number,  $Ka$ , is defined as the ratio of the flame chemical time,  $\tau_c$ , to the timescale of turbulent mixing at the

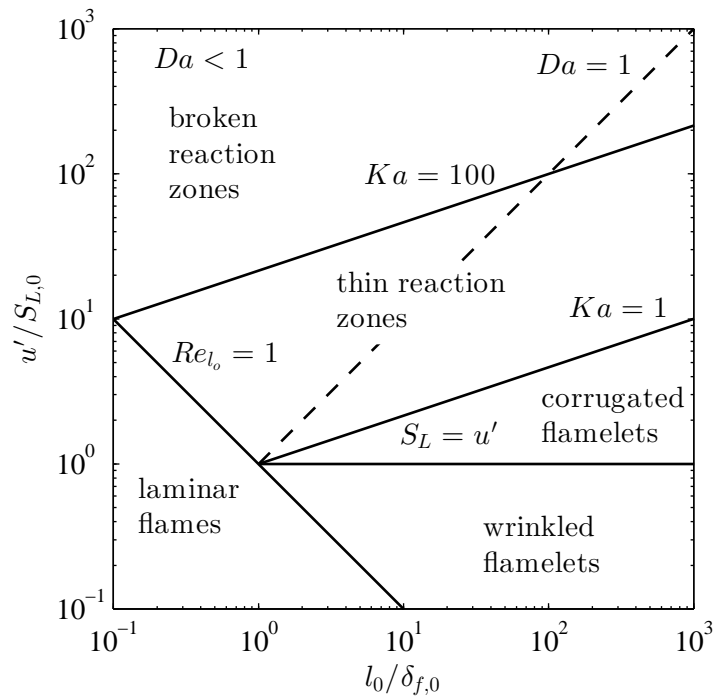


**Figure 5:** Turbulent combustion regime diagram created by Borghi [13] with modifications from Peters [105]

smallest scales, the kolmogorov timescale  $\tau_\eta$  [110]:

$$Ka = \frac{\tau_c}{\tau_\eta} = \frac{\delta_{f,0}/S_{L,0}}{(\delta_{f,0}S_{L,0}l_0)^{1/2}/(u')^{3/2}} = \left(\frac{l_0}{\delta_{f,0}}\right)^{-1/2} \left(\frac{u'}{S_{L,0}}\right)^{3/2} \quad (4)$$

In this region the flame chemistry is occurring faster than all scales of the turbulence, which means that the turbulence cannot affect the flame structure; it can only modify the flame topology. Locally, the flame is propagating like a laminar flame. This region can be subdivided further into:

- wrinkled flamelets: in this region the turbulent fluctuations,  $u'$ , are slower than the chemistry,  $S_{L,0}$ . The turbulence can only wrinkle the flame front.
  - corrugated flamelets: in this region the turbulent fluctuations,  $u'$ , are faster than the chemistry,  $S_{L,0}$ . In this regime the wrinkling becomes strong enough to form pockets of reactants and products.
- The thin reactions zone is characterized by turbulent eddies that are small enough to disrupt the preheat zone of the flame, but are not small enough to affect the structure of the reaction zone. In this manner, the reaction zone of the flame still behaves like a wrinkled, laminar reaction zone. The smallest eddies in turbulence are characterized by the Kolmogorov length scale,  $l_\eta$ , which is related to the largest scale through the turbulent Reynolds number:

$$\frac{l_0}{l_\eta} = Re_{l_0}^{3/4} \quad (5)$$

Thus, as the Reynolds number increases the range of scales increases in turbulent flows. If the Kolmogorov scale is larger than the reaction zone thickness, the turbulence does not affect the reaction zone of the flame. For most turbulent flames, the reaction zone can be estimated to be about one tenth of the total flame thickness. Using this rough order of magnitude approximation we can estimate the upper bound of the

thin reaction zones regime:

$$\frac{l_0}{\delta_{f,0}/10} = \left( \frac{u'}{S_{L,0}} \frac{l_0}{\delta_{f,0}} \right)^{3/4} \quad (6)$$

$$100 = \left( \frac{l_0}{\delta_{f,0}} \right)^{-1/2} \left( \frac{u'}{S_{L,0}} \right)^{3/2} \quad (7)$$

$$Ka = 100 \quad (8)$$

- The broken reactions zone is characterized by turbulent features that are small enough to enter and disrupt the reaction zone of the flame. At this point, the mixing occurs so quickly that the overall reaction rate is limited only by the chemical timescales. The behavior in this region is usually approximated with a well-stirred reactor model [110].

One method by which the behavior of a turbulent premixed flame can change is due to the presence of quenching. Quenching occurs along a flame front when the flame experiences high levels of heat loss or strain, causing pockets of the flame front where no burning is occurring. In the flamelets region of the turbulent combustion diagram the flame surface is continuous; no quenching occurs because the scales of turbulence are not small enough to disrupt the flame. Because of this, the rate at which reactants are consumed increases proportionally to the increase in surface area. This is a common explanation for the linear increase of the turbulent flame speed with turbulence intensity at low  $u'$ . As the turbulence scales become smaller, they are able to enter the flame zone and cause local quenching. At this point the flame surface area is no longer increasing linearly with turbulence intensity, and this is often used to explain the “bending effect” discussed earlier.

In this research, the primary location of the data analyzed will be within the flamelets and thin reaction zone regimes. In these regimes the flame propagates locally like wrinkled laminar flames, or flamelets [104]. Thus, the behavior of the turbulent flame can be modeled as the ensemble average of a large number of flamelets that occupy a finite volume of space. This volume of space is known as the flame brush and is illustrated for a Bunsen burner configuration in Figure 6.

It is important to note that at a given time the probability of finding the flame surface

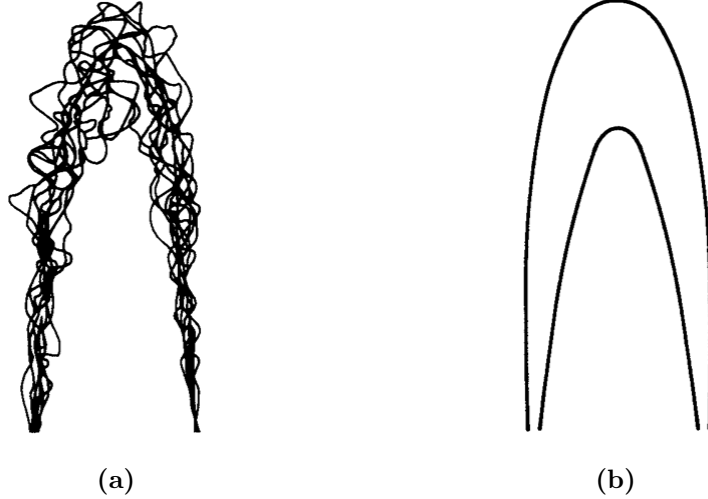


**Figure 6:** (a) Ensemble of flamelets that occupy a finite volume of space known as (b) the turbulent flame brush. Figure reproduced from Turns [131].

at any location inside the flame brush is not uniform. In other words, there is a probability distribution of the flame location and this probability decreases to zero at the boundaries of the flame brush. The cumulative distribution of the flame location will be zero at the boundary of the flame brush and the reactants, and will be one at the boundary of the flame brush and the products. This cumulative distribution is referred to as the average progress variable  $\langle c \rangle$  because it is a measure of the progress of the reaction, with one corresponding to completely burnt and zero corresponding to completely unburned. Instantaneously, the progress variable can be defined in terms of the temperature as:

$$c = \frac{T - T_r}{T_p - T_r} \quad (9)$$

where  $T$  is the temperature, and the subscripts  $r$  and  $p$  refer to reactants and products, respectively. The average progress variable field is a useful parameter for determining turbulent flame properties. For example, it is used in defining equations to experimentally determine the turbulent flame speed as discussed in the subsequent section.

### 1.2.1.3 Turbulent Flame Speed Definitions and Measurement Approaches

The measurement of the turbulent flame speed is also affected by experimental parameters including the velocity distribution, the size of the burner, the geometry, and the boundary

conditions [28]. As an example of the large amount of scatter that results in turbulent flame speed data without consideration of burner geometry, consider the compilation assembled by Bradley [14] presented in Figure 7. This figure presents correlation lines for over 1650 turbulent flame speed measurements taken from v-flame geometries, Bunsen burners, and spherical bombs. To address the high degree of scatter and inconsistencies introduced through the use of different experimental techniques, a group of researchers through a series of workshops developed a set of guidelines for different turbulent flame speed measurement approaches [56]. From these workshops, four definitions of the turbulent flame speed were proposed:

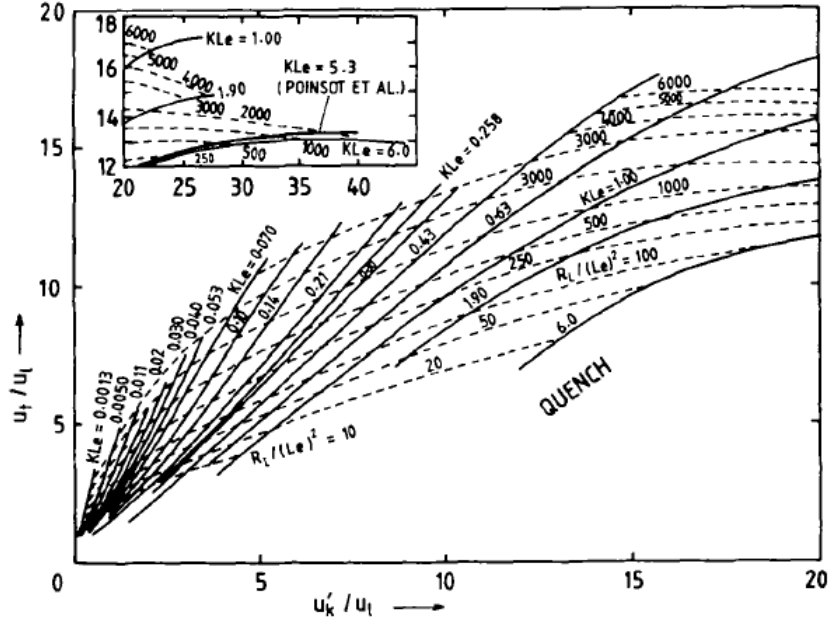


**Figure 7:** Correlation of turbulent flame speed data developed by Bradley [14] from approximately 1650 turbulent flame speed measurements.

- **Turbulent local displacement speed,  $S_{T,LD}$ :** Measures the local propagation velocity of the turbulent flame brush,

$$S_{T,LD} = \left( \vec{U}_f - \vec{U}_r \right) \cdot \vec{n} \quad (10)$$

where  $\vec{U}_f$  and  $\vec{U}_r$  are the velocities of the flame brush and reactants, respectively, in the lab-referenced coordinate system, and  $\vec{n}$ , the flame unit normal vector, is pointing

towards the reactants. This definition is depicted graphically in Figure 8. These quantities are generally taken at the leading edge of the turbulent flame brush (i.e.,  $\langle c \rangle \rightarrow 0$ ) [50]. Burner geometries that use this definition of the turbulent flame speed include v-flame, stagnation flow, and low swirl burners [28].

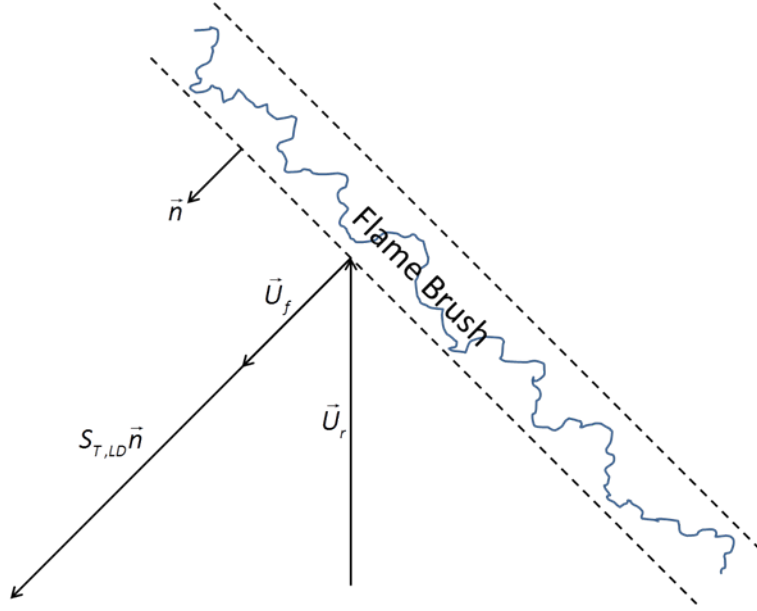


**Figure 8:** Definition of the turbulent local displacement speed,  $S_{T,LD}$ .

- **Turbulent local consumption speed,  $S_{T,LC}$ :** Measures the local rate of consumption of reactants,

$$S_{T,LC} = S_{L,0} I_0 \int_{-\infty}^{\infty} \Sigma d\eta \quad (11)$$

where  $I_0$  is the stretch factor,  $\Sigma$  is the flame surface density, and  $\eta$  is the progress variable normal coordinate. The stretch factor  $I_0$  accounts for the effects of flame stretch on the laminar flame speed  $S_L$ , and the flame surface density  $\Sigma$  is the flame surface to volume ratio [16].

- **Turbulent global displacement speed,  $S_{T,GD}$ :** Measures the spatially averaged propagation velocity of the turbulent flame brush,

$$S_{T,GD} = \frac{\partial r_f}{\partial t} - \vec{U}_r \cdot \vec{n} \quad (12)$$

and is used in spherically expanding flames where  $r_f$  is the spatially-averaged flame radius.

- **Turbulent global consumption speed,  $S_{T,GC}$ :** Measures the total average rate of consumption of reactants by the turbulent flame,

$$S_{T,GC} = \frac{\dot{m}}{\rho_u A_f} \quad (13)$$

where  $\dot{m}$  is the mass flow rate of reactants and  $\rho_u$  is the density of the unburned reactant mixture. This definition is also illustrated in Figure 1. This method of determining the turbulent flame speed requires that all of the reactants pass through the flame and is typically used for envelope flame configurations, such as Bunsen burners. One issue that can cause disagreement between turbulent flame speed data acquired using this approach is the choice of the average progress variable value  $\langle c \rangle$  used to determine the average flame area  $A_f$ . For the statistically 1D representation presented in Figure 1, the area is the same regardless. However, for real flames, like the Bunsen flame depicted in Figure 6, the average area  $A_f$  will depend on this choice. Driscoll recommends using the  $\langle c \rangle = 0.5$  contour [50].

### 1.2.2 Flame Stretch

For 1D, laminar premixed flames the flame surface propagates into the reactants at the unstretched laminar flame speed  $S_{L,0}$ . However, most real flames are not 1D but are curved, strained by the flow, and unsteady, leading to a misalignment of the streamlines and diffusion lines. This misalignment of streamlines and diffusion lines is known as flame stretch, and, depending on the circumstances, can strengthen, weaken, or have no effect on the flame surface. Flame stretch becomes significant when there are large differences between (1) thermal and species diffusivities, known as *non-unity Lewis number effects*, or (2) species diffusivities, known as *preferential diffusion effects*. These two effects are illustrated in Figure 9 and will be discussed further in subsequent paragraphs.

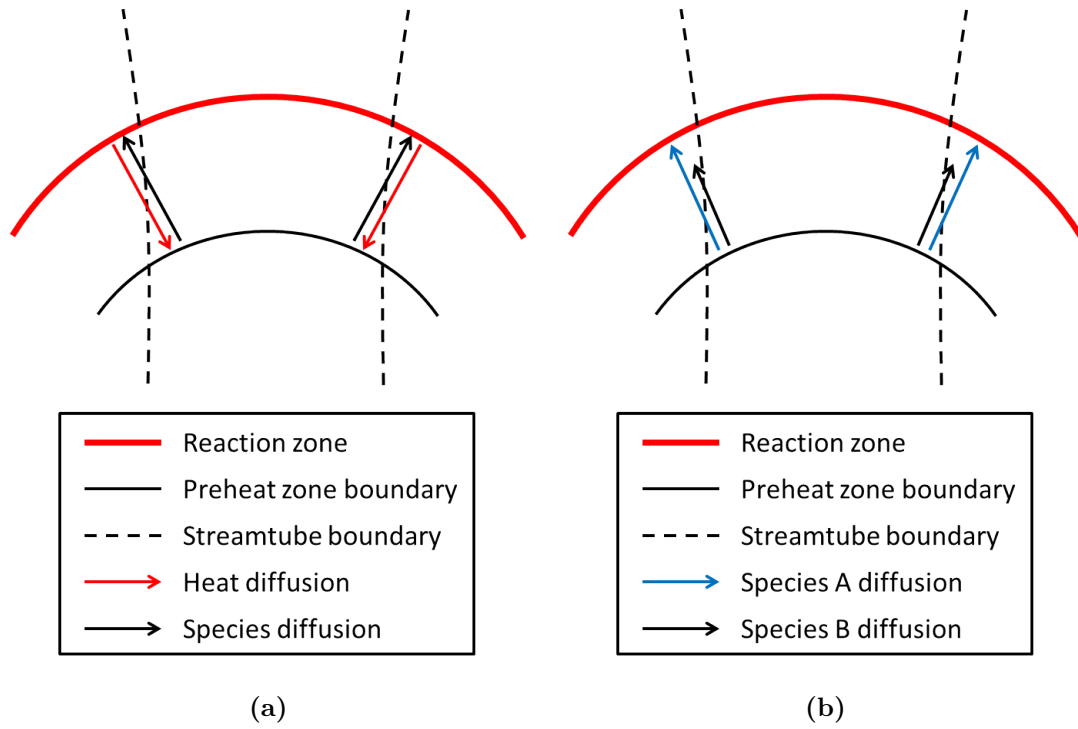


**Figure 9:** Depictions of flame stretch from (a) non-unity Lewis number effects and (b) preferential diffusion effects.

### 1.2.2.1 Flame Stretch Rate Definition

The flame stretch rate is defined by Williams [137] as the material derivative of the logarithm of the flame surface area:

$$\kappa = \frac{1}{A} \frac{DA}{Dt} \quad (14)$$

There are two basic cases of stretch: (1) positive stretch (expanding flame area), and (2) negative stretch (compressed flame area). An infinitesimal flame area element is considered positively (negatively) stretched when its area increases (decreases) over time. It is important to note that even steady flames can be stretched, even if it appears that their area is not changing in time. Consider the tip of a Bunsen flame, which is similar to the situation presented in Figure 9. Drawing flame tangential velocity components along the stream-tube boundaries shows that the flame element is being compressed, and, thus, is negatively stretched. A second example is presented in Figure 10 for a stagnation flame geometry. In this example the flame area is exposed to a positive velocity gradient of magnitude  $a$ , making this a positively stretched flame.

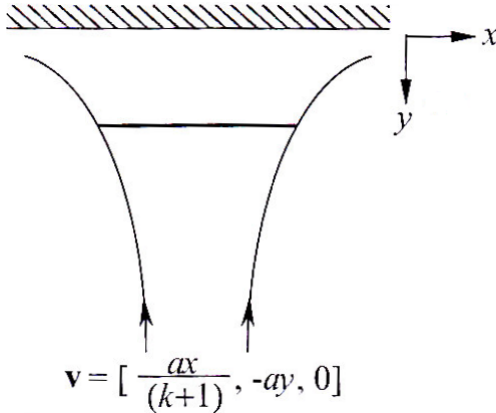


**Figure 10:** Positively stretched stagnation flame model with  $k = 0, 1$  for Cartesian and cylindrical coordinates, respectively. Figure reproduced from [79].

Assuming an infinitely thin flame sheet, Equation 14 can be expanded and manipulated to obtain [19, 110]:

$$\kappa = -\vec{n}\vec{n} : \nabla\vec{u} + \nabla \cdot \vec{u} + S_L(\nabla \cdot \vec{n}) \quad (15)$$

where  $\vec{u}$  is the reactant velocity. The first two terms in this expression are the tangential

strain rate,  $\kappa_s$ , and the third term is the stretch rate contribution due to flame curvature,  $\kappa_c$ . The term  $\nabla \cdot \vec{n}$  is the flame curvature and can be related to the principal radii of curvature  $\mathcal{R}_1$  and  $\mathcal{R}_2$  through:

$$\nabla \cdot \vec{n} = \frac{1}{\mathcal{R}_1} + \frac{1}{\mathcal{R}_2} \quad (16)$$

where the radii of curvature are positive when convex to the reactants.

As discussed earlier, flame stretch manifests itself as a misalignment of streamlines and diffusion lines. It can affect the behavior of the flame through non-unity Lewis number effects and preferential diffusion effects. The next two sections will detail the physical mechanisms behind these two effects to show how they can change the structure of the flame, and, thus, affect the laminar flame speed  $S_L$ .

#### 1.2.2.2 *Non-unity Lewis Number Effects*

Non-unity Lewis number effects become important when there are large differences between thermal and species diffusivities [79]. The Lewis number  $Le$  is defined as:

$$Le = \frac{\alpha}{D} \quad (17)$$

where  $\alpha$  and  $D$  are the thermal and species diffusivities, respectively. The thermal diffusivity is a mixture-averaged value, whereas the species diffusivity chosen is that of the deficient reactant species. This convention is chosen because the deficient species will have a steeper gradient at the flame front and will diffuse faster. Thus, when the flame is lean, the diffusivity of the fuel is chosen, and when the flame is rich, the diffusivity of the oxidizer is chosen. When a flame is negatively stretched, as shown in Figure 9, heat conducts into the control volume defined by the streamtube boundaries and enhances the laminar flame speed  $S_L$ . Conversely, the deficient species will diffuse out of the control volume, moving the equivalence ratio away from unity and diminishing  $S_L$ . With unity Lewis number, the increased energy from the added heat is canceled out by the loss of the deficient species and  $S_L$  remains unchanged. However, if  $Le < 1$ , species diffusion outweighs thermal conduction and  $S_L$  decreases. If  $Le > 1$ , thermal conduction outweighs species diffusion and  $S_L$  increases.

The magnitude of the Lewis number will depend on the molecular weight of the fuel  $MW_{fuel}$  in relation to air  $MW_{air}$  and the equivalence ratio  $\phi$ . First consider a negatively stretched flame, such as that shown in Figure 9:

- **If the fuel is lighter than air**, then  $MW_{fuel} < MW_{mix} < MW_{air}$ . The mixture molecular weight  $MW_{mix}$  is important because the Lewis number uses the mixture thermal diffusivity. For lean mixtures,  $\phi < 1$ ,  $Le = \alpha/D_{fuel} < 1$  and the fuel will diffuse faster than the heat will conduct. This corresponds to  $S_L/S_{L,0} < 1$  that decreases with decreasing  $\phi$ . For rich mixtures,  $\phi > 1$ ,  $Le = \alpha/D_{air} > 1$ ,  $S_L/S_{L,0} > 1$  and increases with increasing  $\phi$ .
- **If the fuel is heavier than air**,  $MW_{fuel} > MW_{mix} > MW_{air}$ . For  $\phi < 1$ ,  $Le = \alpha/D_{fuel} > 1$ . This corresponds to  $S_L/S_{L,0} > 1$  that increases with decreasing  $\phi$ . For rich mixtures,  $\phi > 1$ ,  $Le = \alpha/D_{air} < 1$ ,  $S_L/S_{L,0} < 1$  and decreases with increasing  $\phi$ .

Similar arguments can be made for a positively stretched flame, as shown in Figure 10, to show that the opposite behaviors occur. For clarity, these results are summarized in Tables 1 and 2.

**Table 1:** Dependence of Lewis number on equivalence ratio and molecular weight of fuel.

	Lean ( $\phi < 1$ )	Rich ( $\phi > 1$ )
$MW_{fuel} < MW_{air}$	$Le < 1$	$Le > 1$
$MW_{fuel} > MW_{air}$	$Le > 1$	$Le < 1$

**Table 2:** Effect of flame stretch on the laminar flame speed for different Lewis number.

	$Le < 1$	$Le = 1$	$Le > 1$
$\kappa < 0$	$S_L < S_{L,0}$	$S_L = S_{L,0}$	$S_L > S_{L,0}$
$\kappa > 0$	$S_L > S_{L,0}$	$S_L = S_{L,0}$	$S_L < S_{L,0}$

### 1.2.2.3 Preferential Diffusion Effects

Preferential diffusion effects become important when there are large differences in species diffusivities and the mixture is near-stoichiometric [79], where non-unity Lewis number effects are weak. Consider, for example, a  $\text{H}_2$ :air mixture burning in a Bunsen burner, similar to the situation depicted in Figure 9. At the tip of the flame, both species will diffuse out of the control volume as shown in Figure 9b. Since  $\text{H}_2$  has a much higher diffusivity than air, the  $\text{H}_2$  will diffuse out faster. The equivalence ratio at the tip will decrease and  $S_L$  will decrease if the mixture is lean and increase if the mixture is rich. The opposite effects will occur if the fuel is heavier than the air. For positive stretch, such as that shown in Figure 10, both species will diffuse into the control volume, with the lighter one diffusing faster. For the  $\text{H}_2$ :air example, the equivalence ratio will increase, causing  $S_L$  to increase if the mixture is lean and decrease if the mixture is rich.

### 1.2.2.4 Stability of Perturbed Flames

Another aspect to consider when determining the response of a flame to stretch is whether these perturbations to the flame area will grow or decay over time. If the perturbations decay over time the flame is said to be thermodiffusively stable, whereas, if the perturbations grow the flame is thermodiffusively unstable. This is an important concept, for example, in the study of turbulent premixed flames where it is observed that the turbulent flame speed is enhanced for thermodiffusively unstable mixtures [88]. To determine the stability of a flame, first consider the response due to heat conduction. For a positively curved bump on a flat flame, the heat will be defocused from the center of the bump. This will cause the laminar flame speed at the tip of the bump to decrease and the bump will decay. For a negatively curved bump on a flat flame the heat will be focused to the center of the bump and the bump will speed up and also decay. Thus, heat conduction always causes perturbations to decay. For species diffusion, a positively curved bump will focus the deficient reactant to the tip of the bump, causing the perturbation to grow in time. For a negatively curved bump, the deficient reactant will diffuse away from the center of the bump and the bump will slow down further, causing the perturbation to grow. Species diffusion will always

cause perturbations to grow. Thus, a flame will be thermodiffusively stable if  $Le \geq 1$  and thermodiffusively unstable if  $Le < 1$ . From Table 1, this corresponds to light fuels in lean mixtures or heavy fuels in rich mixtures.

#### 1.2.2.5 Flame Stretch Rate Calculations

To this point, the discussion of flame stretch has centered around trends and physical arguments to describe the flame's behavior when subjected to stretch. The purpose of this section is to provide a more rigorous and quantitative understanding of the flame's response. Through asymptotic analyses, a first order expression for the laminar flame speed can be developed for weakly stretched flames [137]:

$$S_L = S_{L,0} - l_M \kappa \quad (18)$$

where  $l_M$  is the Markstein length, a measure of the sensitivity of the flame speed to stretch. The Markstein length is often nondimensionalized to obtain the Markstein number  $Ma$ :

$$Ma = \frac{l_M}{\delta_{f,0}} \quad (19)$$

The stretch rate  $\kappa$  can also be nondimensionalized to form the Karlovitz number  $Ka$ :

$$Ka = \frac{\delta_{f,0} \kappa}{S_{L,0}} \quad (20)$$

Note that there are numerous ways to define the Karlovitz number and that this definition is different from that defined in Equation 4. With these nondimensionalizations, Equation 18 can be modified to obtain:

$$\frac{S_L}{S_{L,0}} = 1 - MaKa \quad (21)$$

This linear relationship between flame speed and stretch rate has found justification in experiments, for example in the work of Tseng et al. [129], shown in Figure 11 for  $\text{CH}_4$ :air flames at various equivalence ratios. Note in this figure that the y-axis is the inverse of the left side of Equation 21. Since  $\text{CH}_4$  is lighter than air, these results agree with the previous discussion that the laminar flame speed under positive stretch should be enhanced for lean mixtures and diminished for rich mixtures.

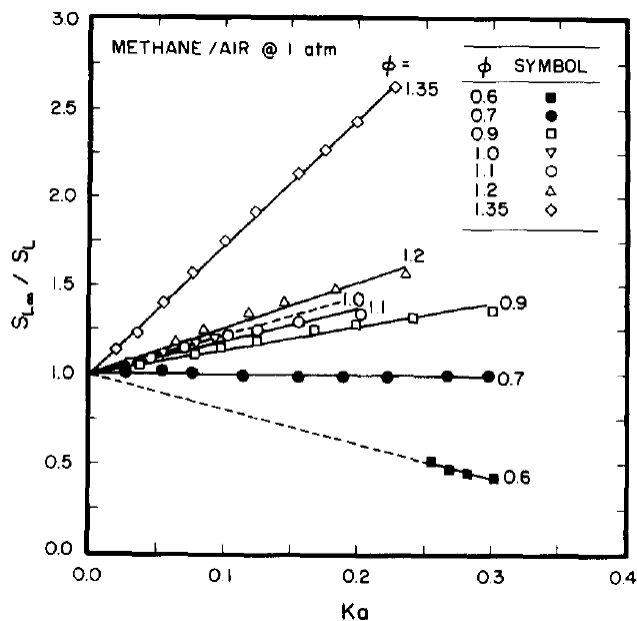


**Figure 11:** Dependence of the laminar flame speed on Karlovitz number for  $\text{CH}_4$ :air flames at different equivalence ratios. Figure reproduced from [129].

When a flame becomes strongly stretched, such as in highly turbulent flows, the linear relationship of Equation 21 is no longer valid. Numerical simulations with detailed kinetics and transport models are needed to determine the response of a flame to strong stretch. One method is to use the OPPDIF module [67] in CHEMKIN to simulate symmetric, premixed flames in an opposed jet burner, as shown in Figure 12. In this simulation the nozzle exit velocities of both jets are increased to increase the stretch rate on the flames. Figure 13 presents example OPPDIF calculations for several different fuel mixtures. The Davis mechanism [43] and GRI-Mech 3.0 [119] were used for the chemical kinetics mechanisms for the  $\text{H}_2$ :CO mixtures and  $\text{CH}_4$ , respectively. Eventually the stretch rate becomes too strong for the chemistry of the flames to sustain themselves, and extinction occurs at the extinction stretch rate,  $\kappa_{ext}$ . Near this point the solver uses an arc length continuation method to find the extinction stretch rate and the branch of the curve that turns back on itself. This region where the curve turns around is an unstable solution to the system of equations.

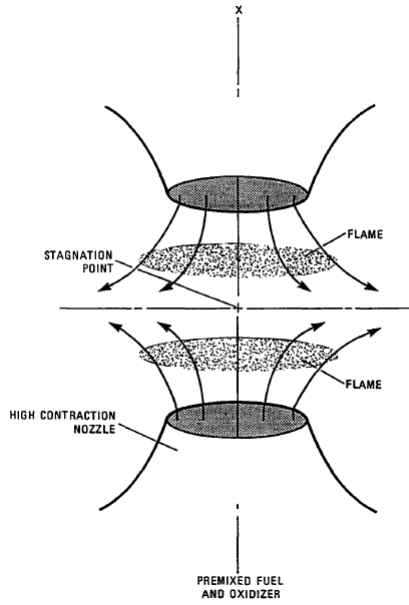


**Figure 12:** Representation of the twin, premixed flames in an opposed jet burner configuration used in the OPPDIF software module. Figure reproduced from [67].

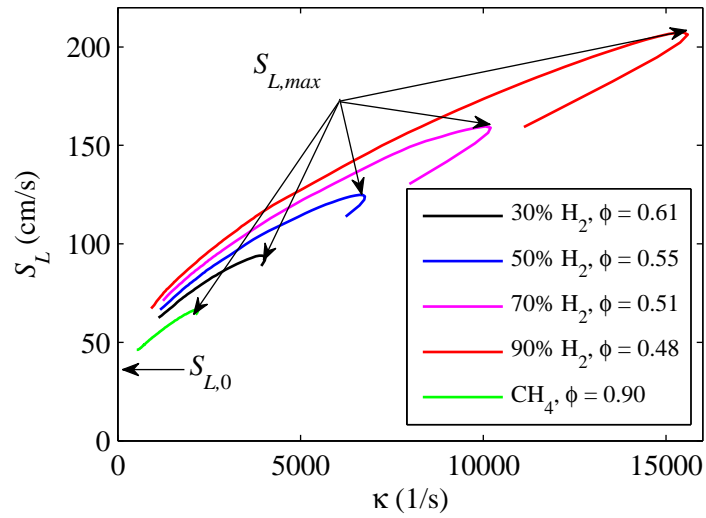


**Figure 13:** Stretch sensitivity calculations of H<sub>2</sub>:CO fuel blends and CH<sub>4</sub> [133].

### 1.2.2.6 Unsteady Stretch Effects

So far the discussion on flame stretch effects has focused on the response of a flame to a steady stretch rate. However, turbulent flows are unsteady, and the response of a flame to unsteady stretch becomes important to understand. At high enough frequencies the internal structure of the flame cannot adjust itself to the perturbations. The frequency at which the internal flame structure no longer responds in a quasi-steady manner is proportional to the inverse of the flame's characteristic chemical time,  $\tau_c = \delta_{f,0}/S_{L,0}$  [62]. This allows flames to exist at stretch rates above the steady-state  $\kappa_{ext}$ . These ideas are illustrated in Figure 14, which plots the laminar flame speed as a function of Karlovitz number for the steady case and a range of frequencies. Notice from this figure that as the oscillation frequency increases, the laminar flame speed becomes less sensitive to the stretch rate. At the highest frequency of 1000 Hz the flame speed is nearly insensitive to the imposed stretch rate.

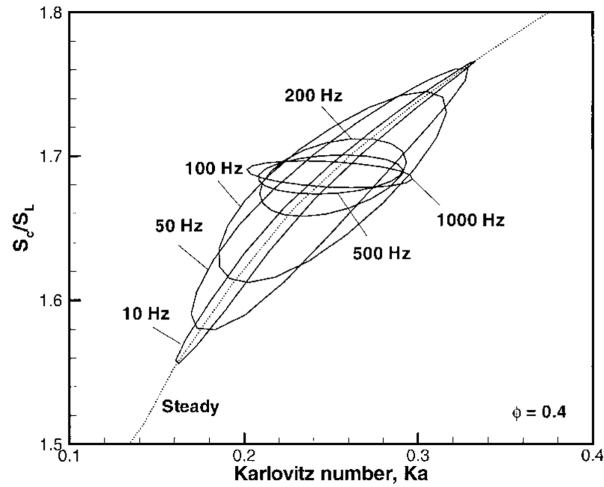


**Figure 14:** Dependence of the laminar flame speed on Karlovitz number for steady and oscillating stretch rates for a  $\text{H}_2$ :air flame at  $\phi = 0.4$ . Figure reproduced from [62].

### 1.3 Literature Review

The turbulent flame speed is commonly correlated using:

$$S_T = S_{L,0} f(u'/S_{L,0}) \quad (22)$$

where  $S_{L,0}$  is the unstretched laminar flame speed and  $u'$  is the turbulence intensity [87, 88]. The unstretched laminar flame speed is defined as the speed at which an adiabatic, flat, laminar flame front propagates into unburned reactants. For a given mixture, it is a function of pressure and temperature [131]. The turbulent flame speed has an analogous definition to the laminar flame speed, but does not depend solely on the chemical and thermal properties of the mixture. As suggested by Equation 22, it is also affected by the conditions of the flow such as the turbulence intensity. However, Equation 22 fails to capture the entire physics of the problem [87]. Numerous studies have shown that the turbulent flame speed is also affected by turbulent length scales [7, 78], bulk flow velocity [53], experimental configuration [50, 28], and fuel composition [88, 97, 70]. The effect of fuel composition on the turbulent flame speed has been well-documented in the literature [88]. For example, Kido et al. [97, 70] obtained data for mixtures of  $H_2$ , methane ( $CH_4$ ), and propane ( $C_3H_8$ ) where, by adjusting the dilution and stoichiometries of the different fuel blends, they obtained different mixtures with the same unstretched laminar flame speed,  $S_{L,0}$ . Their data clearly show that these mixtures have substantially different turbulent flame speeds, with the high  $H_2$  mixtures having an order of magnitude larger  $S_T$  value than the propane mixture at the same turbulence intensity for the same experimental configuration. In addition, Venkateswaran et al. [133] have reported measurements of  $H_2:CO$  blends showing factor of three variations in  $S_T$  across fuel blends with identical  $S_{L,0}$  values, even at turbulence intensities  $u'_{rms}/S_{L,0}$  up to 40. Similar observations were made by Wu et al. [140], Bradley et al. [15], Brutscher et al. [17] and others, as summarized in the review of Lipatnikov and Chomiak [88].

The sensitivity of the turbulent flame speed to fuel composition is associated with the stretch sensitivity of the reactant mixture, which leads to variations in the local consumption speed along the turbulent flame front. In particular, the high mass diffusivity of  $H_2$  makes HHC mixtures highly stretch sensitive. Stretch effects can be manifested through both non-unity Lewis number and preferential diffusion effects [79]. While various modeling approaches have been put forth, conceptual models based upon leading points concepts appear to be one of the most natural approaches for capturing these stretch sensitivities [88, 78, 64]. Leading points concepts were proposed by Zeldovich [143] and expanded upon

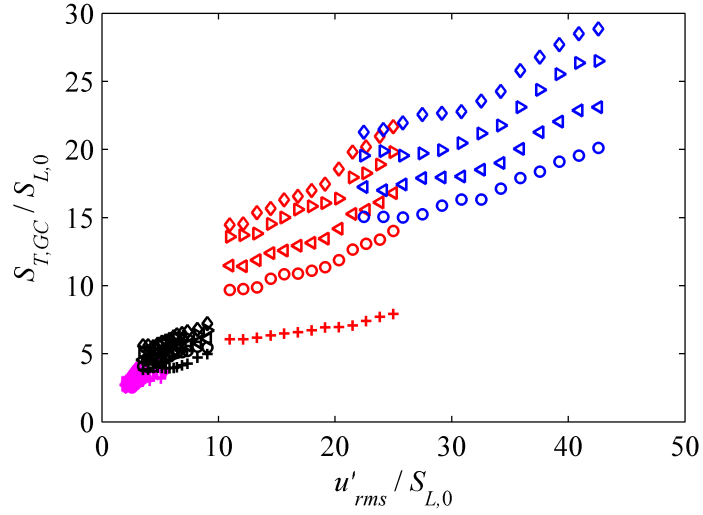
by a number of groups, as summarized by Lipatnikov and Chomiak [88]. Leading points are loosely defined as positively curved (convex to the reactants) points on the flame front that propagate out farthest into the reactant mixture and can be shown to control the overall propagation velocity of the turbulent flame under certain conditions [78]. This can be shown, for example, by applying the Kolmogorov-Petrovskii-Piskunov (KPP) theorem [74] to the propagation of a one-dimensional turbulent premixed flame in frozen turbulence, where, under certain circumstances,  $S_T$  is controlled by the conditions at the leading edge of the flame brush, defined as the point where the average progress variable,  $\langle c \rangle$ , approaches zero [57, 51]. For negative Markstein length mixtures, the burning rate of this positively curved leading point increases [79]. As discussed in Section 1.2.2.5, the Markstein length measures the linear response of the laminar flame speed to stretch rate.

These leading points ideas are particularly revealing for negative Markstein length mixtures, as calculations of laminar flame stretch sensitivities show that the positively curved leading point flame speed can substantially exceed  $S_{L,0}$ , as shown in Figure 13 [79]. Assuming that  $S_T$  is controlled by the leading point characteristics, the ensemble averaged laminar burning rate of this leading point turns out to be a very significant turbulent flame property. Directly following these ideas, Venkateswaran et al. [133, 132] developed a scaling law for the turbulent flame speed of negative Markstein length flames that collapses a wide range of turbulent flame speed data. This scaling law uses the maximum stretched laminar flame speed,  $S_{L,max}$ , as the normalizing parameter as opposed to the traditional approach of using the unstretched laminar flame speed,  $S_{L,0}$ . The form of this scaling law is given by the relation:

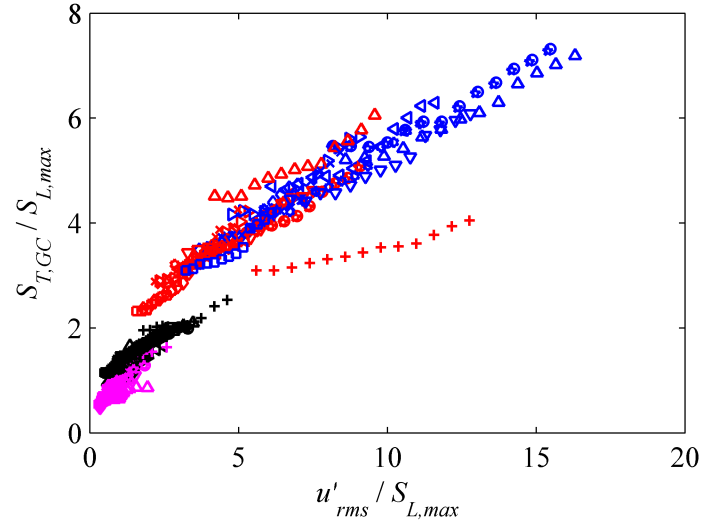
$$\frac{S_T}{S_{L,max}} \leq 1 + \frac{u'_{LP}}{S_{L,max}} \quad (23)$$

where  $u'_{LP}$  is the turbulence intensity at the leading point of the flame.  $S_{L,max}$  is found from opposed flow, strained flame calculations using detailed kinetics. An example of these calculations is shown in Figure 13. The dynamical significance of  $S_{L,max}$  in negative Markstein length mixtures arises from the fact that this velocity/strain rate at the leading point is a steady-state attracting point for constant density flames with positively curved wrinkles [133]. This idea that  $S_{L,max}$ , and not  $S_{L,0}$ , is the suitable velocity scale for correlating  $S_T$

was suggested by [78] and has found justification in data from Venkateswaran et al. [133], as shown in Figure 15, which plots data obtained with a range of H<sub>2</sub>:CO mixtures normalized by  $S_{L,0}$  (Figure 15a) and  $S_{L,max}$  (Figure 15b). Note the strong fuel effects manifested in the  $S_{L,0}$  scaled data, but the good collapse of the data using the  $S_{L,max}$  scaling.



(a)



(b)

**Figure 15:** (a) Measured dependence of the turbulent flame speed,  $S_{T,GC}$ , upon turbulence intensity,  $u'_{rms}$ , normalized by  $S_{L,0}$  at various conditions for several  $H_2:CO$  ratios and pure  $CH_4$ . (b)  $S_{T,GC}$  data from (a) normalized by  $S_{L,max}$ . See Venkateswaran et al. [133] for details on experimental conditions.

## 1.4 Thesis Overview

This simple scaling law is a promising method to correlate turbulent flame speeds, using a physics-based approach, over a wide range of conditions. However, there are several key issues that still need to be addressed.

As discussed in Section 1.2.1, the turbulent flame speed can be defined globally over the entire flame or locally at a point or differential volume element [56]. The measurements acquired by Venkateswaran et al. [133] with a Bunsen burner measure the turbulent global consumption speed,  $S_{T,GC}$ . Bunsen burners produce a flame that is attached at the burner exit. Thus, the turbulent flame brush, defined as the time-averaged spatial region that the flame occupies [131], is spatially varying, and  $S_{T,GC}$  measurements average over variations in the turbulent flame speed along the turbulent flame brush. The scaling law developed by Venkateswaran et al. [133] is based around the local propagation rate at the leading points of the flame and should be adjusted to account for the spatially developing flow field and flame brush.

Thus, measurements of local flame properties, such as the flame stretch rate and turbulence intensity, at these leading points may prove useful to the understanding of the scaling law. For example, Figure 13 clearly shows the monotonic increase in  $S_{L,max}$  with increasing  $H_2$  content. However, it also shows that the flame stretch rate at  $S_{L,max}$  varies strongly with  $H_2$  content, a prediction that can be evaluated from computations or measurements. If the physical arguments leading to this scaling approach are correct, then the flame stretch characteristics at its leading points should exhibit systematic differences that scale with  $S_T$ . In particular, Figure 13 suggests that mixtures with higher  $S_T$  values should have leading points with higher stretch rates.

These measurements can be acquired using a burner developed by Cheng et al. [25] known as the low swirl burner (LSB), discussed in more detail in Section 2.1.3. In addition, this burner can also be used to obtain turbulent local displacement speed,  $S_{T,LD}$ , measurements, discussed in Section 1.2.1. These measurements, along with measurements of the local turbulence intensity, can be used to test the validity of the leading points scaling model.

The rest of this thesis is organized as follows. Chapter 2 discusses the methods used in this research. This includes a detailed overview of the experimental facility and the techniques used to obtain measurements of the flow field and flame quantities. Chapter 3 characterizes the flow field of the burner from laser Doppler velocimetry (LDV) and particle image velocimetry (PIV) experiments. Chapter 4 presents turbulent flame speed measurements acquired in both the Bunsen burner and low swirl burner configurations over a wide range of pressures, velocities, fuel compositions, equivalence ratios and turbulence intensities. In Chapter 5, flame front topology and stretch statistics are extracted from the high-speed PIV data. This includes measurements of curvature and tangential strain rate globally across the entire flame brush and locally at the flame leading points. The purpose of these measurements is to test the validity of the leading points model for collapsing turbulent flame speeds. Finally, Chapter 6 summarizes the contributions and conclusions of this work and presents suggested directions for future research in this area. This thesis also includes two appendices for further details on this work. Appendix A presents details of the facility used to meter flow rates, methods used to calibrate the meters, and results of these calibrations. Appendix B presents an expanded flow field dataset compared to the overview presented in Chapter 3.

## CHAPTER II

### METHODS

The purpose of this chapter is to give a detailed overview of the experimental facility used to perform this research and the methods implemented to obtain and process the data. Section 2.1 details the four most important subsystems of the experimental facility: the flow facility for control and metering of gas flow rates, the unique turbulence generator, used to create variable turbulence independent of any other flow quantities, the low swirl burner with independent flow control of the central and swirl channels, and the high pressure vessel used to obtain data at conditions simulating the operating pressures of real combustors. Section 2.2 describes the techniques used to obtain detailed information about the turbulent flow field characteristics, including single point measurements and 2D velocity field measurements. Finally, Section 2.3 explains the processing techniques used to obtain information on the flame front topology and values for the turbulent flame speed.

#### *2.1 Experimental Facility*

This research focuses mainly on the measurement of  $S_{T,LD}$  using flames generated with a low swirl burner (LSB), an approach recommended by Gouldin and Cheng [56]. Along the centerline of flames generated from the LSB, the turbulent flame brush is statistically stationary in the lab reference frame and normal to the approach flow, thus,  $\vec{U}_f = 0$  and  $-\vec{U}_r \cdot \vec{n} = |\vec{U}_r| = U_r$ . This leads to the following simplified relationship for  $S_{T,LD}$ :

$$S_{T,LD} = U_r \tag{24}$$

and reduces the task of determining  $S_{T,LD}$  to measuring the mean axial flow velocity along the axial centerline at some prescribed progress variable or other well-defined feature. Another unique aspect of the LSB is that it produces a lifted flame that is quasi-1D in the central, non-swirling region. This makes the flame convenient to access with laser diagnostic techniques and amenable to analysis of statistical quantities such as flame curvatures and

tangential strain rates.

### 2.1.1 Flow Facility

A significant task in the development of the high pressure experimental facility was the design and implementation of a fully remotely operable control and metering system for mixtures containing multicomponent fuels being delivered to two independent flow channels. In addition, the flow facility is designed to be capable of running with heated or unheated air over a significant range of flow rates and operating pressures. This section divides the flow facility into three main systems: the regulators used for controlling fuel flow rates, the fuel metering and mixing system via critical orifice meters, and, finally, the system for metering air flow rates and premixing with the fuel before entering the burner.

Figure 16 presents the system developed in order to control multicomponent fuel mixtures over a wide range of conditions. Table 3 lists the instruments and valves used in this system.  $H_2$  and CO are supplied from high pressure gas cylinders stored inside of continuously exhausting gas cabinets. Natural gas is supplied from the building high pressure natural gas system, and, although not pictured, would connect to regulators 2 and 4 in place of CO. A nitrogen purge/leak check system is used to check for leaks in the gas supply lines and also to purge  $H_2$  from the lines after testing to lessen the damaging effects of  $H_2$  embrittlement. The high pressure gases are controlled via air-loaded regulators combined with electropneumatic pressure controllers. The downstream pressure setpoint of the air-loaded regulators is controlled via an electronic pressure transducer coupled to a proportional-integral-derivative (PID) controller contained in the electropneumatic pressure controllers. A pressure setpoint is commanded from the data acquisition (DAQ) system and the pressure controller adjusts the air load on the pressure regulator until the desired setpoint is achieved.

After the regulators, the gases are metered and mixed via critical orifice meters as shown in Figure 17. Table 4 lists the instruments and valves used in this system. Check valves are used to prevent back flow of gases. The pressure and temperature are measured just upstream of the choked orifice, and the pressure is measured downstream of the orifice to

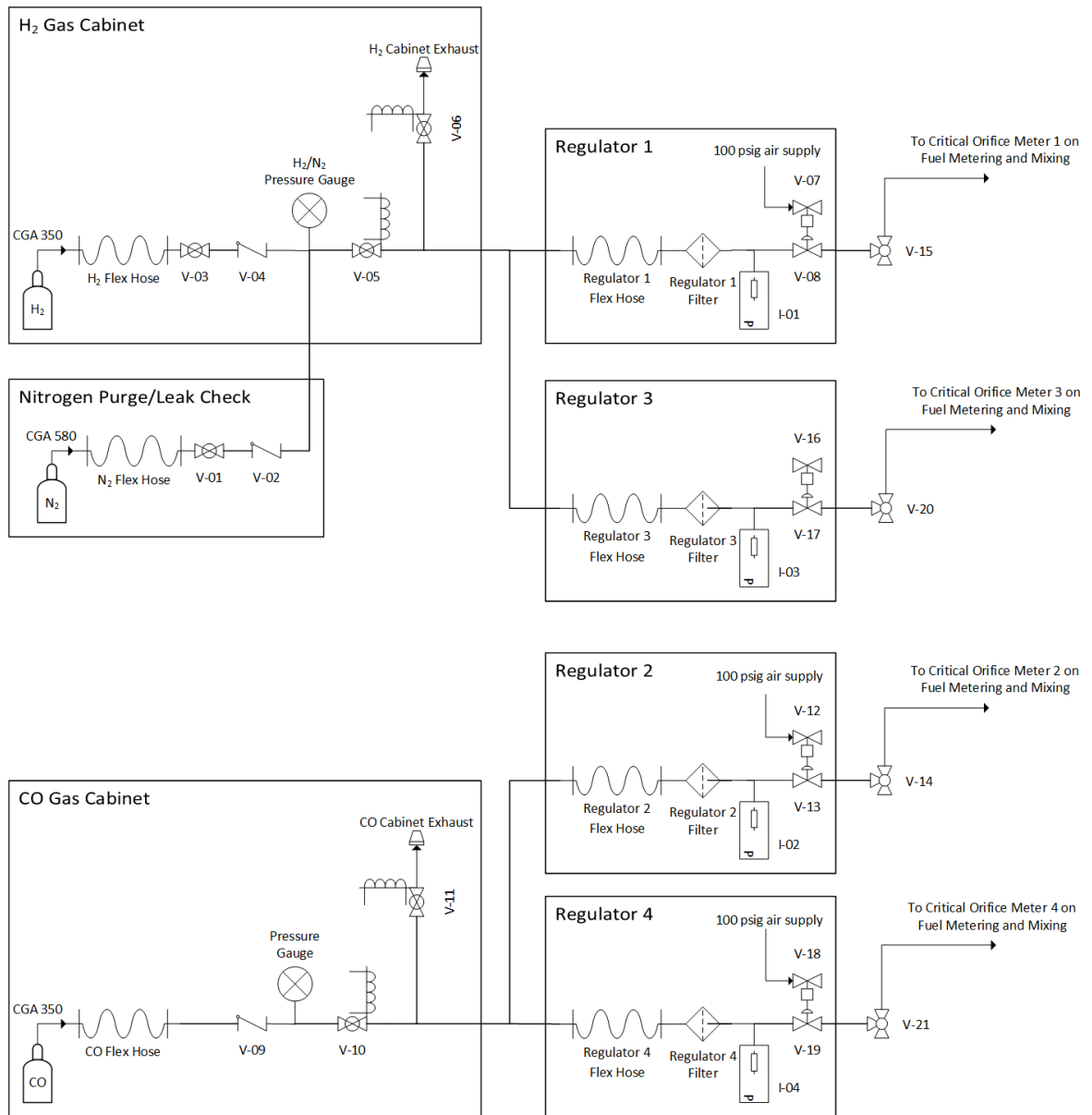


**Figure 16:** Diagram of the experimental facility for control of fuel regulators.

ensure that the flow is choked. A wide range of orifice sizes are used to achieve different flow rate ranges. Assuming ideal gas behavior and that the flow is choked, the mass flow rate is calculated from:

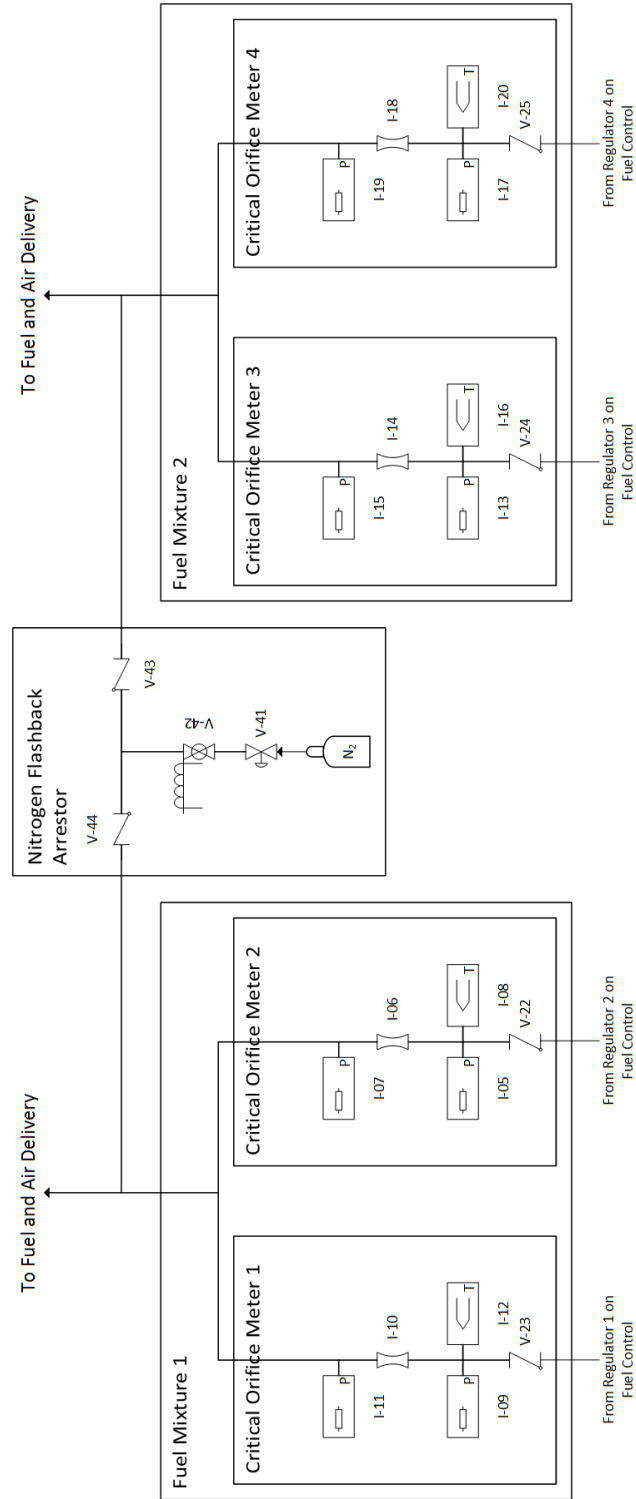
$$\dot{m} = C_d A p \left( \frac{\gamma MW}{RT} \left( \frac{2}{\gamma + 1} \right)^{\left( \frac{\gamma + 1}{\gamma - 1} \right)} \right)^{1/2} \quad (25)$$

where  $C_d$  is the discharge coefficient,  $A$  is the choked orifice area,  $p$  is the pressure upstream of the orifice,  $\gamma$  is the ratio of specific heats,  $MW$  is the molecular weight, and  $R$  is the universal gas constant. The discharge coefficients for different orifice diameters were found by calibrating the orifices using a drum-type gas meter. A detailed overview of the methods and results of these critical orifice calibrations for a wide range of orifice sizes and gases is presented in Appendix A. The fuel flow rates can be controlled by controlling the upstream pressure  $p$  with the air-loaded regulators as discussed in the previous paragraph.

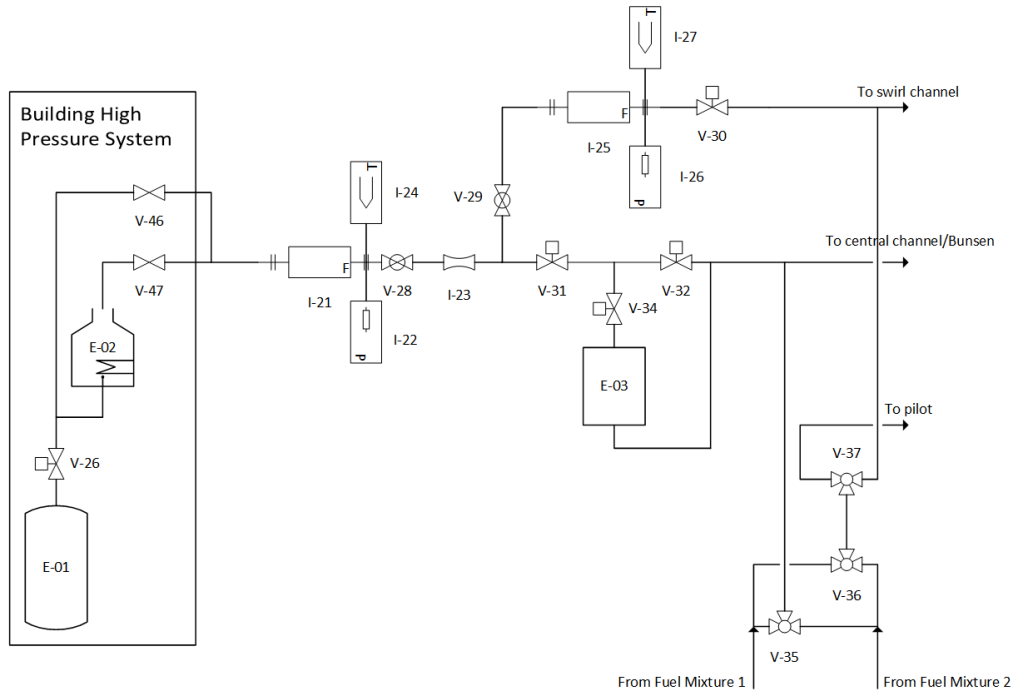
After the critical orifices, the individual gas components are mixed to create two multicomponent fuel mixtures. The fuel mixtures then enter the fuel and air delivery system to be mixed before entering the burner. There is also a system in place that is designed to purge the lines with  $N_2$  in the event that a flashback is detected. This is a safety feature meant to extinguish the flame as quickly as possible during flashback.

Figure 18 details the system used to deliver premixed fuel and air into the burner. The building high pressure air supply comes from storage tanks at a pressure of 200 atm with a storage capacity of 3,000,000 standard liters. The tanks are filled by a five stage piston compressor. The high pressure air is controlled via a controllable regulator with a maximum downstream pressure of 50 atm. This air supply then takes two paths: one that is unheated and the other that is heated by a Stahl air heater capable of producing outlet temperatures of 800 K at 50 atm. The outlet temperature of the air heater is controlled by a closed-loop feedback system. In this experimental facility, the hot and cold lines are combined, but only a single valve is opened for a given experiment. This allows the facility to be run using either heated or unheated air.

The total air volumetric flow rate is metered using a vortex flow meter, and then converted to a mass flow rate using the pressure and temperature sensors located downstream



**Figure 17:** Diagram of the experimental facility for metering and mixing of fuels.



**Figure 18:** Diagram of the experimental facility for fuel and air delivery to the burner.

of the vortex flow meter. The air is then choked to eliminate acoustic feedback to the control system. The air then splits into two channels, one of which goes to the swirl channel of the LSB and the other goes to the central channel of the LSB or the Bunsen burner, depending on which nozzle is installed. The swirl channel is metered with a vortex flow meter to determine the split between the two channels and, thus, have the ability to calculate the swirl number,  $S$ . Pneumatically-actuated globe valves are used to control the split between the swirl and central channels. Along the central channel line, a second pneumatically-actuated globe valve is used to divert part of the flow through the high pressure seeder for velocimetry experiments. This seeder also has a pneumatically-actuated ball valve located upstream of it to turn the air supply to the seeder on and off remotely. Downstream of the air supply the fuel mixtures are added to both the central and swirl channels in order to premix the reactants before they enter the burner. On entering the burner, the flow in the central channel passes through the turbulence generator, which creates a nearly isotropic, highly turbulent flow [135], before exiting out of the nozzle and burning. The swirl channel passes through the swirler of the LSB before exiting out of the nozzle and burning. The

turbulence generator is discussed in the next section, and the LSB is discussed in Section 2.1.3.

## 2.1.2 Turbulence Generator

### 2.1.2.1 Background

Understanding the behavior of turbulent flames at conditions that realistically simulate the operating conditions of practical devices such as boilers and gas turbine burners continues to be an important need. Typical systems operate at bulk flow velocities,  $U_0$ , ranging from a few m/s to values of several hundred m/s, relative turbulence intensities,  $u'/U_0$ , up to 30%, preheat temperatures of several hundred Kelvin, and pressures from one to 10s of atmospheres [77]. However, there is relatively little fundamental data of turbulent flame properties at these conditions, due to the severity of the environment. For example, consider the premixed, turbulent flame literature, where measurement of quantities such as turbulent flame speed, flame brush thickness, or various measures of flame front topology (e.g., fractal dimension, surface density, curvature) are required. Much of the turbulent flame speed data in the literature is obtained at normalized turbulence intensity,  $u'/S_{L,0}$ , values less than fifty, with the majority of it less than ten or even five. Very little high pressure, preheated turbulent flame speed data is available. Moreover, much of the data showing sensitivities of turbulent burning velocity to turbulence intensity have been obtained while varying mean flow velocity and turbulence intensity simultaneously, despite the fact that it is known that the flame exhibits separate dependencies upon these quantities [114]. There exists a large literature on the use of turbulence generating systems to actively manipulate the length scales and turbulence intensities in combustion and aerodynamics. These involve the use of perforated plates, spinning/oscillating rods, and auxiliary fluid jets. The rest of this section briefly reviews several prior approaches and discusses their suitability for turbulent combustion applications.

Many turbulent flame studies use grid or perforated plate-generated turbulence. While the characteristics of grid generated turbulence are documented extensively [84], the range of achievable turbulent fluctuations is on the order of 2-10% [6]. Moreover, either the grid

or the flow velocity must be changed in order to alter the turbulence intensity. Hardware changes are inconvenient for combustion studies, particularly high pressure ones involving pressure vessels, as it requires shutting down and disassembling the experiment for each test point. Mean velocity changes are problematic as they confuse the underlying sensitivity of the turbulent flame property to potentially separate dependencies on  $u'$  and  $U_0$  [50].

High turbulence intensity levels have been achieved by active-grid turbulence generators in wind tunnels, which use oscillating rods with diamond-shaped agitator wings to add turbulent kinetic energy to the flow [91, 95, 96]. The rods are oscillated independently using a random frequency generator to change the direction of oscillation. Using this configuration, Makita [91] reported relative turbulence intensities up to 37% at 10 grid spacing lengths behind the turbulence generator. However, the turbulence was highly anisotropic at this location, and he recommended taking measurements at least 50 grid spacing lengths downstream, where the turbulence was more isotropic. At this location, the relative turbulence intensity was approximately 16%. While this system significantly increases the turbulence levels compared to traditional grid-generated turbulence, there are drawbacks. The cost of implementing such a system is high compared to some of the other turbulence generation systems; e.g., the design described by Makita [91] uses 15 stepper motors and motor drivers.

Variable turbulence levels in high pressure environments can be readily achieved using fan-stirred bombs [1]. This is a transient experiment where the flame generally is initiated at the flow centerline and expands spherically. Fans are used to stir the mixture at the center of the bomb and generate isotropic turbulence [18]. While very useful for some types of studies, the fact that the experiment is unsteady and that there is no average flow along the flame limits the range of applicability of data obtained from these systems.

Another method of generating turbulence, developed independently by Thole et al. [126] and Shavit et al. [113], is based on injecting high speed jets normal to the mean flow. The advantage of this system is that the turbulence intensity can be varied independently of the mean flow by adjusting the ratio of the transverse jet velocity to the main flow velocity. In the study by Thole et al. [126], the configuration was implemented in a wind tunnel to study surface heat transfer rates in gas turbines. They were able to achieve relative turbulence

intensities of 20% while maintaining uniform mean and turbulence quantities across the span of the test plate. In the study by Shavit et al. [113], the principle was applied to generate turbulence in a twin-fluid atomizer, where the effect of turbulence characteristics of the outer air jet on the atomization of the inner liquid jet was investigated. In their study, they were able to achieve relative turbulence intensities ranging from 10% to 24% over mean flow velocities ranging from 27 m/s to 53 m/s. This approach does not appear to have been implemented in combustion applications.

Videto and Santavicca [135] developed a system where the flow passes through slots in a blockage plate, leading to the generation of vortical structures. These vortical structures impinge on the walls of an axially contracting section, breaking down into fine scale turbulence before exiting the burner [10, 75, 135]. They were able to achieve isotropic turbulence profiles across the burner width, with relative intensities up to  $u'/U_0 \sim 40\%$ . The turbulence level can be varied by either changing the plate gap width, thereby changing the flow velocity through the gap, or by varying the mean flow velocities. The configuration was only tested for velocities up to 2 m/s, so there is some question as to whether these levels will be achievable at higher mean flow velocities. Bédard and Cheng [10] iterated upon this design by utilizing azimuthal slots to enable use of the turbulence generator in axisymmetric geometries. Coppola and Gomez [37] employed a similar strategy of laser cutting slots with various shapes into metal plates through which the flow passes.

The approach described in this chapter was motivated by these latter studies, with some generalizations to enable remote operation in a high pressure, preheated flow. This approach was pursued for these studies for several reasons. First, as noted above, very high levels of spatially uniform turbulence intensity can be generated at a fixed flow velocity. Second, the device is amenable to remote variation of blockage ratio. The rotating plate design utilized here was selected because of minimal problems with sticking over the wide range of air preheat temperatures used, and the single access point made high pressure sealing straightforward. Key features of this system and its characteristics are described in the rest of this chapter.

### 2.1.2.2 Turbulence Generator Setup

This section describes the experimental facility with particular emphasis on the design and implementation of the turbulence generator. It was important in the development of this facility to design a robust system capable of operating over a range of mean flow velocities, inlet temperatures, and pressures. As such, careful consideration had to be taken in regards to the selection of materials and the method of sealing the system from the surrounding environment.

Figure 19 shows a schematic of the experimental facility in which the velocity characterization studies were conducted. The facility consists of a contoured nozzle burner used for turbulent premixed flame experiments. The smoothly contoured nozzle was designed in order to suppress boundary layer formation along the walls and create a uniform top-hat velocity profile at the exit. The air supply is delivered from blow down tanks that store compressed air from the main facility compressors. The air flow is metered upstream of the burner assembly using a subcritical orifice plate. Once the flow is near the burner, a small percentage of the flow is bypassed through the seeder and then rejoined to the main air line to ensure that there is no loss of mass flow rate. The seeded flow then enters the plenum through four ports and passes through a layer of ball bearings to minimize jetting effects from the smaller reactant feed lines.

The flow then passes through the turbulence generator plates, shown in Figure 20. The turbulence generating plates are secured 84 mm upstream of the burner exit, as shown in Figure 19. Both plates have an identical annular slot pattern milled in them so the turbulence intensity can be varied by rotating the top plate, resulting in a change in the blockage ratio, depicted in Figure 20. This design is motivated by the systems developed by Video and Santavicca [135] and Bdat and Cheng [10]. The main flow passes through these slots, generating vortical structures that then impinge on the inclined wall of the converging section of the nozzle, breaking down into finer scale turbulence.

At very high blockage ratios, the mixture passes through the slots at an angle, leading to swirl in the flow, as shown in Figure 21a. This effect was reduced by the addition of straighteners shown in Figure 21b. We used the criterion that the swirl velocity remains

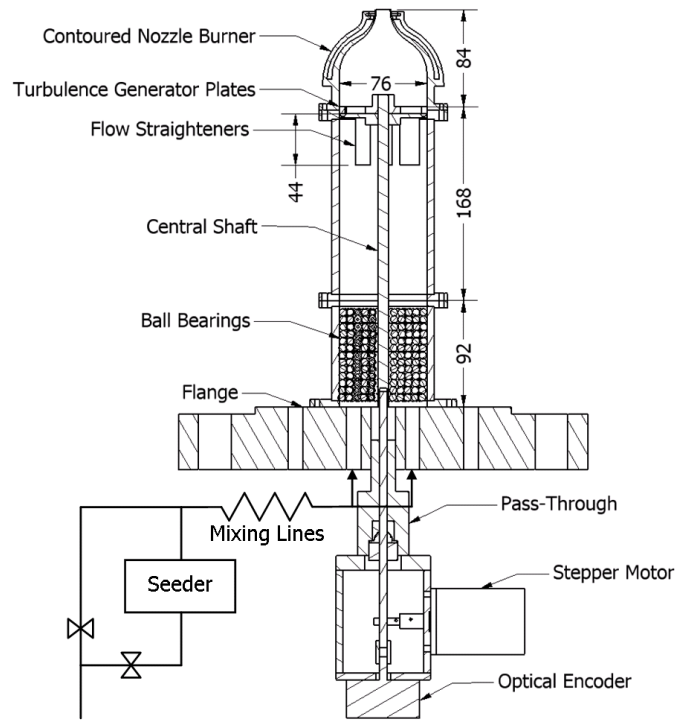


**Figure 19:** Schematic of the experimental facility for characterization of the turbulence generator. Dimensions in mm.

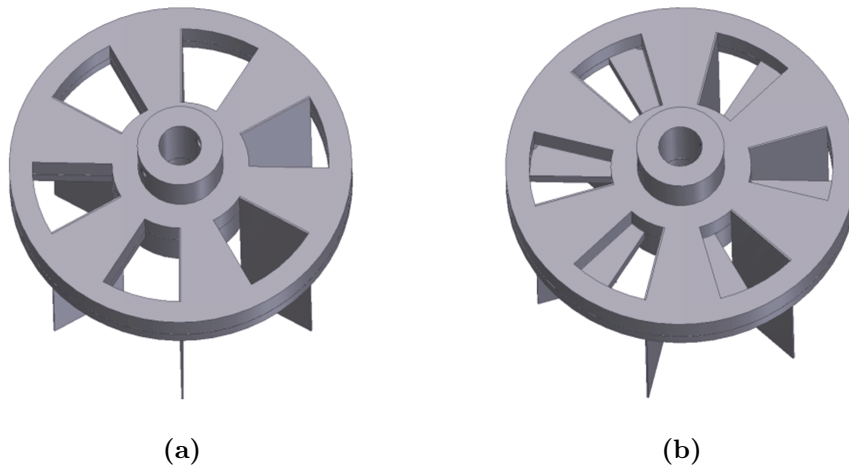


**Figure 20:** Schematic of the turbulence generating plates: (a) fully open and (b) partially closed.

less than 20% of the mean axial flow velocity, which limited the maximum usable blockage ratio to 93% for all flame speed experiments.

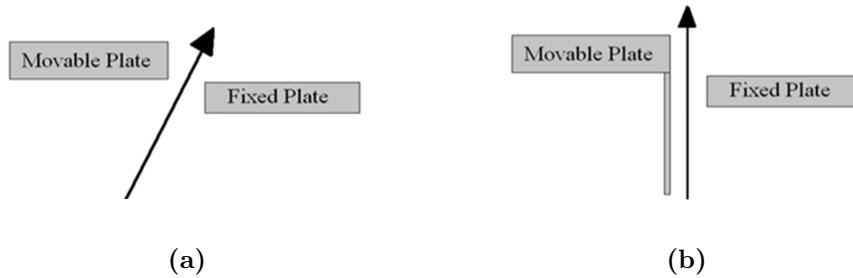


**Figure 21:** Flow characteristics (a) without and (b) with flow straighteners.

After passing through the turbulence generator plates, the flow impinges on the walls of the contoured nozzle, as detailed in Figure 22. This is an important design element, as nozzles with too large of a diameter, or blockage plates with too small a diameter of the open area, allow the large scale structure generated at the blockage plate to exit the nozzle without impinging upon the walls of the contoured nozzle. Since we are aiming to achieve homogeneous turbulence with no narrowband spectral features, this is undesirable. As such, the inner diameter of the radial slots was set to 30 mm, 1.5 times larger than our largest nozzle diameter. Measurements and characterization studies were conducted under isothermal flow conditions with burner diameters of 12 and 20 mm to achieve different ranges of length scales and assess their influence on the turbulent flame properties.

The turbulence generator is a unique aspect of this experimental facility and substantial effort was invested to meet key goals that were derived from shortcomings of turbulence generators used in other studies. The criteria set forth in designing the turbulence generator were to (1) have the ability to vary the turbulence intensity without changing out plates or changing mean flow velocity, (2) access a wide range of turbulence intensities, (3) have uniform exit mean and turbulent quantities, (4) be able to operate at high air temperatures and pressures, (5) be remotely operable, and (6) have very thin boundary layers to prevent flashback of high flame speed fuels, such as high  $H_2$  mixtures. The need for remote operability and continuously variable turbulence intensity was motivated by the need to access a range of turbulence intensities in high pressure situations without having to shut down

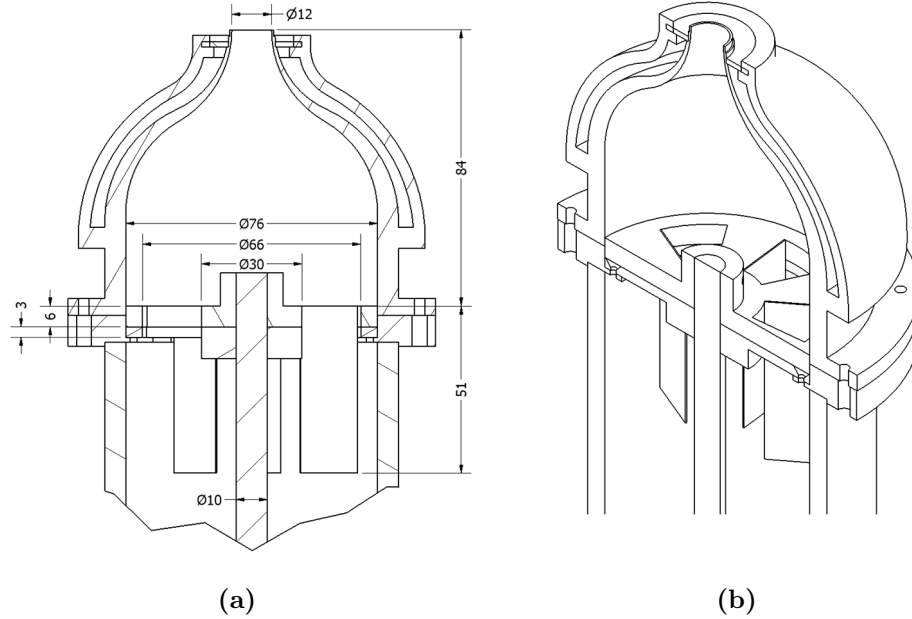


**Figure 22:** Detailed views of the turbulence generator plates and contoured nozzle (12 mm nozzle diameter shown) (a) with dimensions and (b) isometric cut-away. Dimensions in mm.

and cool the experiment to replace blockage plates. Furthermore, due to the influence of the mean flow velocity on the turbulent flame speed, we wanted the ability to change the turbulence intensity independently of the mean flow velocity.

The turbulence generator system consists of a 3 mm thick bottom plate that is secured to the plenum and a 6 mm thick top plate attached to a central shaft. This central shaft passes through the flange as shown in Figure 23. A significant amount of work was put into the design of the pass-through assembly in order to ensure that the system would not leak at high pressures. The system was designed so that increased chamber pressure would induce a force imbalance on the pass-through components (hemispherical nut and outer seal), thereby effectively enhancing their ability to seal. This pass-through has been leak tested at pressures up to 20 atm. Outside the flange, the central shaft is coupled to a DC stepper motor through a 50:1 worm and worm gear. This system has been tested to successfully rotate the turbulence plates at inlet temperatures up to 600 K and pressures up to 20 atm. In addition, the worm and worm gear were chosen for the low amount of

backlash inherent in their design. The plate’s angular position is measured with an optical encoder, attached to the other end of the central shaft, to an accuracy of  $\pm 0.1^\circ$ . The range of blockage ratios possible with this setup is 69-97%, corresponding to angular slot openings from  $30^\circ$ - $2^\circ$ . The  $30^\circ$  angular slot opening corresponds to the fully open position, where the two plates are aligned. It will be shown later that the turbulence intensity increases monotonically with increasing blockage ratio.

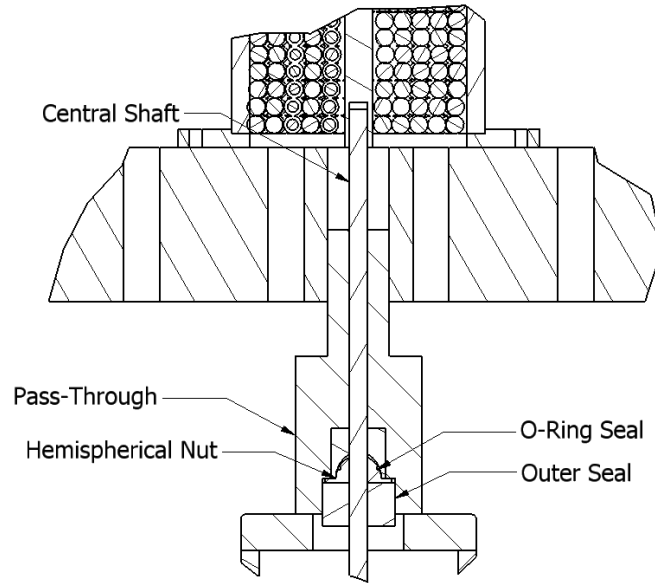


**Figure 23:** Detailed view of the pass-through assembly for the central shaft of the turbulence generator.

### 2.1.3 Low Swirl Burner

#### 2.1.3.1 Background

The low swirl burner was developed by Cheng et al. [25] as a method of generating a freely propagating flame that does not rely on flow recirculation for flame stabilization. The original design, shown in Figure 24, consists of a central channel of premixed fuel and air surrounded by a co-flow of swirling air. The swirl in the outer region is generated by tangential air jets. The outer, swirling region generates flow divergence that causes the axial velocity to decay linearly in the axial direction. This occurs because the amount of swirl generated in the outer region is below the threshold where vortex breakdown occurs. The

flame stabilizes where the flame speed matches the axial velocity. The flame brush in the central region is flat and, thus, provides a close approximation to a statistically 1D planar turbulent flame. In Cheng's follow-up paper, work was done to characterize in more detail the flow field using laser Doppler velocimetry (LDV) [27]. Results were also compared to non-reacting flow field data. One of the significant findings from this study was that the central region of the flow was found to be free of swirl, and, thus, the flame zone was not influenced by the outer swirl component.

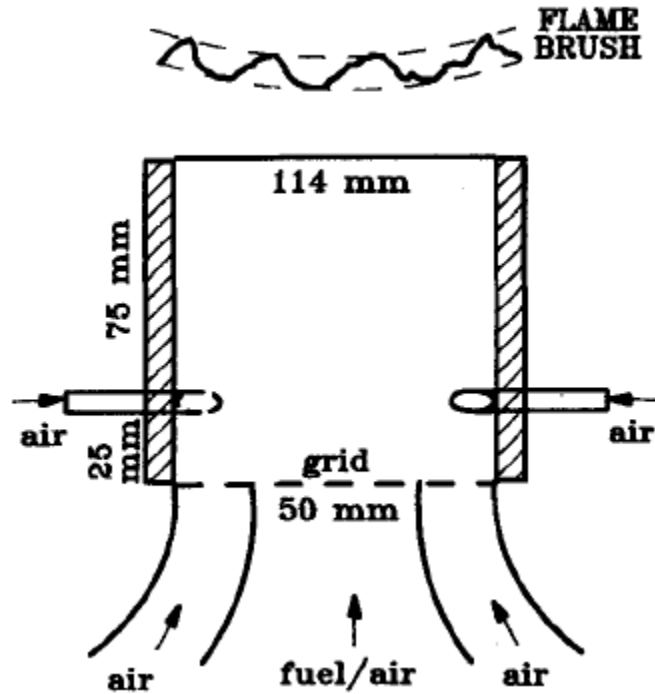
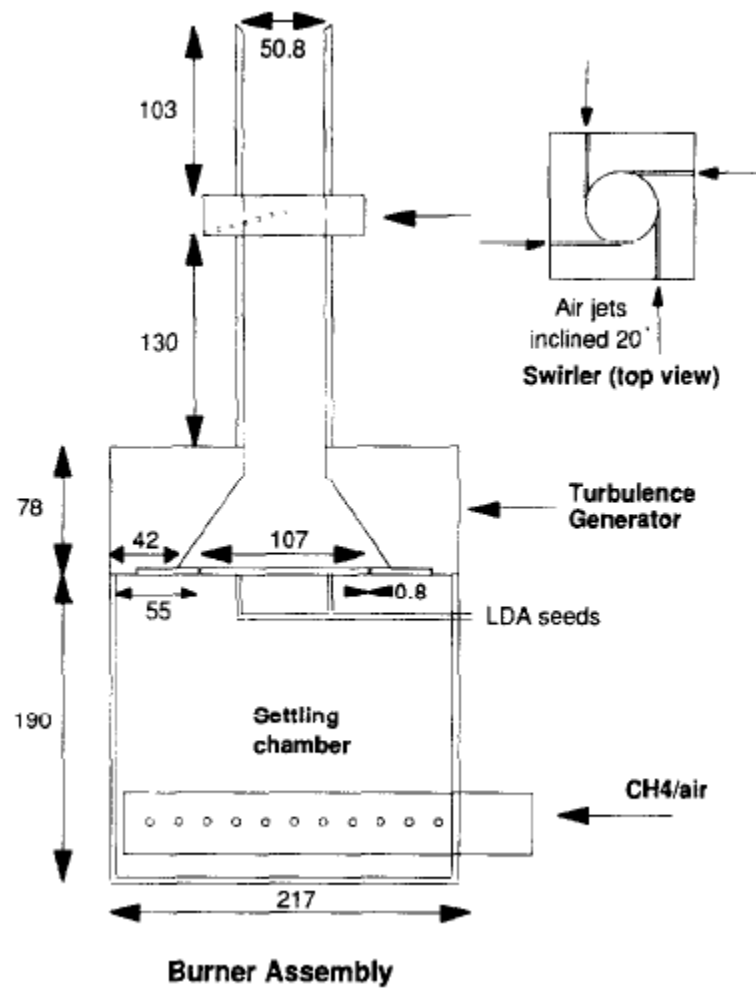


Figure 24: Schematic of the original LSB [25].

In order to obtain higher turbulence levels the burner was modified, as shown in Figure 25, [10] to use a turbulence generator based on the slot design developed by Videto and Santavicca [135]. The reactant mixture went through an annular slot to generate high levels of turbulence before the outer region was swirled via the tangential air jets. The higher turbulence levels generated by this system are closer to the levels observed in real combustors such as those in gas turbines and furnaces. The wider range of turbulence levels achievable allowed investigation of the flame structure in different regimes of the Borghi diagram [13],

from corrugated flamelets into the distributed reaction zones. The boundary separating these two regions, known as the Klimov-Williams criterion [136], was originally believed to be the point at which turbulent eddies became small enough to enter the flame and alter its structure. Below this boundary the turbulence scales are larger than the flame scales, and eddies can only wrinkle the flame. However, it was found that the flame speed increased linearly with turbulence intensity even in the high turbulence cases located in the distributed reaction zones regime. In addition, Rayleigh scattering measurements showed no significant changes in flame structure between low and high turbulence cases, suggesting that the Klimov-Williams criterion underestimates the point at which the reaction zone is affected by turbulence. Peters proposed defining an additional regime where turbulent eddies may enter the preheat zone but are still too large to penetrate the reaction zone. He calls this the thin reaction zones regime [105], discussed in detail in Section 1.2.1.2 of Chapter 1. The next paragraph details experimental work with the LSB to argue for the reasonableness of the thin reaction zones regime.

Investigations using planar laser-induced fluorescence (PLIF) of the hydroxyl radical (OH-PLIF) showed that the probability of an eddy entering the reaction zone is low for cases located in the distributed reaction zones regime [33]. Probability density functions (PDFs) of flame curvature were generated from the OH-PLIF images in order to determine the probability of flame wrinkles of a given size. Additional measurements using the Rayleigh laser sheet technique were obtained to examine the changes in the flame zone with increasing turbulence [115]. The results were compared against laminar flame situations to show that there is little evidence of changes in flame parameters as the flames entered the distributed reaction zones regime. The dominant effect was observed to be from flame wrinkling, which caused increases in the flame surface density and burning rate and resulted in broader curvature PDFs. They argued that the important length scale parameter for combustion/turbulence interactions is the reaction zone thickness. Further investigation using dual-sheet Rayleigh/OH-PLIF measurements showed that the primary effect of turbulence on the local flame structure for flames in the thin reaction zones regime is to cause a temperature rise ahead of the preheat zone. This temperature rise is caused by the



**Figure 25:** Schematic of the LSB [10] with the turbulence generator of Videto and Santavicca [135].

transport of heat by small eddies entering the preheat zone [75, 46].

A number of studies have performed 2D/3D laser diagnostic techniques on the LSB. Plessing et al. [109] performed OH-PLIF combined with either Rayleigh thermometry or PIV. The data showed the turbulent flame brush thickness to be independent of turbulence intensity,  $u'/S_{L,0}$ . Petersson et al. [107] performed simultaneous PIV/OH-PLIF, Rayleigh thermometry/OH-PLIF and stereo PIV measurements in order to develop a database of properties for Large Eddy Simulation (LES) model validation. A new LSB was used in this study, with the tangential air jets replaced by an eight vane annular swirler. Measurements of conditional velocities, progress variable, Favre-averaged progress variable and scalar fluxes were obtained. Laser diagnostic data from this new LSB has been compared to an LES model [101, 99, 100] and direct numerical simulations (DNS) [44] of the LSB to investigate the structure and stabilization of low swirl flames.

Recently, studies have investigated the effects of fuel composition on flames generated by the LSB. A summary of the fuels investigated is shown in Table 6. Littlejohn et al. [89] and Cheng et al. [31] investigated flow field characteristics and turbulent flame speeds of various hydrocarbon and hydrogen fuels. They found that the flame functions as an aerodynamic blockage, increasing the divergence rate compared to non-reacting cases at the same conditions. In addition, a linear correlation of the turbulent flame speed with turbulence intensity was observed for hydrocarbon fuels and hydrogen-containing fuels with the slope of the line steeper for the latter class [30, 32, 90].

Another notable feature of the LSB is that the flame remains stationary over a wide range of flow velocities [89, 90, 98]. This is a result of the self-similarity of the near-field flow and a linear relation of the turbulent flame speed with turbulence intensity. To better understand this phenomenon, the linear behavior of the mean axial flow velocity in the near-field flow can be written as:

$$\frac{U_{ax}}{U_0} = 1 + a_{ax}(y - y_0) \quad (26)$$

where  $a_{ax} = (dU_0/dy)/U_0$  is the normalized mean axial strain rate and  $y_0$  is the virtual origin. The virtual origin is the location where Equation 26 yields  $U_{ax} = U_0$ . At the leading

edge of the flame brush,  $y_f$ , the expression becomes:

$$\frac{S_{T,LD}}{U_0} = 1 + a_{ax}(y_f - y_0) = \frac{S_{L,0}}{U_0} + K \frac{u'_{ax}}{U_0} \quad (27)$$

where  $K$  is a proportionality constant found from experimental data and  $u'_{ax}$  is the axial turbulence intensity. Due to the self-similarity of the near-field,  $a_{ax}$ ,  $u'_{ax}/U_0$ , and  $y_0$  do not change with  $U_0$ . The proportionality constant  $K$  depends on fuel type [30, 32, 90], but does not change with  $U_0$ . The term  $S_{L,0}/U_0$  will change with bulk flow velocity, however, this term is generally small for  $S_{L,0} = O(0.1 \text{ m/s})$ ,  $U_0 = O(10 \text{ m/s})$ .

### 2.1.3.2 Low Swirl Burner Experimental Facility

The LSB nozzle, shown in Figure 26a, was designed to be interchangeable with the Bunsen burner nozzle presented previously in Figure 22. This allows for the LSB to be run with the variable turbulence generator presented in Section 2.1.2. This is the only LSB that allows for on-the-fly variations in the turbulence intensity, without varying the bulk flow velocity or changing blockage plates. The swirler, shown in Figure 26b, is similar to that of Cheng et al. [31] except that the central channel blockage plate, used to generate turbulence and control the split between the central and swirl channels, has been removed. In this setup it is unnecessary, since the turbulence is generated upstream of the contoured nozzle by the variable turbulence generator, and the flow facility uses motorized valves to control the flow split between the central and swirl channels. This gives the added benefit of being able to vary the swirl number  $S$  on-the-fly.  $S$  is defined as the ratio of angular to axial flow momentum nondimensionalized by the burner radius  $R_b$  [34]:

$$S = \frac{\int \rho w u r dA}{R_b \int \rho u^2 dA} \quad (28)$$

where  $w$  and  $u$  represent the azimuthal and axial velocities, respectively, and  $\rho$  is the density. Under some simplifying assumptions [29], the following relation for the swirl number is obtained:

$$S = \frac{2}{3} \tan \theta \frac{1 - \mathcal{R}^3}{1 - \mathcal{R}^2 + m^2 \mathcal{R}^2 (1/\mathcal{R}^2 - 1)^2} \quad (29)$$

where  $\theta$  is the swirler vane angle,  $\mathcal{R}$  is the ratio of the central channel to burner exit radii,  $R_c/R_b$ , and  $m$  is the ratio of the central channel to swirler mass flow rates,  $\dot{m}_c/\dot{m}_s$ . For the

LSB shown in Figure 26,  $\theta = 41^\circ$  and  $\mathcal{R} = 0.66$ .

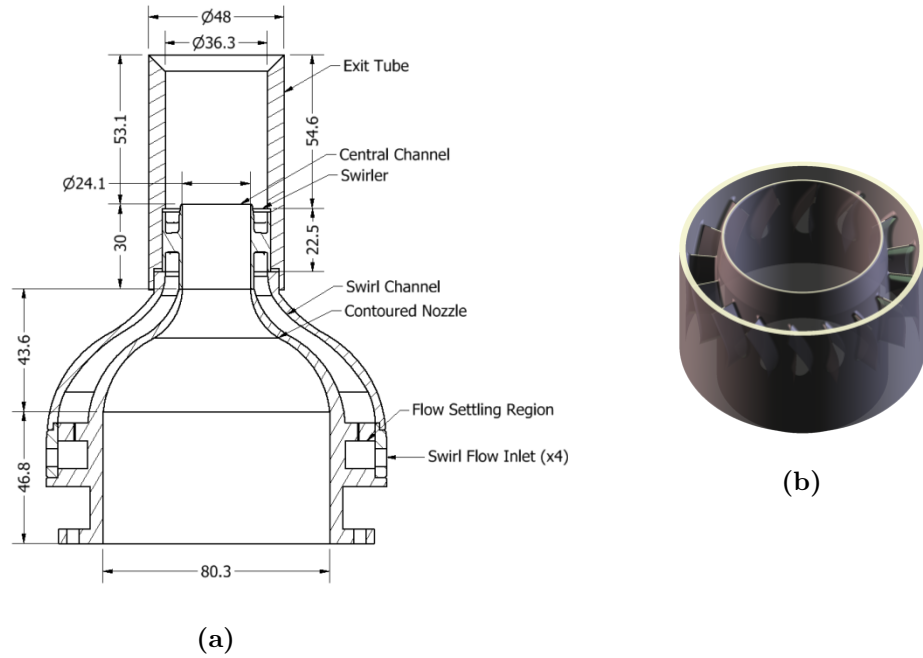


**Figure 26:** Detailed views of the (a) LSB nozzle and (b) swirler model. Dimensions in mm.

#### 2.1.4 High Pressure Capabilities

The vessel used to perform high pressure experiments is shown in Figure 27. The vessel has been tested in both non-reacting and reacting conditions at chamber pressures up to 20 atm and inlet reactant temperatures up to 600 K. The vessel is equipped with four, orthogonal 3" by 8" by 1" quartz windows located at the exit of the burner with effective viewing areas of 2" by 7". Fuel and air for the central channel of the LSB enters through four ports located in the flange that the burner plenum is attached to. The swirl channel enters through two ports in the flange located outside the diameter of the burner plenum. Inside the vessel stainless steel tubing is welded to these ports and then routed into the annular region of the contoured nozzle to supply fuel and air to the swirler of the LSB. To ignite the flame, one of the quartz windows is replaced with a carbon steel blank with two pass-through ports: one port passes a ceramic-insulated igniter probe made of tungsten carbide into the vessel and the second port passes a 1/4" stainless steel tube into the vessel that is connected to

a tank of  $H_2$ . The  $H_2$  line is opened or closed with two solenoid valves placed in series and actuated via a 120 VAC supply through a relay switch. The igniter is also controlled via a 120 VAC supply through a relay switch. The igniter arcs from the tungsten carbide probe to the  $H_2$  line, igniting the  $H_2$  and producing a nonpremixed flame that penetrates into the main flow. Once this  $H_2$  flame is lit, the fuel for the burner is introduced and the  $H_2$  flame is turned off when a stable flame is achieved in the main burner. Two ports located opposite of each other on the pipe section below the quartz windows are used to supply a co-flow of cold air to help pressurize and cool the vessel. This co-flow passes through a layer of ball bearings to help break up large scale features from the inlet air jets. The pipe sections downstream of the reaction zone are cooled by a water jacket. The pressure inside the chamber is controlled by a motorized globe valve located downstream of the pressure vessel (not shown in Figure 27). By changing the choked area of the vessel, this allows for independent control of the bulk flow velocity and chamber pressure.

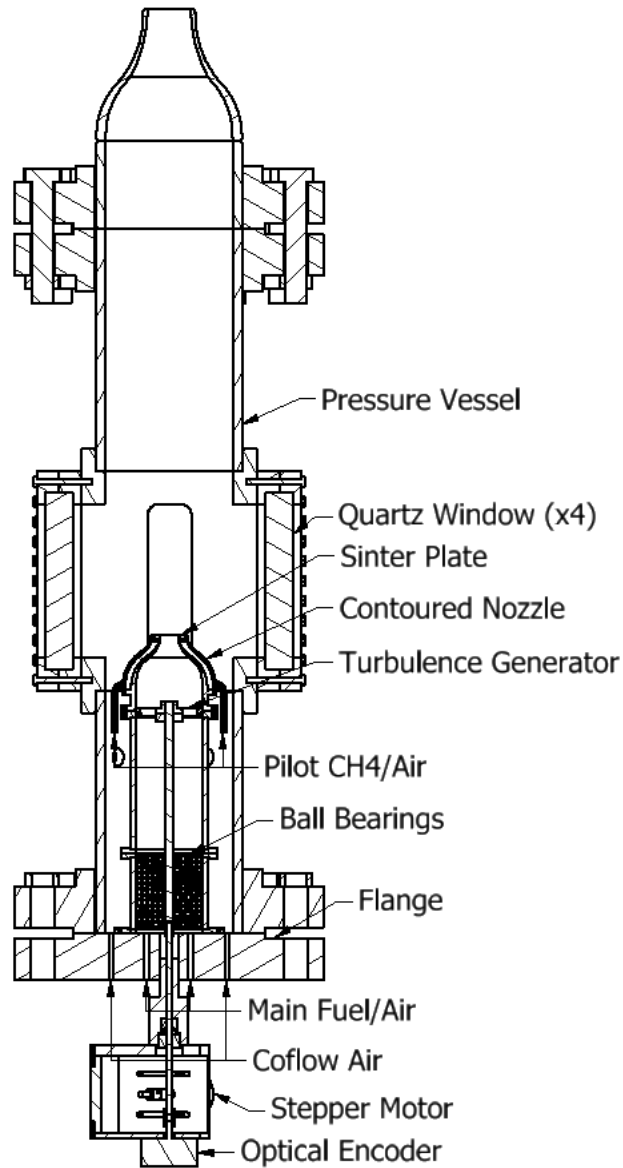


**Figure 27:** Schematic of the pressure vessel used to perform high pressure experiments. Pressure vessel is shown with the 20 mm Bunsen burner installed.

**Table 3:** Instrument and valve list for Figure 16

---

Displayed Text	Description
I-01	0-3000 psig Pressure Transducer
I-02	0-3000 psig Pressure Transducer
I-03	0-3000 psig Pressure Transducer
I-04	0-3000 psig Pressure Transducer
V-01	N <sub>2</sub> Ball Valve
V-02	N <sub>2</sub> Check Valve
V-03	H <sub>2</sub> Ball Valve
V-04	H <sub>2</sub> Check Valve
V-05	Pneumatically Actuated Ball Valve
V-06	Pneumatically Actuated Ball Valve
V-07	Pressure Controller
V-08	Air Loaded Regulator
V-09	CO Check Valve
V-10	Pneumatically Actuated Ball Valve
V-11	Pneumatically Actuated Ball Valve
V-12	Pressure Controller
V-13	Air Loaded Regulator
V-14	3-Way Ball Valve
V-15	3-Way Ball Valve
V-16	Pressure Controller
V-17	Air Loaded Regulator
V-18	Pressure Controller
V-19	Air Loaded Regulator
V-20	3-Way Ball Valve
V-21	3-Way Ball Valve

---

**Table 4:** Instrument and valve list for Figure 17

---

Displayed Text	Description
I-05	Pressure Transducer
I-06	Critical Orifice
I-07	Pressure Transducer
I-08	Type K Thermocouple
I-09	Pressure Transducer
I-10	Critical Orifice
I-11	Pressure Transducer
I-12	Type K Thermocouple
I-13	Pressure Transducer
I-14	Critical Orifice
I-15	Pressure Transducer
I-16	Type K Thermocouple
I-17	Pressure Transducer
I-18	Critical Orifice
I-19	Pressure Transducer
I-20	Type K Thermocouple
V-22	Check Valve
V-23	Check Valve
V-24	Check Valve
V-25	Check Valve
V-41	Spring Loaded Regulator
V-42	Pneumatically Actuated Ball Valve
V-43	Check Valve
V-44	Check Valve

---

**Table 5:** Equipment, instrument and valve list for Figure 18

Displayed Text	Description
E-01	High Pressure Air Storage
E-02	Furnace Heater
E-03	Seeder
I-21	Vortex Flowmeter
I-22	Pressure Transducer
I-23	Critical Orifice
I-24	Type K Thermocouple
I-25	Vortex Flowmeter
I-26	Pressure Transducer
I-27	Type K Thermocouple
V-26	Controllable Regulator
V-28	Ball Valve
V-29	Ball Valve
V-30	Pneumatically Actuated Valve
V-31	Pneumatically Actuated Valve
V-32	Pneumatically Actuated Valve
V-34	Pneumatically Actuated Ball Valve
V-35	3-Way Ball Valve
V-36	3-Way Ball Valve
V-37	3-Way Ball Valve
V-46	Gate Valve
V-47	Gate Valve

**Table 6:** Summary of literature investigations of fuel effects on the LSB.

Author	Year	Fuels Investigated	$(u'/S_{L,0})_{max}$	$(S_T/S_{L,0})_{max}$
Littlejohn [89]	2007	CH <sub>4</sub> , C <sub>2</sub> H <sub>4</sub> , C <sub>3</sub> H <sub>8</sub> , H <sub>2</sub> , CH <sub>4</sub> /CO <sub>2</sub> , CH <sub>4</sub> /N <sub>2</sub> , CH <sub>4</sub> /H <sub>2</sub> , H <sub>2</sub> /CO <sub>2</sub>	5	10
Cheng [31]	2008	Natural Gas (NG), NG/CO <sub>2</sub>	10	20
Cheng [30]	2008	H <sub>2</sub> , H <sub>2</sub> /N <sub>2</sub>	20	60
Cheng [32]	2009	H <sub>2</sub> , H <sub>2</sub> /CH <sub>4</sub>	30	65
Littlejohn [90]	2010	H <sub>2</sub> /CO/CH <sub>4</sub> , H <sub>2</sub> /CO/CO <sub>2</sub> , H <sub>2</sub> /CO	20	60

## **2.2 Flow Field Measurements**

### **2.2.1 Single Point Measurements**

Velocity measurements were obtained with a TSI 3-component laser Doppler velocimetry (LDV) system. The air flow was seeded using 5  $\mu\text{m}$  alumina ( $\text{Al}_2\text{O}_3$ ) particles. The LDV transmitter probes were mounted on a computer-controlled, three-axis traverse to enable axial and radial scanning across the burner exit along three orthogonal directions. The LDV system is comprised of an Innova 90C 2.4 W, 514.5 nm continuous wave argon-ion laser with an FBL-3 multicolor beam generator. The multicolor beam generator has a Bragg cell that shifts one beam of each of the three pairs by 40 MHz. Two fiber optic transceiver probes were mounted  $90^\circ$  apart and operated in backward-scatter mode. The signal from the transceiver probe was connected to a PDM 1000-3 three-channel photodetector module. The output frequencies were downmixed and sent through a bandpass filter before being processed by an FSA 3500-3 signal processor to record three components of velocity in non-coincidence mode. The amount of downmixing and the range of the bandpass filter varied depending on the channel and the expected measurement velocity range. Approximately 30,000 realizations, divided roughly equally among the three channels, were used to generate the quoted velocity statistics. Data were taken in two perpendicular radial cuts 3 mm above the nozzle exit with the distance between sequential data points at 1 mm as illustrated in Figure 28. The radial cuts were aligned so that one cut would pass over a solid portion of the turbulence generator, and the other cut would pass over open slots, as depicted in Figure 29. The purpose of this was to verify azimuthal symmetry in the flow.

Time-series velocity data were also acquired at the burner centerline using a Dantec Streamline Constant Temperature hotwire Anemometer (CTA) with a 5  $\mu\text{m}$  diameter, 1.25 mm length model 55p11 straight probe. The system was calibrated over the range of velocities for flow characterization using a Dantec 90H02 calibration unit to an accuracy of 2%. The probe was held in place with a straight probe holder at 1 mm above the nozzle exit centerline, oriented downward. Data were taken at 100 kHz with sample sizes of  $10^5$  points.

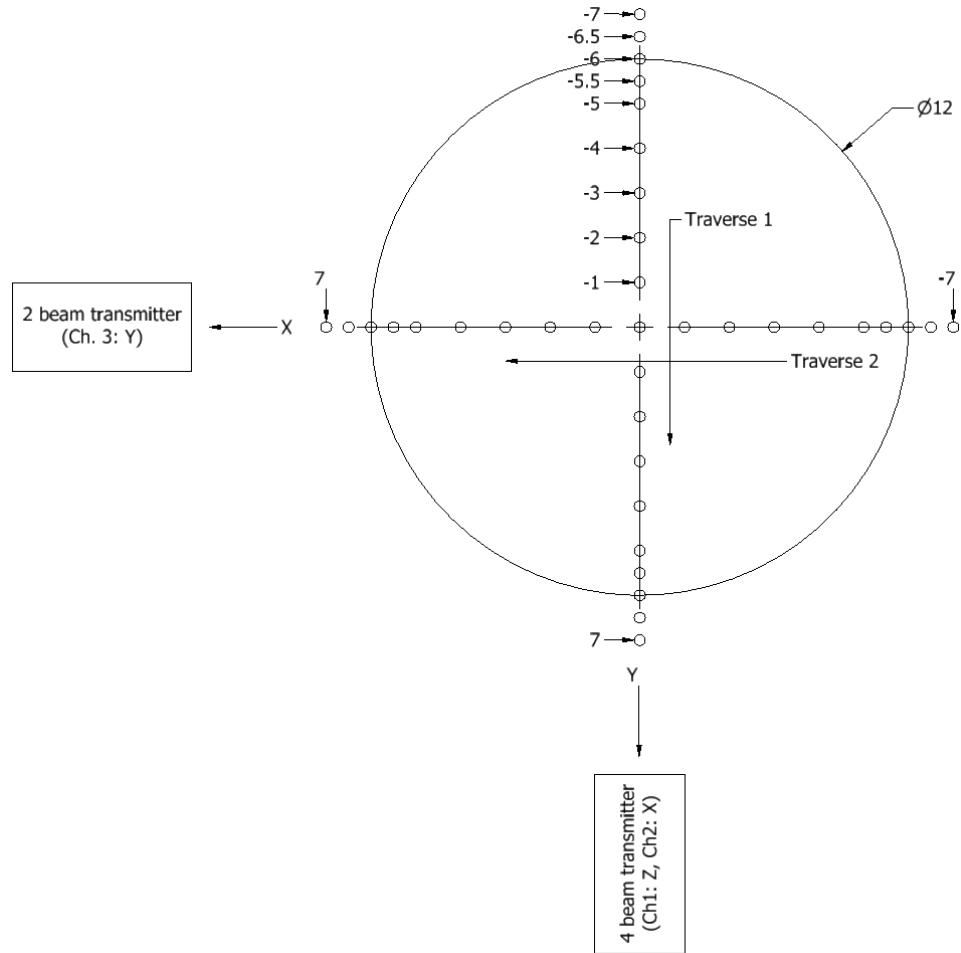


**Figure 28:** Illustration of direction and orientation of cuts and location of data points acquired in LDV characterization.

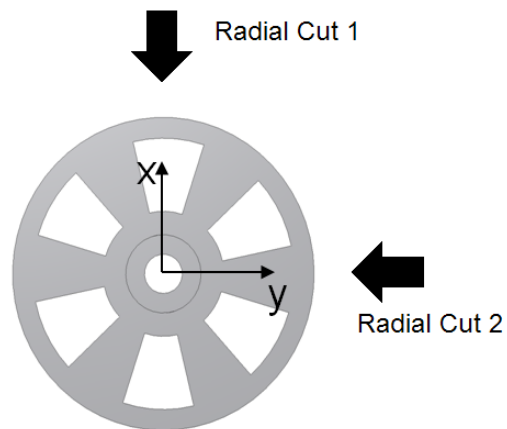


**Figure 29:** Illustration of direction and orientation of cuts performed in LDV velocity characterization relative to the turbulence generator top plate.

### 2.2.1.1 Flow Length and Time Scales

Longitudinal integral time scales,  $\tau_{int}$ , were calculated from the LDV time series data at the burner centerline, and also used to calculate a characteristic longitudinal length scale by multiplying by the mean flow velocity,  $l = \tau_{int}U_0$ . For  $u'/U_0 \ll 1$ , this characteristic length scale is equal to the integral length scale, as per Taylor's hypothesis. However, at the higher turbulence levels used in this experiment, these two length scales are different [125]. The longitudinal integral time scale was calculated from the normalized autocorrelation function as a function of lag time from the LDV time series data. Since the LDV data is sampled in unequal time intervals, the autocorrelation function  $\rho_{ac}$  was determined from Equation 30 using the slotting technique of Mayo [92] with the local normalization improvement described by Tummers [130],

$$\rho_{ac}(k\Delta\tau) = \frac{\sum_{i=1}^{N-1} \sum_{j=i+1}^N u_i u_j(k\Delta\tau)}{\left( \sum_{i=1}^{N-1} u_i^2(k\Delta\tau) \sum_{j=i+1}^N u_j^2(k\Delta\tau) \right)^{1/2}} \quad (30)$$

for:  $k = 0, 1, \dots, M - 1$

where  $(k - 1/2)\Delta\tau < t_i - t_j < (k + 1/2)\Delta\tau$ ,  $M - 1 = \tau_{max}/\Delta\tau$ ,  $\tau_{max}$  is the maximum lag time, and  $\Delta\tau$  is the slot width. The integral time scale was defined using the relationship,

$$\tau_{int} = \int_0^{\infty} \rho_{ac}(\tau) d\tau \quad (31)$$

Because of the high uncertainties associated with the autocorrelation at large time lags (because of its low value), an exponential expression of the form  $\rho_{ac}(\tau) = ae^{-b\tau} + (1-a)e^{-c\tau}$  was fit to the autocorrelation function and used to evaluate this integral, so that  $\tau_{int}$  is given by Equation 32,

$$\tau_{int} = \frac{a}{b} + \frac{1-a}{c} \quad (32)$$

## 2.2.2 Velocity Field Measurements

Velocity characterizations of non-reacting and reacting flow fields were obtained using PIV. The laser used in these experiments was a Litron Lasers Ltd. LDY303He Nd:YLF twin

head frequency doubled laser with a wavelength of 527 nm. The camera was a Photron FASTCAM SA1.1 high-speed camera with a full resolution of 1024 x 1024 pixels at repetition rates up to 5 kHz. Velocity vector field calculations were performed using DaVis 7.2 software from LaVision. The window size used in the calculations was  $32 \times 32$  pixels with an overlap of 50% giving a spatial resolution of approximately 2 mm. Experiments were performed for  $\text{H}_2:\text{CH}_4$  and  $\text{H}_2:\text{CO}$  mixtures. Experimental parameters and conditions are outlined in Table 7.

**Table 7:** Experimental parameters and conditions for the two datasets acquired using PIV

Experiments:	$\text{H}_2:\text{CH}_4$	$\text{H}_2:\text{CO}$
Repetition rate (kHz)	1	9
Pulse energy (mJ/pulse)	23	1.3
Time between shots ( $\mu\text{s}$ )	15	18
Resolution (pixels $\times$ pixels)	$704 \times 704$	$384 \times 704$
Viewing area (mm $\times$ mm)	$87 \times 87$	$44 \times 80$
Number of image pairs	1000	10,000
Seed particles	1-2 $\mu\text{m}$ $\text{Al}_2\text{O}_3$	0.3-0.7 $\mu\text{m}$ $\text{TiO}_2$
Swirl number, $S$	0.57-0.6	0.58
Mean flow velocity, $U_0$ (m/s)	20, 30, 40	30, 50
Fuel Composition (% $\text{H}_2$ )	0-75	50-100
$S_{L,0}$ (cm/s)	34	34

### 2.2.2.1 Errors in Particle Image Velocimetry

Before discussing errors and uncertainty in PIV, we start with a brief discussion of the basics of error and uncertainty analysis. It is important to note that the terms error and uncertainty are used in similar manners but have different definitions. The error is the difference between the measured value and the true value and, thus, is never known in measurements since it requires the true value (if the true value is known, there is no use in

making a measurement!). The sources of errors can be divided into bias and random errors.

Bias errors, also known as systematic errors or accuracy, occur when the measurement technique systematically measures values off from the true value. If the bias error is known, it is usually eliminated or minimized with a proper calibration of the measurement equipment. Random errors, also known as precision errors or noise, are the errors that occur each time a measurement is taken and a different value is obtained. The effects of random errors on measurements are usually minimized through averaging over a large number of samples  $N$ . Statistical methods are often used to analyze random errors.

Uncertainty refers to statistical methods used to estimate the error present in a measurement technique. The uncertainty of a measurement is a range around the measured value that is assumed to contain the true value with some level of statistical confidence. This range, and its associated confidence value, are known as a confidence interval.

Particle image velocimetry is a relatively new velocimetry technique when compared to laser Doppler velocimetry (LDV) or hotwire anemometry. The advantage over these techniques is clear: PIV provides a 2D (or quasi-3D in the case of stereoscopic techniques) velocity field at very high data rates (10 kHz is a common data acquisition rate in modern laboratory systems). However, despite the advantages of PIV, there is no standard, universally accepted error analysis procedure.

One of the first error sources identified in PIV was particle lag. This error causes a difference in velocity between the fluid and tracer particle due to acceleration in the flow and the difference in density between the particle and the fluid [93, 94]. This velocity difference is known as the “slip velocity.” In highly turbulent flows this term can become significant due to the small length scales present and the unsteadiness of the flow.

The amount of lag as a function of frequency of the flow is estimated in Figure 30, which plots the ratio of the kinetic energy of the particle to that of the fluid as a function of frequency for various particle relaxation frequencies,  $C$ . The Stokes number is a dimensionless quantity that measures the ratio of inertial to viscous forces for a particle and is related to the relaxation frequency  $C$  through:

$$Stk = \frac{U_0/l_0}{C} \tag{33}$$

where  $U_0$  and  $l_0$  are the characteristic velocity and length scales, respectively, of the flow. For these experiments, air at 300 K seeded with  $\text{TiO}_2$  particles with an average diameter of  $0.5 \mu\text{m}$ , this yields a relaxation frequency of  $C \approx 3.1 \times 10^5 \text{ s}^{-1}$ . For the range of velocities studied this yields a Stokes number of  $Stk \approx 0.005\text{-}0.009$ . According to [127], for  $Stk \ll 0.1$ , errors in velocity measurements are less than 1%.

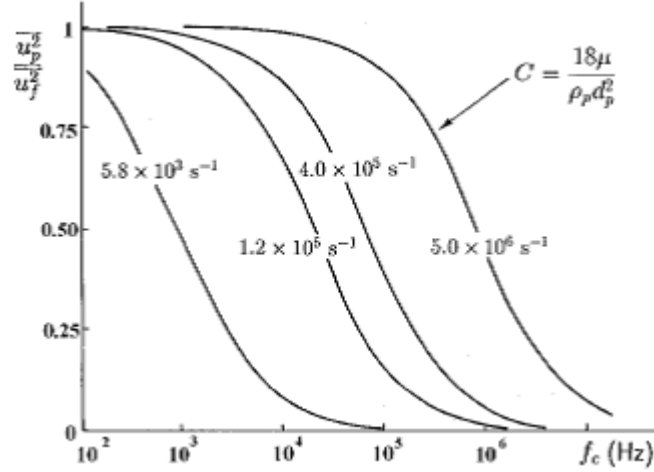


**Figure 30:** Particle kinetic energy normalized by fluid kinetic energy as a function of cutoff frequency  $f_c$  for a range of relaxation frequencies  $C$  [93].

Thermophoretic effects are another source of error in PIV measurements, where temperature gradients in a flow lead to forces on the particles. Thermophoretic effects in flames can account for differences in velocities of several centimeters per second [122], as demonstrated in Figure 31 for particle diameters of 2 and 5  $\mu\text{m}$ . This effect becomes important in the low velocity regions of the flow where a flame tends to stabilize. If we assume that the region where the flame stabilizes instantaneously has a velocity near the laminar flame speed ( $S_L \approx 40 \text{ cm/s}$ ), this leads to errors for the  $\text{Al}_2\text{O}_3$  particles of around 5-7% and for the  $\text{TiO}_2$  particles of around 1.5-3%.

Additional uncertainty in velocities calculated using PIV can arise from a variety of error sources including loss of seed particles between frames (due to out-of-plane velocities), inconsistent seeding levels, optical aberration, and error in the calibration technique [121]. Errors from these sources are dependent on the flow field examined and the experimental

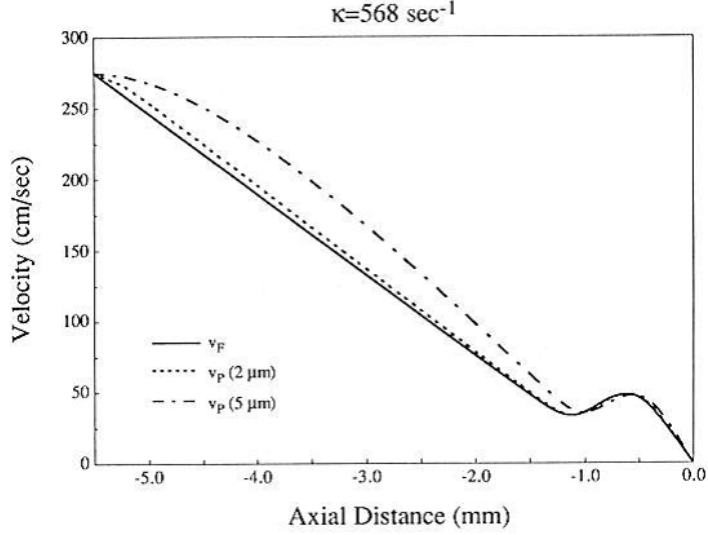


**Figure 31:** Particle velocity  $v_P$  and fluid velocity  $v_F$  versus axial distance in a  $\text{CH}_4$ -air stagnation flame [122].

setup. Because of this they are difficult to quantify, however, for a well calibrated system and a uniform flow these errors are on the order of 1-2% [80].

Combining the sources of uncertainty mentioned in the previous paragraphs using the root sum of the squares yields an uncertainty range from 2-7%. This value is highly dependent on the particles used, the range of flow velocities being considered (which also means the uncertainty varies depending on the region of the flow under examination), and the fidelity of the experimental setup.

Another method to estimate errors is to use statistical approaches based around confidence intervals. The advantage of this method is that it does not require identification and quantification of every individual source of experimental uncertainty. The disadvantage of this method is that it does not take into account bias errors.

Confidence intervals for a measured quantity  $x$  are determined by first calculating the standard error  $SE_{\bar{x}}$  of the sample mean  $\bar{x}$ , defined as:

$$SE_{\bar{x}} = \frac{s_x}{\sqrt{N}} \quad (34)$$

where  $s_x$  is the sample standard deviation and  $N$  is the number of samples. Assuming that the measurements are normally distributed, the relationship between the sample mean  $\bar{x}$

and the true mean  $\mu$  is given by:

$$\bar{x} = \mu \pm a_c SE_{\bar{x}} \quad (35)$$

where  $a_c$  is the confidence coefficient, determined by selecting a probability  $c\%$  that the measured mean lies within the confidence interval defined by Equation 35. For  $c = 95\%$ ,  $a_c = 1.96$ . In other words, there is a 95% probability that the true mean lies within  $\pm 1.96 SE_{\bar{x}}$  of the measured sample mean.

In the rest of this thesis, when error bars are presented on a plot, these error bars represent the 95% confidence interval. The relative standard error is defined to be the standard error normalized by the sample mean expressed as a percentage. For the PIV measurements in this thesis, and presented in detail in the subsequent chapter, the relative standard error is less than 1%, due in large part to the high number of samples taken. It is important to note that this does not mean the measured values are within 1% of the true value, but that they are within 1% of the true mean value. The difference between the true value and the true mean value is the bias error.

## 2.3 Flame Measurements

### 2.3.1 Chemical Kinetic Calculations

This section describes the calculation approaches used for relating  $S_T$  values to detailed kinetic properties of the mixture. Estimates of the unstretched laminar flame speed,  $S_{L,0}$ , and thickness,  $\delta_{f,0}$ , were determined using the PREMIX module [66] in CHEMKIN with the Davis mechanism for  $H_2:CO$  mixtures [43] and GRI-Mech 3.0 for  $H_2:CH_4$  mixtures [119]. The flame thickness is calculated using:

$$\delta_{f,0} = \frac{T_p - T_r}{(dT/dx)_{max}} \quad (36)$$

where  $T_p$  and  $T_r$  are the burned and unburned temperatures, respectively. To determine the response of the mixtures to stretch, symmetric, opposed-flow premixed flame simulations were performed using the OPPDIF module with an arc-length continuation approach [67] in CHEMKIN. Typical calculation results are shown in Figure 13 in Chapter 1. Note the flame's sensitivity to high stretch is not a unique function of stretch rate, but depends on the

stretch profile through the flame. Thus, the geometry of the model, as well as unsteadiness, influences these results, points discussed in greater detail in our other works [3, 132].

### 2.3.2 Flame Front Topology

The density ratio of seed particles in the reactants and products scales linearly with the density ratio across the flame due to gas expansion through the flame. Because of this, Mie scattering images from PIV experiments can be utilized to estimate the instantaneous flame front positions and have been shown to be in good agreement with contours obtained from simultaneous OH and CH<sub>2</sub>O PLIF [108]. The resolution in this work is 0.11 mm/pixel, smaller than the critically stretched flame thickness for the pure hydrogen case of  $\delta_f|_{S_{L,max}} = 0.16$  mm.

It is important to note that PIV gives a 2D slice of an inherently 3D flow field and flame surface. This issue has been addressed by a number of workers. Assuming isotropy, 3D mean statistics can be estimated from 2D information, e.g.,  $\langle 1/\mathcal{R} \rangle_{3D} = \frac{\pi}{2} \langle 1/\mathcal{R} \rangle_{2D}$  and  $\langle \kappa_s \rangle_{3D} = 2 \langle \kappa_s \rangle_{2D}$  [60]. It is also assumed in this analysis that the out of plane direction is statistically homogeneous, a fair assumption for the central region of the low swirl burner considered in this study. In addition, recent experimental work by Kerl et al. [68] have shown that 2D and 3D measured quantities have qualitatively similar PDFs and are correlated to each other. Finally, Gashi et al. [54] compared curvature from 2D OH-PLIF and 3D direct numerical simulation (DNS) data and found that the PDFs were qualitatively similar, with the 3D DNS giving similarly shaped, but broader, distributions, as expected based on the above expression. Thus, while 2D data cannot be used to obtain absolute measurements of leading point stretch rates, it can be used for examining trends associated with changing various quantities such as fuel composition and turbulence intensity.

The procedure for analyzing these images is demonstrated in Figure 32. To better distinguish reactants and products, the raw image, shown in Figure 32a, is median-filtered using a  $5 \times 5$  filter to obtain 32b. Once filtered, the image is binarized with the threshold intensity selected using Otsu's method [102], as shown in Figure 32c, to separate reactants from products and find the flame edge. Figure 32c shows the resulting instantaneous progress

variable  $c$  field, which is defined to be 0 in the reactants and 1 in the products [110].

This method of binarization chooses a threshold by maximizing the total variance between the two regions, also known as the class separability [102]. If we imagine a gray-level histogram of the flame image consisting of a bimodal distribution, with the lower peak corresponding to the reactants, and the upper peak corresponding to the products, then Otsu’s method automatically chooses a threshold value nearly halfway between the peaks. This corresponds to an instantaneous progress variable of  $c \approx 0.5$ . According to laminar flame theory, the location of this flame front is upstream of the peak heat release rate, which occurs near the maximum flame temperature [55].

The flame edge, shown in green in Figure 32d, can also be used to calculate 2D flame front curvatures and tangential strain rates. Information on flame stretch statistics is useful for examining the effects of flame stretch on the propagation rate of turbulent premixed flames. In order to extract flame front curvatures, additional processing steps are required. The arc length of the edge,  $s$ , is calculated from the  $x$ - and  $y$ -coordinates of the flame edge found from binarization of the image. The 2D curvature  $1/\mathcal{R}$  is calculated from the following equation:

$$\frac{1}{\mathcal{R}} = \frac{y'x'' - x'y''}{((x')^2 + (y')^2)^{3/2}} \quad (37)$$

where  $(\ )'$  denotes derivatives with respect to the arc length  $s$ . The flame curvature is defined to be positive when the flame surface is convex to the reactants. Because of pixelation effects and noise, curvatures were not calculated directly from  $x(s)$  and  $y(s)$  via finite differences. Instead, an algorithm was developed to fit spline curves to the parameterized coordinates  $x(s)$  and  $y(s)$ . Two steps were taken in this fitting process in order to further reduce the effects of pixelation and noise. First, the  $x$ - and  $y$ -coordinates were resampled over an arc length interval  $ds$ . The choice of interval length  $ds$  is an important one. If the value of  $ds$  is too small, the spline curves will capture pixelation and noise artifacts present in the image. If the value of  $ds$  is too large, the spline curves effectively filter out high curvature values. We used a value of  $ds$  based on the laminar flame thickness,  $\delta_{f,0}$ , following Lee et al. [83], as this is the smallest potential scale of flame wrinkling [82]. Thus,  $ds = (\pi/2)\delta_{f,0}$ .

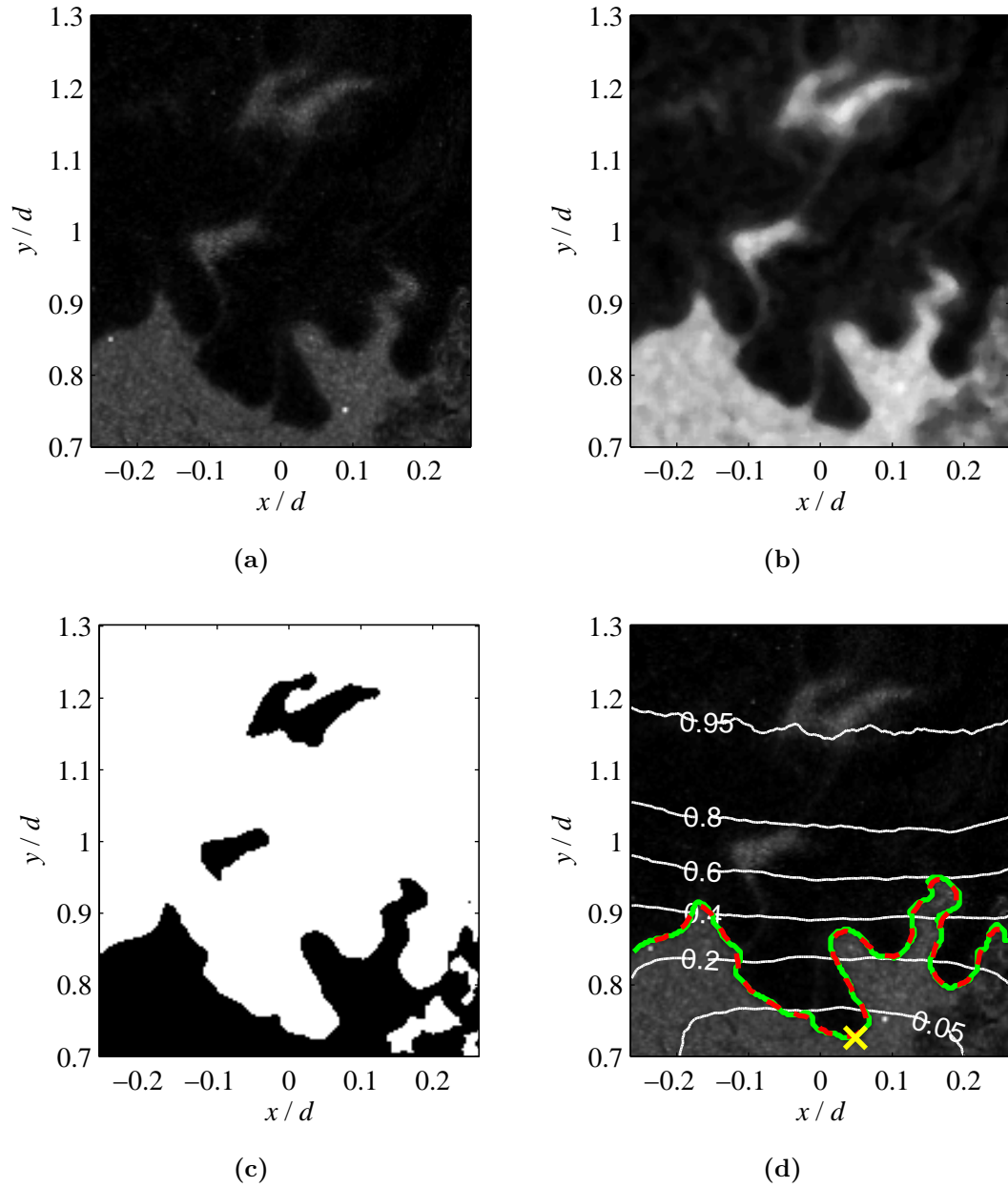


**Figure 32:** Demonstration of the post-processing procedure used to identify the flame edge from PIV images. (a) raw image, (b) median-filtered image, (c) thresholded image used to identify reactants and products and find the flame edge, and (d) flame edge (green), fitted spline curve (red), instantaneous leading point (yellow x) and average progress variable,  $\langle c \rangle$ , (white) overlaid onto raw image. Data presented are for a 50:50  $\text{H}_2$ :CO fuel mixture at STP for a swirl number of  $S = 0.58$ , mean flow velocity  $U_0 = 30$  m/s, and equivalence ratio  $\phi = 0.55$ .

The second step taken to minimize errors is the use of cubic smoothing splines to fit the resampled edge data. For a given edge, the cubic smoothing spline,  $f_{p_s}(x)$ , is found from minimizing [45]:

$$p_s \sum_{i=1}^N (y_i - f_{p_s}(x_i))^2 + (1 - p_s) \int_{x_1}^{x_N} (f_{p_s}''(x))^2 dx \quad (38)$$

where  $p_s$  is known as the smoothing parameter. Minimization of this function offers a compromise between following the data and obtaining a smooth function. The smoothing parameter  $p_s$  is determined automatically using the generalized cross-validation estimate [39]. The resulting parameterized curve is overlaid onto the raw image in red in Figure 32d.

One concern in this processing technique was if it would be sufficiently precise to resolve the smallest curvature associated with critically curved, high hydrogen flames. We spent significant time checking this point and are confident that this value is able to fully resolve the curvatures present. First, in Chapter 5, curvature statistics will be presented that show that the PDF gets broader with turbulence intensity, even for the pure H<sub>2</sub> fuel composition case. If this technique was unable to resolve the finest curvatures present than the PDFs should experience a saturation at some turbulence intensity. The fact that they continue to broaden with increasing turbulence intensity is strong evidence that this limit has not yet been reached. Second, the resolution requirements for capturing critical curvature radii are approximately  $\delta_f|_{S_{L,max}} = 0.16$  mm, while our resolution is roughly 0.11 mm/pixel. Finally, we studied the influence of arc length interval  $ds$  on the generated statistics and found no significant changes in the PDFs even under a factor of two decrease in arc length interval, as shown in Figure 33. This gives further confidence that the technique is resolving the curvature accurately.

The tangential strain rate is calculated from:

$$\kappa_s = -n_i n_j \frac{\partial u_i}{\partial x_j} + \frac{\partial u_i}{\partial x_i} \quad (39)$$

where  $n_i$  and  $n_j$  are the components of the unit normal  $\vec{n}$  to the fitted spline curve, and the spatial derivatives of the velocity are found from finite differences of the instantaneous velocity fields. Since the spline fitted curve was sampled over an even arc length interval

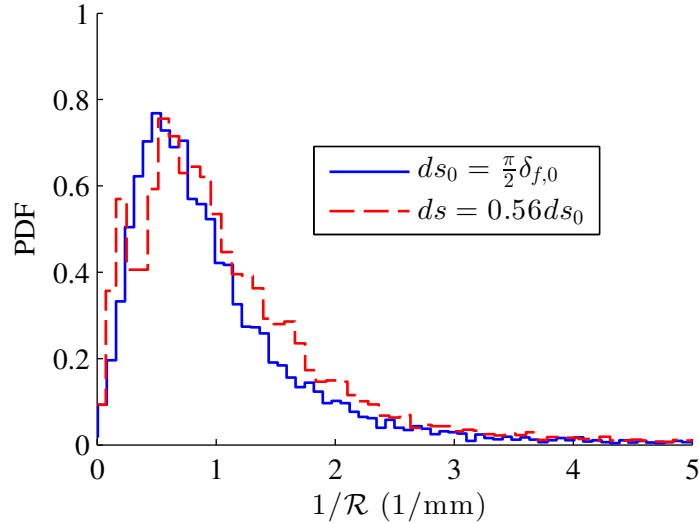


**Figure 33:** Comparison of curvature PDFs generated using two arc length intervals for a 50:50 H<sub>2</sub>:CO mixture at  $U_0 = 30$  m/s.

$ds$  and the velocity vector field is coarser than the original image, the derivatives are not available at the same physical location as the spline curve values.

This leads to an additional error source in the calculation of the tangential strain rate. Reactant velocities are needed at the flame front in order to calculate the tangential strain rate; however, if an interrogation window for calculating velocity vectors is intersected by the flame front, then the downstream, higher product velocities will bias calculations of velocities at the flame front. This is important to avoid because the flame is not affected by velocities downstream of the flame surface.

Thus, it is important to mask out the downstream region in the raw Mie scattering images (described earlier and demonstrated in Figure 32c), process the velocity fields with these masked images, and then use these reactant-conditioned velocities to calculate flame front velocities for tangential strain rate calculations. The problem that arises from this technique is that now there are no velocity vectors at the actual flame front, only upstream of the flame front, and this requires an extrapolation technique to fill in the missing information. This 2D extrapolation is performed using sparse linear algebra and PDE discretizations [47] to get velocity vectors just downstream of the flame front. Then, because the resolution of the flame front is higher than the resolution of the velocity field, the

velocities are interpolated to the flame front using bilinear interpolation.

The error introduced from this procedure is difficult to quantify; however, it is related to the size of the interrogation window. Making the interrogation window too small will, unfortunately, increase the errors in the velocity vectors due to too few seed particles to calculate statistically significant cross correlations between the image pairs. Experimentation with different interrogation window sizes was performed to determine the smallest dimensions that could be used without compromising the integrity of the velocity data. From this experimentation, the Mie scattering was processed with an interrogation window size of  $12 \times 12$  pixels with 50% overlap, resulting in a velocity vector every six pixels or 0.69 mm, which is on the order of the flame thickness.

The “instantaneous leading points” are defined as the part of the flame that instantaneously lies the farthest into the reactants, and are extracted by finding the minimum  $y$ -value of the edge at each time instance, and removing realizations where this location occurs at the edge of the domain. A representative instantaneous leading point is identified by the yellow  $x$  in Figure 32d. It is important to note that since these images are two-dimensional slices of a three-dimensional flow that the instantaneous leading point identified in the images will not generally correspond to the “true” leading point of the flame, since that point may lie outside of the plane of the laser sheet.

Returning to the binarized images, the values at each pixel are then averaged over all realizations, leading to the average progress variable  $\langle c \rangle$ -fields. These iso-contours are overlaid onto the instantaneous Mie scattering image in Figure 32d. In addition, the axial dependence of  $\langle c \rangle$  is plotted in Figure 34. The average progress variable can be used to precisely determine the location of a specific progress variable for  $S_{T,LD}$  calculations, flame brush thicknesses, conditional velocity statistics, and flame front topologies. It can also be used in combination with binarized images in order to determine the 2D flame surface density as a function of progress variable, an important quantity used in models [20] and LES [11, 59].

In addition to calculating flame properties conditioned on the instantaneous leading

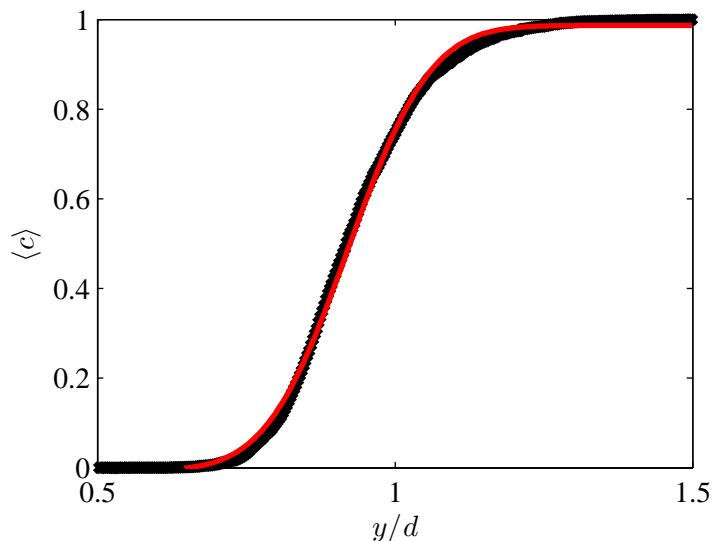


**Figure 34:** Average progress variable  $\langle c \rangle$  along the axial centerline of the burner. The red line is an error function fit to the data. Conditions are the same as in Figure 32.

points of the flame surface, another definition of the leading point of the flame can be obtained by applying the Kolmogorov-Petrovskii-Piskunov (KPP) theorem [74] to the propagation of a one-dimensional turbulent premixed flame in frozen turbulence [57, 51]. This method shows that the turbulent flame speed is controlled by the conditions at the leading edge of the flame brush, defined as the point where  $\langle c \rangle \rightarrow 0$ . We will refer to this location as the “flame brush leading point,” to distinguish from the “instantaneous leading point” illustrated in Figure 32d. Of course, in any finite size data set, a vanishing number of experimental realizations occur as the  $\langle c \rangle \rightarrow 0$ , so the flame characteristics were estimated by analyzing flame properties conditioned upon  $0 < \langle c \rangle < 0.1$  and  $0 < \langle c \rangle < 0.01$ .

The relationship between these two leading point definitions can be understood from Figure 32d, which overlays average progress variables on top of instantaneous flame fronts. In addition, Figure 35 presents a PDF of the location of the instantaneous leading point in  $\langle c \rangle$ -space for several fuel compositions; for reference, the average location of the instantaneous leading point occurs at  $\langle c \rangle \approx 0.25$ .

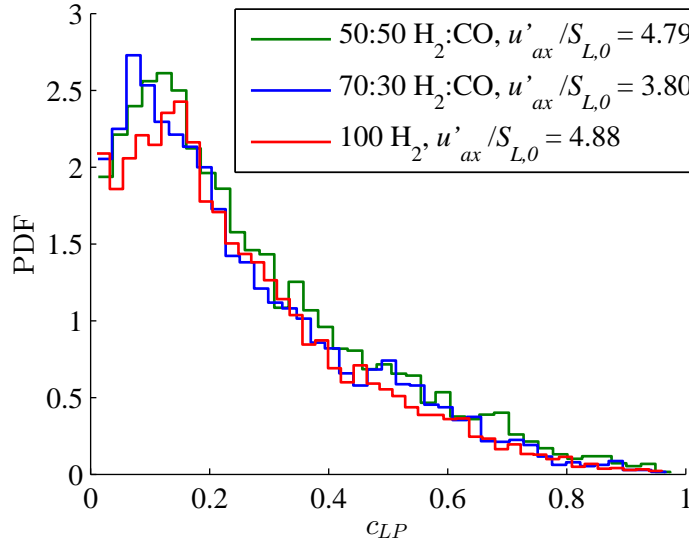


**Figure 35:** PDF of locations of instantaneous leading points in  $\langle c \rangle$ -space for three different fuel compositions.

### 2.3.3 Turbulent Flame Speed

$S_{T,LD}$  is an important parameter to study because, unlike  $S_{T,GC}$ , it is defined at a specific point in space and thus does not average over spatial variations in the turbulent flame brush and flow field. It is directly controlled by the local turbulent flow field and flame speed. By acquiring measurements of the local turbulent displacement speed and turbulence characteristics at the leading edge of the flame, it is possible to test the validity and applicability of the leading points modeling approach.

#### 2.3.3.1 Linear Fit Method

As discussed in Section 2.1.3 the velocity along the centerline of the LSB decays linearly in the near-field and the flame stabilizes where the local axial flow velocity matches the turbulent flame speed,  $S_{T,LD}$ , making determination of the flame speed a relatively simple task. Figure 36 presents the mean velocity along the centerline of the burner for a reacting  $\text{CH}_4/\text{air}$  case at STP. Figure 36 also contains a linear fit to the near-field region, which is used in the determination of the virtual origin,  $y_0$ , the normalized mean axial strain rate,  $a_{ax}$ , and the local displacement speed,  $S_{T,LD}$ .  $S_{T,LD}$  is determined by finding the location

where the axial velocity deviates from the linear fit. This is defined in this work as the location preceding the point where the error between the fit and axial velocity exceeds 1% and is marked in Figure 36 with a red  $x$ .

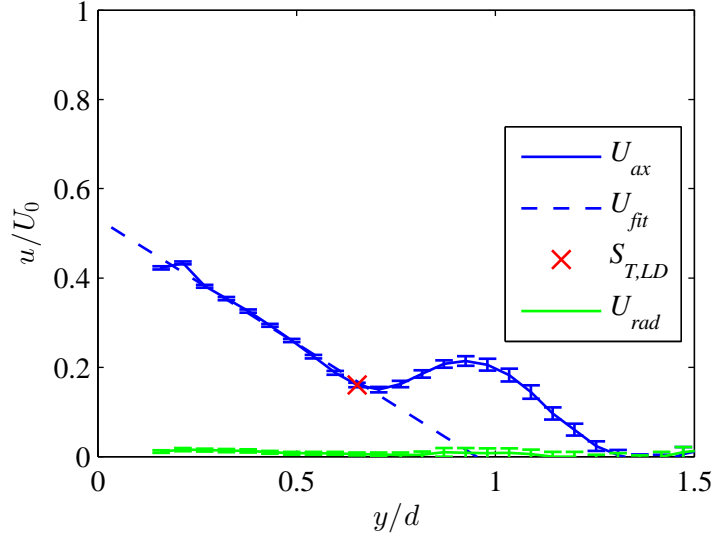


**Figure 36:** Mean velocity normalized by  $U_0$  in the axial direction along the burner centerline for a reacting (100%  $\text{CH}_4$ ,  $\phi = 0.9$ ) case at STP.  $U_0 = 20$  m/s,  $S = 0.57$ , and  $BR = 69\%$ .

### 2.3.3.2 Average Progress Variable Method

Another definition of  $S_{T,LD}$  can be obtained from velocity measurements at a defined average progress variable value. This can be accomplished using Mie scattering from the raw PIV images to track the flame edge. This has two advantages for calculating the turbulent flame speed. One, by identifying regions of reactants and products, vectors fields can be calculated for just the reactants by masking out the product region and vice versa. This allows for more accurate measurements of the incoming mean and fluctuating velocities that the turbulent flame is affected by. Two, an ensemble-averaged progress variable map for the flame brush can be generated from information about the flame front position as demonstrated in Figure 34. This allows for rigorously defining the turbulent flame speed at a specific progress variable value as opposed to taking the velocity characteristics at the

point identified in Figure 36.

## CHAPTER III

### FLOW FIELD CHARACTERIZATION

The purpose of this chapter is to provide an overview of the fluid mechanical aspects of the experimental facility. It is important in experimental studies of turbulent combustion to have a detailed understanding of the flow characteristics of the burner. This chapter is divided into two main sections. Section 3.1 details the behavior and flow characteristics of the variable turbulence generator using the Bunsen burner nozzle using both laser Doppler velocimetry (LDV) and hotwire anemometry (CTA). The simpler geometry of the Bunsen burner was chosen to develop a better understanding of the underlying physics of the turbulence generator without adding unnecessary flow features due to the presence of a swirler. Section 3.2 examines the two-dimensional flow field of the low swirl burner obtained from particle image velocimetry (PIV) experiments.

#### *3.1 Turbulence Generator Characterization*

The goal of this section is to present a comprehensive characterization of the flow field behavior of the turbulence generator over a range of operating pressures, preheat temperatures, and mean flow velocities. For benchmarking purposes, the data were acquired using the simple Bunsen burner configuration detailed in Section 2.1.2.

Data were obtained with a TSI 3-component laser Doppler velocimetry (LDV) system. The air flow was seeded using 5  $\mu\text{m}$  alumina ( $\text{Al}_2\text{O}_3$ ) particles. Time-series velocity data were also acquired at the burner centerline using a Dantec Streamline Constant Temperature hotwire Anemometer (CTA) with a 5  $\mu\text{m}$  diameter, 1.25 mm length model 55p11 straight probe. Data were obtained at mean flow velocities from  $U_0 = \dot{m}/\rho A = 4\text{-}50$  m/s, which correspond to geometric Reynolds numbers of  $Re_D = U_0 d/\nu = 5,100\text{-}206,000$  and turbulent Reynolds numbers of  $Re_{l_0} = u'_{rms} l_0/\nu = 140\text{-}9000$ . The following sections give an overview of the mean and turbulence profiles, followed by an investigation of integral length scales and power spectra.

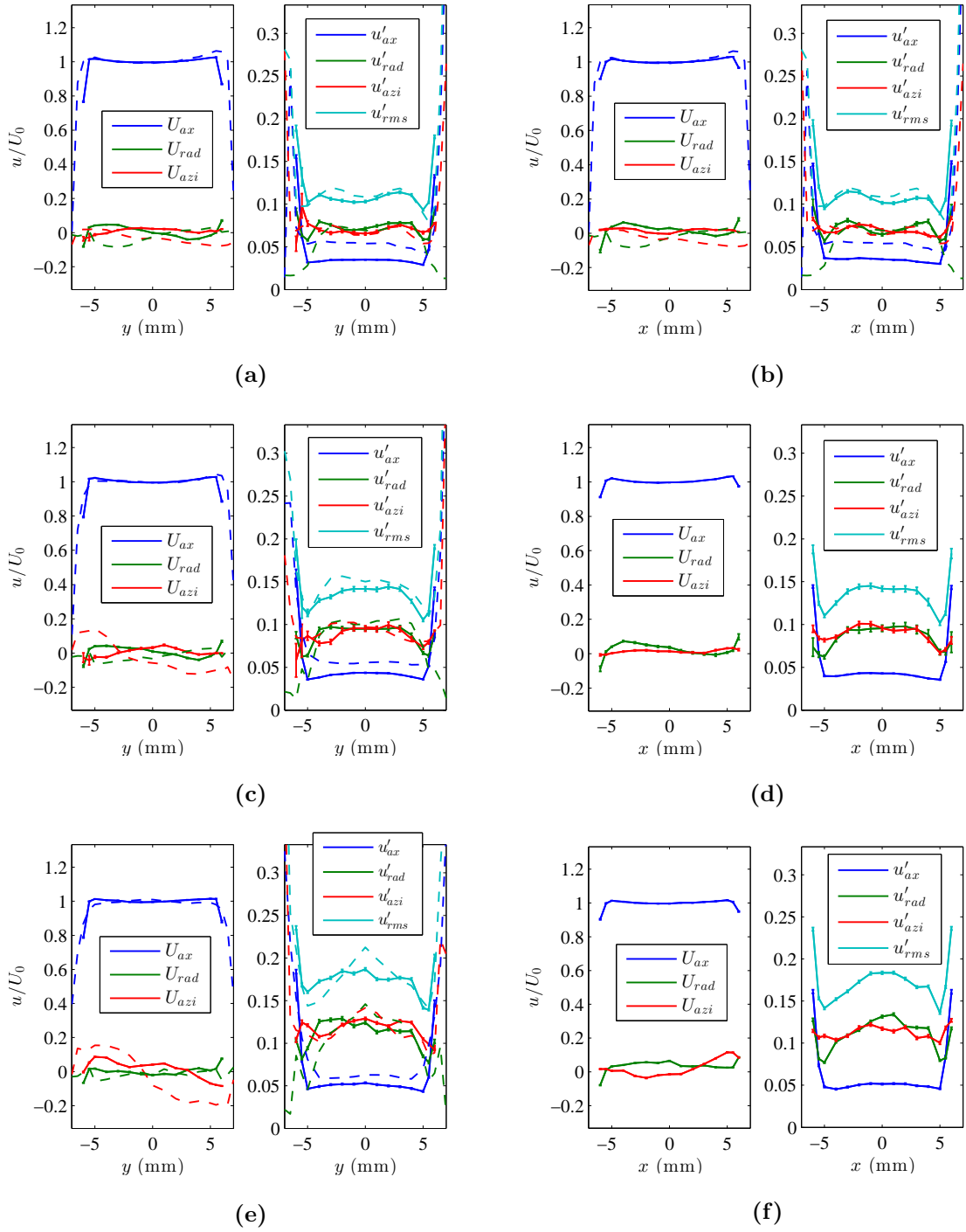
### 3.1.1 Mean and Turbulence Profiles

Figure 37 and 38 plot representative profiles of the mean and fluctuating axial, radial, and azimuthal velocities as a function of the radial distance from the center of the burner for low, medium and high blockage ratios for the 12 and 20 mm burner diameters, respectively. All velocities have been normalized by the mean axial velocity calculated in a region including all points within  $\pm 3$  mm around the center of the burner. Total turbulence intensity is calculated from  $u'_{rms} = ((u'_{ax})^2 + (u'_{rad})^2 + (u'_{azi})^2)^{1/2}$ . The solid lines correspond to a chamber pressure of 5 atm, while the dashed lines correspond to atmospheric data. In order to verify azimuthal symmetry, data are shown for the two perpendicular traverses described in Section 2.2 and illustrated in Figures 28 and 29. These data show a monotonic increase in turbulence intensity with blockage ratio, as desired. The data also show a well-defined top-hat mean axial velocity, along with low radial velocity. The azimuthal velocity increases with increasing blockage ratio. The radial variation of the mean flow velocity is low, as noted in Table 8. Also noted in Table 8 are maximum values of the mean radial and azimuthal velocities relative to the mean axial velocity. As shown in Figure 37, the radial velocity is low, less than  $0.05U_0$ , and independent of blockage ratio while the mean azimuthal velocity increases monotonically with blockage ratio. These results are typical for the other velocities and the 20 mm burner diameter.

**Table 8:** Maximum values of normalized mean axial, radial, and azimuthal velocity at three different blockage ratios.

$BR$ (%)	$\left  \frac{U_{ax}(r) - U_0}{U_0} \right _{\max}$ (%)	$\left  \frac{U_{rad}(r)}{U_0} \right _{\max}$ (%)	$\left  \frac{U_{azi}(r)}{U_0} \right _{\max}$ (%)
69	3.1	4.6	6.9
81	1.4	5.8	13.3
93	1.8	4.3	21.3

These figures also show that the turbulent fluctuations in the axial direction are about half of the fluctuations in the transverse directions. This is due to the well understood phenomenon of turbulent flow dynamics through a contraction [111, 123]. Essentially, the



**Figure 37:** LDV profiles for the 12 mm burner at (a,b)  $BR = 69\%$ , (c,d)  $BR = 81\%$ , and (e,f)  $BR = 93\%$ . (left) Mean axial, radial and azimuthal velocities and (right) RMS of the fluctuating axial, radial, azimuthal and total velocities as a function of radial distance from the center of the burner for  $U_0 = 30$  m/s. Dashed and solid lines correspond to pressures of 1 and 5 atm, respectively.

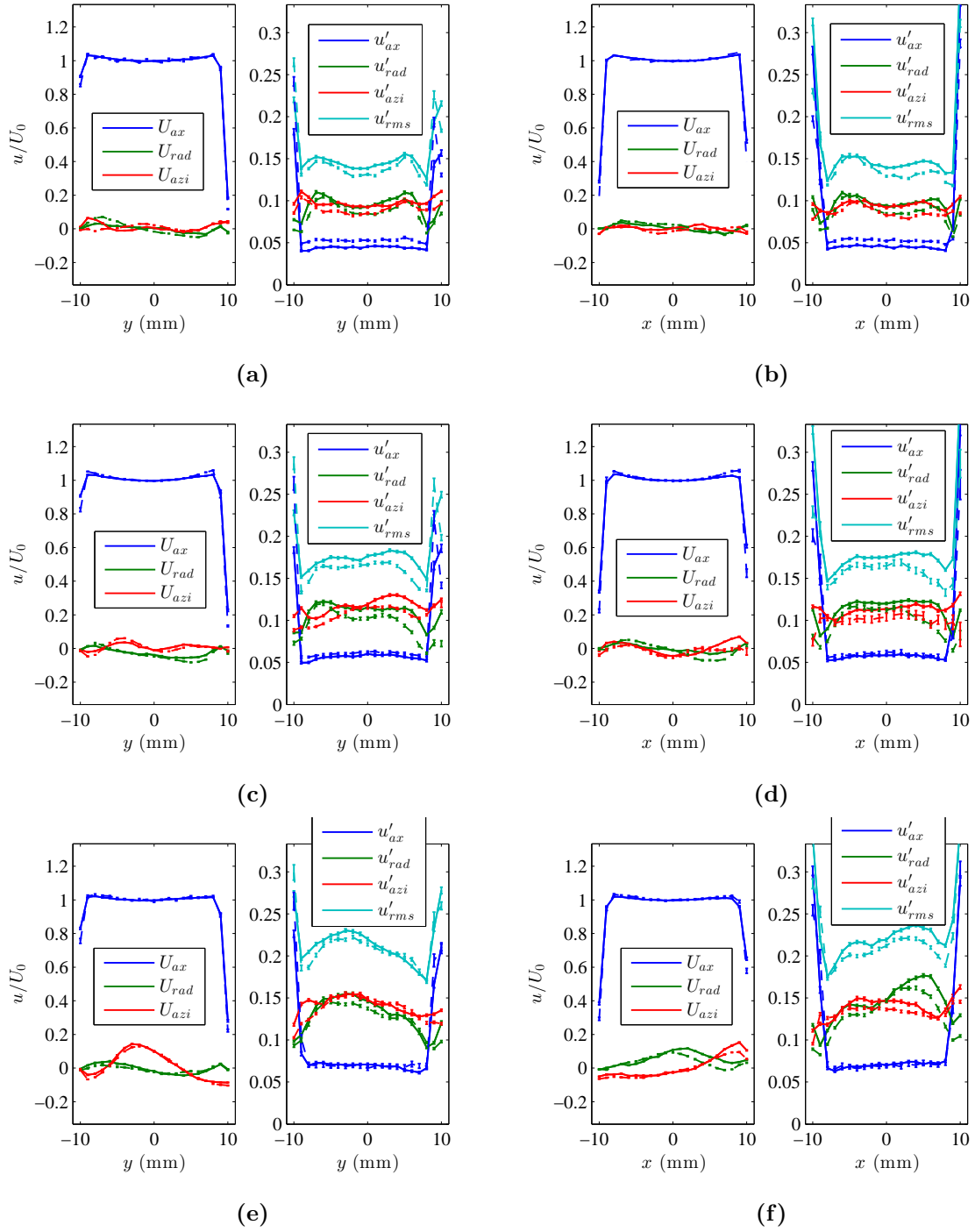


**Figure 38:** LDV profiles for the 20 mm burner at (a,b)  $BR = 69\%$ , (c,d)  $BR = 81\%$ , and (e,f)  $BR = 93\%$ . (left) Mean axial, radial and azimuthal velocities and (right) RMS of the fluctuating axial, radial, azimuthal and total velocities as a function of radial distance from the center of the burner for  $U_0 = 50$  m/s. Dashed and solid lines correspond to pressures of 1 and 5 atm, respectively.

vortex tubes that are aligned with the main axis of the burner are elongated as the flow accelerates through the contraction, increasing their vorticity and increasing the transverse velocity fluctuations ( $u'_{azi}$ ,  $u'_{rad}$ ). In addition, the vortex tubes aligned perpendicular to the main axis are contracted, reducing their vorticity and decreasing the axial velocity fluctuations ( $u'_{ax}$ ). This is different from the results reported by Videto and Santavicca [135], who reported nearly isotropic turbulence. It is common to use a contraction after a turbulence generator (i.e. grid, perforated plate, etc.) to improve the isotropy of the turbulence [36], because the resulting flow turbulence is strongest in the axial direction. The contraction causes vortex stretching which equilibrates the three components. However, this is generally a weak contraction; an area contraction ratio of 1.27 and 2.6 were used in the studies of Comte-Bellot [36] and Videto and Santavicca [135], respectively. Our area contraction ratios are 40 and 14 for nozzle diameters of 12 and 20 mm, respectively. These high area contraction ratios produce radially uniform velocity profiles as shown above, as well as flashback-resistant burners, but also lead to this anisotropy in turbulence intensity.

Figure 39 summarizes the performance of the turbulence generator by plotting the total centerline turbulence intensity,  $u'_{rms}/U_0$ , as a function of the blockage ratio over a range of pressures, temperatures, and mean flow velocities for two burner diameters. It shows that the turbulence intensity monotonically increases with blockage ratio. The 12 mm burner has lower turbulence intensities than the 20 mm burner at the same blockage ratio, because the flow velocity through the blockage plate gaps is lower for the smaller burner (note that the nozzle exit velocity is the fixed parameter, not the velocity through the plates). Figure 39 also presents the linear fit of the combined data with the associated 95% confidence levels. The data tend to follow the same trend regardless of pressure, temperature, or bulk flow velocity.

One question that should be considered when performing combustion experiments (such as determining the turbulent flame speed) is the appropriate location to characterize the turbulence intensity. This is an important question since (1) the turbulence intensity varies radially and axially, (2) there is strong shear-generated turbulence at the jet edges, and (3) the location of the flame surface is constantly changing. While there is no clear consensus

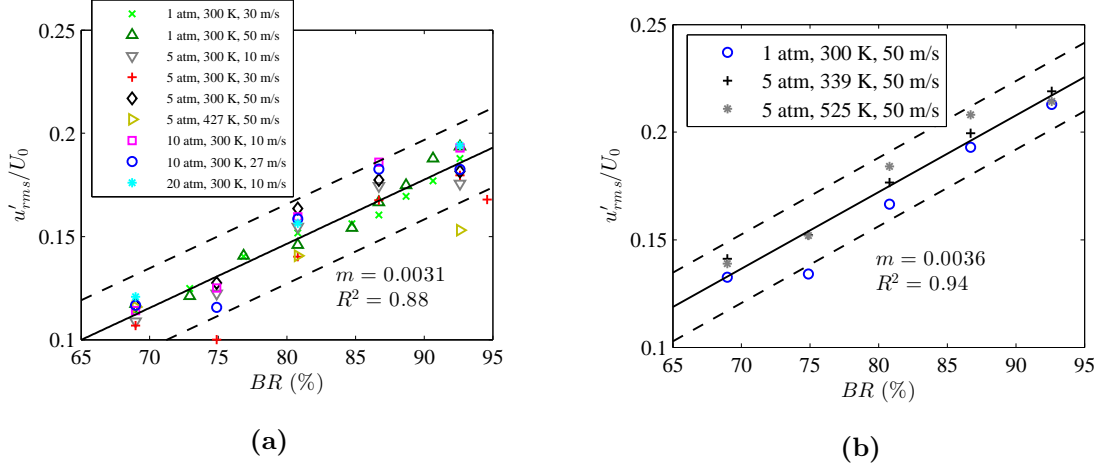


**Figure 39:** Dependence of the burner centerline total turbulence intensity on blockage ratio for the (a) 12 mm and (b) 20 mm diameter burners. The solid line corresponds to the linear fit of the data, and the dashed lines correspond to the 95% confidence level. Slopes and  $R^2$  values of the linear fits are displayed on the graphs

on the appropriate location, note that the centerline turbulence intensity scales well with that at other locations. To illustrate, Figure 40 presents a comparison between the shear layer (or, more precisely, at  $r = 10$  mm) and centerline turbulence intensities for the 20 mm diameter burner. Note the one-to-one correspondence between the two, with  $u'_{rms}(r = 10 \text{ mm}) = 0.8u'_{rms}(r = 0 \text{ mm}) + 6.9U_0$ .

### 3.1.2 Flow Length and Time Scales

A typical autocorrelation function is shown in Figure 41 for the 20 mm diameter burner. With the LDV system and experimental configuration used it was difficult to get data rates high enough to obtain the roll-off region at low time lag constants. The roll-off is noticeable in Figure 41b; however, it appears to start at an autocorrelation value of approximately 0.9. This occurs in all cases and indicates very low correlation time random noise in the measurements.

Figure 42 summarizes the calculated  $l/d$  values at mean flow velocities of 4, 30, and 50 m/s for the 20 mm burner and 30 and 50 m/s for the 12 mm burner at various blockage ratios. The data indicate that  $l/d$  do exhibit some sensitivity to blockage ratio, but that they

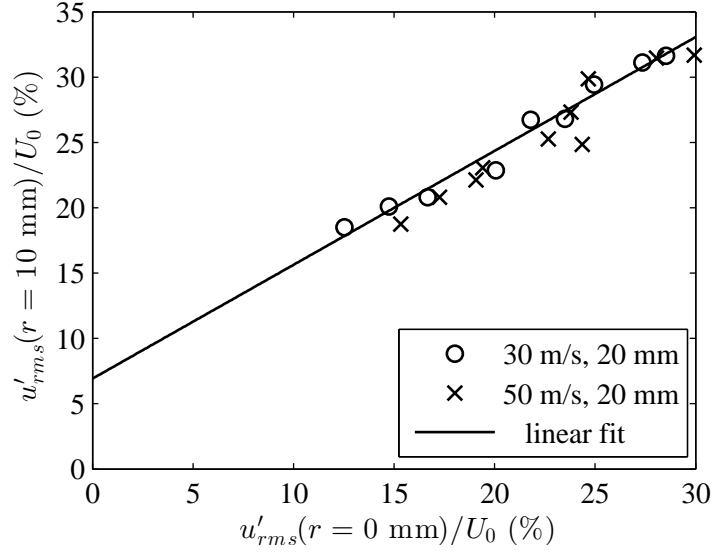


**Figure 40:** Comparison of turbulence intensity in the shear layer to turbulence intensity along the nozzle centerline.

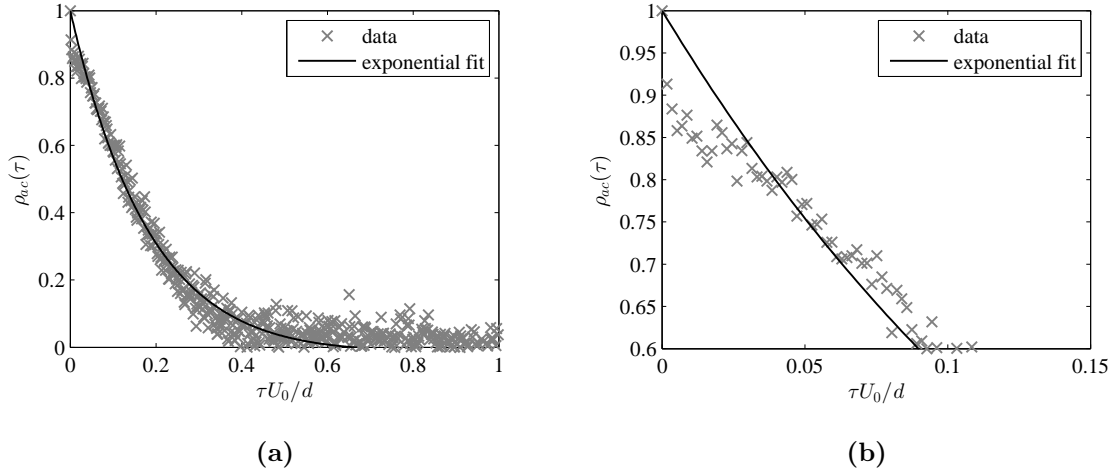


**Figure 41:** Autocorrelation function plotted against normalized lag time for the 20 mm diameter burner at  $U_0 = 4$  m/s,  $BR = 75\%$ . (a) Over one time constant and (b) zoomed in on initial roll-off region.

are not changing proportionally to blockage gap width. The blockage gap width changes by a factor of six from the fully open position to the highest blockage ratio, while  $l$  changes at most by a factor of two. The increase in length scale at the highest blockage ratios is apparently a manifestation of the growing presence of a large scale organized structure, and provides another reason to avoid blockage ratios greater than about 93%.

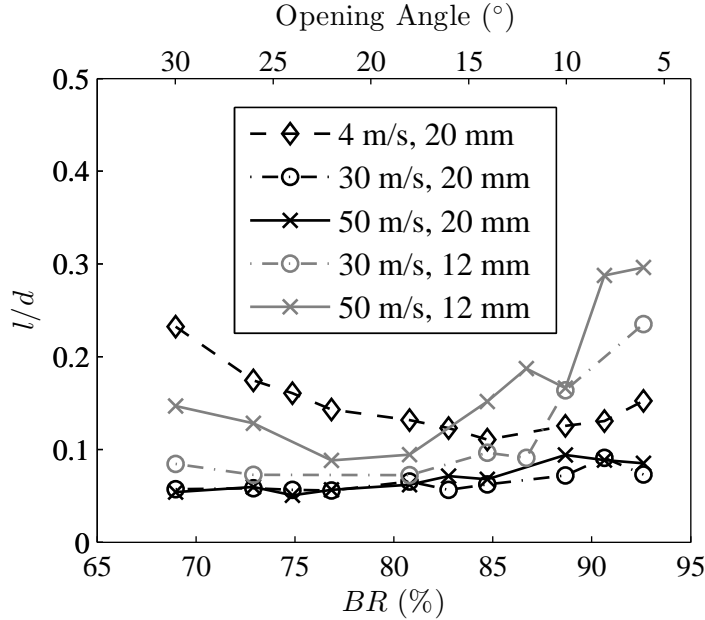


**Figure 42:** Comparison of characteristic longitudinal length scale,  $l$  (normalized by burner diameter  $d$ ) as a function of blockage ratio for the two burner diameters over a range of mean flow velocities.

### 3.1.3 Power Spectra

Power spectra were obtained from velocity time-series data using hotwire anemometry. The power spectra were ensemble-averaged over 50 ensembles with 50% overlap. Figure 43a presents the non-dimensionalized turbulent power spectra at the burner centerline for several blockage ratios at  $U_0 = 10$  m/s. The spectra show a smooth roll-off with increasing frequency and no discrete peaks, as desired. In addition, the spectra have virtually the same shape at each blockage ratio. Figure 43b presents the turbulent power spectra at a fixed blockage ratio of 77% at 4, 10, and 50 m/s for the 20 mm burner to illustrate mean velocity effects. The figure shows the collapse of the spectra at lower frequencies, but also

that increasing flow velocity broadens the high frequency spectral range over which kinetic energy is distributed, as also expected [125].

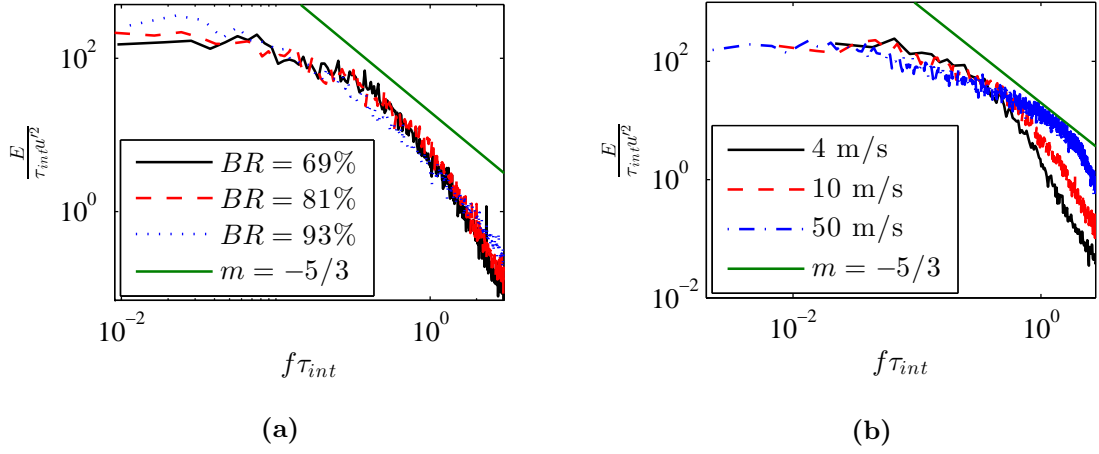


**Figure 43:** Turbulent power spectra for the 20 mm burner at (a)  $U_0 = 10 \text{ m/s}$  at three different blockage ratios and (b)  $BR = 77\%$  at three different mean flow velocities.

### 3.1.4 Summary

This section presented a turbulence generation system developed for combustion studies. While grids, perforated plates, or slots are commonly used for turbulence generators, they have the disadvantage that the grid or plate must be changed in order to access a different turbulence level at a given flow velocity. The turbulence generator described in this section was found to achieve a range of relative turbulence intensities from 10% to 30% and turbulent Reynolds numbers from 240 to 2,200 without exchanging plates or varying the mean flow velocity. This allowed for independently studying the effects of mean flow velocity and turbulence on combustion characteristics such as the turbulent flame speed.

The maximum useful turbulence intensities of the device are primarily limited by the increasing azimuthal flow at high blockage ratios. This is manifested by deterioration in turbulent flow profiles, as shown in Figures 37 and 38, and indications of an organized structure in the flow, as shown in Figure 42.

## 3.2 Low Swirl Burner Velocity Field Characterization

### 3.2.1 Mean and Turbulence Profiles

The data presented in this section were acquired at STP. Figure 44 compares mean velocity fields obtained in non-reacting and reacting flows. These profiles show the typical features of LSB flow fields. The velocity is higher in the outer swirling region due to the fact that more of the flow (approximately 68%) passes through the swirler. In the central, non-swirling portion of the flow the velocity profile is relatively flat with almost no radial component, an important feature when determining  $S_{T,LD}$ . The reacting flow field also exhibits increased divergence compared to the non-reacting case. This is consistent with the observation that the flame acts as an aerodynamic blockage against the flow [89].

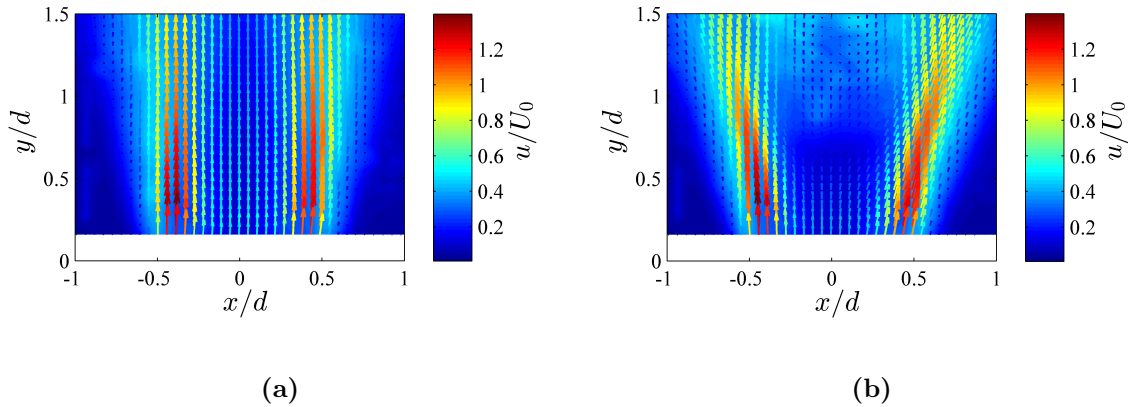


**Figure 44:** Mean velocity normalized by  $U_0$  for (a) non-reacting and (b) reacting (100%  $\text{CH}_4$ ,  $\phi = 0.9$ ) cases at STP.  $U_0 = 20$  m/s,  $S = 0.57$ , and  $BR = 69\%$ .

The velocity along the centerline of the LSB decays linearly in the near-field and the flame stabilizes where the axial flow velocity matches the turbulent flame speed,  $S_{T,LD}$ . Figure 45 presents the mean velocity along the centerline of the burner for non-reacting and reacting cases. For the non-reacting case the axial velocity decays monotonically with downstream distance. As desired, the radial velocity is near zero for both reacting and non-reacting cases. The presence of the flame causes an increase in the magnitude of the mean axial strain rate,  $dU_0/dy$ , in the near-field region ( $y/d < 0.65$ ) and an increase in velocity through the flame ( $0.65 < y/d < 1$ ) due to gas expansion effects. The axial velocity

then decays to zero around  $y/d = 1.4$ . Figure 5(b) also contains a linear fit to the near-field region, which is used in the determination of the virtual origin,  $y_0$ , and the mean axial strain rate. Figure 46 compares axial velocity profiles for two different mean flow velocities and fuel compositions. These plots demonstrate the self-similarity of the LSB in the region upstream of the flame zone.

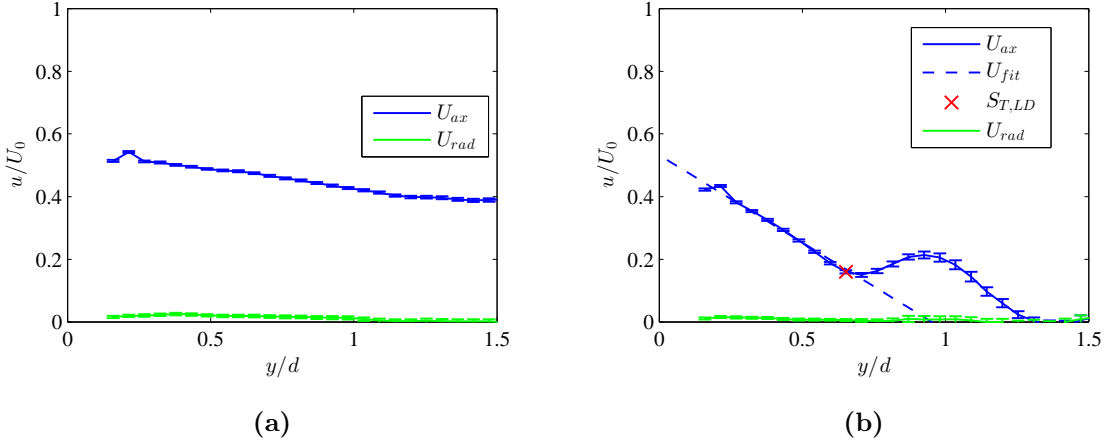


**Figure 45:** Mean velocity normalized by  $U_0$  in the axial direction along the burner centerline for (a) non-reacting and (b) reacting (100%  $\text{CH}_4$ ,  $\phi = 0.9$ ) cases at STP.  $U_0 = 20$  m/s,  $S = 0.57$ , and  $BR = 69\%$ .

Figure 47 compares RMS velocities along the centerline for non-reacting and reacting cases. The turbulence intensities remain relatively constant in the non-reacting case, increasing slightly downstream. The axial turbulence intensity is on average, 75% of the radial turbulence intensity. The presence of the flame increases the divergence of the flow, causing the axial flow upstream of the flame to decelerate faster. This deceleration compresses vortex tubes aligned with the axial direction, decreasing  $u'_{rad}$ , and will stretch vortex tubes aligned with the radial direction, increasing  $u'_{ax}$ . This effect is evident in Figure 47b.  $u'_{rms}$  is plotted to compare turbulence levels with the results presented in Figure 39. The red  $x$  in Figure 47b on the  $u'_{ax}$  line marks the location of  $S_{T,LD}$  given in Figure 45b.

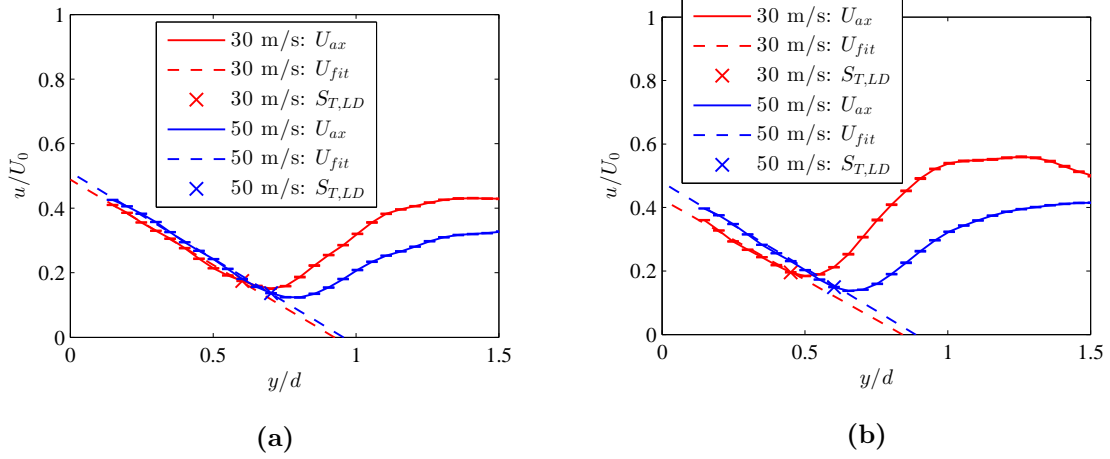


**Figure 46:** Mean axial velocity normalized by  $U_0$  in the axial direction along the burner centerline for (a) 70:30  $\text{H}_2$ :CO ( $\phi = 0.51$ ) and (b) 100%  $\text{H}_2$  ( $\phi = 0.46$ ) cases at STP for  $U_0 = 30$  and 50 m/s.  $S = 0.58$  and  $BR = 69\%$ .

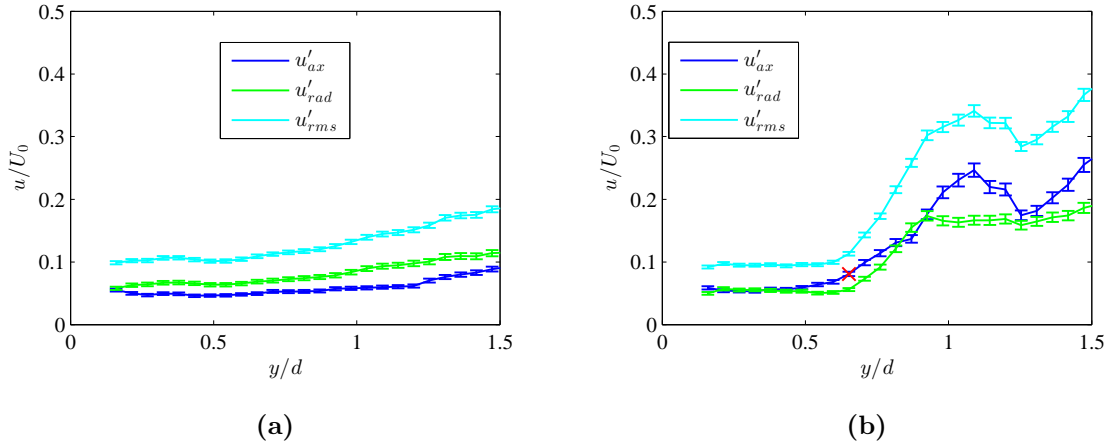


**Figure 47:** RMS velocity normalized by  $U_0$  in the axial direction along the burner centerline for (a) non-reacting and (b) reacting (100%  $\text{CH}_4$ ,  $\phi = 0.9$ ) cases at STP.  $U_0 = 20$  m/s,  $S = 0.57$ , and  $BR = 69\%$ .

### 3.2.2 Integral Length Scales

Figure 48 presents integral length scales  $l_0$  of the LSB calculated from the PIV vector fields along the axial centerline of the burner. The resolution of the camera and the size of the PIV interrogation windows resulted in a vector spacing of approximately 0.69 mm. This is the reason for the relatively large error bars present on the plots. From these figures it is evident that the integral length scale remains relatively constant with downstream distance up until  $y/d \approx 1$ . These plots also show that the integral length scale is relatively insensitive to blockage ratio (Figure 48a), bulk flow velocity (Figure 48b), and fuel composition (Figure 48c). In general, the normalized integral length scale is  $l_0/d \approx 0.08$ , which corresponds to an integral length scale of  $l_0 \approx 3$  mm.

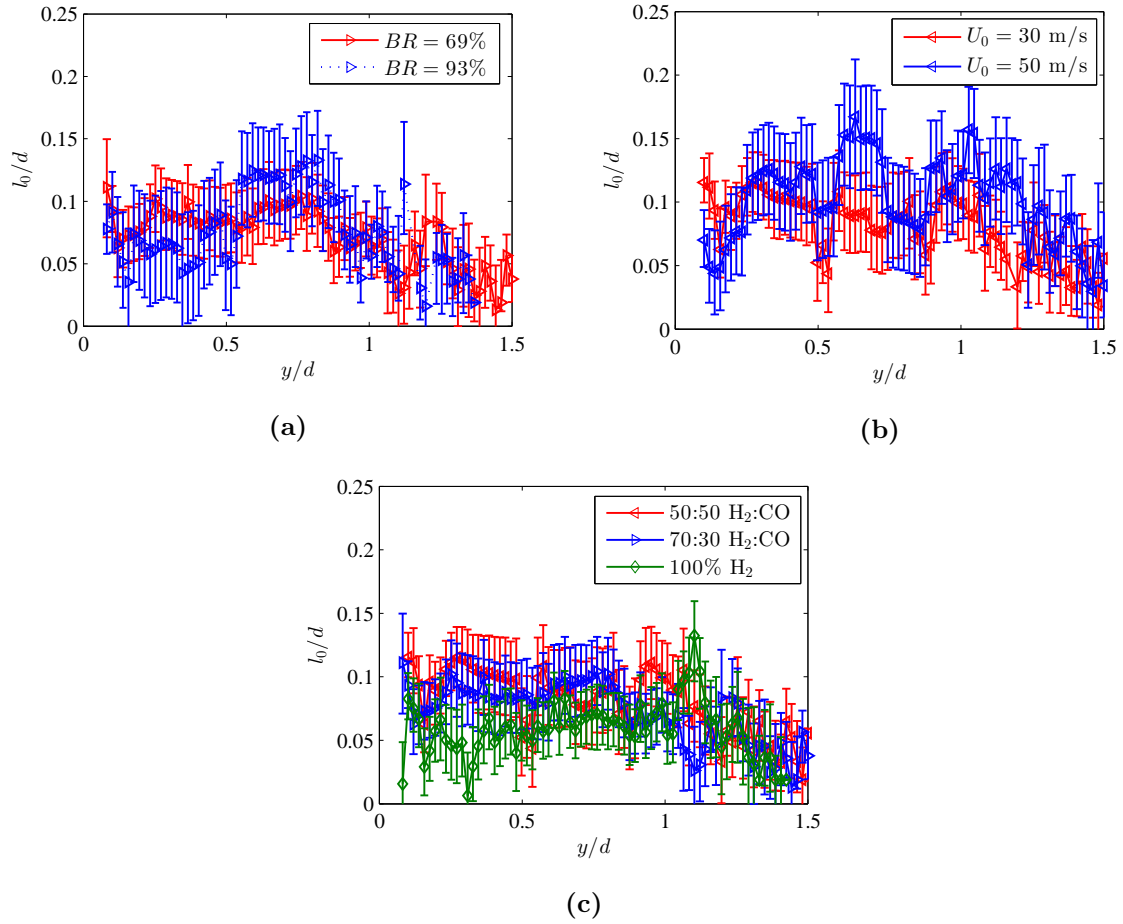


**Figure 48:** Integral length scale  $l_0$  (normalized by burner diameter  $d$ ) as a function of downstream distance  $y/d$  for (a) low and high blockage ratios ( $S = 0.58$ ,  $U_0 = 30$  m/s, 70:30  $\text{H}_2$ :CO), (b) low and high bulk flow velocity ( $S = 0.58$ , 50:50  $\text{H}_2$ :CO,  $BR = 69\%$ ), and (c) three different fuel compositions ( $S = 0.58$ ,  $U_0 = 30$  m/s,  $BR = 69\%$ ). Errors bars are for the 95% confidence interval.

## CHAPTER IV

### TURBULENT FLAME SPEED MEASUREMENTS

The purpose of this chapter is to present and analyze turbulent flame speed data acquired for this thesis. The first section gives an overview of some of the global consumption turbulent flame speed data acquired by Venkateswaran [134]. The goal of this section is to present in more detail some of the background work that laid the foundation for the development of the low swirl burner facility and the acquisition of localized flow and flame measurements for validation of the leading points model. This section will present global consumption speed  $S_{T,GC}$  measurements with a focus on the effects of fuel composition and pressure. The data are also analyzed using the leading points model. Some of the deficiencies of the leading points model are noted from this data, and an attempt to understand these deficiencies in terms of non-quasi-steady effects on the flame is presented. The next section presents measurements and analysis of local displacement turbulent flame speed data acquired in the LSB. These measurements were acquired to supplement the global consumption measurements, and, thus, were acquired at similar operating conditions. In addition, this data is also analyzed using the leading points model to see how this model works on data acquired from a different experimental configuration.

As discussed in Section 1.3 of Chapter 1 leading points concepts can be used to develop an inequality for scaling the turbulent flame speed that is similar to the classical Damköhler turbulent flame speed scaling [40], except the parameter arising from the analysis is the maximum stretched laminar flame speed,  $S_{L,max}$  [133]. The form of this scaling law is given by Equation 23. In certain situations this inequality can be replaced by an equality. For example, because the mixtures investigated in this work are thermodiffusively unstable,  $S_{L,0}$  is a repelling point since a positively curved perturbation on a flat flame will grow with increasing curvature and correspondingly increasing flame speeds. In fact, it can be rigorously shown that  $S_{L,max}$  is a steady-state attracting point for constant density flames

with positively curved wrinkles [133]. As such, if the turbulent eddies evolve over a time scale that is slow relative to that required for the leading points to be attracted to the  $S_{L,max}$  point, then Equation 23 can be replaced by an equality:

$$\frac{S_T}{S_{L,max}} = 1 + \frac{u'_{LP}}{S_{L,max}} \quad (40)$$

Another important caveat is that  $S_{L,max}$  is itself a frequency dependent quantity. In other words, the augmentation of the laminar burning velocity by stretch decreases, while the extinction stretch rate increases, for unsteady flames [62]. Thus, there are two important non-quasi-steady effects which influence this scaling, one related to the geometry of the turbulent flame brush, and the other related to the internal flame structure.

## 4.1 *Turbulent Global Consumption Flame Speeds*

### 4.1.1 Overview

This section describes measurements and correlations of turbulent consumption speeds,  $S_{T,GC}$ , of hydrogen and carbon monoxide ( $H_2:CO$ ) fuel mixtures, with a focus on elevated pressure data. Turbulent consumption speed data were obtained at mean flow velocities and turbulence intensities of  $30 < U_0 < 50$  m/s and  $5 < u'_{rms}/S_{L,0} < 30$ , respectively, for  $H_2:CO$  mixtures ranging from 30-90%  $H_2$  by volume from 1-10 atm. Experiments were conducted where the mixture equivalence ratio,  $\phi$ , was adjusted at each fuel composition to have nominally the same unstretched laminar flame speed,  $S_{L,0}$ . In comparing two blends with the same composition,  $S_{L,0}$  value, and flow conditions, the 5 and 10 atm data have  $S_{T,GC}$  values that are consistently about 1.8 and 2.2 times larger than the 1 atm data, respectively. These data are also correlated with the scaling law derived from quasi-steady leading points concepts using detailed kinetics calculations of highly stretched flames. For a given pressure, these scalings do an excellent job in scaling data obtained across the  $H_2:CO$  fuel composition and fuel/air range. However, the pressure sensitivities are not captured by this scaling. This pressure sensitivity may be more fundamentally a reflection of the non-quasi-steady nature of the flame leading points. In support of this argument, the spread in the data can largely be correlated with the ratio of a chemical time scale to a flow time scale.

### 4.1.2 Background

This section analyzes the scaling relation given by Equation 23 as well as coupled pressure and fuel effects. There are limited data of this kind in the literature. Turbulent consumption speed measurements of  $\phi = 0.9$  CH<sub>4</sub>/air were reported by Kobayashi et al. [73]. It was concluded that  $S_{T,GC}/S_{L,0}$  increased with pressure due to  $S_{L,0}$  decreasing but that  $S_{T,GC}$  itself was independent of pressure. Kitagawa et al. [72] reported measurements of turbulent flame speeds of H<sub>2</sub>/air mixtures at pressures ranging from 1-5 atm. They found that pressure had an influence on  $S_T/S_{L,0}$  through the pressure effect on  $S_{L,0}$ , however, the influence on  $S_T$  is unclear. Daniele et al. [41] report  $S_{T,GC}$  measurements of H<sub>2</sub>:CO mixtures for pressures of 1-20 atm at 623 K. They found that  $S_{T,GC}/S_{L,0}$  increased with pressure at each given H<sub>2</sub>:CO ratio and  $u'_{rms}/S_{L,0}$  value.

### 4.1.3 Methods

#### 4.1.3.1 Image Processing

The image processing methodology has been extensively documented in [133], but is briefly overviewed here. Global consumption speeds were calculated using Equation 13, whose key measurement input is the progress variable surface area,  $A_f$ .

Digital images of the flame emission were captured with a 16-bit intensified charge-coupled device (ICCD) camera. Line-of-sight images of the flame were obtained over five seconds and time-averaged. To estimate the time-averaged flame brush location from the line-of-sight images, a three-point Abel deconvolution scheme [42] was used. The axial distribution of the centerline intensity was then fit to a Gaussian curve, from which the location of the maximum intensity was identified. This point is associated with the most probable location of the flame, and defined as the  $\langle c \rangle = 0.5$  progress variable contour. The estimated uncertainty in identifying this point is 1-2%. Straight lines are then drawn from this point to the two flame anchoring points and rotated about the line of symmetry to generate a cone; i.e., the “angle method” [73, 8, 118]. The overall uncertainty in the  $S_{T,GC}$  value is estimated to be 3%.

#### 4.1.3.2 Stretch Sensitivity Calculations

Stretch sensitivity calculations were performed for the mixtures investigated in Table 9. Stretch sensitivities were calculated using an opposed flow calculation of two premixed flames with a nozzle separation distance of 20 mm using the OPPDIF [67] module in CHEMKIN. An arc length continuation method was used to determine the extinction point. From these calculations, various stretched properties of the mixture were extracted. In this work, the displacement laminar flame speed is considered, determined from the minimum velocity just upstream of the reaction zone as suggested by Wu and Law [139].

### 4.1.4 Results

#### 4.1.4.1 Experimental Conditions

Measurements of  $S_{T,GC}$  were obtained at 1, 5, and 10 atm as a function of  $u'_{rms}/S_{L,0}$  using a 12 mm diameter Bunsen burner. Data were acquired at mean flow velocities from 20-50 m/s and volumetric H<sub>2</sub>:CO ratios ranging from 30:70-90:10, keeping  $S_{L,0}$  and reactant temperature fixed at 34 cm/s and 300 K, respectively.  $S_{L,0}$  was kept nominally constant by adjusting the stoichiometry at each H<sub>2</sub>:CO ratio.  $S_{L,0}$  estimates were determined using the PREMIX module [66] in CHEMKIN with the Davis H<sub>2</sub>/CO mechanism for H<sub>2</sub>:CO mixtures [43]. The parameter ranges explored in this study along with the symbol type and color scheme are summarized in Table 9. Figure 49 summarizes where the measured data are located on the Borghi-Peters diagram [13, 105], where the Karlovitz number  $Ka$  was previously defined in Chapter 1, Equation 4. The data fall within the thin reaction zones regime ( $1 < Ka < 100$ ), implying that Kolmogorov eddies may enter the preheat zone but are still too large to enter the reaction zone where they may lead to quenching [105].

#### 4.1.4.2 H<sub>2</sub>:CO Sweeps at Constant $S_{L,0}$

In this section,  $S_{T,GC}$  data acquired at 1, 5 and 10 atm are reported. As described earlier, data were acquired for mixtures where the H<sub>2</sub>:CO ratio and equivalence ratio were simultaneously adjusted to maintain the same mixture  $S_{L,0}$  of 34 cm/s.

Figure 50 plots  $S_{T,GC}$  as a function of  $u'_{rms}$  normalized by  $S_{L,0}$  for the range of conditions

**Table 9:** Investigated 12 mm burner data set

Parameter	Value (Legend Designation)			
$U_0$ (m/s)	20 (Green markers)			
	30 (Red markers)			
	50 (Blue markers)			
$H_2$ (%)	30 (●)	50 (◀)	70 (▶)	90 (◆)
$\phi$ ( $p = 1$ atm)	0.61 (no fill)	0.55 (no fill)	0.51 (no fill)	0.48 (no fill)
$\phi$ ( $p = 5$ atm)	0.75 (red fill)	0.68 (red fill)	0.63 (red fill)	0.59 (red fill)
$\phi$ ( $p = 10$ atm)		0.75 (black fill)		

reported in Table 9. Note that the 5 atm data were acquired for mean flow velocities of 30 and 50 m/s and the 10 atm data for 30 m/s.

Several important observations can be made from this figure. First, the “fuel effect” is clearly present at the elevated pressure conditions; i.e., different  $H_2$ :CO blends at constant  $S_{L,0}$  and  $u'_{rms}$  have different turbulent flame speeds. Second, it is clear that  $S_{T,GC}$  at 5 atm is approximately double its value at 1 atm, and increases slightly further at 10 atm. This increase is quantified in Figure 51, which plots the ratio of  $S_{T,GC}$  at 5 and 10 atm to 1 atm for each mixture and mean flow velocity as a function of turbulence intensity. This ratio has values of about 1.8 and 2.2 at 5 and 10 atm, respectively. Note that this is not an  $S_{L,0}$  effect, as  $S_{L,0}$  is kept fixed at 34 cm/s. The next section describes analysis and discussion of the data.

#### 4.1.5 Analysis

In this section, the data presented in Figure 50 are correlated using the steady-state leading points scaling law of Equation 40. Before doing so, it is useful to present pressure effects on the calculated stretch sensitivity of the mixtures investigated. Figure 52 plots the stretch sensitivity of 70:30  $H_2$ :CO mixtures whose  $S_{L,0}$  is kept constant at 34 cm/s across the pressures by adjusting the equivalence ratio.

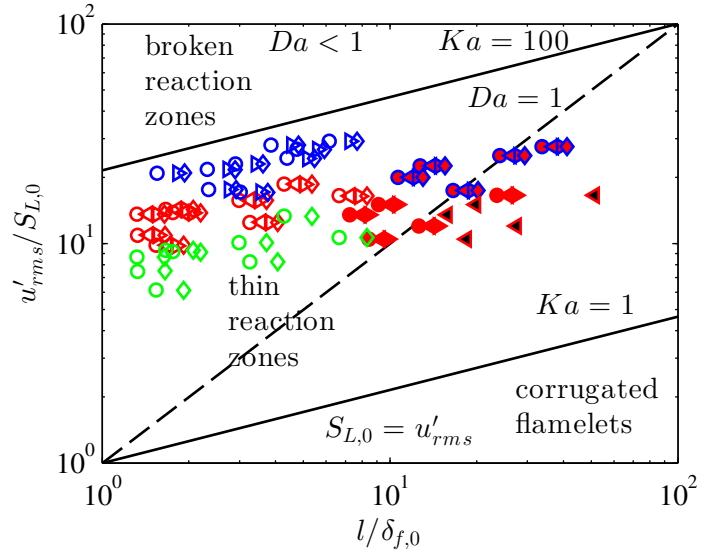


**Figure 49:** Borghi-Peters diagram showing location of 12 mm burner data points at 1, 5 and 10 atm.

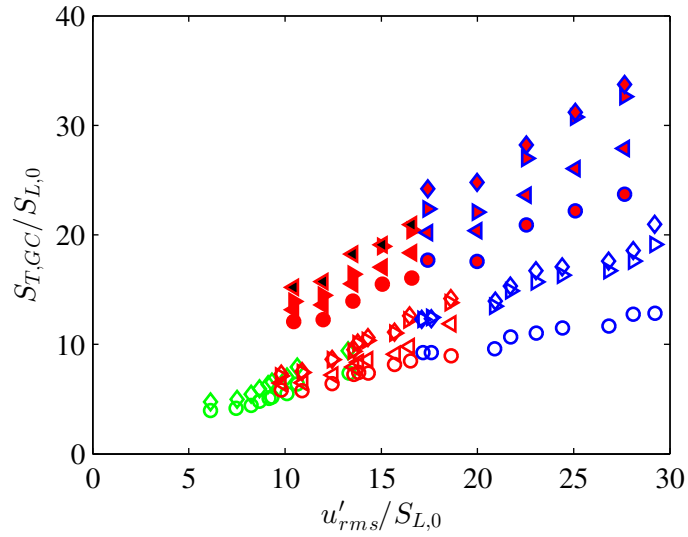


**Figure 50:**  $S_{T,GC}$  as a function of  $u'_{rms}$  normalized by  $S_{L,0}$  at various mean flow velocities,  $H_2:CO$  ratios, and pressures for the 12 mm diameter burner (See Table 9 for the legend of mixture conditions, flow velocities and pressures).

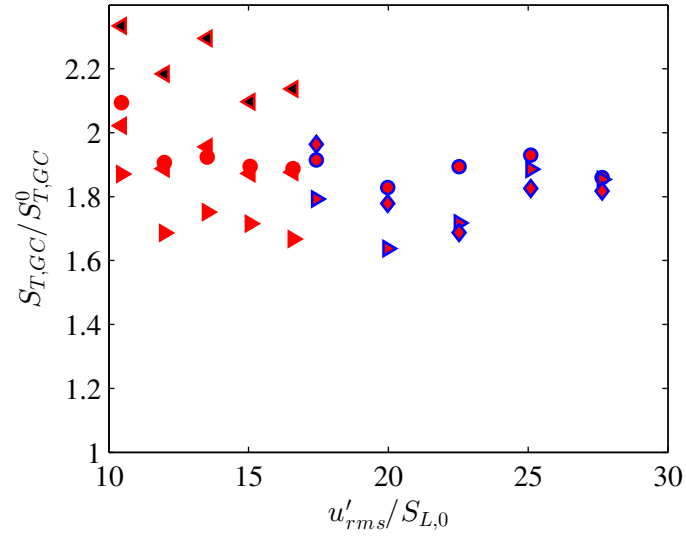


**Figure 51:** Ratio of  $S_{T,GC}$  at 5 and 10 atm to 1 atm across the range of turbulence intensities investigated.

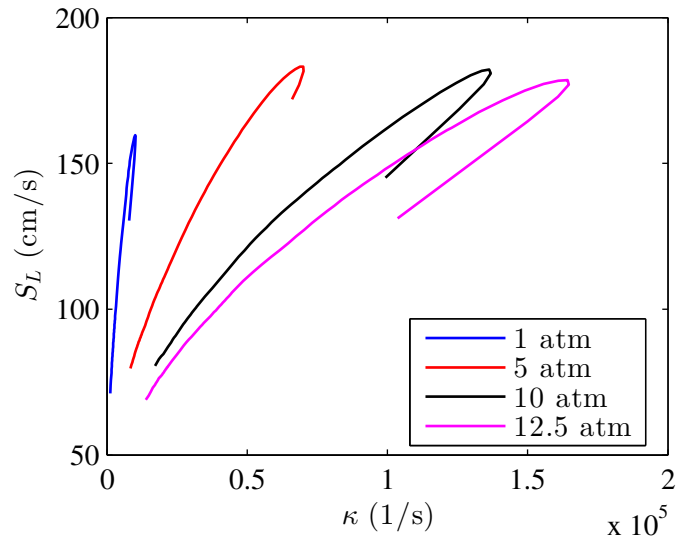


**Figure 52:** Pressure effect on mixture stretch sensitivity for 70:30  $H_2:CO$  mixtures at constant  $S_{L,0}$ .

Note from Figure 52 that the extinction stretch rate,  $\kappa_{ext}$ , and the Markstein length,  $l_M$ , scale with the pressure. In other words, if the pressure is increased by a factor of 5, the extinction stretch rate and Markstein length increase and decrease by a factor of approximately 5, respectively. This can be explained by the thinning of the flame with pressure. These two effects compensate so that  $S_{L,max}$  is relatively insensitive to pressure. In fact, above 5 atm  $S_{L,max}$  remains almost constant and actually decreases beyond 12.5 atm.

Similar calculations were performed to normalize the measured turbulent flame speed data, as shown in Figure 53. This figure shows that both the 5 atm and 1 atm data sets collapse quite well individually but that there are systematic differences between them. No similar comparison can be made for the 10 atm data set, since only one composition was examined.

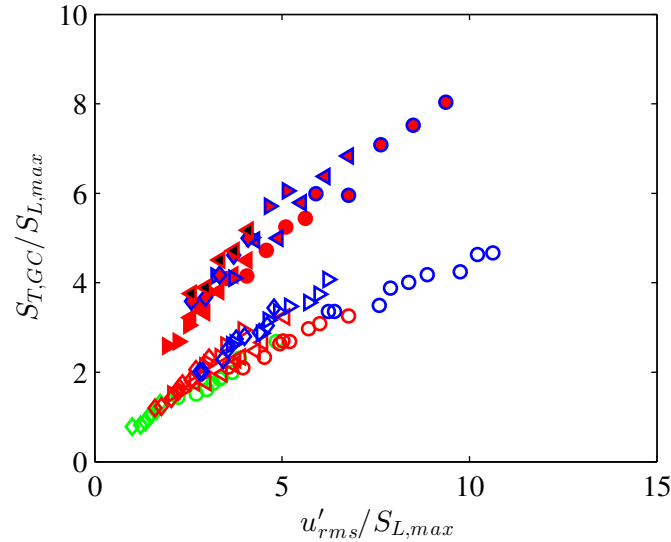


**Figure 53:**  $S_{T,GC}$  as a function of  $u'_{rms}$  normalized by  $S_{L,max}$  at various mean flow velocities,  $H_2:CO$  ratios and pressures using the 12 mm diameter burner (See Table 9 for legend of mixture conditions, flow velocities and pressures).

In addition to the 12 mm diameter burner dataset presented in this section, an extensive set of atmospheric pressure consumption speed measurements using a 20 mm diameter burner was also acquired [133]. This data was previously presented in Chapter 1, Figure

15a and normalized using  $S_{L,max}$  in Figure 15b. This normalization produced the interesting result that the 30 m/s  $\text{CH}_4$  data did not collapse with the  $\text{H}_2:\text{CO}$  data. However, all constant  $S_{L,0}$  data and equivalence ratio sweep data collapse very well.

To summarize, all the data taken consistently show that Equation 40 collapses data across all  $\text{H}_2:\text{CO}$  and equivalence ratio values at a given pressure. However, it does not collapse the 30 m/s  $\text{CH}_4$  data nor does it collapse data taken at different pressures. The rest of this section analyzes potential reasons for this and particularly focuses on non-quasi-steady chemistry effects.

In starting this discussion of the data, it is important to note that  $S_{L,max}$  is itself not a fundamental property of the mixture. For example, the burning velocity of highly stretched flames is a function of the manner in which the flame is stretched, i.e., by tangential flow straining or curvature, as well as the stretch profile through the flame (manifested by, for example, moderate sensitivities of  $S_{L,max}$  or  $\kappa_{ext}$  to the opposed flow nozzle separation distance or velocity profile) [52]. Note that these calculations derive  $S_{L,max}$  from a tangentially stretched flame, while the actual flame leading points are curved. Our research group has also performed expanding cylindrical flame and tubular flame computations that indicate that  $S_{L,max}$  varies by about 20-40%, depending on the manner in which the flame stretch is applied [3]. In addition, very different  $S_{L,max}$  values are obtained when using consumption and displacement based burning velocities [103]. Finally,  $S_{L,max}$  is itself a frequency dependent quantity [62]; the steady state values used here are only appropriate if the internal structure of the leading point is quasi-steady. The rest of this discussion focuses on the non-quasi-steady chemical processes, as the calculations presented next suggest that this is the largest effect.

To investigate this influence, a chemical time scale associated with  $S_{L,max}$  was calculated from:

$$\tau_{S_{L,max}} = \frac{\delta_f|_{S_{L,max}}}{S_{L,max}} \quad (41)$$

where  $\delta_f|_{S_{L,max}}$  is the flame thickness at  $S_{L,max}$  and is calculated from:

$$\delta_f = \frac{T_p - T_r}{(dT/dx)_{max}} \quad (42)$$

The variation in the chemical time scale across  $\text{H}_2$ :CO mixtures and pressures is shown in Figure 54. The point corresponding to 0%  $\text{H}_2$  is the pure  $\text{CH}_4$ /air case that was used in the constant  $S_{L,0}$  studies with the 20 mm burner.

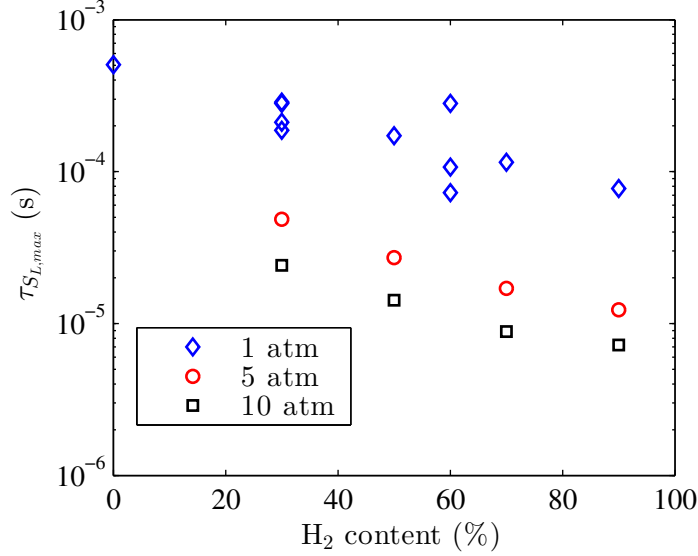


**Figure 54:** Variation in  $\tau_{S_{L,max}}$  as a function of  $\text{H}_2$  content for the different mixtures and conditions investigated. 0%  $\text{H}_2$  corresponds to the pure  $\text{CH}_4$  mixture.

Within the  $\text{H}_2$ :CO mixtures,  $\tau_{S_{L,max}}$  increases by about a factor of 3.5 as the  $\text{H}_2$  content is increased from 30% to 90% at 1 atm. The difference between the  $\text{CH}_4$  case and the 90:10  $\text{H}_2$ :CO mixture is about a factor of 6.5. In addition, for a fixed  $\text{H}_2$  content of 30%, there is a factor of 6 reduction in  $\tau_{S_{L,max}}$  for a pressure increase from 1 to 5 atm.

Figure 55 plots  $S_{T,GC}/S_{L,max}$  as a function of  $\tau_{S_{L,max}}/\tau_{flow}$ , where  $\tau_{flow} = D/U_0$ , at two turbulence intensity conditions for the 12 mm burner. Also shown are power law fits to the data, where the fit parameter,  $b$ , is defined by  $S_{T,GC}/S_{L,max} \sim (\tau_{S_{L,max}}/\tau_{flow})^b$ .

Note the clear correlation between turbulent flame speed and time scale ratio across the entire range of pressure and fuel composition. Slower chemistry is associated with lower values of the normalized turbulent flame speed, as would be expected, since the effective flame speed of the non-quasi-steady flame is lower than its quasi-steady value. While the time scale ratios are much less than unity (indicating that the chemistry is actually quasi-steady with respect to the large scales), the corresponding ratios calculated using Kolmogorov time

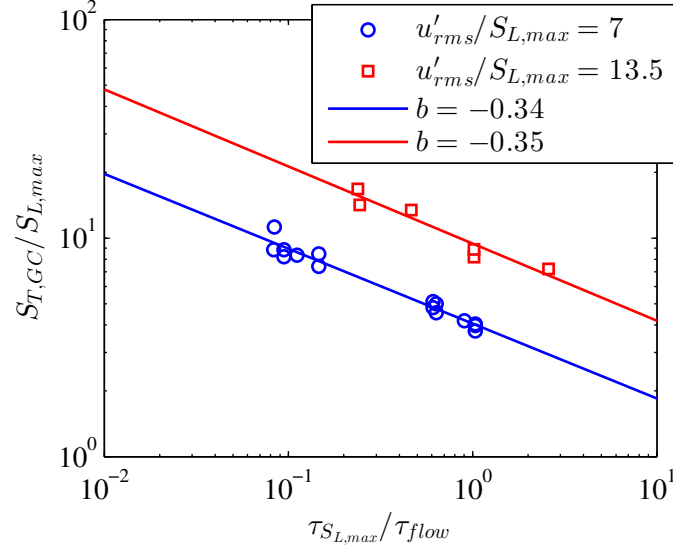


**Figure 55:** Dependence of  $S_{T,GC}/S_{L,max}$  on  $\tau_{S_{L,max}}/\tau_{flow}$  at two turbulence intensities  $u'_{rms}/S_{L,max} = 7$  and  $13.5$  for the 12 mm diameter burner. Power law fits with the corresponding slopes are also included.

scales range from 20-95 for the same data. In other words, significant non-quasi-steady chemistry effects would be expected for small flow length scale-flame interactions.

Similar analysis at other turbulence intensities showed good correlations. In addition, the 1 atm data from the 20 mm burner, shown in Figure 15b, also showed good correlations for the 4 and 10 m/s data. The 30 m/s  $\text{CH}_4$  data, however, did not collapse well. Results for the 20 mm diameter burner are presented in Figure 56 for two turbulence intensities. Again, notice the clear decreasing trend of turbulent flame speed values with increasing time scale ratio. In the subsequent section, turbulent local displacement flame speed,  $S_{T,LD}$ , results obtained using the low swirl burner geometry are presented over a wide range of fuel compositions, mean flow velocities, and turbulence intensities. These results are normalized using the conventional  $S_{L,0}$  normalization and then normalized with  $S_{L,max}$  to compare the efficacy of the leading points scaling model for a different burner geometry and flame speed definition.

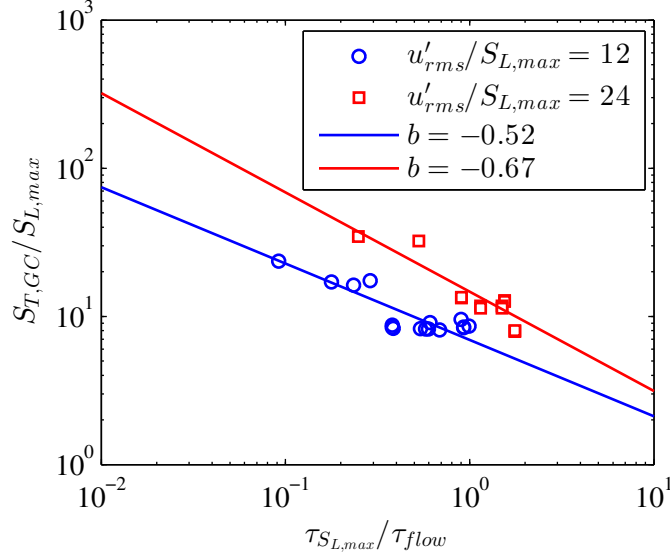


**Figure 56:** Dependence of  $S_{T,GC}/S_{L,max}$  on  $\tau_{S_{L,max}}/\tau_{flow}$  at two turbulence intensities  $u'_{rms}/S_{L,max} = 12$  and  $24$  for the 20 mm diameter burner. Power law fits with the corresponding slopes are also included.

## 4.2 Turbulent Local Displacement Flame Speeds

### 4.2.1 Overview

This section details measurements and correlations of turbulent local displacement speeds,  $S_{T,LD}$ , of hydrogen - carbon monoxide ( $H_2:CO$ ) and hydrogen - methane ( $H_2:CH_4$ ) fuel mixtures. Turbulent local displacement speed data were obtained at mean flow velocities and turbulence intensities of  $30 < U_0 < 50$  m/s and  $3 < u'_{ax}/S_{L,0} < 12$ , respectively, for  $H_2:CO$  mixtures ranging from 50-100%  $H_2$  and  $H_2:CH_4$  mixtures from 0-75%  $H_2$  by volume. As for the global consumption measurements, experiments were conducted where the mixture equivalence ratio,  $\phi$ , was adjusted at each fuel composition to have nominally the same unstretched laminar flame speed,  $S_{L,0}$ , of 34 cm/s. The data are also correlated with the leading points scaling law using detailed kinetics calculations of highly stretched flames.

## 4.2.2 Results

### 4.2.2.1 Experimental Conditions

Measurements of  $S_{T,LD}$  were obtained at atmospheric conditions as a function of  $u'_{ax}/S_{L,0}$  using a 36 mm diameter LSB. Data were acquired at mean flow velocities from 30-50 m/s, keeping  $S_{L,0}$  and reactant temperature fixed at 34 cm/s and 300 K, respectively.  $S_{L,0}$  estimates were determined using the PREMIX module [66] in CHEMKIN with the Davis H<sub>2</sub>/CO mechanism for H<sub>2</sub>:CO mixtures [43] and GRI-Mech 3.0 [119] for CH<sub>4</sub>-containing mixtures. Figure 57 summarizes where the measured data are located on the Borghi-Peters diagram [13, 105], where the Karlovitz number  $Ka$  was previously defined in Chapter 1, Equation 4. As was true for the 12 mm Bunsen burner, the data fall within the thin reaction zones regime ( $1 < Ka < 100$ ), implying that Kolmogorov eddies may enter the preheat zone but are still too large to enter the reaction zone where they may lead to quenching [105].

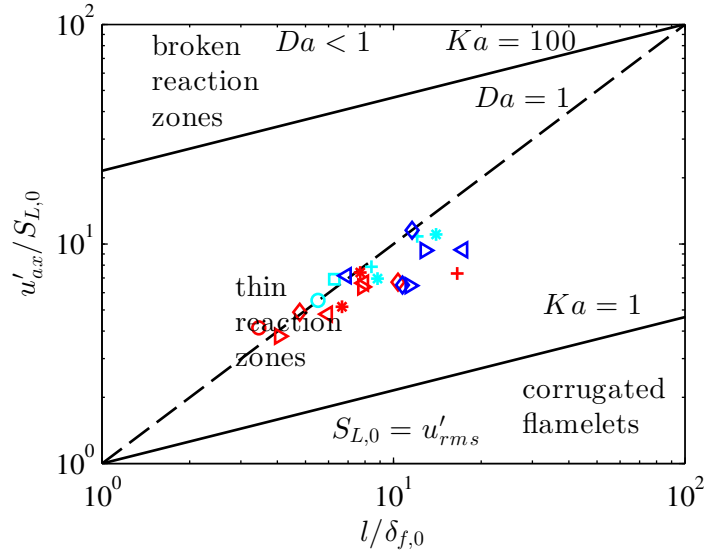


**Figure 57:** Borghi-Peters diagram showing location of LSB data points. See Figures 58 and 59 for legends.

### 4.2.2.2 H<sub>2</sub>:CO Sweeps at Constant $S_{L,0}$

In this section,  $S_{T,LD}$  data acquired for H<sub>2</sub>:CO mixtures are reported. As described earlier, data were acquired for mixtures where the H<sub>2</sub>:CO ratio and equivalence ratio were

simultaneously adjusted to maintain the same mixture  $S_{L,0}$  of 34 cm/s.

Figure 58 plots  $S_{T,LD}$  as a function of  $u'_{ax}$  normalized by  $S_{L,0}$  over a wide range of conditions. Note that the “fuel effect” is clearly present in this data as it was for the 12 mm Bunsen burner; i.e., different H<sub>2</sub>:CO blends at constant  $S_{L,0}$  and  $u'_{ax}$  have different turbulent flame speeds. For example, at  $u'_{ax}/S_{L,0} \approx 7$ , the  $S_{T,LD}$  values increase by about 50% from the lowest H<sub>2</sub>-containing fuel (50:50) to the pure H<sub>2</sub> fuel. Again, for all these data points the equivalence ratio was adjusted to have nominally the same unstretched laminar flame speed of 34 cm/s.

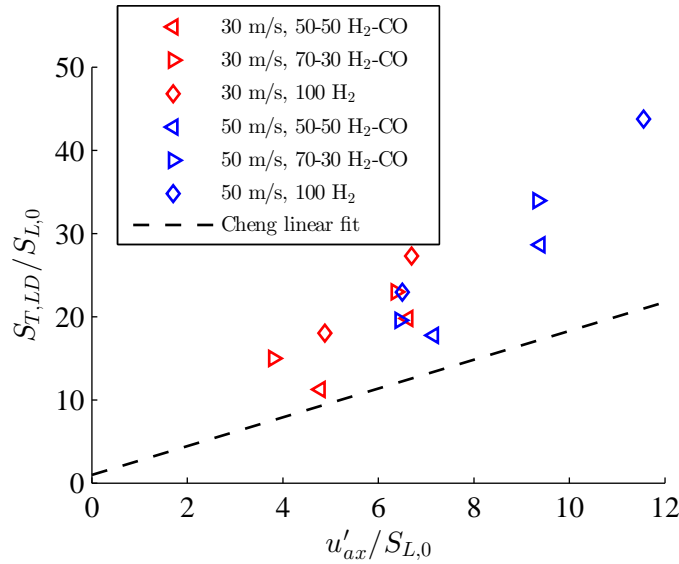


**Figure 58:**  $S_{T,LD}$  as a function of  $u'_{ax}$  normalized by  $S_{L,0}$  at various mean flow velocities and H<sub>2</sub>:CO ratios for the LSB.

#### 4.2.2.3 H<sub>2</sub>:CH<sub>4</sub> Sweeps at Constant $S_{L,0}$

In this section,  $S_{T,LD}$  data acquired for H<sub>2</sub>:CH<sub>4</sub> mixtures are reported. Again, data were acquired for mixtures where the H<sub>2</sub>:CH<sub>4</sub> ratio and equivalence ratio were simultaneously adjusted to maintain the same mixture  $S_{L,0}$  of 34 cm/s.

Figure 59 presents  $S_{T,LD}$  as a function of  $u'_{ax}$  normalized by  $S_{L,0}$  along with a correlation line found by Cheng et al. [32]. The results show reasonable agreement with the correlation. Note that the “fuel effect” is not as clearly present in this data as it was for the 12 mm

Bunsen burner (Figure 50) and for the H<sub>2</sub>:CO LSB data (Figure 58); for example, at  $u'_{ax}/S_{L,0} \approx 7$ , the  $S_{T,LD}$  values increase starting with the 60:40 mixture, the 50:50 mixture, the pure CH<sub>4</sub>, and, finally, the 50:50 mixture.

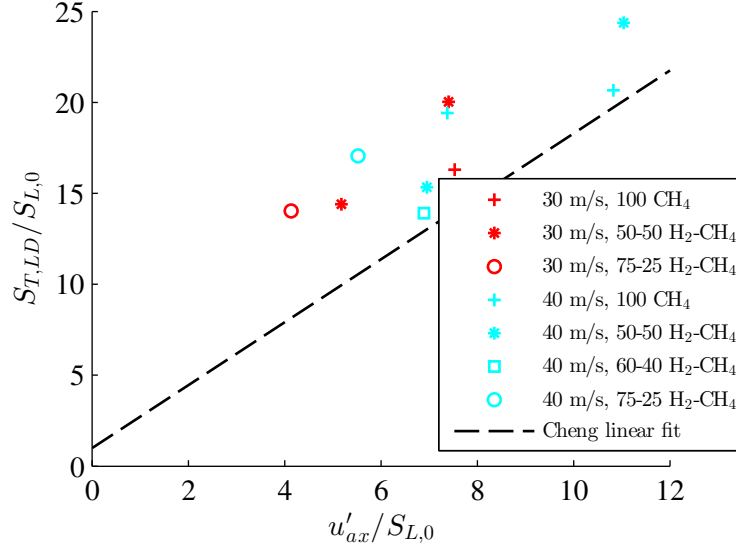


**Figure 59:**  $S_{T,LD}$  as a function of  $u'_{ax}$  normalized by  $S_{L,0}$  at various mean flow velocities and H<sub>2</sub>:CH<sub>4</sub> ratios for the LSB.

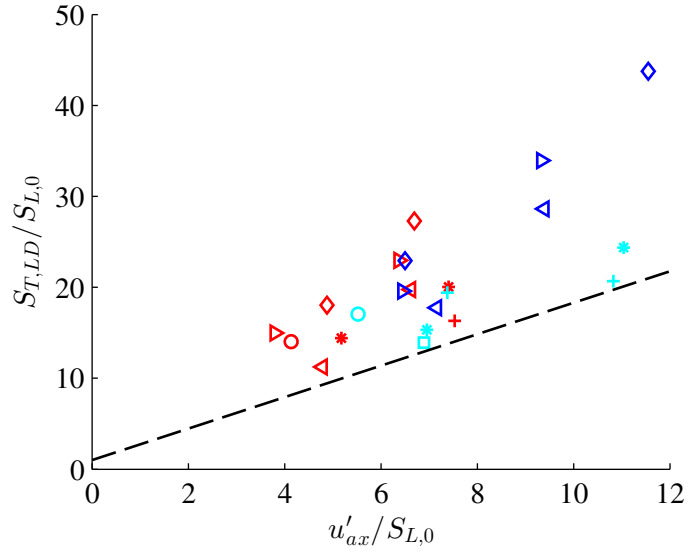
Figure 60 presents  $S_{T,LD}$  as a function of  $u'_{ax}$  normalized by  $S_{L,0}$  for all of the H<sub>2</sub>:CO and H<sub>2</sub>:CH<sub>4</sub> mixtures investigated. Note that the H<sub>2</sub>:CO mixtures have generally higher  $S_{T,LD}$  values than the H<sub>2</sub>:CH<sub>4</sub> mixtures.

### 4.2.3 Analysis

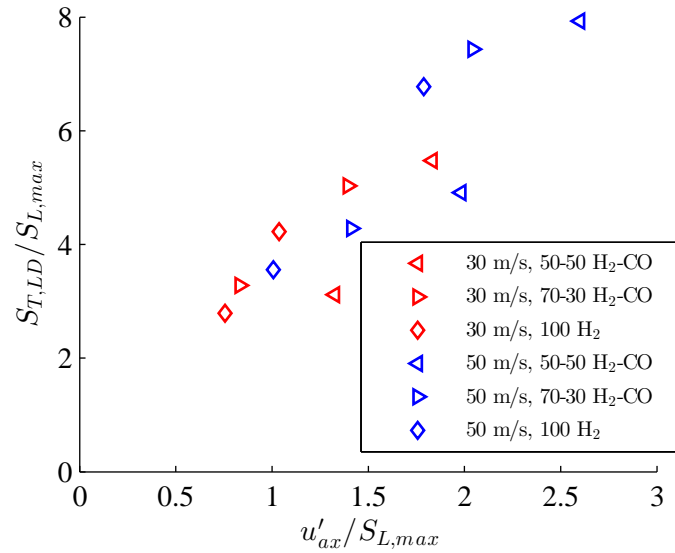
In this section, the data presented in Figure 60 are correlated using the steady-state leading points scaling law of Equation 40.

Figure 61 plots  $S_{T,LD}$  as a function of  $u'_{ax}$  normalized by  $S_{L,max}$ . While the effects of this normalization are not as drastic as those observed with the Bunsen burner geometry, note that with the exception of the 50:50 H<sub>2</sub>:CO points at  $u'_{ax}/S_{L,0} = 1.4$  and 2, the data do tend to follow a clear trend-line.

Figure 62 plots  $S_{T,LD}$  as a function of  $u'_{ax}$  normalized by  $S_{L,max}$ . Note that although there was significant scatter in the data presented in Figure 59, when normalized instead



**Figure 60:**  $S_{T,LD}$  as a function of  $u'_{ax}$  normalized by  $S_{L,0}$  at various mean flow velocities for  $H_2:CO$  and  $H_2:CH_4$  mixtures obtained in the LSB. See Figures 58 and 59 for legends.



**Figure 61:**  $S_{T,LD}$  as a function of  $u'_{ax}$  normalized by  $S_{L,max}$  at various mean flow velocities and  $H_2:CO$  ratios for the LSB.

with  $S_{L,max}$  that the  $H_2:CH_4$  data appear to collapse onto a single curve. This indicates that the data are well-correlated using the leading points model.

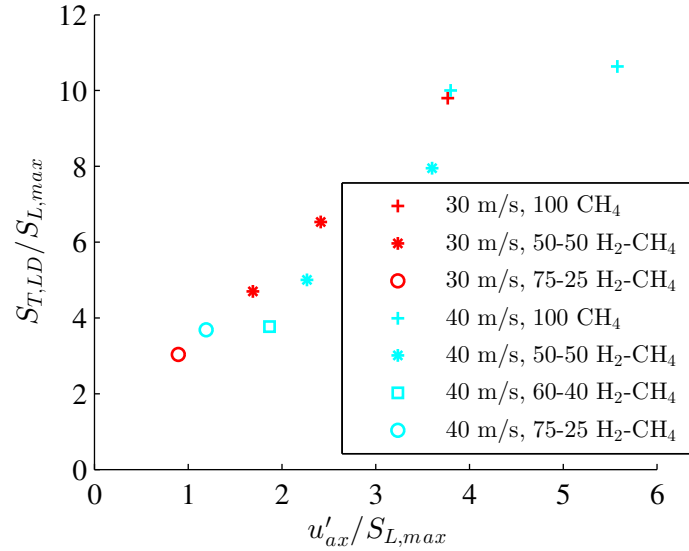


**Figure 62:**  $S_{T,LD}$  as a function of  $u'_{ax}$  normalized by  $S_{L,max}$  at various mean flow velocities and  $H_2:CH_4$  ratios for the LSB.

Finally, combining the two datasets onto one plot results in Figure 63. Note that while in Figure 60 the  $H_2:CO$  had consistently higher  $S_{T,LD}$  values than the  $H_2:CH_4$  mixtures, when normalized instead with  $S_{L,max}$  that all the  $S_{T,LD}$  data appear to collapse onto a single curve, indicating again that the leading points model performs well for this data.

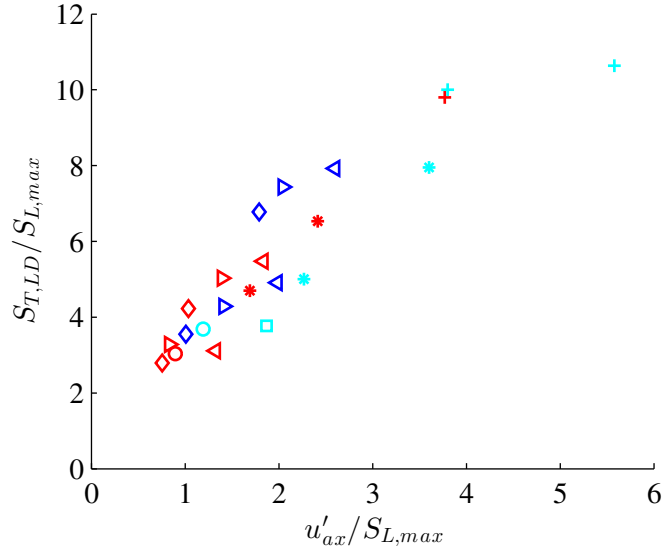


**Figure 63:**  $S_{T,LD}$  as a function of  $u'_{ax}$  normalized by  $S_{L,max}$  at various mean flow velocities for  $H_2:CO$  and  $H_2:CH_4$  mixtures obtained in the LSB. See Figures 58 and 59 for legends.

### 4.3 Conclusions

In this chapter, we reported turbulent consumption speed measurements of  $H_2:CO$  blends from 1-10 atm and turbulent local displacement speed measurements for  $H_2:CO$  and  $H_2:CH_4$  mixtures. Experiments were conducted for mean flow velocities from 30-50 m/s for  $H_2:CO$  mixtures ranging from 50-100%  $H_2$  by volume and  $H_2:CH_4$  mixtures ranging from 0-75%  $H_2$  by volume. For the consumption speed data it was found that at the same  $S_{L,0}$  when the pressure was increased by a factor of 5, the consumption speed increased by almost a factor of 2. For the displacement speed data it was found that the  $H_2:CO$  mixtures exhibited clear “fuel effects” whereas the  $H_2:CH_4$  mixtures did not appear to follow the same trends. It was also observed that the  $H_2:CO$  mixtures had generally higher  $S_{T,LD}$  values than the  $H_2:CH_4$  mixtures.

The data were then normalized with  $S_{L,max}$  as per the scaling law discussed in Chapter 1. For the consumption speed data from the Bunsen burner, the data show that, at a given pressure, different fuel compositions and equivalence ratio data collapse. However, systematically different trends are observed with the 5 and 10 atm data. There is some evidence that these systematic differences are more fundamentally due to non-quasi-steady

effects, as the pressure differences can be reasonably correlated with a computed chemical time scale for the 12 mm burner. For the displacement speed data acquired with the LSB, the leading points scaling model did an excellent job in collapsing the data over a very wide range of turbulence intensities and fuel compositions. This gives merit to the leading points model as a method that can be implemented across geometries and still produce meaningful results.

## CHAPTER V

### FLAME FRONT TOPOLOGY AND STRETCH STATISTICS

Fuel composition has a strong influence on the turbulent flame speed, even at very high turbulence intensities. An important implication of this result is that the turbulent flame speed cannot be extrapolated from one fuel to the next using only the laminar flame speed and turbulence intensity as scaling variables. These fuels effects are associated with reactant thermal-diffusive properties and stretch sensitivities, causing local variations in the burning rate along the flame front. This chapter is motivated by leading point descriptions of the turbulent flame speed, which argue that  $S_T$  is controlled by the flame characteristics at its positively curved leading edge. It has been argued that the leading edge of the flame approaches “critically stretched” values in thermo-diffusively unstable flames, implying that the appropriate laminar flame speed to parameterize the turbulent flame speed is the maximum flame speed across all potential values of flame stretch,  $S_{L,max}$ , as opposed to its unstretched value,  $S_{L,0}$ .

This chapter presents the results of planar measurements of the curvature and tangential strain rate for fuel lean, high hydrogen flames, where hydrogen content varies from 50%-100%. The data were acquired with high speed particle image velocimetry (PIV) in a low swirl burner (LSB). We attained measurements for several  $H_2:CO$  mixtures over a range of mean flow velocities and turbulence intensities. Results are analyzed for the overall turbulent flame brush ( $0 \leq \langle c \rangle \leq 1$ ), as well as those conditioned on its leading edge ( $0 \leq \langle c \rangle \leq 0.01$ ). The latter characterizations are motivated by leading point arguments, which suggest that the augmentation of the turbulent flame speed can be explained by the increase in the local, laminar flame speed at the positively curved leading edge of the flame. Indeed, recent work has shown that global turbulent consumption speed measurements can be correlated with critically stretched laminar flame speeds for different fuel compositions.

Results of the sensitivity of curvature and tangential strain rate to turbulence intensity

are consistent with prior computations and measurements; e.g., the mean tangential strain rate increases and the minimum curvature decreases with increases in turbulence intensity. The results show that, counter to our expectations, fuel composition has a systematic yet weak effect on curvatures at the leading points. The effect on tangential strain rates is stronger, indicating that this term might better explain fuel effects. However, for both curvature and tangential strain rate, the time-averaged values are observed to be much lower than what would be expected for critically stretched flames. It has been argued that the increased turbulent flame speeds seen with increasing hydrogen content are the result of increasing flame stretch rates, and therefore  $S_{L,max}$  values, at the flame leading points. However, the differences observed with changing fuel compositions are not significant enough to support this hypothesis. Additional analysis is needed to understand the physical mechanisms through which the turbulent flame speed is altered by fuel composition effects.

### 5.1 Introduction

This chapter presents measurements and analysis performed to improve the understanding of turbulent flame propagation characteristics of premixed, high stretch sensitivity fuel/air mixtures. A more detailed discussion of the relevant background information was presented in Chapter 1, however, to reiterate, we will briefly overview the most important background literature in this section.

Traditional models of the turbulent flame speed commonly use the form:

$$S_T = S_{L,0}f(u'/S_{L,0}) \quad (43)$$

where  $S_{L,0}$  is the unstretched laminar flame speed and  $u'$  is the turbulence intensity [87, 88]. In reality, the turbulent flame speed exhibits dependencies on other parameters as well, such as turbulent length scales [7, 78], bulk flow velocity [53], experimental configuration [50, 28], and fuel composition [69, 88, 97, 132]. Of particular interest to this chapter is the effect of fuel composition, which has been well-documented in the literature [88]. For example, our group has reported measurements of H<sub>2</sub>:CO blends showing factor of three variations in  $S_T$  across fuel blends with identical  $S_{L,0}$  values, even at turbulence intensities  $u_{rms}/S_{L,0}$  up to 40.

This fuel composition sensitivity of the turbulent flame speed is attributed to the reactant mixture's stretch sensitivity, leading to variations in the local flame speed throughout the turbulent flame surface. In particular, the high mass diffusivity of  $\text{H}_2$  makes high hydrogen content (HHC) mixtures very sensitive to stretch, such as shown in the illustrative calculations in Figure 64. These calculations, which include detailed kinetics and transport mechanisms, incorporate both non-unity Lewis number and preferential diffusion effects [79]. For an infinitely thin flame sheet, these sensitivities are manifested throughout the turbulent flame brush, due to flame curvature and strain, as given by the following equation [19, 110]:

$$\kappa = -\vec{n}\vec{n} : \nabla\vec{u} + \nabla \cdot \vec{u} + S_L(\nabla \cdot \vec{n}) \quad (44)$$

where  $\vec{u}$  is the reactant velocity. The first two terms in this expression are the tangential strain rate,  $\kappa_s$ , and the third term is the stretch rate contribution due to flame curvature,  $\kappa_c$ . The term  $\nabla \cdot \vec{n}$  is the flame curvature and can be related to the principal radii of curvature  $\mathcal{R}_1$  and  $\mathcal{R}_2$  through:

$$\nabla \cdot \vec{n} = \frac{1}{\mathcal{R}_1} + \frac{1}{\mathcal{R}_2} \quad (45)$$

where the radii of curvature are positive when convex to the reactants.

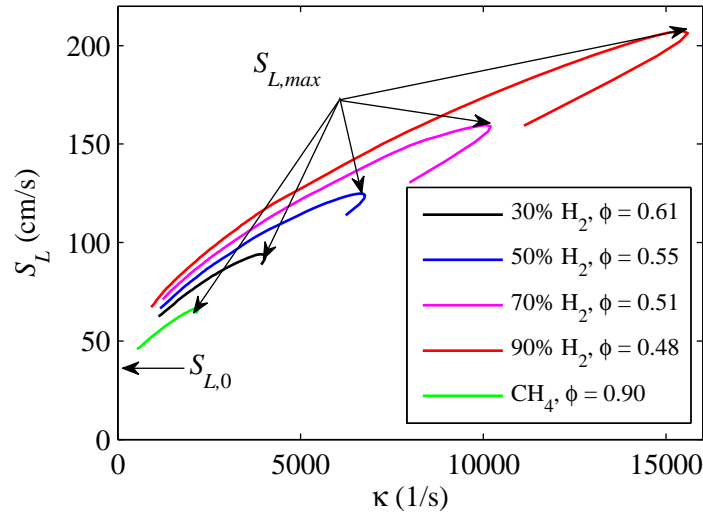


**Figure 64:** Stretch sensitivity calculations of  $\text{H}_2$ :CO fuel blends and  $\text{CH}_4$  [133].

Two-dimensional, experimental measurements of these quantities have been previously

reported. Planar curvature measurements are the most common [82, 116, 83, 5, 76, 58, 115, 63, 120, 54, 4, 12, 142, 9, 141]. A general observation from these measurements is that the curvature statistics are nearly symmetric about a zero mean, especially with increasing turbulence [82, 116, 83, 76, 58, 12, 142]. In addition, a widening of the PDF with increasing turbulence intensity [82, 116, 83, 76, 58, 115, 63] is always observed. This indicates that the curvature over the entire flame surface has an equal probability of both positive and negative values, and the increase in flame wrinkling with turbulence intensity is due to the presence of finer scales at higher turbulence conditions.

Several studies have examined fuel effects [81, 58, 54, 142], and have shown very little effect on curvature from fuel composition when examining statistics over the entire flame surface ( $0 \leq \langle c \rangle \leq 1$ ). Lee et al. [81] examined propane/air mixtures in a pulsed flame flow reactor over lean, stoichiometric, and rich conditions and concluded that curvature statistics were determined by turbulence conditions. Haq et al. [58] examined methane/air and iso-octane/air mixtures at 1 and 5 bar pressures in a fan stirred bomb. They similarly noticed very little effect of the fuel composition, with increasing turbulence and pressure both serving to broaden the distribution of curvatures equally for both positive and negative wrinkles. For other work containing high hydrogen content fuels, Gashi et al. [54] studied methane/air and hydrogen/air mixtures in a fan-stirred bomb at  $u'/S_L$  values up to 5.25 and 2.21 for  $\text{CH}_4/\text{air}$  and  $\text{H}_2/\text{air}$  mixtures, respectively. Over these conditions they also noticed very little difference between  $\text{CH}_4/\text{air}$  and  $\text{H}_2/\text{air}$  mixtures in terms of curvature PDFs.

Planar strain rate measurements are less common, most likely due to the added difficulty associated with planar velocity field measurements. Donbar et al. [48] used simultaneous planar laser-induced fluorescence (PLIF) and particle image velocimetry (PIV) to measure strain rates in turbulent, non-premixed  $\text{CH}_4/\text{N}_2/\text{O}_2$  jet flames. Unlike curvature measurements, the strain rates were found to have non-zero mean values that increased with increasing turbulence. Renou et al. [112] examined low turbulence, freely propagating flames for three different mixtures of methane/air, propane/air, and hydrogen/air using PIV with oil droplets. The oil droplets evaporated through the flame surface, and the authors used

this in order to define the instantaneous flame surface. They observed that the tangential strain rate statistics appeared to be independent of the fuel composition.

Three-dimensional measurements of curvature and tangential strain rates are even less frequent [26, 121, 117, 128, 68], due the added cost and complexity of multi-plane laser measurement techniques. Chen et al. [26] used two Nd:YAG crossed-plane lasers to get Mie scattering signals from smoke-seeded flows in order to extract flame front normals and curvatures. They examined propane/air and hydrogen/air mixtures and found similar curvature PDFs for these mixtures.

In addition to analysis of these quantities over the entire flame brush, the flame stretch characteristics at the leading edge (i.e., for  $\langle c \rangle \rightarrow 0$ ) may be particularly significant. The reasons for this follow from leading points models [88, 78, 64]. These leading points concepts were originally proposed by Zeldovich [143] and expanded upon by a number of groups, as summarized in the review paper by Lipatnikov and Chomiak [88]. To provide a succinct definition, leading points are the positively curved (convex to the reactants) points on the flame front that propagate out farthest into the reactant mixture. Under certain conditions they can be shown to control the overall propagation velocity of the turbulent flame [78]. For example, by applying the Kolmogorov-Petrovskii-Piskunov (KPP) theorem [74] to the propagation of a one-dimensional turbulent premixed flame in frozen turbulence, it is shown that, under certain circumstances,  $S_T$  is controlled by the conditions at the leading edge of the flame brush, defined as the point where the average progress variable,  $\langle c \rangle$ , approaches zero [57, 51]. The burning rate of this positively curved leading point increases for negative Markstein length mixtures [79]. These leading points ideas are particularly important for negative Markstein length mixtures, as calculations of laminar flame stretch sensitivities show that the positively curved leading point flame speed can substantially exceed  $S_{L,0}$  [79], as demonstrated in Figure 64.

If we assume that  $S_T$  is controlled by the characteristics at the flame leading point, the ensemble averaged laminar burning rate of this leading point turns out to be a very important turbulent flame property. From this, Venkateswaran et al. [133, 132] developed a scaling law for the turbulent flame speed of negative Markstein length flames that collapses

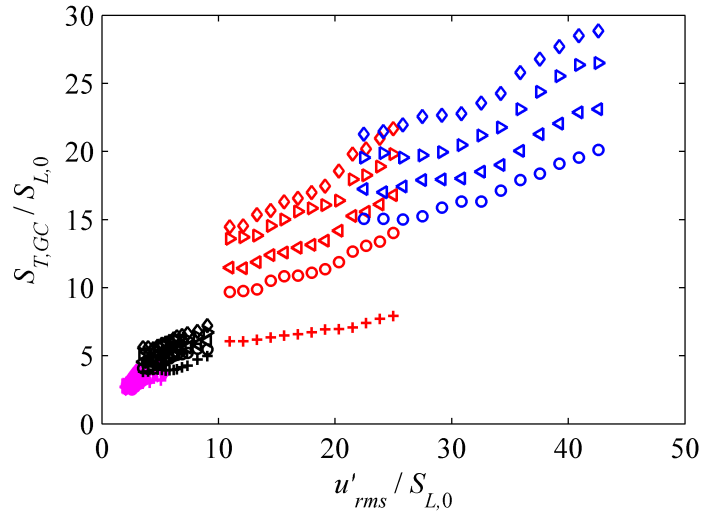
turbulent flame speed data over a wide range of conditions including fuel compositions, mean flow velocities, and turbulence intensities. Instead of the traditional approach of using the unstretched laminar flame speed,  $S_{L,0}$ , to scale the data, this scaling law uses the maximum stretched laminar flame speed,  $S_{L,max}$ , instead. These two flame speeds are both identified in Figure 64. A flamelet burning at the flame speed  $S_{L,max}$  and the associated stretch rate  $\kappa_{crit}$  is referred to as “critically stretched.” The form of this scaling law is given by:

$$\frac{S_T}{S_{L,max}} \leq 1 + \frac{u'_{LP}}{S_{L,max}} \quad (46)$$

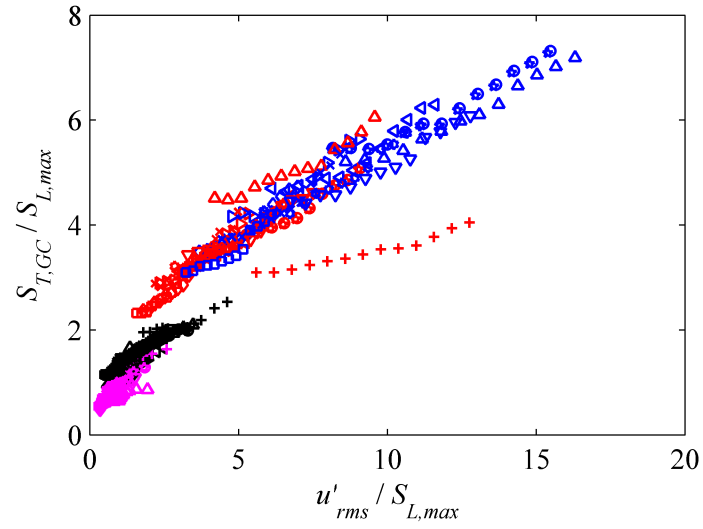
where  $u'_{LP}$  is the turbulence intensity at the flame leading point.  $S_{L,max}$  is calculated from opposed flow, strained flame simulations using detailed chemical kinetics. An example of these calculations is shown in Figure 64.

$S_{L,max}$  in negative Markstein length mixtures is a dynamically significant quantity due to the fact that this velocity, and the corresponding strain rate  $\kappa_{crit}$ , at the flame leading point is a steady-state attracting point for constant density flames with positively curved wrinkles [133]. This idea that  $S_{L,max}$ , and not  $S_{L,0}$ , is the suitable velocity scale for correlating  $S_T$  was suggested by [78] and has found justification in data from Venkateswaran et al. [133], as shown previously in Chapter 1 and repeated here in Figure 65. This figure plots data obtained over a wide range of H<sub>2</sub>:CO mixtures, mean flow velocities, and turbulence intensities normalized by  $S_{L,0}$  (Figure 15a) and normalized by  $S_{L,max}$  (Figure 15b). Note that in the  $S_{L,0}$  scaled data the effect of fuel composition is strongly evident, but using the  $S_{L,max}$  scaling, the data collapse very well into a single grouping.

However, questions remain concerning the application of leading points ideas to data. Of particular focus for this chapter is the fact that the scaling in Figure 15 is “global” in nature and work is needed to assess key assumptions of the leading point model concerning local attributes of the flame. For example, Figure 64 clearly shows the monotonic increase in  $S_{L,max}$  with increasing H<sub>2</sub> content. However, it also shows that the flame stretch rate at  $S_{L,max}$  varies strongly with H<sub>2</sub> content, a prediction that can be evaluated from computations or measurements. If the physical arguments leading to this scaling approach are



(a)



(b)

**Figure 65:** (a) Measured dependence of the turbulent flame speed,  $S_{T,GC}$ , upon turbulence intensity,  $u'_{rms}$ , normalized by  $S_{L,0}$  at various conditions for several  $H_2:CO$  ratios and pure  $CH_4$ . (b)  $S_{T,GC}$  data from (a) normalized by  $S_{L,max}$ . See Venkateswaran et al. [133] for details on experimental conditions.

correct, then the flame stretch characteristics at its leading points should exhibit systematic differences that scale with  $S_T$ . Particularly, Figure 64 suggests that mixtures with higher  $S_T$  values should have leading points with higher stretch rates. The objective of this chapter is to evaluate this hypothesis, by determining the flame stretch characteristics at the flame leading point, and determining whether systematic differences exist that correlate with the measured turbulent flame speeds. This is done by obtaining measurements from a high turbulence intensity burner fueled with several HHC blends, and comparing the flame leading edge characteristics across these fuels.

## **5.2 Methods**

The low swirl burner (LSB) is a useful geometry for local measurements of turbulent flame characteristics, and has been recommended as a canonical geometry for turbulent displacement speed measurements [56]. The LSB was developed by Cheng et al. [25] as a method of generating a freely propagating flame that does not rely on flow recirculation for flame stabilization; the flame stabilizes where the flame speed matches the axial velocity. The flame brush in the central region is flat, providing a close approximation to a statistically 1-D planar turbulent flame [27]. The experiments in this work were performed for  $\text{H}_2:\text{CO}$  and  $\text{H}_2:\text{CH}_4$  mixtures over a wide range of conditions outlined in Table 10. Further details on the LSB facility, the PIV setup, and the post-processing procedure can be found in Chapter 2.

**Table 10:** Experimental parameters and conditions for the two datasets acquired using PIV

Experiments:	H <sub>2</sub> :CH <sub>4</sub>	H <sub>2</sub> :CO
Repetition rate (kHz)	1	9
Pulse energy (mJ/pulse)	23	1.3
Time between shots ( $\mu$ s)	15	18
Resolution (pixels $\times$ pixels)	704 $\times$ 704	384 $\times$ 704
Viewing area (mm $\times$ mm)	87 $\times$ 87	44 $\times$ 80
Number of image pairs	1000	10,000
Seed particles	1-2 $\mu$ m Al <sub>2</sub> O <sub>3</sub>	0.3-0.7 $\mu$ m TiO <sub>2</sub>
Swirl number, $S$	0.57-0.6	0.58
Mean flow velocity, $U_0$ (m/s)	20, 30, 40	30, 50
Fuel Composition (% H <sub>2</sub> )	0-75	50-100
$S_{L,0}$ (cm/s)	34	34

### 5.3 Results and Discussion

To investigate the effects of flame stretch, we calculated curvatures and tangential strain rates along the flame front, which represent two components of the overall flame stretch rate. As demonstrated in Figure 64, as these mixtures become more positively stretched, their laminar flame speed increases. For negative stretch, the laminar flame speed decreases. Thus, locally along the flame front, the rate of consumption of reactants varies. Tables 11 and 12 present the key operational conditions and summarize measured results presented in this chapter, reporting turbulence intensities,  $u'_{ax}/S_{L,0}$ , turbulent local displacement speeds,  $S_{T,LD}/S_{L,0}$ , and mean and standard deviations of the curvature (Table 11) and tangential strain rate (Table 12) at the leading points. Although these blends have nominally the same  $S_{L,0}$  value, note the increase in measured  $S_{T,LD}$  with hydrogen content at nearly constant turbulence intensity, also shown in the previous chapter for both  $S_{T,LD}$  and  $S_{T,GC}$  measurements.

**Table 11:** Local displacement turbulent flame speeds,  $S_{T,LD}/S_{L,0}$ , average curvature,  $\overline{1/R}$ , and standard deviation of the curvature,  $\sigma$ , at the instantaneous leading points (ILP) and at the flame brush leading points (FBLP). Uncertainties are for a 95% confidence interval.

	$\frac{u'_{max}}{S_{L,0}}$		ILP		FBLP			
	$\frac{S_{T,LD}}{S_{L,0}}$	$\frac{S_{T,LD}}{S_{L,0}}$	$\overline{1/R}$	$\sigma$	$\overline{1/R}$	$\sigma$		
			(mm <sup>-1</sup> )	(mm <sup>-1</sup> )	(mm <sup>-1</sup> )	(mm <sup>-1</sup> )		
50% H <sub>2</sub>	4.8	9.4	0.88 ± 0.01	0.63	0.32 ± 0.004	0.91	0.40 ± 0.02	0.9
$\phi = 0.55$	6.6	19.8	1.24 ± 0.02	1.01	0.29 ± 0.005	1.12	0.31 ± 0.02	1.02
$ds = 0.95$ mm	7.2	17.7	1.09 ± 0.02	0.81	0.34 ± 0.005	1.04	0.53 ± 0.02	0.98
	9.4	25.2	1.47 ± 0.03	1.2	0.32 ± 0.006	1.3	0.44 ± 0.03	1.34
70% H <sub>2</sub>	3.8	15.4	0.93 ± 0.01	0.64	0.35 ± 0.004	0.88	0.49 ± 0.02	0.74
$\phi = 0.51$	6.4	23	1.25 ± 0.02	0.98	0.29 ± 0.006	1.21	0.76 ± 0.07	1.15
$ds = 0.88$ mm	6.5	19.6	1.13 ± 0.02	0.82	0.33 ± 0.005	1.3	0.52 ± 0.02	0.97
	9.3	28.5	1.51 ± 0.03	1.22	0.29 ± 0.006	1.37	0.39 ± 0.04	1.33
100% H <sub>2</sub>	4.9	17.3	0.94 ± 0.02	0.64	0.33 ± 0.004	0.92	0.42 ± 0.02	0.84
$\phi = 0.46$	6.5	22.9	1.24 ± 0.02	0.93	0.32 ± 0.005	1.15	0.48 ± 0.05	0.95
$ds = 0.83$ mm	6.8	24.9	1.15 ± 0.02	0.79	0.33 ± 0.005	1.13	0.46 ± 0.02	1.07
	11.3	37.5	1.58 ± 0.03	1.28	0.28 ± 0.006	1.42	0.52 ± 0.05	1.33

**Table 12:** Local displacement turbulent flame speeds,  $S_{T,LD}/S_{L,0}$ , average tangential strain rate,  $\overline{\kappa}_s$ , and standard deviation of the tangential strain rate,  $\sigma$ , at the instantaneous leading points (ILP) and at the flame brush leading points (FBLP). Uncertainties are for a 95% confidence interval.

	$\frac{u'_{\theta,ax}}{S_{L,0}}$		$\frac{S_{T,LD}}{S_{L,0}}$		ILP		FBLP	
					$\overline{\kappa}_s$	$\sigma$	$0 \leq \langle c \rangle \leq 0.1$	$0 \leq \langle c \rangle \leq 0.01$
					$(s^{-1})$	$(s^{-1})$	$(s^{-1})$	$(s^{-1})$
50% H <sub>2</sub>	4.8	9.4	949 ± 26	1247	519 ± 5	1168	559 ± 22	1107
$\phi = 0.55$	6.6	19.8	729 ± 23	1080	581 ± 5	1077	637 ± 21	1017
$ds = 0.95$ mm	7.2	17.7	1699 ± 35	1650	981 ± 7	1623	1240 ± 32	1435
	9.4	25.2	1509 ± 30	1441	1007 ± 6	1470	1094 ± 29	1466
70% H <sub>2</sub>	3.8	15.4	911 ± 28	1273	668 ± 6	1265	936 ± 26	1290
$\phi = 0.51$	6.4	23	1003 ± 26	1188	678 ± 5	1162	1011 ± 72	1181
$ds = 0.88$ mm	6.5	19.6	1419 ± 30	1399	885 ± 6	1359	1087 ± 27	1282
	9.3	28.5	1651 ± 33	1594	1046 ± 6	1472	1262 ± 42	1587
100% H <sub>2</sub>	4.9	17.3	1742 ± 50	2197	1011 ± 9	2003	1321 ± 37	1806
$\phi = 0.46$	6.5	22.9	1502 ± 34	1548	903 ± 7	1591	915 ± 240	4986
$ds = 0.83$ mm	6.8	24.9	1717 ± 36	1616	1090 ± 7	1620	1436 ± 33	1713
	11.3	37.5	1897 ± 35	1628	1168 ± 7	1632	1374 ± 66	1874

### 5.3.1 Global (Unconditioned) Stretch Statistics

We start with global flame statistics – PDFs of flame curvature and tangential strain rate calculated over the entire extracted surface (i.e.,  $0 \leq \langle c \rangle \leq 1$ ). Figure 66 plots curvature and tangential strain rate PDFs for three different fuel compositions at low and high turbulence intensities. From these plots it is evident that the overall curvature and tangential strain rate are only weakly affected by fuel composition.

While there is a slight preference for positive curvatures, the curvature PDFs are still nearly symmetric about zero, consistent with other measurements [82, 116, 83, 76, 58, 12, 142]. The PDFs tend to shift towards more positive curvatures as the percent of  $\text{H}_2$  in the fuel increases (i.e., as the fuel becomes more sensitive to stretch). However, these changes are slight, and the minor differences make it hard to explain the approximate  $1.8\times$  increase in  $S_{T,LD}$  from a 50:50  $\text{H}_2$ :CO mixture to a pure  $\text{H}_2$  mixture. To give an idea of the magnitude of the curvature relative to the flame thickness, the top axis of Figure 66b is the curvature nondimensionalized by the flame thickness of the pure  $\text{H}_2$  mixture. From this we can see that the majority of the flame front features have radii of curvature larger than the unstretched flame thickness.

Unlike curvature the tangential strain rate PDFs have a non-zero mean, consistent with other results [48, 53]. Similar to the curvature, they exhibit a weak sensitivity to the fuel composition. The tangential strain rate PDF of the pure hydrogen case at  $U_0 = 30$  m/s is an exception, as it shows a significantly broader range of strain values. This behavior may be the result of the flame sitting closer to the exit of the burner, which could give the pure hydrogen mixture a higher average strain rate than the other fuel compositions. This behavior is not observed at the higher mean flow velocity of  $U_0 = 50$  m/s, where the tangential strain rate is essentially insensitive to fuel composition.

To examine this further, Figure 67 plots mean strain rates ( $E_{ij} = \partial\langle u_i \rangle / \partial x_j$ ) with average progress variable through the flame, for the 50:50  $\text{H}_2$ :CO and 100%  $\text{H}_2$  mixtures at low and high turbulence intensities. The major difference for the pure hydrogen case at  $U_0 = 30$  m/s (Figure 67c) is that the  $E_{yy}$  strain term rises earlier and is at a higher level throughout the flame region ( $0 \leq \langle c \rangle \leq 1$ ).

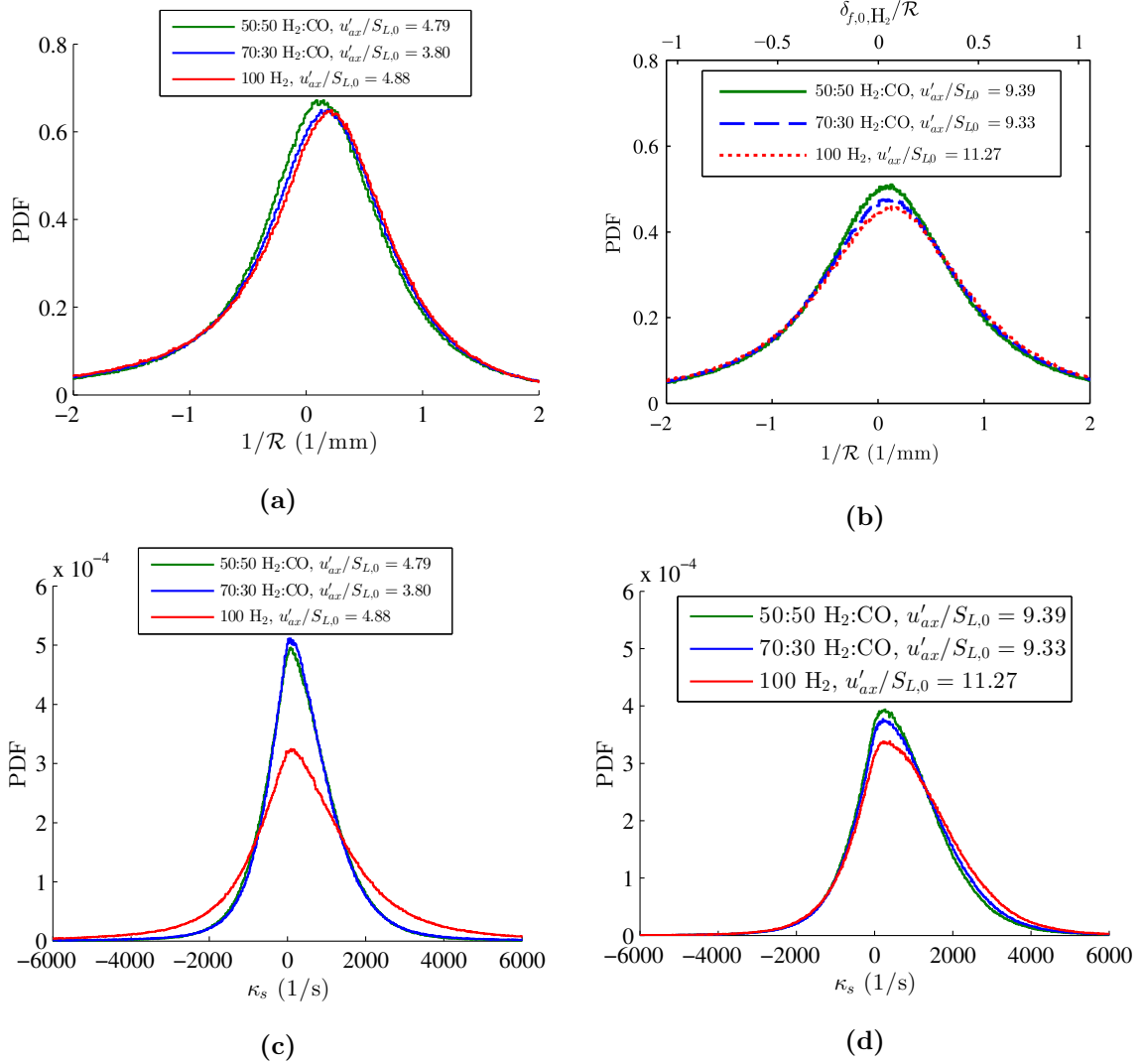


**Figure 66:** Unconditioned ( $0 \leq \langle c \rangle \leq 1$ ) (a, b) curvature and (c, d) tangential strain rate PDFs for varying fuel compositions at (a, c)  $U_0 = 30$  m/s and (b, d)  $U_0 = 50$  m/s. Secondary top-axis in (b) shows curvature normalized by the unstretched flame thickness for the 100% H<sub>2</sub> case.

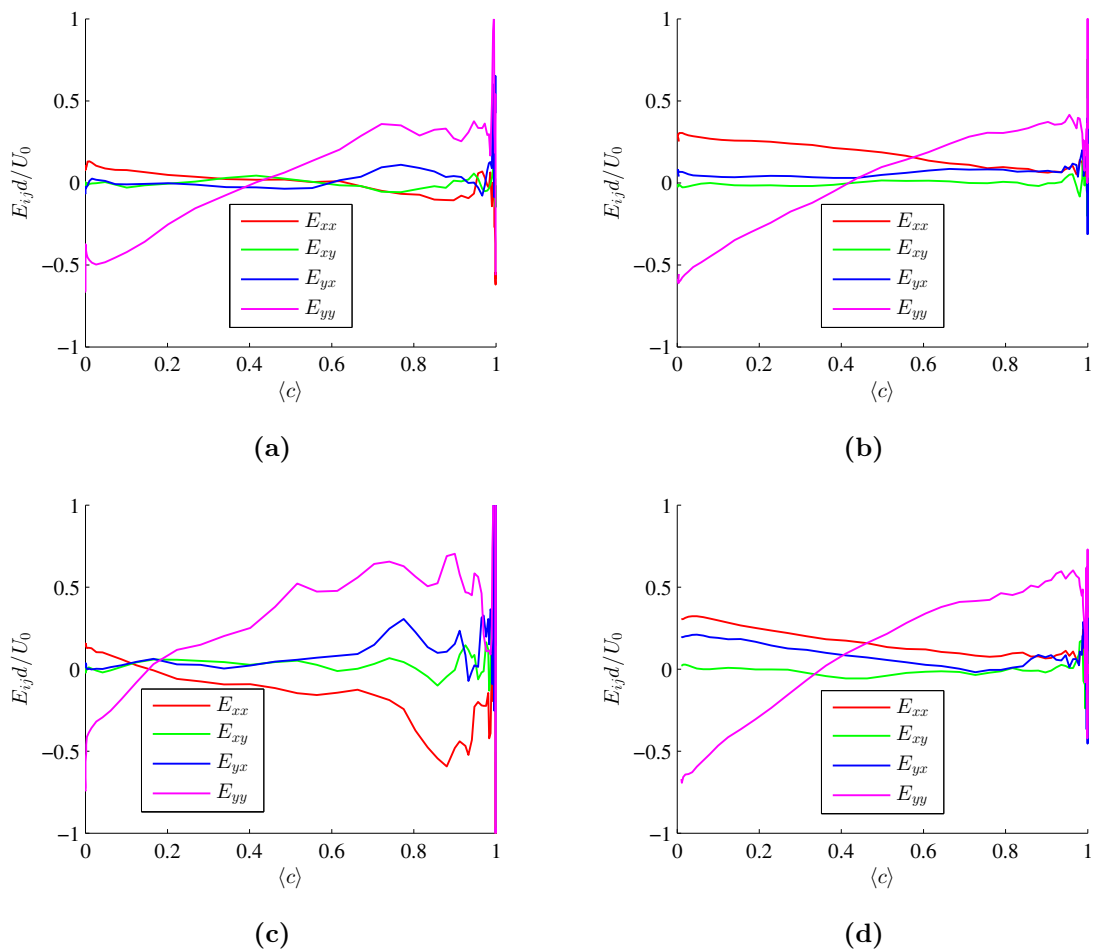


**Figure 67:** Normalized strain rates as a function of average progress variable along the burner center line at (a, c)  $u'_{rms}/S_{L,0} \approx 5$  and (b, d)  $u'_{rms}/S_{L,0} \approx 10$  for (a, b) 50:50  $H_2:CO$  and (c, d) 100%  $H_2$ .

To provide some context, consider the corresponding sensitivity of curvature and tangential strain rate to turbulence intensity. While the effect of fuel composition on the curvature PDFs is weak, turbulence intensity has a much stronger effect, as shown in Figure 68a,b for two different fuel compositions over a wide range of turbulence intensities. It is evident from these figures that as the turbulence intensity increases, the curvature PDF becomes broader, indicating increased occurrence of both high positive and negative curvature values. This result is consistent with previous studies [82, 116, 83, 76, 58, 115, 63].

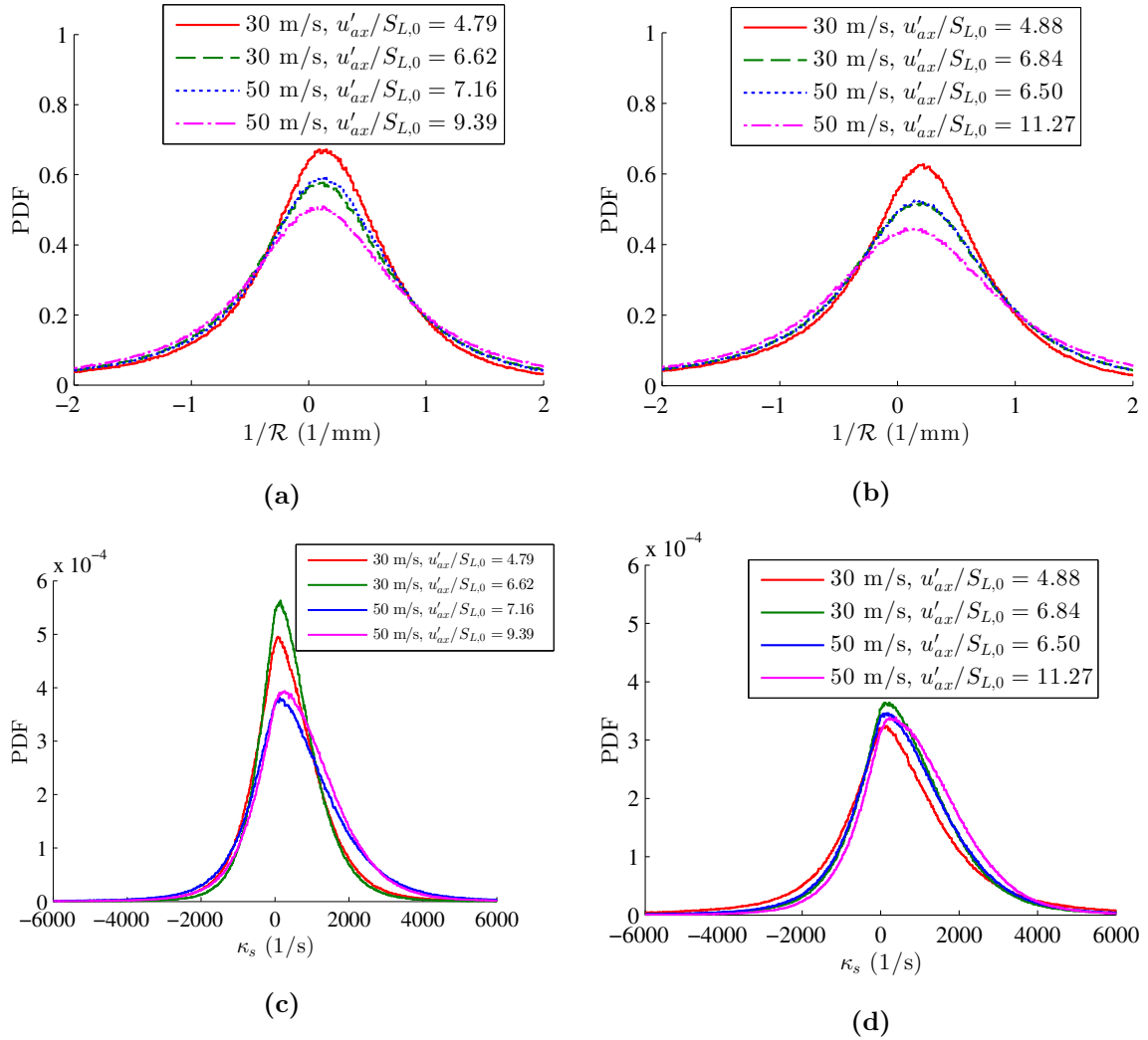


**Figure 68:** Unconditioned (a, b) curvature and (c, d) tangential strain rate PDFs for (a, c) 50:50 H<sub>2</sub>:CO and (b, d) 100% H<sub>2</sub>.

The velocity and turbulence intensity sensitivities of the tangential strain rate are quite

different. For the 50% H<sub>2</sub> mixture (Figure 68c), there appears to be a strong similarity between the shapes of the PDFs at a given mean flow velocity. This could indicate that the mean strain rate of the flow is a strong determining factor in the shape of the overall PDF. The pure H<sub>2</sub> case (Figure 68d) exhibits an entirely different behavior, and is largely unaffected by the turbulence level or mean flow velocity.

So far we have examined statistics of curvature and tangential strain rate independently of each other. To examine the correlation between these two quantities, consider Figure 69, which plots joint PDFs of curvature and tangential strain rate at low and high turbulence intensities for the three different fuel compositions studied. In this figure, the low turbulence condition is the left three figures and the high turbulence intensity is the right three figures. Hydrogen content, and thus stretch sensitivity, increases from top to bottom.

Here again we can observe the relative insensitivity of the joint PDF to fuel composition and the much stronger sensitivity to turbulence intensity. The latter effect is observed by the broadening of the joint PDFs in both directions. The broadening of the tangential strain rate axis for the pure hydrogen, low turbulence intensity condition was observed in Figure 66 and possibly is attributed to a shift in the mean flame position at the low turbulence condition that altered the mean strain field.

Correlation coefficients of unconditioned curvature and tangential strain rate were calculated for each condition to get a numerical quantity to describe the sensitivity of one term to the other. For each case the value was less than 0.1, with no noticeable dependence on fuel composition or turbulence intensity. This indicates that the curvature and tangential strain rate in these measurements are uncorrelated.

DNS results show that the correlation between these two quantities is dependent on the iso-scalar surface  $c$  where the curvature and tangential strain rate are measured from [24, 71]. It is important to note the distinction between  $c$  and  $\langle c \rangle$ :  $c$  measures the reaction progress instantaneously within the flame zone, whereas  $\langle c \rangle$  measures the time-averaged reaction progress variable. They found that for intermediate values of  $c$  ( $0.4 < c < 0.8$ ), there is a strong correlation between curvature and tangential strain rate. However, for low values ( $0.05 < c < 0.15$ ) the correlation is much weaker. They argue that this correlation

is due to the dilatation term,  $\partial u_i / \partial x_i$ , of the tangential strain rate equation. This effect manifests itself most strongly near the reaction zone of the flame where this term is most significant.

As discussed in Section 2.3.2, the velocity measurements for the tangential strain rate calculations were reactant-conditioned by masking out the product region using Otsu’s method [102]. This leads to a flame surface at an iso-contour of  $c \approx 0.5$ . However, since the velocity vectors are spaced apart by roughly one flame thickness, the distance from the flame front to the nearest upstream, reactant-conditioned velocity vector will be  $0 < r < \delta_f$ . Assuming that the average distance from the flame front iso-contour to the nearest velocity vector will be  $\delta_f/2$ , and since the chosen iso-contour is located roughly midway through the flame, leads to the result that these velocities are measured at progress variable values of  $c \rightarrow 0$ . Thus, these results of low correlation are similar to those observed in DNS results [24, 71] for the low range of  $c$  values.

### 5.3.2 Instantaneous Leading Point Stretch Statistics

This section analyzes curvature and tangential strain rate PDFs conditioned on the instantaneous leading points of the flame. Figure 70 presents instantaneous leading point stretch statistics for three different fuel compositions at low (Figure 70a,c) and high (Figure 70b,d) turbulence levels. As must be the case by geometric necessity, curvatures at instantaneous leading points are always positive.

From the least stretch sensitive mixture (50% H<sub>2</sub>) to the most stretch sensitive (100% H<sub>2</sub>), the measured turbulent displacement speed values,  $S_{T,LD}/S_{L,0}$ , increase by 84% for the low turbulence cases (Figure 70a,c) and 49% for the high turbulence cases (Figure 70b,d); thus, the turbulent displacement speed varies appreciably over this range of fuel compositions.

These plots show that the curvature at the leading points of the flame is only weakly influenced by fuel composition. For example, the mean curvature increases by only 7% from the lowest to highest H<sub>2</sub> content for the 50 m/s case, as tabulated in Table 11.

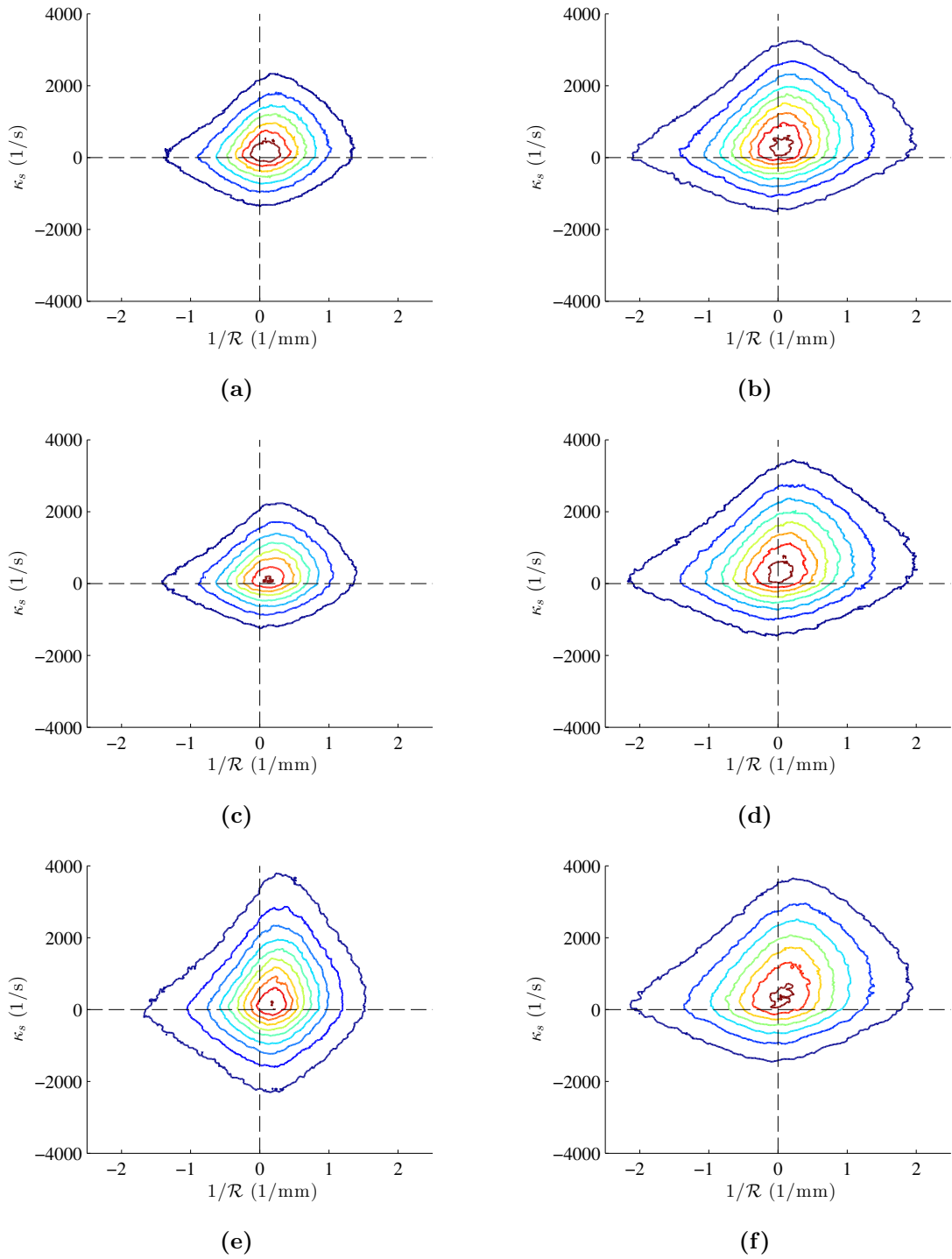


**Figure 69:** Unconditioned joint PDFs of curvature and tangential strain rate at (a, c, e)  $u'_{rms}/S_{L,0} \approx 5$  and (b, d, f)  $u'_{rms}/S_{L,0} \approx 10$  for (a, b) 50:50  $H_2:CO$ , (c, d) 70:30  $H_2:CO$  and (e, f) 100%  $H_2$ .

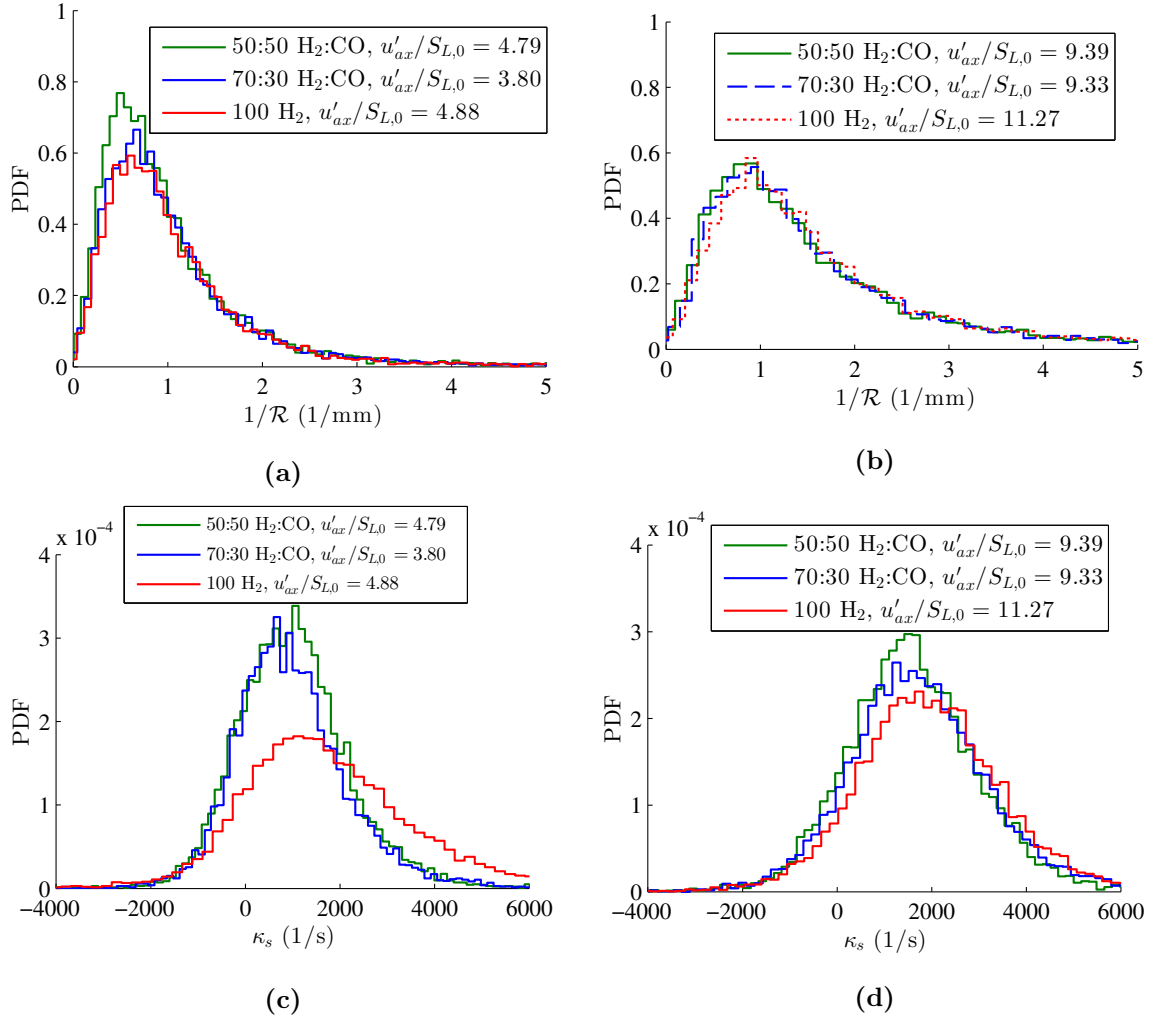


**Figure 70:** Instantaneous leading point (a, b) curvature and (c, d) tangential strain rate PDFs for (a, c)  $U_0 = 30$  m/s and (b, d)  $U_0 = 50$  m/s.

On the contrary, for the tangential strain rate there appears to be a stronger fuel composition effect. From the least stretch sensitive mixture (50% H<sub>2</sub>) to the most stretch sensitive (100% H<sub>2</sub>), the time-averaged tangential strain rate increases by 84% for the low turbulence cases (Figure 70a,c) and 26% for the high turbulence cases (Figure 70b,d). These increases are much closer to the observed 84% and 49% increases in the turbulent flame speed for the low and high turbulence cases, respectively.

A caveat to this, however, is that the time-averaged tangential strain rates for these mixtures range from 900-1900 1/s, well below the critical stretch rates at  $S_{L,max}$  observed in Figure 64 ( $\sim 7000$ - $15,000$  1/s for these fuel mixtures). Thus, while the relative percent changes observed in tangential strain rate with increasing stretch sensitivity are similar to the relative changes in the turbulent flame speed, the mean values of the tangential strain rate are low compared to critically stretched values. This does not support the argument that the leading points of these flames are critically stretched.

Next, for context, we present results of the effects of turbulence at the instantaneous leading points. Figure 71 plots the PDFs of instantaneous leading point curvatures and tangential strain rates at different turbulence levels for a 50:50 H<sub>2</sub>:CO mixture and a pure H<sub>2</sub> mixture. As the turbulence increases, the curvature PDF broadens in the direction of positive curvature. As tabulated in Table 11, the mean curvature of the 50% H<sub>2</sub> mixture increases from 0.88 to 1.47 1/mm ( $\sim 67\%$ ) over this 96% increase in turbulence intensity. Thus, statistically significant differences in leading point curvature exist with varying turbulence levels and are resolved by these measurements.

For the tangential strain rate PDFs, the 50:50 mixtures further emphasize that the tangential strain rate is more strongly affected by the mean flow rather than the turbulence level, especially since the green and blue curves have similar turbulence intensities but different PDFs. For the pure H<sub>2</sub> case, the PDFs are relatively independent of turbulence level or mean flow velocity. This change in behavior for the pure H<sub>2</sub> case is an interesting phenomenon and requires further examination and analysis.

Another way to look at the effect of fuel composition on stretch statistics is to plot the time-averaged curvature and tangential strain rate at the instantaneous leading points as a

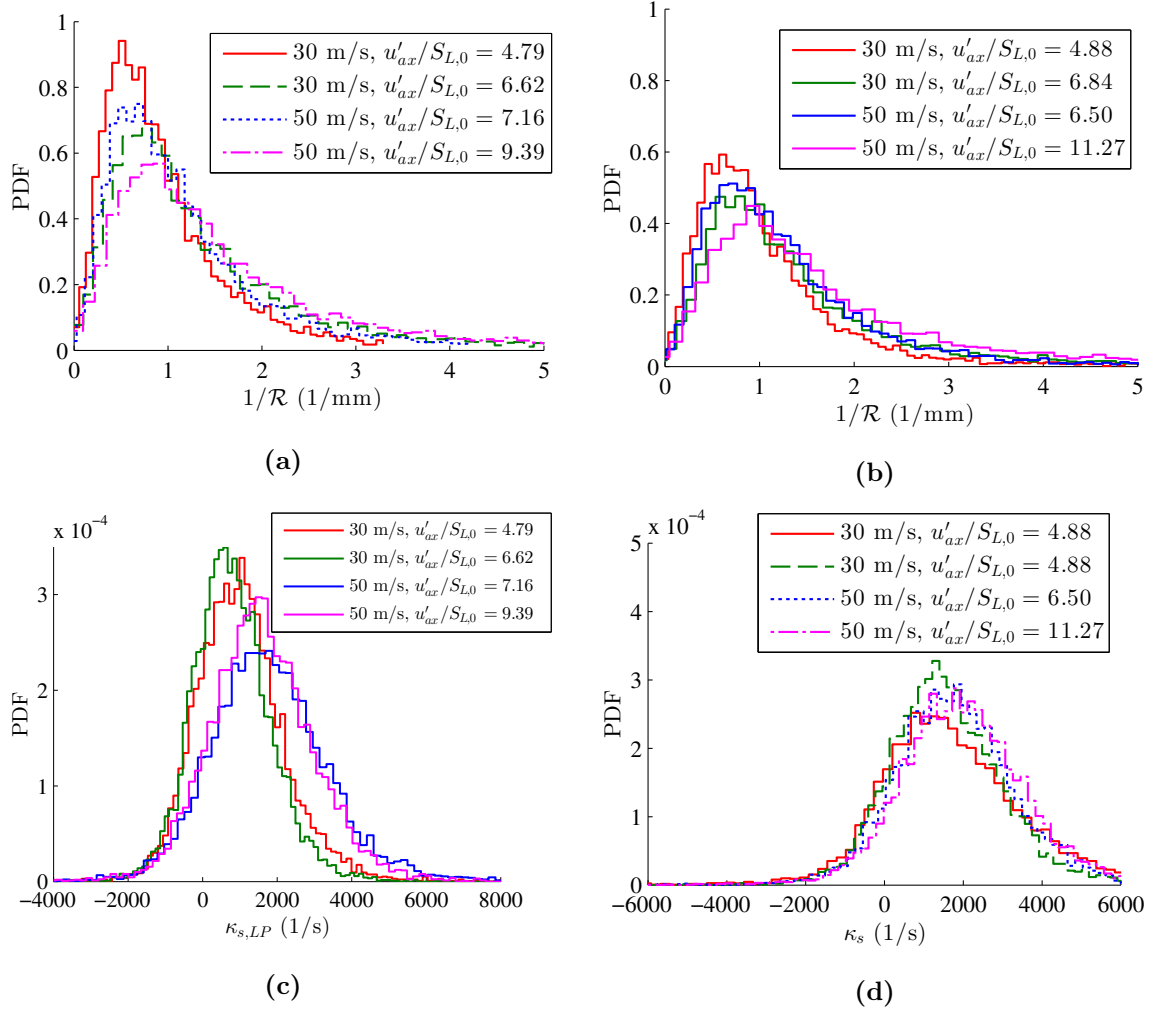


**Figure 71:** Instantaneous leading point (a, b) curvature and (c, d) tangential strain rate PDFs for (a, c) 50:50  $\text{H}_2:\text{CO}$  and (b, d) 100%  $\text{H}_2$ .

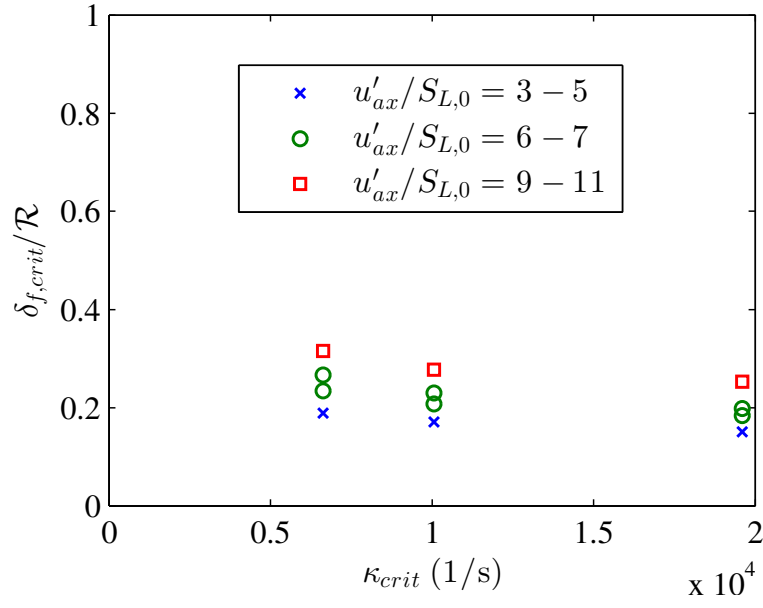
function of the flame’s critical stretch rate  $\kappa_{crit}$ , as shown in Figure 72. The critical stretch rate is the stretch rate that the flame experiences at the maximum stretched flame speed  $S_{L,max}$ , which increases monotonically with the stretch sensitivity of the fuel, as shown in Figure 64.

In Figure 72, the y-axes are normalized by the curvature (Figure 72a) or strain rate (Figure 72b) at  $S_{L,max}$ . The stretch sensitivity of the mixtures increases to the right (i.e., with increasing  $\kappa_{crit}$ ); however, the average stretch rates at the leading points do not increase with increasing stretch sensitivity and are well below the critically-stretched values. For the normalization in these figures, the flames would be critically-stretched at a y-axis value of one.

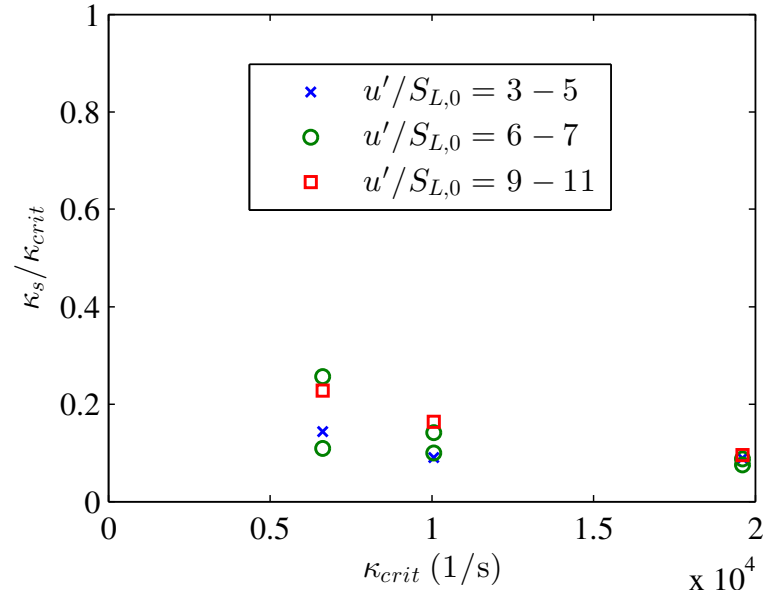
For context, consider the time-averaged curvature and tangential strain rate as a function of the turbulence intensity, as shown in Figure 73. As the turbulence increases, the time-averaged curvature and tangential strain rate increase as well, indicating that the stretch rate at the leading points is affected by turbulence. Notice, however, that even at the highest turbulence intensities, the flames are still well below the critically-stretched values of curvature and tangential strain rate; thus, the hypothesis of the leading points model that these flames should approach critically-stretched values is not justified by this data.

As discussed in detail in Section 2.3.2 of Chapter 2, One concern when considering this diagnostic technique is whether or not it is capable of resolving the finest curvatures for critically-stretched high hydrogen content flames. To reiterate our confidence that these curvatures are resolved, consider again the results (shown previously in Section 2.3.2 of Chapter 2) presented here in Figure 74 that compare the instantaneous leading point curvature PDFs for two different arc length intervals. Even with a factor of two decrease in the arc length interval, the shape of the PDF remains the same, indicating that both choices are fully resolving the finest curvatures present.

Next we present results of the joint PDFs of curvature and tangential strain rate at the instantaneous leading points of the flame. Similar conclusions are drawn here as for the unconditioned joint PDFs presented in Figure 69, with low correlation (below 0.1) between curvature and tangential strain rate. This correlation was again not found to have

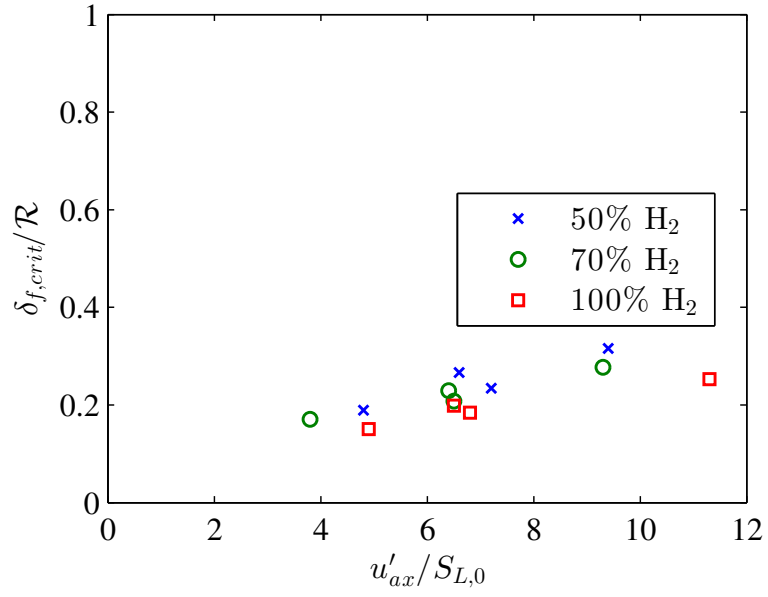


(a)

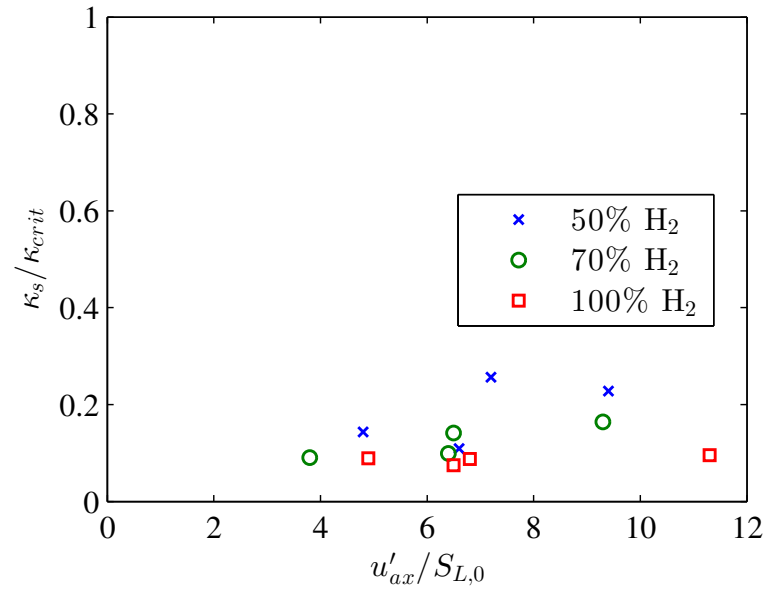


(b)

**Figure 72:** Instantaneous leading point average (a) curvature and (b) tangential strain rate vs. the critical stretch rate at  $S_{L,max}$  for varying fuel compositions at various turbulence levels.



(a)



(b)

**Figure 73:** Instantaneous leading point average (a) curvature and (b) tangential strain rate vs. turbulence intensity normalized by the unstretched laminar flame speed for varying fuel compositions.

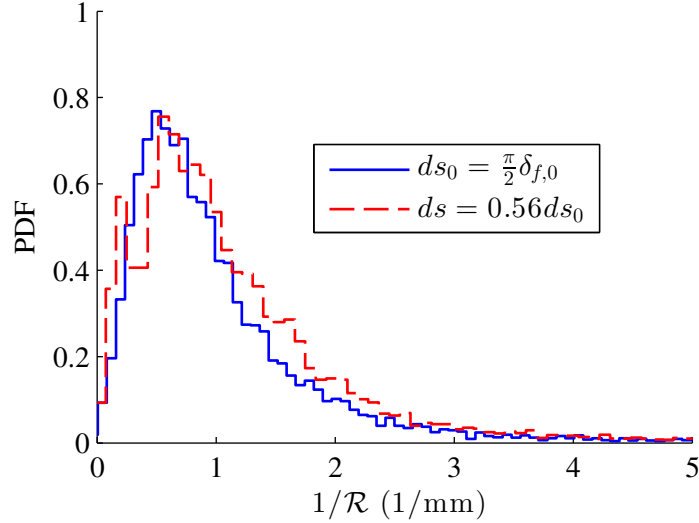


**Figure 74:** Comparison of curvature PDFs generated using two arc length intervals for a 50:50 H<sub>2</sub>:CO mixture at  $U_0 = 30$  m/s.

any relationship to the turbulence intensity or the fuel composition. Again, this result is attributed to the velocities being measured at low  $c$  values and is consistent with results from the literature [24, 71].

### 5.3.3 Flame Brush Leading Point Stretch Statistics

This section presents results for the flame brush based definition of the leading point. As a reminder, the flame brush leading point is based off of values of stretch statistics conditioned over a defined range of progress variable values. Figure 76 presents curvature and tangential strain rate PDFs conditioned on the flame brush leading point for three different fuel compositions over  $0 \leq \langle c \rangle \leq 0.01$ .

These results again show only mild changes in the curvature PDFs with changing fuel composition. For the highest turbulence intensity cases (Figure 76b), Table 2 shows that for the progress variable range  $0 \leq \langle c \rangle \leq 0.1$  the mean curvature actually decreases by 13% while the standard deviation of the curvature increases by only 9% with increasing H<sub>2</sub> content. For  $0 \leq \langle c \rangle \leq 0.01$  the mean curvature increases by 18% and the standard deviation does not change with increasing H<sub>2</sub> content. However, care should be taken when interpreting results over such a narrow range of progress variable values as the number

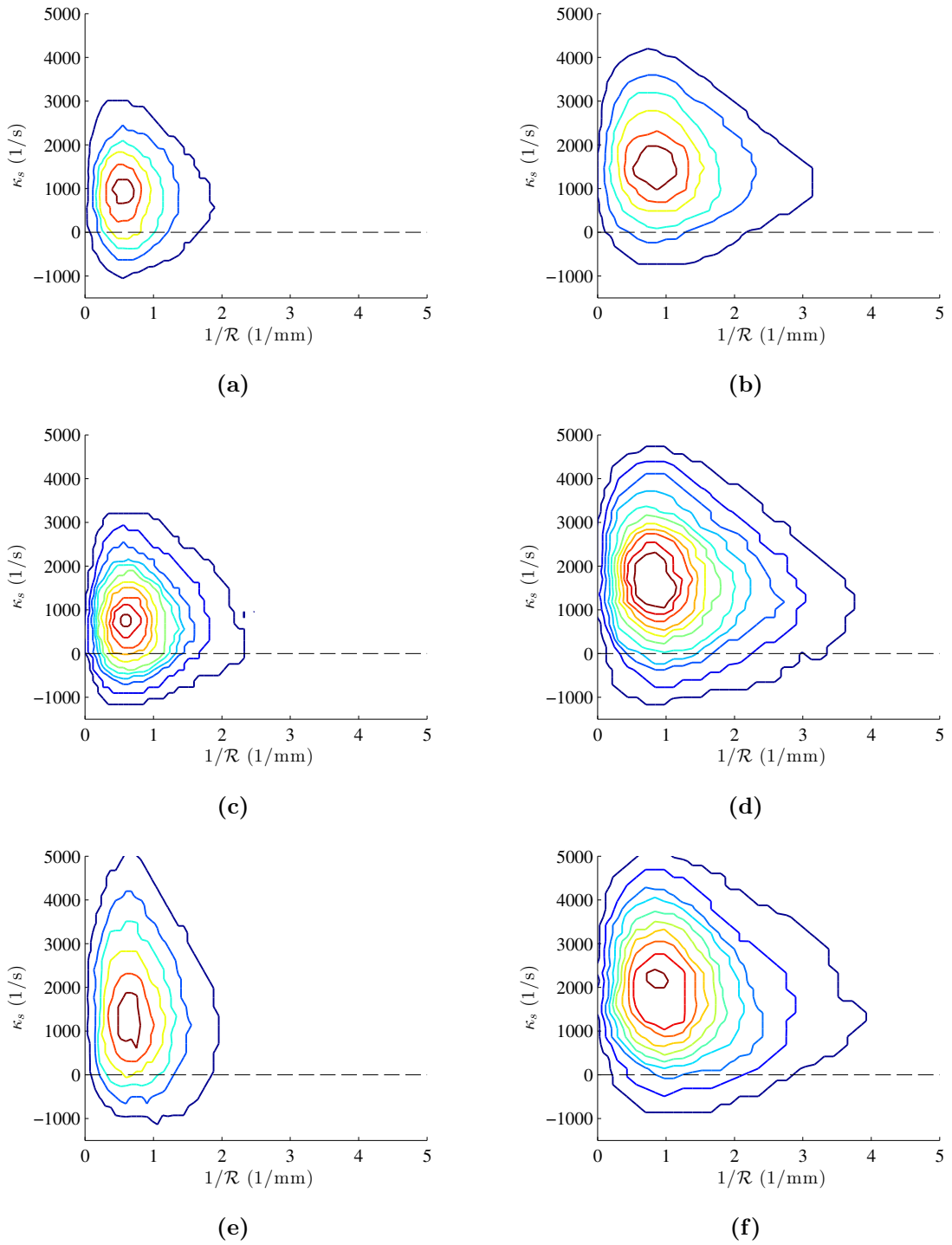


**Figure 75:** Instantaneous leading point conditioned joint PDFs of curvature and tangential strain rate at (a, c, e)  $u'_{rms}/S_{L,0} \approx 5$  and (b, d, f)  $u'_{rms}/S_{L,0} \approx 10$  for (a, b) 50:50  $\text{H}_2:\text{CO}$ , (c, d) 70:30  $\text{H}_2:\text{CO}$  and (e, f) 100%  $\text{H}_2$ .

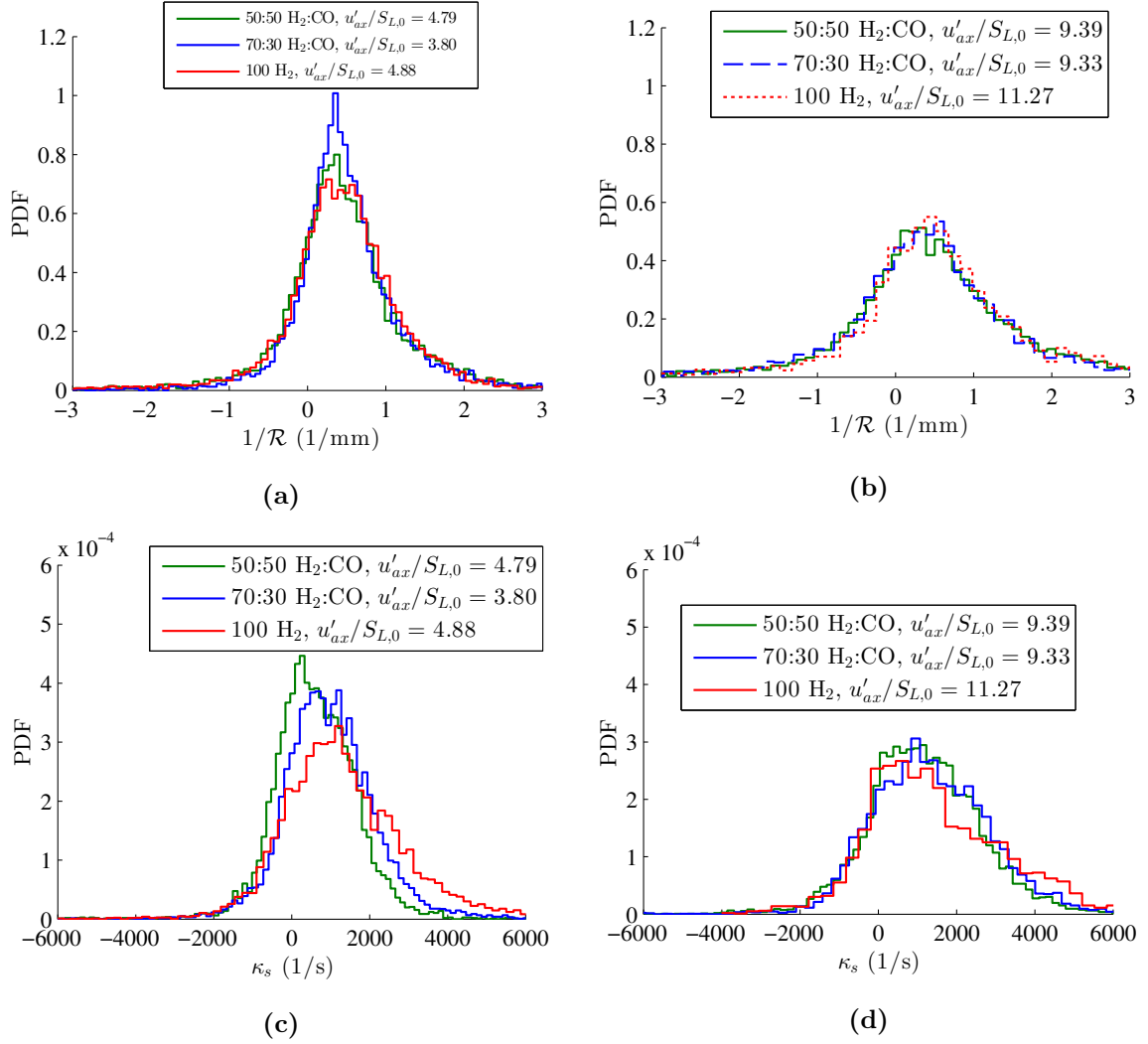


**Figure 76:** Flame brush leading point ( $0 \leq \langle c \rangle \leq 0.01$ ) (a, b) curvature and (c, d) tangential strain rate PDFs for (a, c)  $U_0 = 30$  m/s and (b, d)  $U_0 = 50$  m/s.

of experimental realizations is an approximate order of magnitude smaller than the range  $0 \leq \langle c \rangle \leq 0.1$ , leading to  $\sqrt{10} \approx 3.2$  increases in error. These changes in time-averaged curvature are small when compared to the 49% increase in turbulent flame speed and 140% increase in stretch rate of critically stretched flames at those conditions.

Note that even if the curvature at the leading points does not vary with fuel composition, the local consumption speed of the leading points will still increase with the stretch sensitivity of the mixture, a fact that can be observed in Figure 64 (i.e., the laminar flame speed increases with H<sub>2</sub> content at a fixed stretch rate). Furthermore, the curvature-induced strain rate,  $\kappa_c$ , also increases, even if the average radius of curvature does not change, since  $\kappa_c = S_L/\mathcal{R}$ . The strain sensitivity calculations in Figure 64 were used to estimate the magnitude of this effect by estimating the laminar flame speed using  $\kappa_c = S_L/\mathcal{R}$ . This calculation shows that, for the high turbulence intensity cases (Figure 76b), the time-averaged strain rate at the instantaneous leading points increases by 39% and the calculated laminar consumption speed increases by approximately 20% from the 50% H<sub>2</sub> mixture to the pure H<sub>2</sub> mixture. Over the same fuel composition range, the strain rate at  $S_{L,max}$  increases by 133%,  $S_{L,max}$  increases by 65% and  $S_{T,LD}$  increases by 50%. Thus, the measured variations are much weaker than the calculated increase of local consumption speed at  $S_{L,max}$  or the observed increases in  $S_{T,LD}$ .

For the tangential strain rates at the flame brush leading points, the time averaged values increase by 136% for Figure 76c and 26% for Figure 76d; far more comparable to the corresponding 84% and 49% increases in the turbulent flame speed. This provides some evidence that the tangential strain rate is influenced by fuel composition and may play a role in explaining the stretch sensitivity of the turbulent flame speed.

However, the range of time-averaged tangential strain rates for these mixtures is only from around 500 to 1,400 1/s, well below the critically stretched values for these mixtures of 7,000 to 15,000 1/s. This is inconsistent with the change that would be expected based upon the theoretical explanation put forward in our prior study [133], which used a stability argument to suggest that the flame stretch rate at the leading point, and the corresponding  $S_L$  value, should approach critically stretched values, leading to increased turbulent flame

speeds.

Another way to examine stretch sensitivities for these mixtures is to plot the time-averaged curvature and tangential strain rate as functions of the average progress variable  $\langle c \rangle$ , as is done in Figure 77. These plots help to elucidate the behavior of the flame over the entire flame surface, rather than just the leading point behavior. From these plots it is evident that both the curvature and tangential strain rate become more positive towards the leading edge of the flame front. For the curvature, from  $0 < \langle c \rangle < 0.5$  the more stretch sensitive the mixture is the higher the curvature, but this increase is very slight.

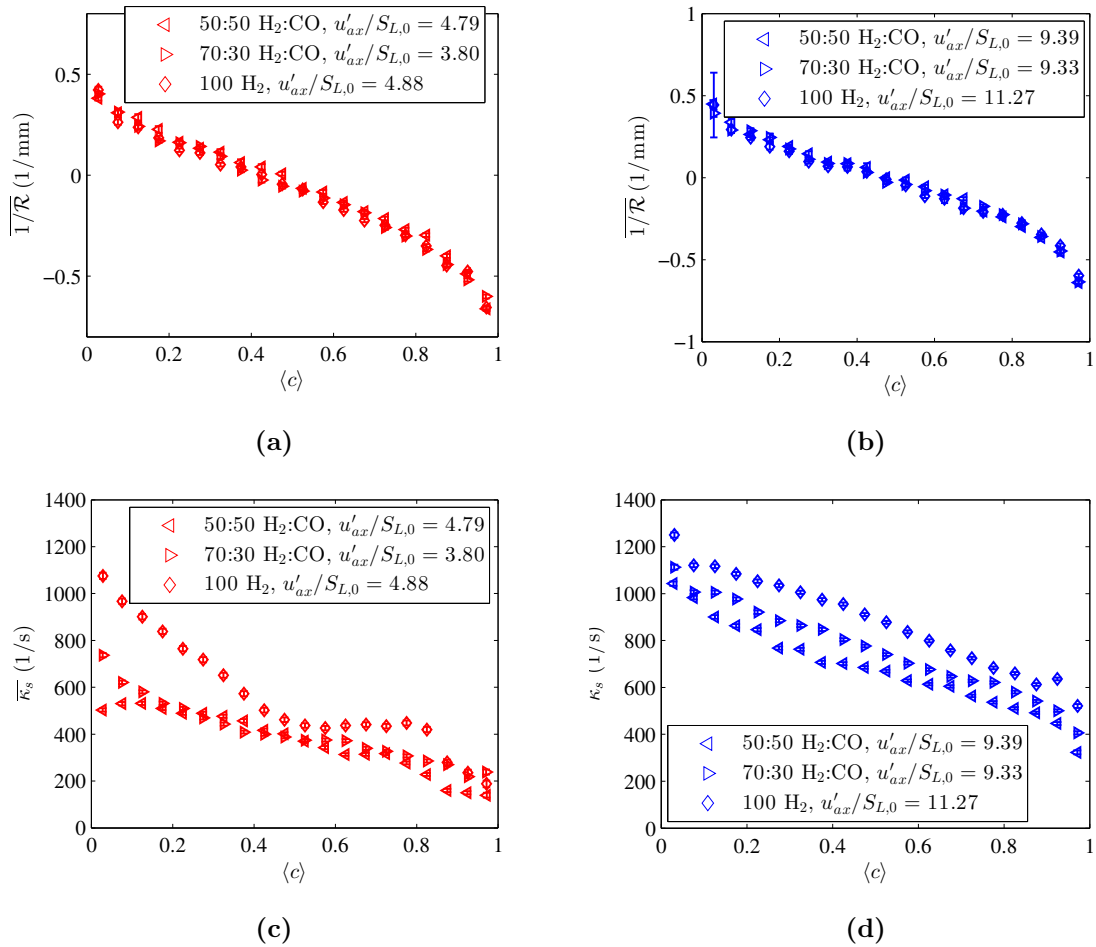


**Figure 77:** Time-averaged (a, b) curvature and (c, d) tangential strain rate as a function of progress variable  $\langle c \rangle$  for (a, c)  $U_0 = 30$  m/s and (b, d)  $U_0 = 50$  m/s.

However, these plots do provide evidence that there is a more significant effect of fuel

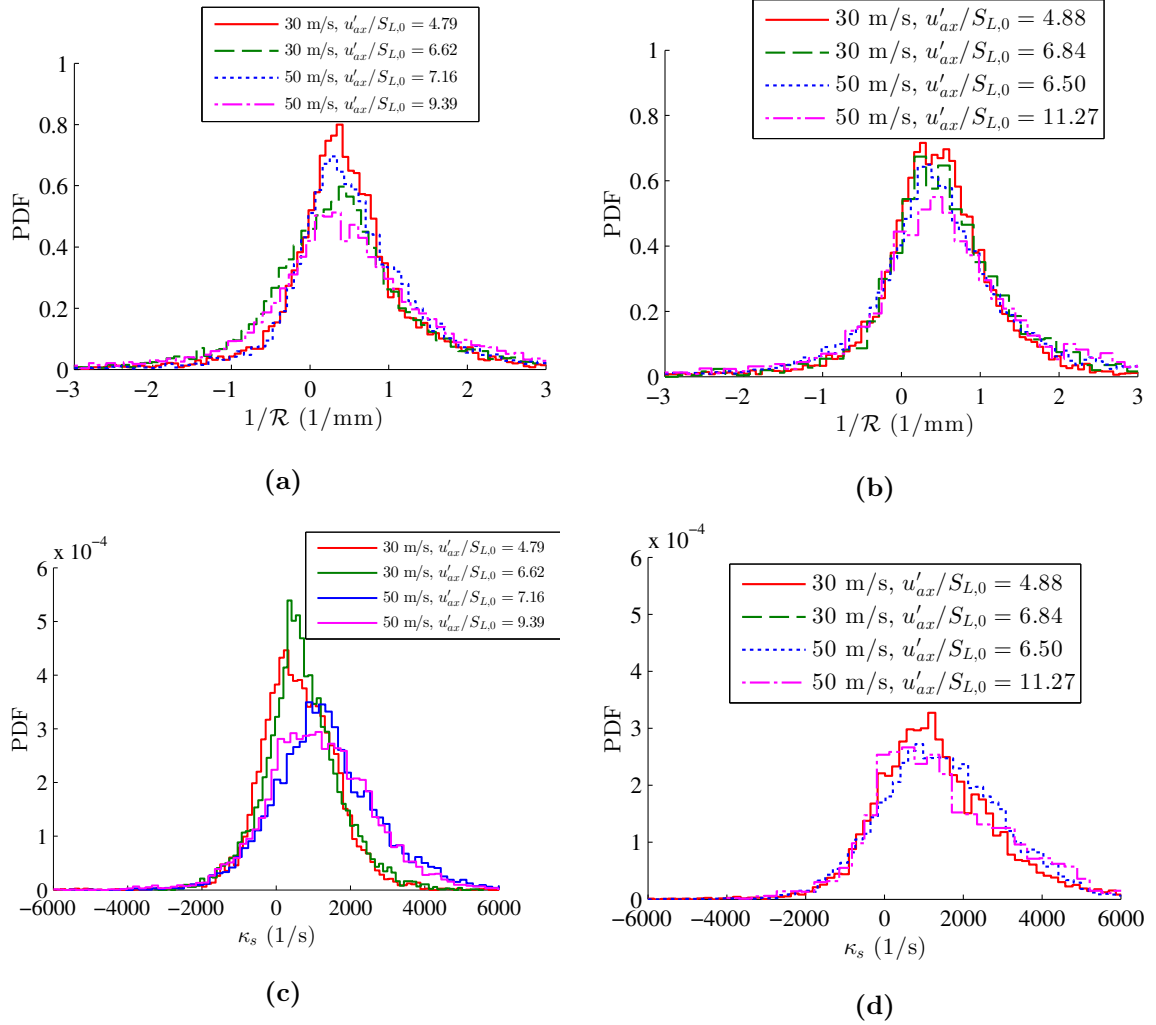
composition upon the tangential strain rate at the flame leading points. For example, for the low turbulence intensity case (Figure 77c) the time-averaged curvature at the lowest progress variable region increases from  $\sim 500 - 1100$  from the 50% H<sub>2</sub> to the 100% H<sub>2</sub> mixtures, an approximate 120% increase. This aligns well with the results presented throughout this work that show a stronger sensitivity of the tangential strain rate to fuel composition.

Now consider the sensitivity of the flame brush leading point stretch statistics to turbulence and mean flow velocity. Results are presented in Figure 78 for two fuel compositions over a wide range of turbulence intensities at two mean flow velocities. For the curvature PDFs, as the turbulence increases, the peak drops and the tails get broader, indicating increased occurrence of finer scale wrinkling. Again, the tangential strain rate shows more dependence on mean flow velocity for the 50:50 H<sub>2</sub>:CO mixture. The pure H<sub>2</sub> mixture is generally insensitive to both mean flow velocity and turbulence conditions.

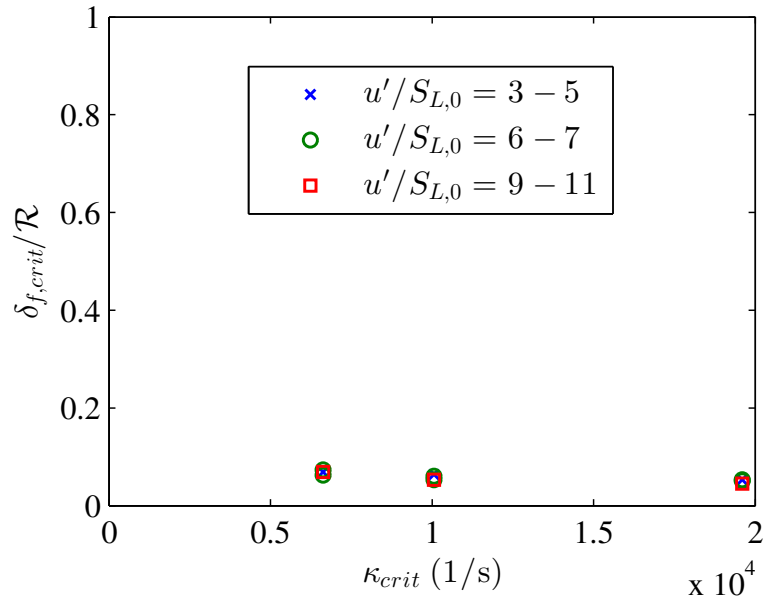
As in the previous section, another method to look at the effects of fuel composition on stretch is to plot average curvatures and tangential strain rates as functions of the critical stretch rate  $\kappa_{crit}$  as shown in Figure 79. Similar conclusions can be drawn from this figure as for Figure 72. First, the curvatures and tangential strain rates at the flame leading points do not increase with increasing stretch sensitivity of the mixture. Second, the leading point stretch rates are well below critically-stretched. These findings are contrary to the hypotheses of the leading points model.

Figure 80 presents average values of flame brush leading point curvatures and tangential strain rates as a function of turbulence intensity. The results presented here are different than those observed for the instantaneous leading points shown in Figure 73, with almost no effect of turbulence level on the mean values of curvature and tangential strain rate.

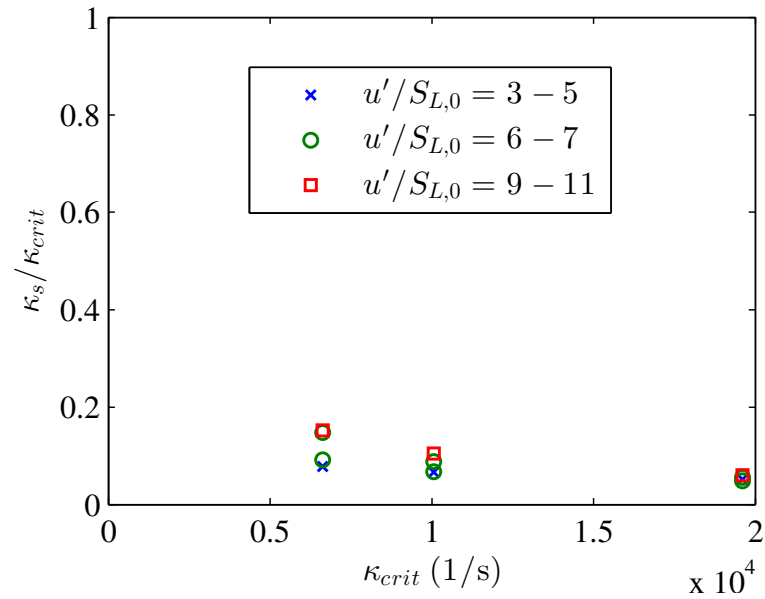
One possible explanation for this is that turbulence will equally increase the likelihood of both positive and negative stretch rates along the flame front. Since the instantaneous leading point will always be positively curved, the effect of turbulence on the negative curvature side of the PDF is not captured. However, for flame brush leading points, the definition is based off of a region of the flow, thus positive and negative curvature effects are captured. Because of this, Figure 81 presents the same data except plotting the standard deviations of



**Figure 78:** Flame brush leading point ( $0 \leq \langle c \rangle \leq 0.01$ ) (a, b) curvature and (c, d) tangential strain rate PDFs for (a, c) 50:50  $\text{H}_2$ :CO and (b, d) 100%  $\text{H}_2$ .

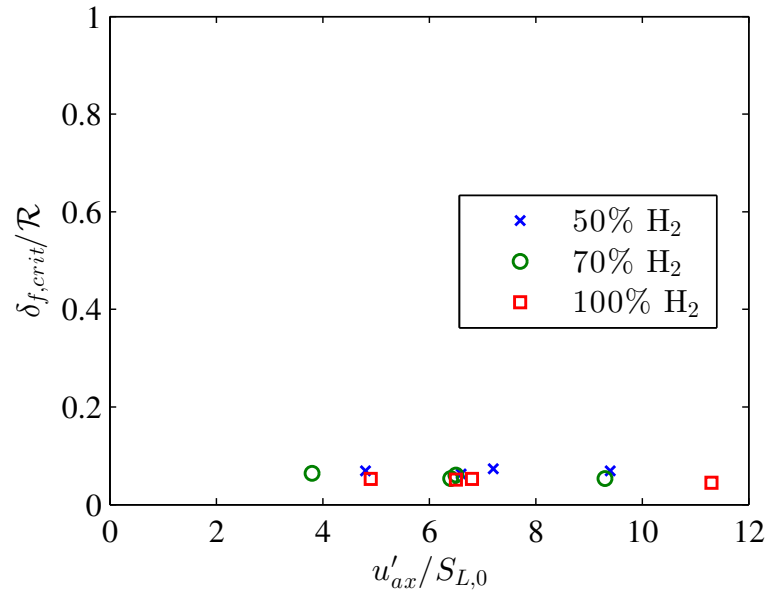


(a)

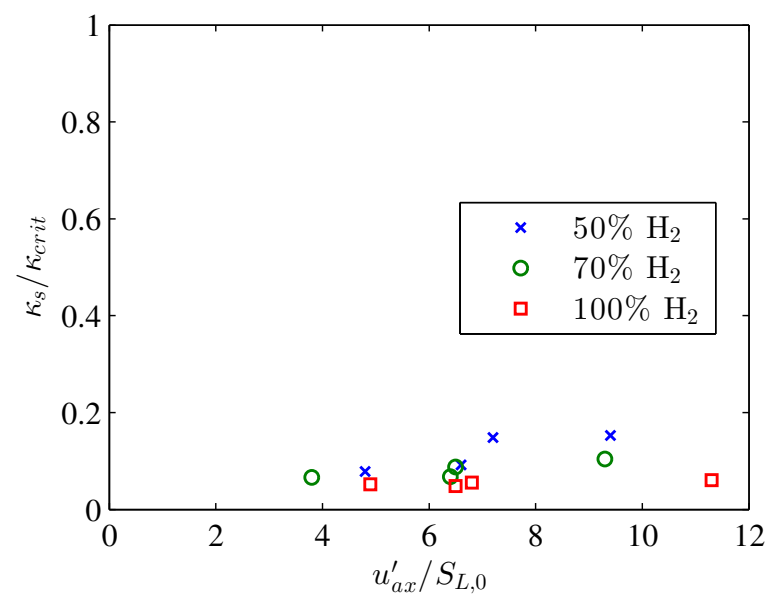


(b)

**Figure 79:** Flame brush leading point average (a) curvature and (b) tangential strain rate vs. the critical stretch rate at  $S_{L,max}$  for varying fuel compositions at various turbulence levels.



(a)

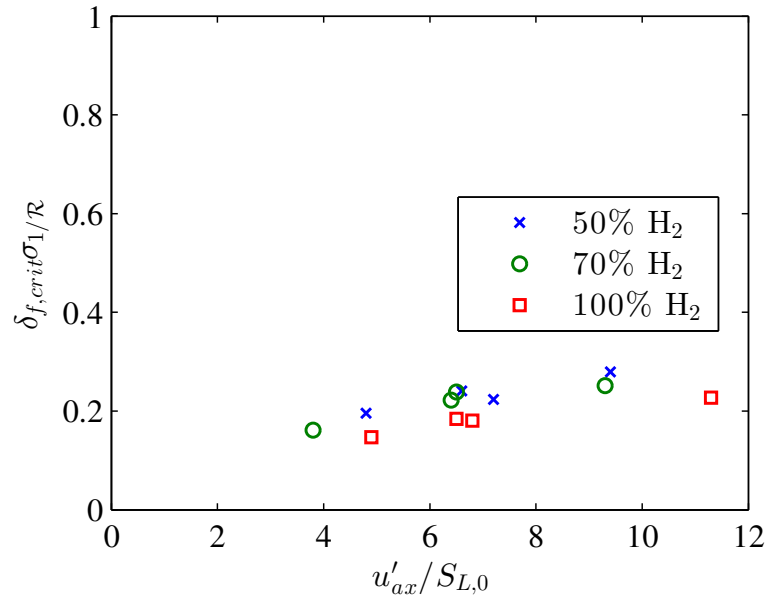


(b)

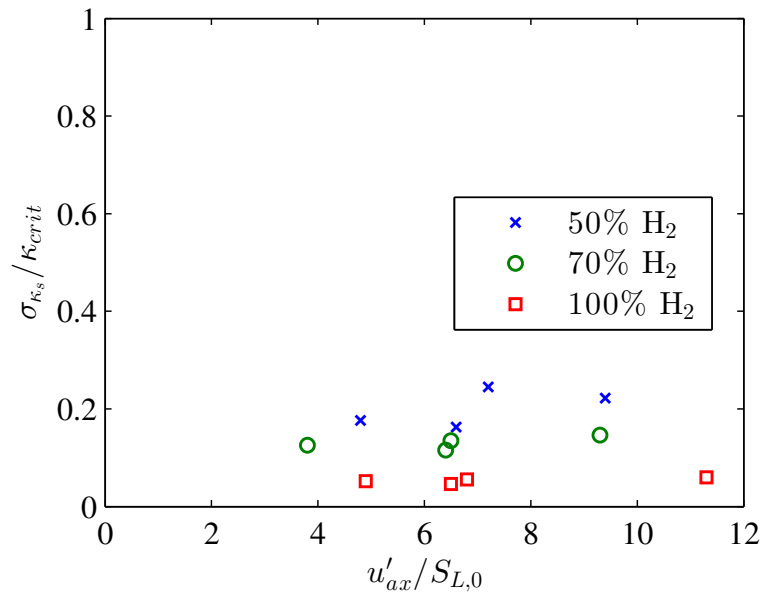
**Figure 80:** Flame brush leading point average (a) curvature and (b) tangential strain rate vs. turbulence intensity normalized by the unstretched laminar flame speed for varying fuel compositions.

curvature and tangential strain rate as functions of turbulence intensity. For the curvature, it is clear to see that the standard deviation increases with increasing turbulence. The results for the tangential strain rate are not as evident, with no clear trend with increasing turbulence intensity.

Again we have plotted joint PDFs of curvature and tangential strain rate, now for the flame brush leading points, in Figure 82 and observe similar trends as in the unconditioned (Figure 69) and leading point conditioned (Figure 75) versions. Calculations of the correlation coefficient between these two quantities yielded no discernible trend with either fuel composition or turbulence intensity.



(a)



(b)

**Figure 81:** Flame brush leading point standard deviations of (a) curvature and (b) tangential strain rate vs. turbulence intensity normalized by the unstretched laminar flame speed for varying fuel compositions.

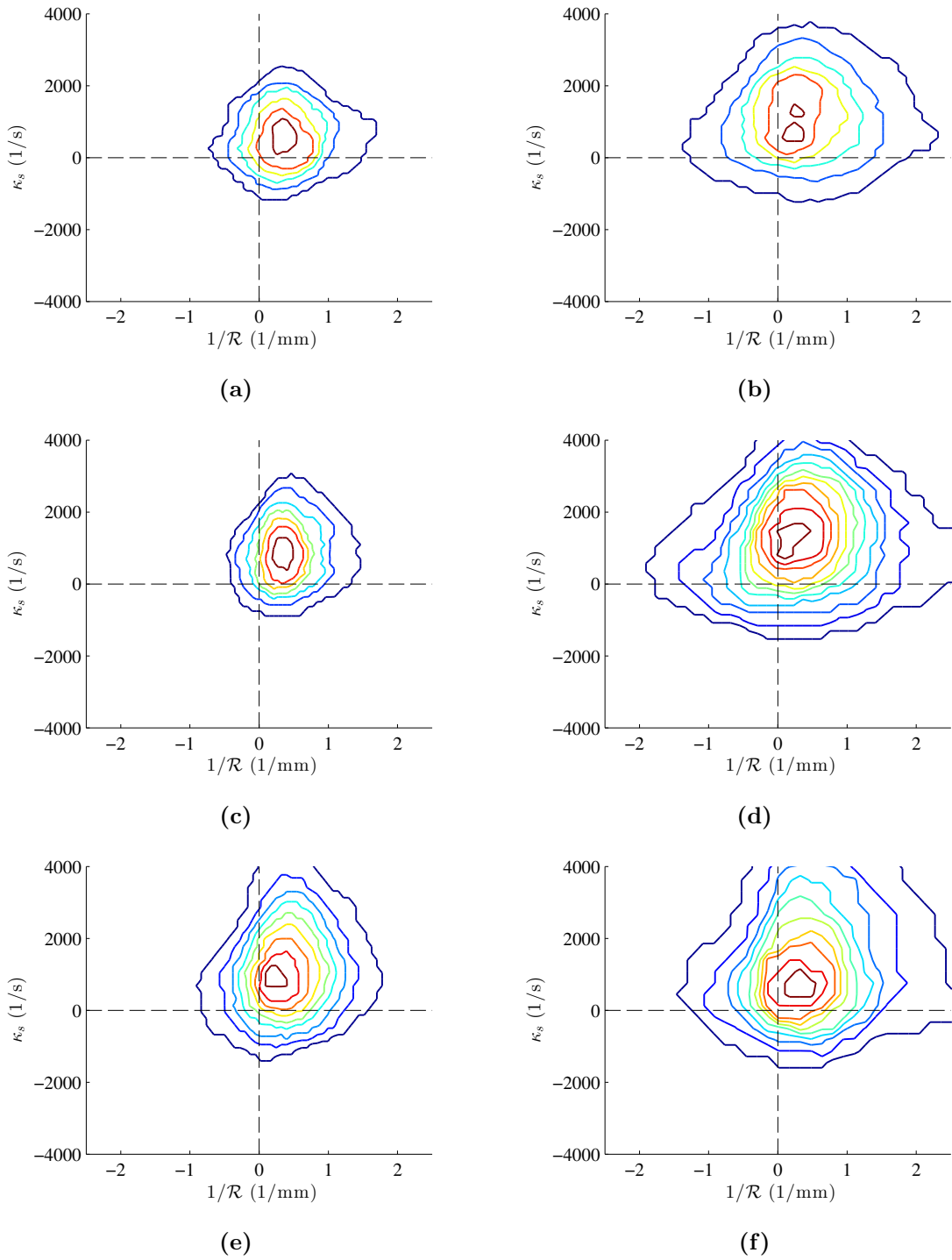


**Figure 82:** Flame brush leading point conditioned ( $0 \leq \langle c \rangle \leq 0.01$ ) joint PDFs of curvature and tangential strain rate at (a, c, e)  $u'_{rms}/S_{L,0} \approx 5$  and (b, d, f)  $u'_{rms}/S_{L,0} \approx 10$  for (a, b) 50:50  $\text{H}_2$ :CO, (c, d) 70:30  $\text{H}_2$ :CO and (e, f) 100%  $\text{H}_2$ .

## 5.4 *Concluding Remarks*

The goal of this chapter was to develop a better physical understanding of the behavior of the leading points of the turbulent flame in order to test the validity of our previously developed leading points model for collapsing turbulent flame speed data. Specifically, this chapter assessed arguments that increasing turbulent flame speeds, observed with high H<sub>2</sub> fuels, were due to higher  $S_{L,max}$ , and therefore higher flame stretch rates at the leading points.

The data presented in this chapter do not fully support this argument. Only minor effects of fuel composition on curvature statistics at the flame leading points are observed. Rather, curvature statistics are dominated by the turbulence intensity. However, there does appear to be a stronger effect of fuel composition on the tangential strain rate statistics. We observed changes in the time-averaged values at the leading points that were similar to the changes observed in the turbulent flame speeds. However, these values of the time-averaged tangential strain rate are still well below those for critically stretched conditions. This goes counter to the argument put forth in our previous study [133] that these leading points will approach critically stretched values.

Joint PDFs of the curvature and tangential strain rate showed no correlation between these two quantities over the entire range of fuel compositions and turbulence intensities studied, regardless of whether the results are taken globally over the entire flame surface or locally at the flame leading points.

Future work will include estimating the contribution of curvature to the overall flame stretch rate, which requires multiplication by the local laminar flame speed. This flame speed will be different for different fuel compositions, and, thus, PDFs of the curvature-stretch term of the flame stretch equation may show a stronger dependence on fuel composition than PDFs of curvature alone. These results show that further work is needed to understand the physical processes through which the turbulent flame speed is altered by differential diffusion effects.

## CHAPTER VI

### CONCLUSIONS AND RECOMMENDATIONS FOR FUTURE WORK

This chapter aims to summarize the major conclusions and contributions of this thesis work. The chapter concludes with recommendations for future work in this area.

#### *6.1 Conclusions and Contributions*

The objective of this research was to develop tools to better understand the physics of turbulent flame propagation in highly stretch sensitive premixed flames in order to predict their behavior at conditions realistic to the environment of gas turbine combustors. The propagation rate of turbulent premixed flames into unburned reactants is characterized by a parameter known as the turbulent flame speed,  $S_T$ .  $S_T$  has a leading order impact on important combustor phenomena such as the life of hot section components, flashback and blowoff limits, and the operating limits before damaging combustion dynamics occur [85].

This thesis presented the results of an experimental study into the flame propagation characteristics of highly stretch-sensitive, turbulent premixed flames. A scaling law, developed in an earlier thesis [134] from leading point concepts for turbulent premixed flames, was used to collapse turbulent flame speed data over a wide range of conditions. The flow and flame structure were characterized using high speed particle image velocimetry (PIV) over a wide range of fuel compositions, mean flow velocities, and turbulence levels. The first part of this thesis examined turbulent flame speeds for these mixtures and applied the previously developed leading points scaling model in order to test its validity in an alternate geometry. The model was found to collapse the turbulent flame speed data over a wide range of fuel compositions and turbulence levels, giving merit to the leading points model as a method that can produce meaningful results with different geometries and turbulent flame speed definitions.

The second part of this thesis examined flame front topologies and stretch statistics of these highly stretch sensitive, turbulent premixed flames. Instantaneous flame front

locations and local flow velocities were used to calculate flame curvatures and tangential strain rates. Statistics of these two quantities were calculated both over the entire flame surface and also conditioned at the leading points of the flames.

The results presented do not support the arguments made in the development of the leading points model that the leading points of the flame should be critically stretched. Only minor effects of fuel composition are noted on curvature statistics, which are mostly dominated by the turbulence. There is a stronger sensitivity for tangential strain rate statistics, however, time-averaged values are still well below the critically stretched values hypothesized from the leading points model.

As discussed in Section 4.1.5 in Chapter 4, analysis by Amato [3] has shown that the value of  $S_{L,max}$  varies by about 20-40% depending on the manner that the flame stretch is applied. In addition, the stretch rate at  $S_{L,max}$  can vary by approximately 15%. As shown in Section 5.3 of Chapter 5, the average leading point curvatures and tangential strain rates are approximately 20% of their critically stretched values. On top of this, the  $S_{L,max}$  and  $\kappa_{crit}$  values used in the stretch analysis of this data were obtained with a plane counterflow flame configuration, whereas using cylindrical counterflow and expanding spherical flames result in higher  $S_{L,max}$  and  $\kappa_{crit}$  values. Thus, changing the manner in which the stretch is calculated would result in an even larger discrepancy between the measured values and the calculated critically stretched values.

Another aspect to consider when comparing these stretch statistics to their critically stretched values is the fact that these are 2D measurements, and higher values are obtained when full 3D measurements can be obtained. As discussed in Section 2.3.2 of Chapter 2, correction factors to convert time-averaged 2D stretch measurements to 3D values can be applied [60]. These correction factors are  $\langle 1/\mathcal{R} \rangle_{3D} = \frac{\pi}{2} \langle 1/\mathcal{R} \rangle_{2D}$  and  $\langle \kappa_s \rangle_{3D} = 2 \langle \kappa_s \rangle_{2D}$  for curvature and tangential strain rate, respectively. Applying these correction factors to the acquired data still results in leading point curvatures and tangential strain rates that are 30-60% of their critically stretched values. While these values are closer, it is important to emphasize that the relative changes in time-averaged values between fuel compositions will not change with correction factors applied. For example, when going from a 50% H<sub>2</sub>

mixture to a pure  $\text{H}_2$  mixture, the time-averaged instantaneous leading point curvature and tangential strain rate increased by 7% and 26%, respectively, compared to the 140% increase observed in the calculated critical stretch rate. Thus, correction factors do not help to explain the observed insensitivity of leading point stretch rates to fuel composition.

Finally, there is also the uncertainty associated with the actual PIV measurements, as discussed in greater detail in Section 2.2.2.1 of Chapter 2. However, in this section it was estimated that the errors in velocity calculations are on the order of 2-7%, which is a small error in comparison to the 3-10 $\times$  differences observed between leading point stretch rates and corresponding critical stretch rates.

The results of this study emphasize the importance of local flame topology measurements towards the development of predictive models of the turbulent flame speed. As discussed in Chapters 1 and 4, the leading points model states that the leading points propagate at  $S_{L,max}$  when the flames are quasi-steady. In the thesis work of Venkateswaran [134] (and overviewed in Chapter 4) non-quasi-steady arguments were used to explain why some turbulent flame speed data did not collapse well using the leading points model. In reality, no leading point in a turbulent flow will ever reach the steady-state value of  $S_{L,max}$ , because all turbulent flames are inherently unsteady. Thus, the appropriate normalizing factor varies depending on the properties of the mixture and of the flow. Since 2D measurements cannot be used to calculate the total stretch rate it is not possible to obtain from the measurements the appropriate leading point flame speed for normalizing the turbulent flame speed data acquired in this thesis. However, ideas for overcoming this are suggested in Section 6.2.1 as a possible future research program.

The subsequent section aims to outline some of the significant contributions that this body of work has contributed to the broader combustion community.

### **6.1.1 Experimental Methodologies**

One of the major contributions from this work is the development of novel experimental methods that have advanced the state of the art in the development of high pressure, high turbulence intensity reacting flow facilities. For example, the design of the turbulence

generator system developed in this work has been used by other research groups in the development of their own experimental facilities [124].

This turbulence generation system was developed for high pressure, high temperature combustion experiments. While grids, perforated plates, or slots are commonly used for turbulence generators, they have the disadvantages that the grid or plate must be changed in order to access a different turbulence level at a given flow velocity. The turbulence generator described in this work was found to achieve a large range of relative turbulence intensities from 10% to 30% and turbulent Reynolds numbers from 140 to 9000 without exchanging plates or varying the mean flow velocity. This gives the ability to independently study the effects of mean flow velocity and turbulence on combustion characteristics such as the turbulent flame speed and stretch statistics.

In addition, the facility was characterized extensively using three component laser Doppler velocimetry over a wide range of flow velocities, turbulence intensities, temperatures, and pressures. These three-dimensional profile measurements provide an extensive database of turbulence characteristics for the turbulence generator making it one of the better characterized systems in the current literature. It is especially difficult to find flow field characterizations at high pressure, high preheat temperatures. This is due to the difficulties with performing velocimetry studies in high pressure, high temperature environments. For example, LDV and PIV require that the flow be seeded with very small particles that follow the flow. A common issue encountered for enclosed, optically accessible experimental facilities is window fogging from seed particles.

Window fogging occurs when seed particles adhere to the surface of the glass. If the fogging becomes too severe, the laser will not be able to pass through and, for PIV, the cameras used cannot get adequate images to track the flow. This is a common problem that hampers many high pressure experimental facilities looking to perform seeded velocimetry experiments. The facility used in this thesis work was able to avoid this difficulty for the Bunsen burner configuration by having a co-flow of unseeded air that surrounded the main burner and kept the seed particles from impinging on the quartz windows. This eliminated window fogging altogether and allowed for longer periods of data acquisition; thus, a very

large database of high pressure measurements was acquired.

### 6.1.2 Turbulent Flame Speed Measurements

This thesis expanded upon measurements of turbulent flame speeds that were first acquired in this facility in the thesis work of Venkateswaran [134]. In this thesis, measurements were acquired in a low swirl burner for fuel mixtures of  $\text{H}_2:\text{CO}$  and  $\text{H}_2:\text{CH}_4$ , and also for pure  $\text{CH}_4$  and  $\text{H}_2$ . The amount of local displacement speed data in the literature for mixtures containing high amounts of hydrogen is relatively small and confined to a few research groups [89, 31, 30, 32, 90]. This work has expanded these measurements and examined new fuel mixtures at high turbulence conditions.

These types of measurements are especially important in the development of combustors operating on alternative fuels that contain hydrogen. With the ever growing concerns over pollutants and climate change, new regulations on emissions are making the study of alternative fuels even more important to manufacturers of gas turbines, reciprocating internal combustion engines, and other industrial burners. Measurements of the turbulent flame speed are especially relevant because modern combustors developed for land-based power generation operate in premixed or partially-premixed mode to reduce emissions of  $\text{NO}_x$  and  $\text{CO}$ . The turbulent flame speed has a leading order effect on premixed combustor performance issues such as flashback and blowoff limits, combustion instabilities, and combustor heat loading.

In addition, the leading points model for collapsing turbulent flame speed data was also used with relative success on the turbulent flame speed data acquired using the LSB. This model was used previously by Venkateswaran [134] to collapse global consumption speed  $S_{T,GC}$  data over a wide range of mean flow velocities, turbulence intensities, fuel compositions, and pressures. To find that it also collapses local displacement turbulent flame speed  $S_{T,LD}$  data acquired in the LSB is further validation of the model.

### 6.1.3 Flame Topology and Stretch Statistics

The primary contribution of this work is in the acquisition and analysis of leading points properties of thermodiffusively unstable, turbulent, premixed flames. The goal of this effort

was to validate the hypothesis that went into the development of the leading points model for collapsing turbulent flame speed data.

Specifically, this hypothesis argued that increasing turbulent flame speeds, observed with high H<sub>2</sub> fuels, were due to higher  $S_{L,max}$  and, therefore, higher flame stretch rates at the leading points. However, as was shown in the previous chapter, the data do not support this hypothesis. It was shown that, while the stretch statistics at the leading points do show changing behavior with flow parameters such as the turbulence intensity and mean flow velocity, that they are relatively insensitive to changes in fuel composition. This behavior was analyzed over a wide range of turbulence intensities, fuel compositions, and mean flow velocities. The data do show drastic fuel composition effects in terms of increasing turbulent flame speeds with H<sub>2</sub> content, however, the stretch statistics at the leading points do not appear to correlate well with the stretch sensitivity of these mixtures.

This work is a good step in developing a stronger understanding of the physical mechanisms behind fuel effects on turbulent flames. Although the findings do not support the hypothesis of the leading points model, this still advances the scientific understanding of the behavior of thermodiffusively unstable flames. This research highlights that there is still a significant amount of work needed in order to better understand the complex physical and chemical processes occurring in turbulent premixed flames.

## ***6.2 Recommendations for Future Work***

The field of turbulent premixed flames is a complex and fascinating problem, with so many different mechanisms at play at the same time, including turbulence, chemical reactions, and heat and mass transfer. It is a rich research problem that still contains many mysteries, and a wide open field of research possibilities exist. In this final section of the thesis I will attempt to address some specific areas of research related to the work presented here to further advance the understanding of the behavior of turbulent premixed flames.

### **6.2.1 Advanced Leading Points Measurements and Analysis**

Future work towards understanding the behavior of the leading points requires advanced measurement and analysis techniques. This includes the use of 3D measurement techniques

such as simultaneous dual plane PLIF and stereoscopic PIV. This allows for more accurate measurements of the terms of the stretch rate equation. In addition, the contribution of the flame curvature to the overall flame stretch rate can be determined. This requires multiplication of the curvature by the local laminar flame speed. This flame speed will be different for different fuel compositions, and, thus, PDFs of the curvature-stretch term of the flame stretch equation may show a stronger dependence on fuel composition than PDFs of curvature alone. The flame displacement speed can be determined locally with these advanced 3D experimental techniques by finding the flame normal direction and the distance traveled between successive images from the dual plane PLIF and the incoming velocity of the reactants from the stereo PIV. DNS measurements at similar conditions can be used to measure 3D flame stretch statistics and to compare results between computations and experiments.

With the ability to calculate the curvature-stretch term, it would then be possible to obtain the total stretch rate at every point along the flame front. There is very limited data of this kind, especially for high hydrogen content fuels. This information would be a valuable addition to the literature and to the understanding of thermodiffusively unstable turbulent premixed flames. It would allow for a better estimation of the stretch rate at the leading points of the flame, which could then be compared to 1D stretched laminar flame calculations and also to 3D DNS calculations of turbulent flames. The comparison with 1D stretched laminar flames would give a better idea of how close these flames come to reaching the stretch rate at the maximum laminar flame speed,  $\kappa_{crit}$ .

Another area that needs to be studied further is joint PDFs of curvature, tangential strain rate, displacement speed, and curvature-stretch, both globally conditioned and conditioned on the leading points of the flame. Some 2D joint PDFs were presented for curvature and tangential strain rate in Chapter 5, however, additional understanding can be developed from leading points analysis from 3D measurement techniques. This analysis includes contributions of both displacement speeds and curvature-stretch, to develop a more thorough understanding of the inter-relationship between these terms. Most of the literature examining joint statistics of the terms of the stretch rate equation does so using DNS

data [61, 24, 22, 21, 23, 2], with only limited experimental results [112]. Analysis of these statistics for a wide variety of fuel mixtures at high turbulence levels would be a valuable contribution to the literature. Comparison with the existing DNS datasets would also be beneficial for validation purposes.

While 3D measurements provide a more direct and accurate measurement of flame stretch rate contributions, a first estimate of the curvature effect is possible with the existing experimental database. This can be accomplished by developing an algorithm to measure the distance that the flame leading point travels between frames of the PIV images. With the known data rate this can be converted into a local, instantaneous flame speed. However, since this is a highly turbulent, three-dimensional environment and PIV provides only a two-dimensional view, the out-of-plane motion will not be taken into consideration. While this is true, recent work by Kerl et al. [68] and Gashi et al. [54] have used three dimensional experimental and numerical techniques, respectively, to show that 2D measurements of the local flame speed are correlated with 3D measurements. In addition, Hawkes et al. [60] have shown that in an isotropic turbulence field, with a statistically 1D flow and flame, the out of plane motion will not have a preferential direction. The LSB is a close approximation to a statistically 1D flow and flame in a highly turbulent environment. Thus, results obtained from a 2D view of the flame may not be the true local flame speed, but will provide useful information in qualitatively determining if statistically significant differences are observed with changing fuel composition.

### **6.2.2 High Pressure and Temperature Flame Topology Measurements**

An important area of premixed turbulent combustion that needs to be examined further is the influence of pressure and temperature on the topology characteristics of stretch sensitive flames. The topology measurements in this thesis were acquired at atmospheric pressure. However, as was shown in the work of Venkateswaran et al. [132], the turbulent flame speed is also affected by pressure, even when keeping the unstretched laminar flame speed  $S_{L,0}$  constant across all cases. When normalized with  $S_{L,max}$ , the data did not collapse across pressures. This was discussed previously in Chapter 4.

As the pressure increases so does the Reynolds number, leading to shorter time scales and smaller length scales of the turbulence – an effect on the flow. At the same time, higher pressures lead to decreases in the length and time scales of the chemistry by increasing the reaction rate (which leads to thinner flames). These two effects will alter the strain field that these flames are subjected to and also how these stretch sensitive flames will respond to this strain field. While increasing the pressure decreases both the flow and chemistry scales, changing the temperature of the incoming reactants will increase the flow scales (by reducing  $Re$ ) and decrease the chemistry scales (by increasing the reaction rate). By varying temperature and pressure, we can start to better understand the independent effects of varying the scales of the chemistry and the flow.

Time-resolved flame topology and flow field measurements at high pressures and temperatures are necessary for answers to these outstanding questions about the behavior of turbulent premixed flames. Measurements of flame stretch statistics at high pressures and temperatures will provide useful information to the driving force behind the changes in the turbulent flame speed observed for these thermodiffusively unstable mixtures.

### **6.2.3 Turbulent Flame Speed Measurements and Analysis**

Switching gears to the subject of turbulent flame speeds, there is still a significant amount of research needed to fill gaps in the available data in the literature. From a fundamental research perspective, the turbulent flame speed is important in developing a more refined understanding of turbulent premixed flames, including concepts such as non-unity Lewis number effects and preferential diffusion. It is also a useful quantity as an input to various reacting flow models and for validation of simulations. From an industry perspective, the turbulent flame speed helps in the development of the next generation of fuel flexible, lean, premixed gas turbines.

One area that is of particular interest to power suppliers is having the flexibility to run their plants off both gas and liquid fuels. Having the ability to run off of liquid fuels gives the supplier a safety net in case of a shortage in natural gas due to price fluctuations or new regulations over extraction techniques. In many developing and growing countries,

especially in the Middle East, liquid fuels are in high supply and are available at low cost. Thus, there is significant interest for developers of gas turbines to make their engines dual fuel capable. These gas turbines are running a combination of nonpremixed and premixed or partially premixed operation when on liquid fuels. For premixed operation the fuel is vaporized and mixed with air upstream of burning. Turbulent flame speeds of liquid fuels are uncommon in the literature [1, 58, 138], and research is necessary to expand the existing database.

Liquid fuels offer an interesting research problem because they are heavier than air. This means that, for lean mixtures, they are thermodiffusively stable. Their response to flame stretch is opposite of the flames studied in this thesis. As lean mixtures of heavier than air fuels become positively stretched, their flame speeds will decrease, as discussed in Chapter 1. This means that the leading points of the flame will propagate slower than every other point along the flame front, and the flame will tend to flatten itself. The flame will no longer be pulled by the leading points, but pushed along by the trailing points of the flame. This means that the leading points model for the turbulent flame speed is most likely invalid for thermodiffusively stable flames. An important question to answer for these flames is what are the important mechanisms affecting the turbulent flame's propagation rate.

In addition to liquid fuels, there is also interest in gas turbines operating on mixtures of natural gas and hydrogen. The high diffusivity of hydrogen can be used to expand flammability limits of the fuel mixture. This allows operation at leaner conditions to reduce  $\text{NO}_x$  emissions. In addition, the amount of CO and  $\text{CO}_2$  produced can be decreased with higher levels of hydrogen relative to natural gas. Turbulent flame speed data for these mixtures is needed at gas turbine relevant conditions. Specifically, mixtures at high operating pressures (up to 20 atm), high preheat temperatures (up to 600 K), and high turbulence intensities (up to 30%) are needed to better understand the behavior of these flames at realistic conditions.

## APPENDIX A

### FLOW METERING AND CALIBRATION

This appendix presents the flow facility and flow rate calibration data for critical nozzles used to meter and mix fuels in the experimental facility. For completeness, important details of the facility are repeated from Chapter 2 in this appendix.

#### *A.1 Flow Metering Facility*

As discussed in Chapter 2, a significant task in the development of the experimental facility was the design and implementation of a flow metering and mixing system for multicomponent fuels.

The gases used in this experimental facility are metered and mixed via critical orifice meters as shown in Figure 83. Table 13 lists the instruments and valves used in this system. Check valves are used to prevent back flow of gases. The pressure and temperature are measured just upstream of the choked orifice, and the pressure is measured downstream of the orifice to ensure that the flow is choked. Different orifice sizes are used to achieve a wide range of flow rate.

For choked flow of ideal gases, the mass flow rate is calculated from:

$$\dot{m} = C_d A p \left( \frac{\gamma MW}{RT} \left( \frac{2}{\gamma + 1} \right)^{\left( \frac{\gamma + 1}{\gamma - 1} \right)} \right)^{1/2} \quad (47)$$

where  $C_d$  is the discharge coefficient,  $A$  is the choked orifice area,  $p$  is the pressure upstream of the orifice,  $\gamma$  is the ratio of specific heats,  $MW$  is the molecular weight, and  $R$  is the universal gas constant. The discharge coefficients for different orifice diameters were found by calibrating the orifices using a drum-type gas meter.

After the critical orifices, the individual gas components are mixed to create two multicomponent fuel mixtures. The fuel mixtures then enter the fuel and air delivery system to be mixed before entering the burner. There is also a system in place that is designed to

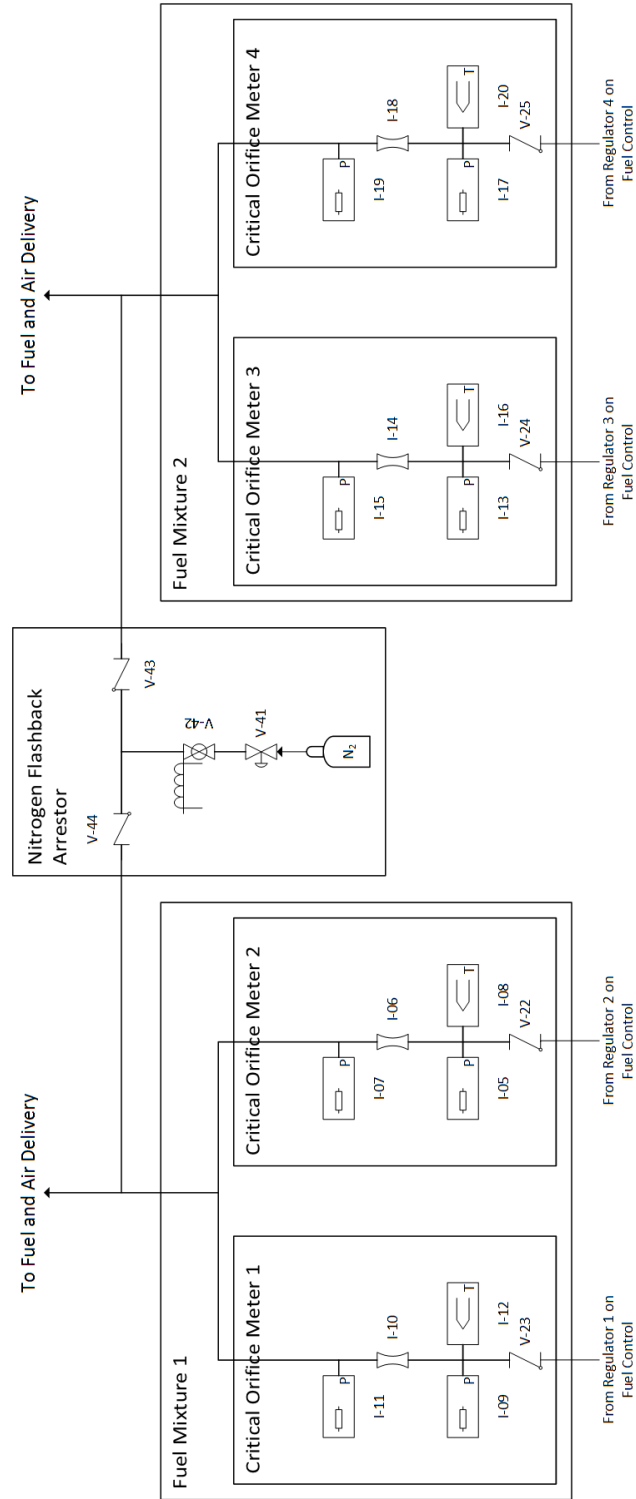


**Figure 83:** Diagram of the experimental facility for metering and mixing of fuels.

purge the lines with  $N_2$  in the event that a flashback is detected. This is a safety feature meant to extinguish the flame as quickly as possible during flashback.

**Table 13:** Instrument and valve list for Figure 17

---

Displayed Text	Description
I-05	Pressure Transducer
I-06	Critical Orifice
I-07	Pressure Transducer
I-08	Type K Thermocouple
I-09	Pressure Transducer
I-10	Critical Orifice
I-11	Pressure Transducer
I-12	Type K Thermocouple
I-13	Pressure Transducer
I-14	Critical Orifice
I-15	Pressure Transducer
I-16	Type K Thermocouple
I-17	Pressure Transducer
I-18	Critical Orifice
I-19	Pressure Transducer
I-20	Type K Thermocouple
V-22	Check Valve
V-23	Check Valve
V-24	Check Valve
V-25	Check Valve
V-41	Spring Loaded Regulator
V-42	Pneumatically Actuated Ball Valve
V-43	Check Valve
V-44	Check Valve

---

## A.2 Methods

Shown in Figure 84 is a drum-type gas meter that measures the volume of flowing gases with very high precision. It was used in this research effort to calibrate the critical orifice meters discussed in the previous section.

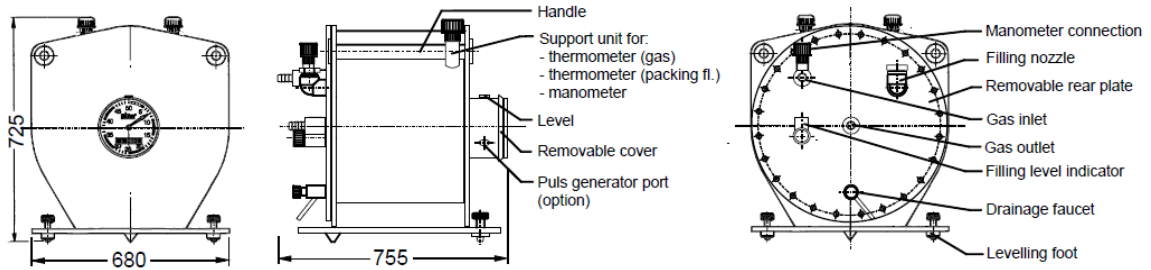


**Figure 84:** Drum-type gas meter used to measure volume flow rates for critical orifice calibrations [49].

The drum-type gas meter measures volume displacement by the gas through a rotating drum partially filled with a low viscosity oil. The drum is essentially a turbine partially submerged in oil. As the gas enters the drum, it causes this turbine to rotate as the gas fills one chamber and is exhausted from the next. By keeping the packing oil at a consistent level within the drum, the amount of volume that is displaced is a known quantity.

The displacement is measured using a rotating dial coupled to the central shaft of the measuring drum. An optical encoder generates a pulse for every 0.25 liters of displaced volume. This pulse signal is read by the data acquisition system, which also records the time between each pulse, in order to calculate the volume flow rate. Because the meter operates at atmospheric conditions, the volume flow rate can be converted to a mass flow rate using the gas temperature to calculate the density.

The meter has a measurement accuracy of  $\pm 0.5\%$  over the measurement range from 3.33 to 300 liters per minute. The factory calibrated measurement error over the entire operable range of the meter is presented in Figure 85.

To calibrate the critical orifices, the pressure upstream of the orifice is controlled using air-loaded regulators combined with electropneumatic pressure controllers. The pressure setpoint upstream of the orifices is controlled via an electronic pressure transducer coupled

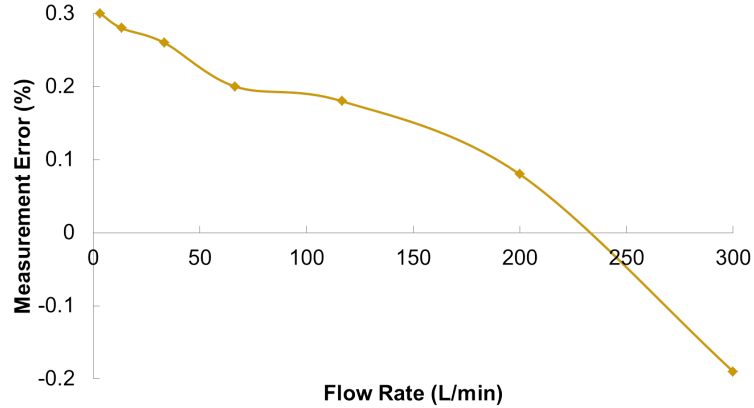


**Figure 85:** Measurement error in the drum-type gas meter.

to a PID controller contained in the electropneumatic pressure controllers. A pressure setpoint is commanded from the DAQ system and the pressure controller adjusts the air load on the regulator until the desired setpoint is achieved.

Volume flow rates from the drum-type gas meter are measured over a range of pressure setpoints that covers the operable flow rate range of the meter. This information is used to generate plots that compare the mass flow rate measured from the meter to the mass flow rate calculated using Equation 47. The inputs to this equation are gas properties, the orifice diameter, and the measured pressure and temperature upstream of the orifice. A linear fit is used to determine the orifice discharge coefficient  $C_d$ . The subsequent section presents results of these calibrations for various input gases over a wide range of orifice sizes.

### ***A.3 Results***

This section presents mass flow rate calibration results for a variety of gases over a range of orifice sizes. The gases that were calibrated include air,  $\text{CH}_4$ , CO,  $\text{H}_2$ , and  $\text{N}_2$ . Orifice sizes are (in thousandths of an inch): 6, 18, 24, 32, 43, 55, 60, and 79. Each figure presents the raw data points with error bars representing the 95% confidence interval and a linear fit for each gas used to determine the discharge coefficient  $C_d$ . The values for these discharge coefficients are given in the legends of each plot.

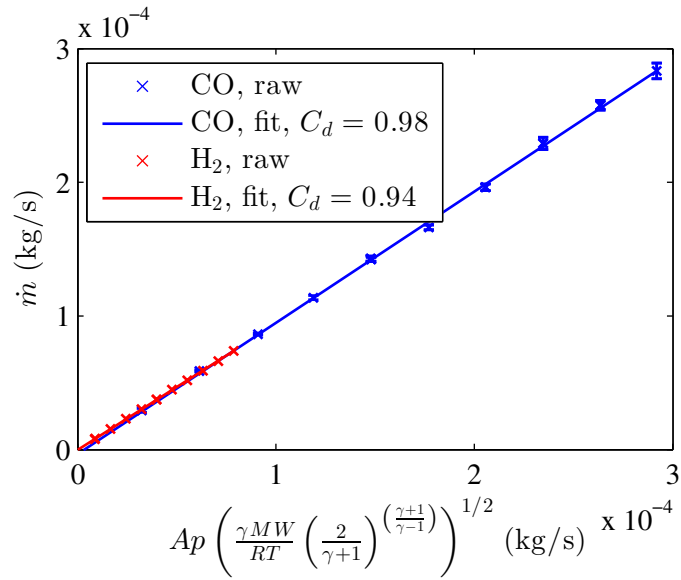


**Figure 86:** Measured mass flow rate as a function of theoretical mass flow rate calculated using measured pressure and temperature as inputs in Equation 47 for an orifice diameter of  $d = 0.006$  in.

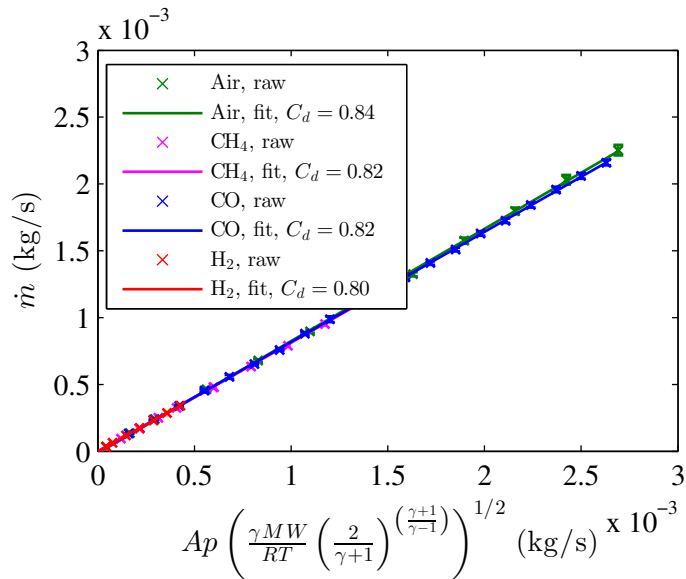


**Figure 87:** Measured mass flow rate as a function of theoretical mass flow rate calculated using measured pressure and temperature as inputs in Equation 47 for an orifice diameter of  $d = 0.018$  in.

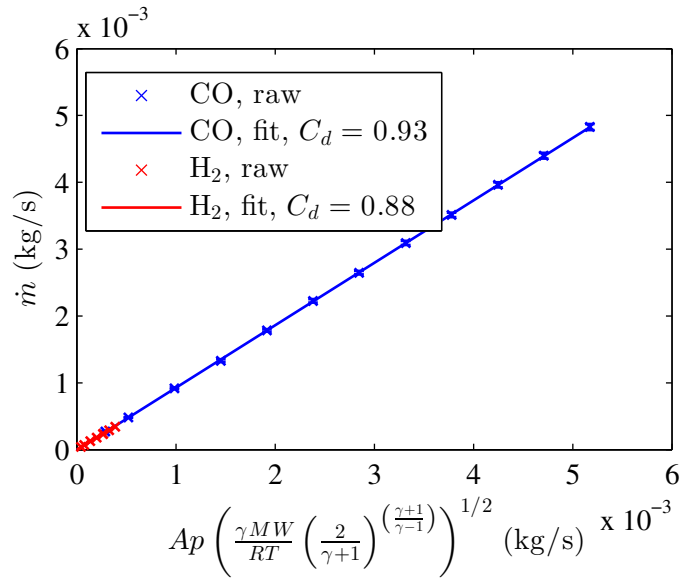


**Figure 88:** Measured mass flow rate as a function of theoretical mass flow rate calculated using measured pressure and temperature as inputs in Equation 47 for an orifice diameter of  $d = 0.024$  in.

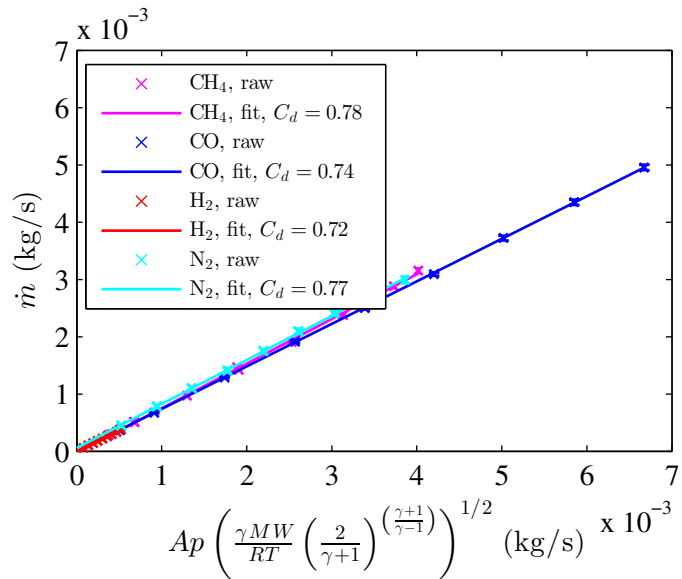


**Figure 89:** Measured mass flow rate as a function of theoretical mass flow rate calculated using measured pressure and temperature as inputs in Equation 47 for an orifice diameter of  $d = 0.032$  in.

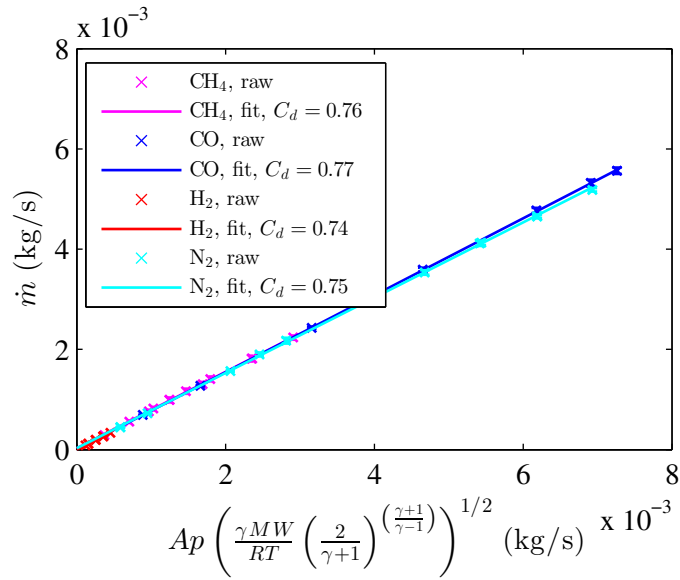


**Figure 90:** Measured mass flow rate as a function of theoretical mass flow rate calculated using measured pressure and temperature as inputs in Equation 47 for an orifice diameter of  $d = 0.043$  in.

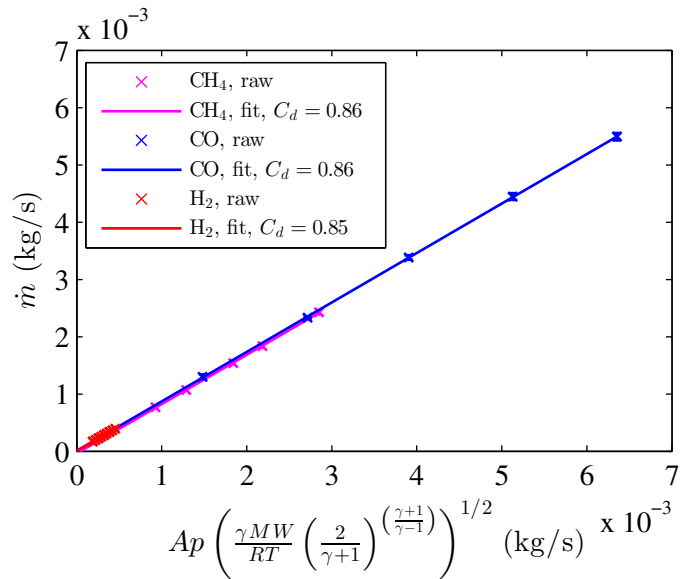


**Figure 91:** Measured mass flow rate as a function of theoretical mass flow rate calculated using measured pressure and temperature as inputs in Equation 47 for an orifice diameter of  $d = 0.055$  in.

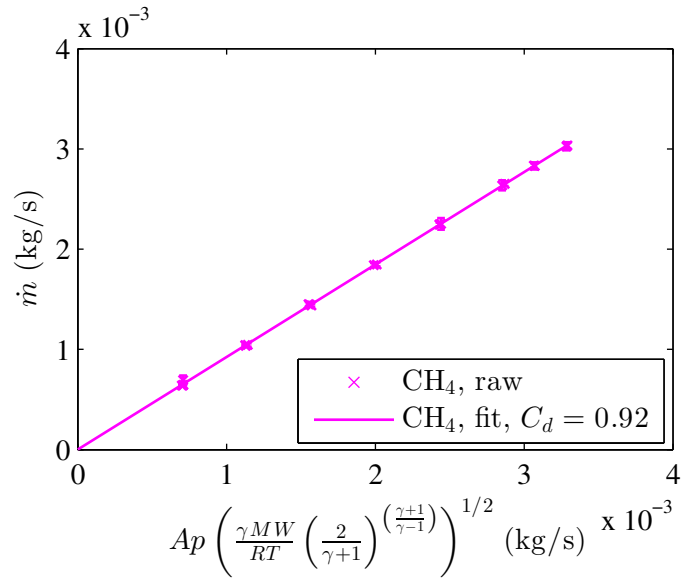


**Figure 92:** Measured mass flow rate as a function of theoretical mass flow rate calculated using measured pressure and temperature as inputs in Equation 47 for an orifice diameter of  $d = 0.060$  in.

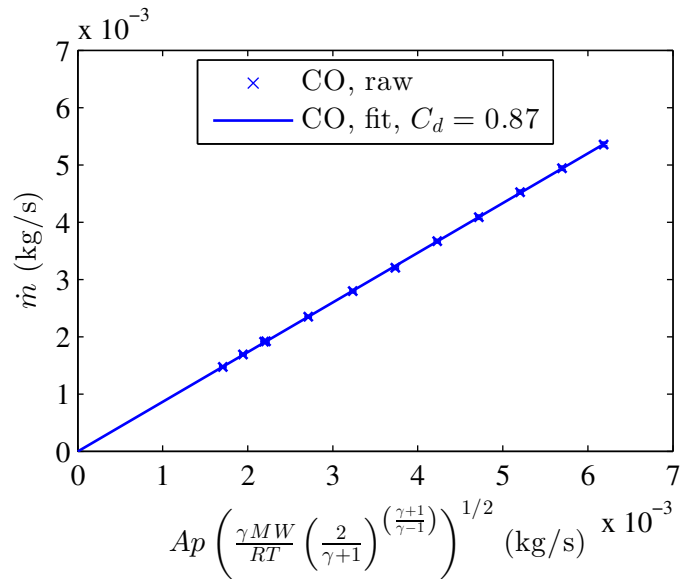


**Figure 93:** Measured mass flow rate as a function of theoretical mass flow rate calculated using measured pressure and temperature as inputs in Equation 47 for an orifice diameter of  $d = 0.079$  in.

## APPENDIX B

### FLOW FIELD DATA

This appendix presents an expanded flow field dataset compared to the overview presented in Chapter 3. The sections are organized in a manner similar to Chapter 3.

#### *B.1 12 mm Burner*

##### **B.1.1 1 atm**

This section presents mean and RMS velocity profiles for the 12 mm burner at a pressure of 1 atm.

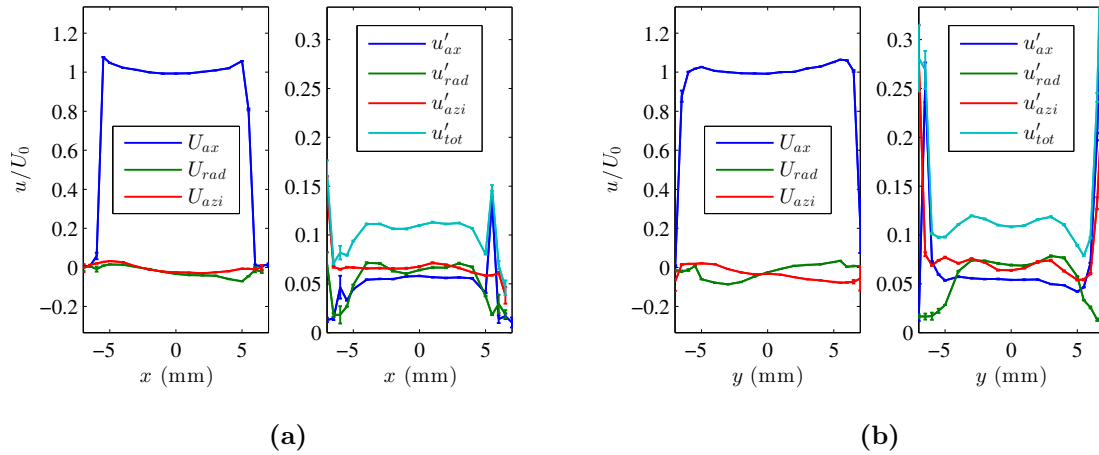


**Figure 94:** Mean and RMS velocity profiles for the 12 mm burner at  $p = 1$  atm,  $T = 300$  K,  $U_0 = 30$  m/s,  $BR = 69\%$  for the (a)  $x$  and (b)  $y$  traverses.

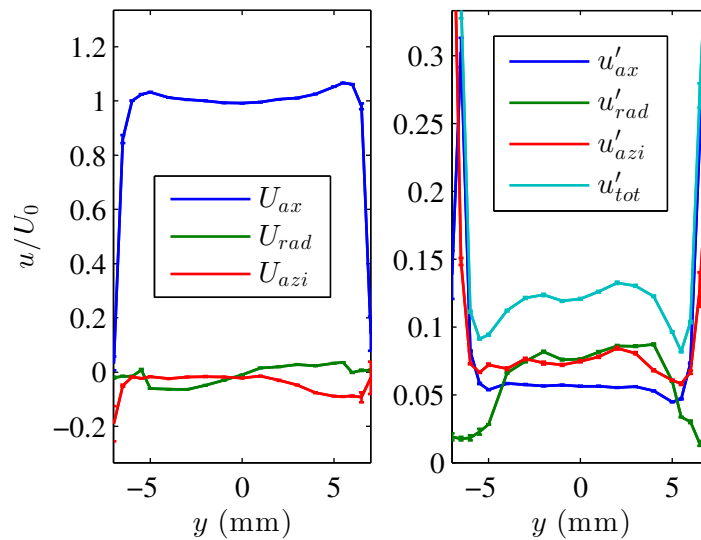


**Figure 95:** Mean and RMS velocity profiles for the 12 mm burner at  $p = 1$  atm,  $T = 300$  K,  $U_0 = 30$  m/s,  $BR = 73\%$ .

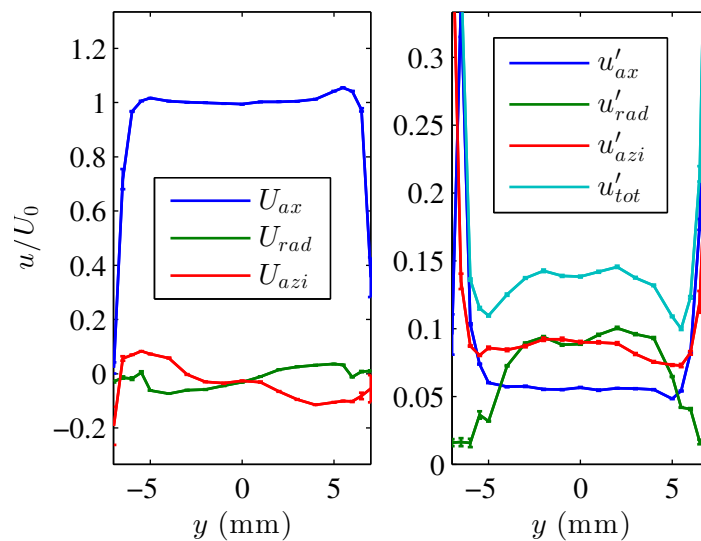


**Figure 96:** Mean and RMS velocity profiles for the 12 mm burner at  $p = 1$  atm,  $T = 300$  K,  $U_0 = 30$  m/s,  $BR = 77\%$ .

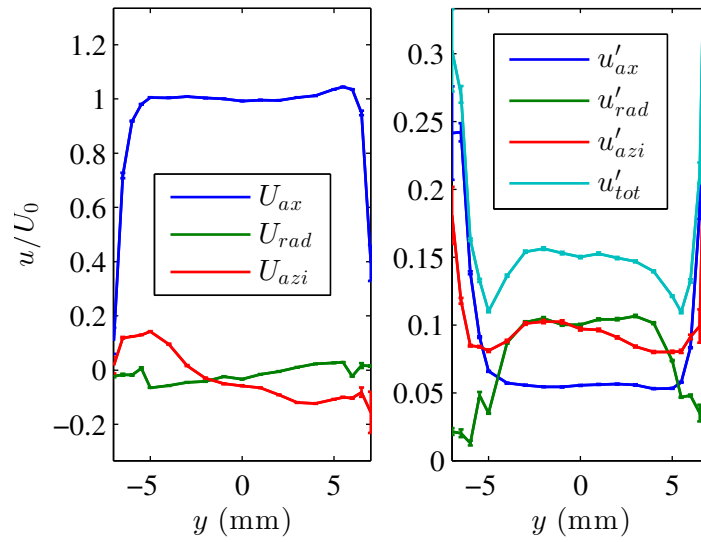


**Figure 97:** Mean and RMS velocity profiles for the 12 mm burner at  $p = 1$  atm,  $T = 300$  K,  $U_0 = 30$  m/s,  $BR = 81\%$ .

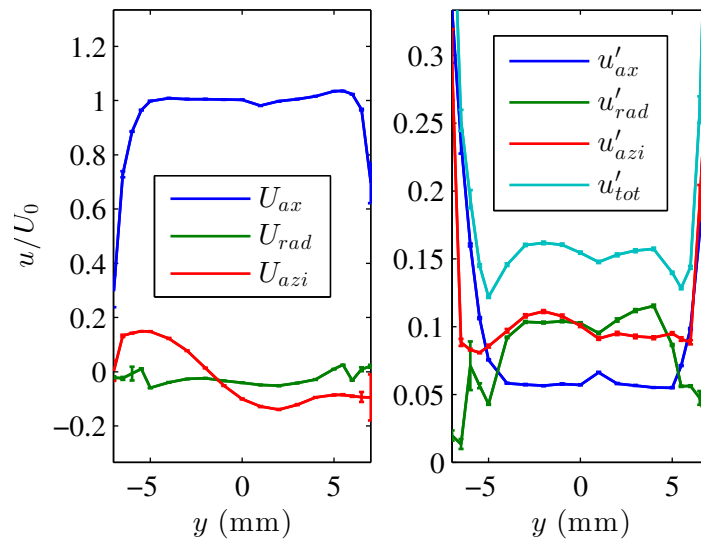


**Figure 98:** Mean and RMS velocity profiles for the 12 mm burner at  $p = 1$  atm,  $T = 300$  K,  $U_0 = 30$  m/s,  $BR = 85\%$ .

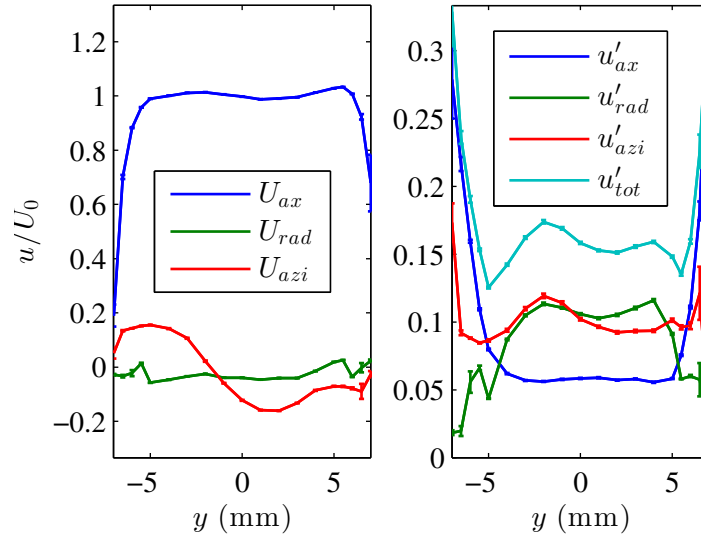


**Figure 99:** Mean and RMS velocity profiles for the 12 mm burner at  $p = 1$  atm,  $T = 300$  K,  $U_0 = 30$  m/s,  $BR = 87\%$ .

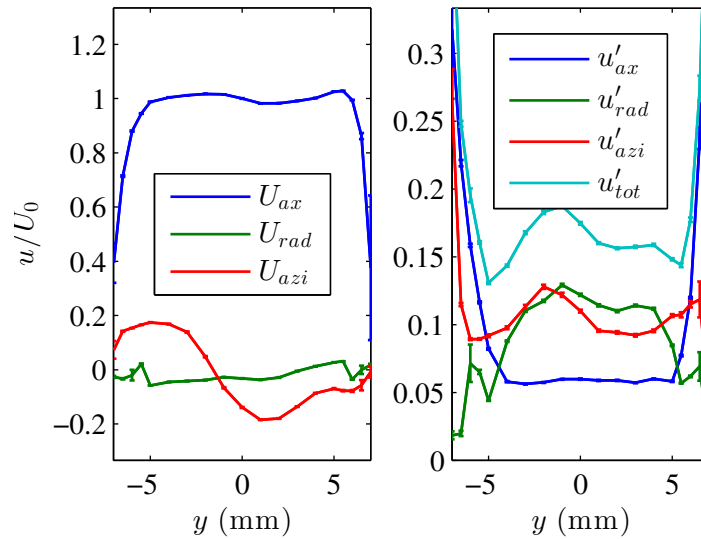


**Figure 100:** Mean and RMS velocity profiles for the 12 mm burner at  $p = 1$  atm,  $T = 300$  K,  $U_0 = 30$  m/s,  $BR = 89\%$ .

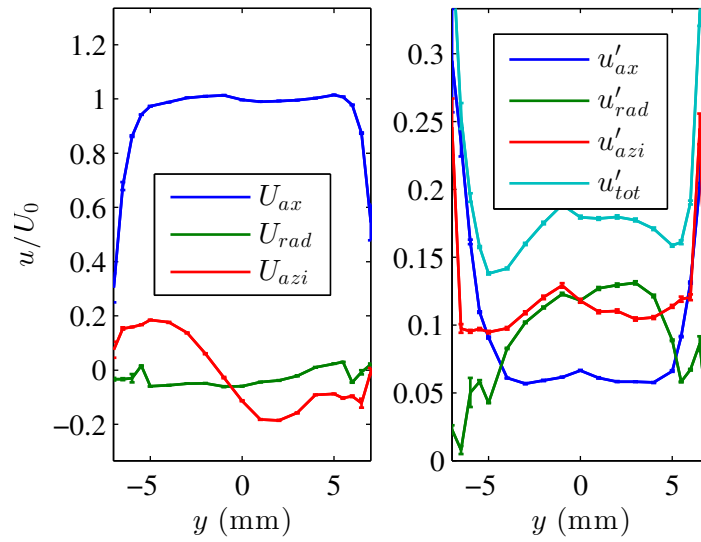


**Figure 101:** Mean and RMS velocity profiles for the 12 mm burner at  $p = 1$  atm,  $T = 300$  K,  $U_0 = 30$  m/s,  $BR = 91\%$ .

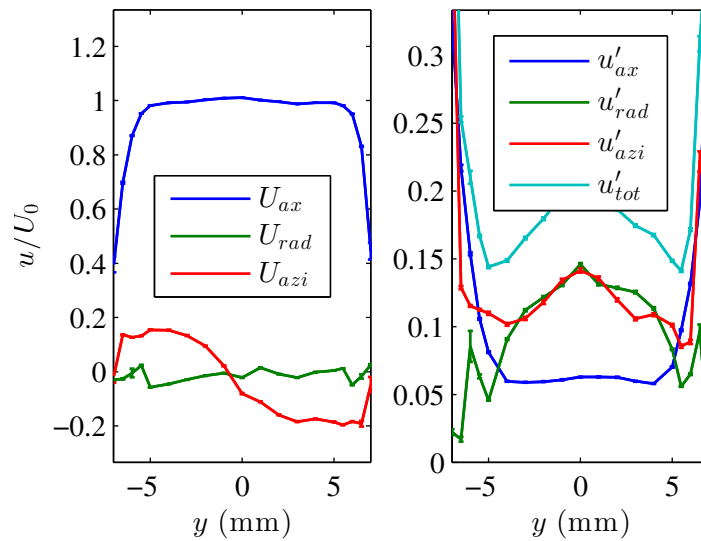


**Figure 102:** Mean and RMS velocity profiles for the 12 mm burner at  $p = 1$  atm,  $T = 300$  K,  $U_0 = 30$  m/s,  $BR = 93\%$ .

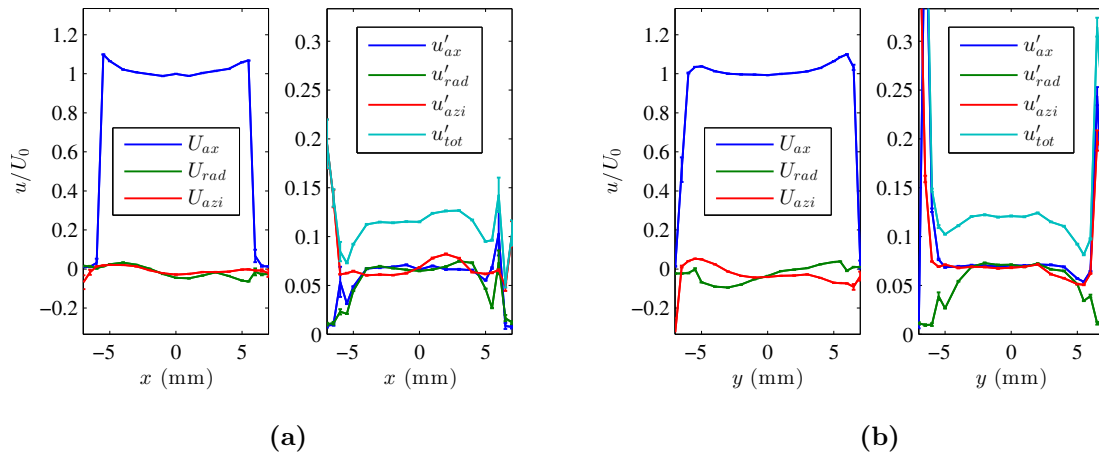


**Figure 103:** Mean and RMS velocity profiles for the 12 mm burner at  $p = 1$  atm,  $T = 300$  K,  $U_0 = 50$  m/s,  $BR = 69\%$  for the (a)  $x$  and (b)  $y$  traverses.

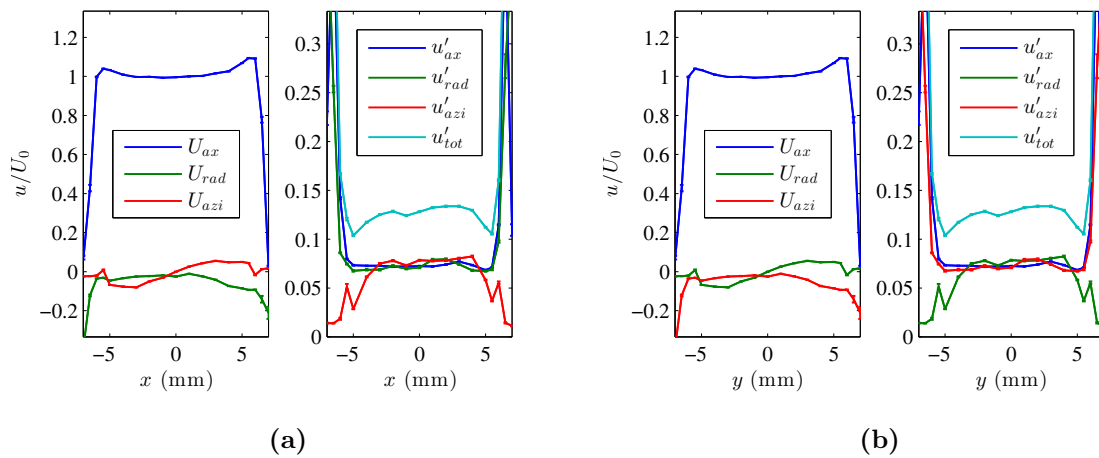


**Figure 104:** Mean and RMS velocity profiles for the 12 mm burner at  $p = 1$  atm,  $T = 300$  K,  $U_0 = 50$  m/s,  $BR = 73\%$  for the (a)  $x$  and (b)  $y$  traverses.

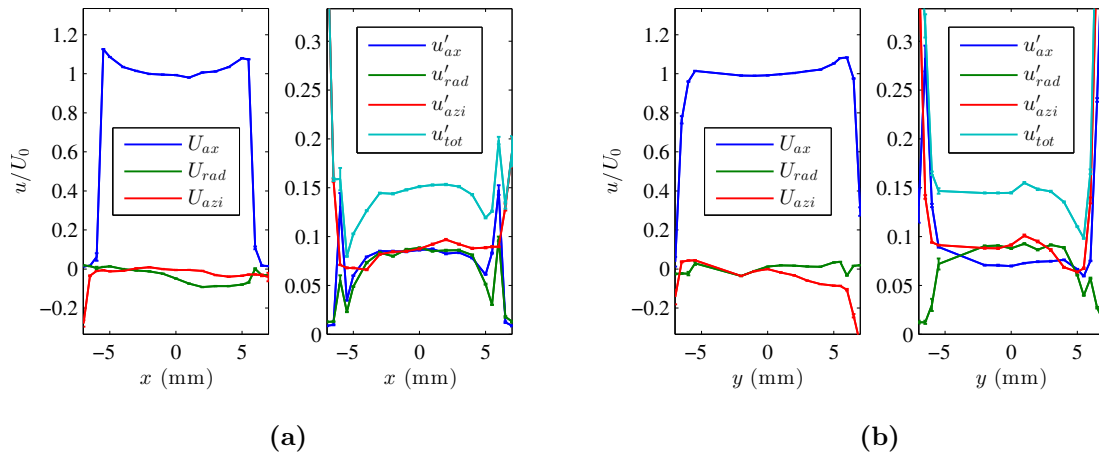


**Figure 105:** Mean and RMS velocity profiles for the 12 mm burner at  $p = 1$  atm,  $T = 300$  K,  $U_0 = 50$  m/s,  $BR = 77\%$  for the (a)  $x$  and (b)  $y$  traverses.

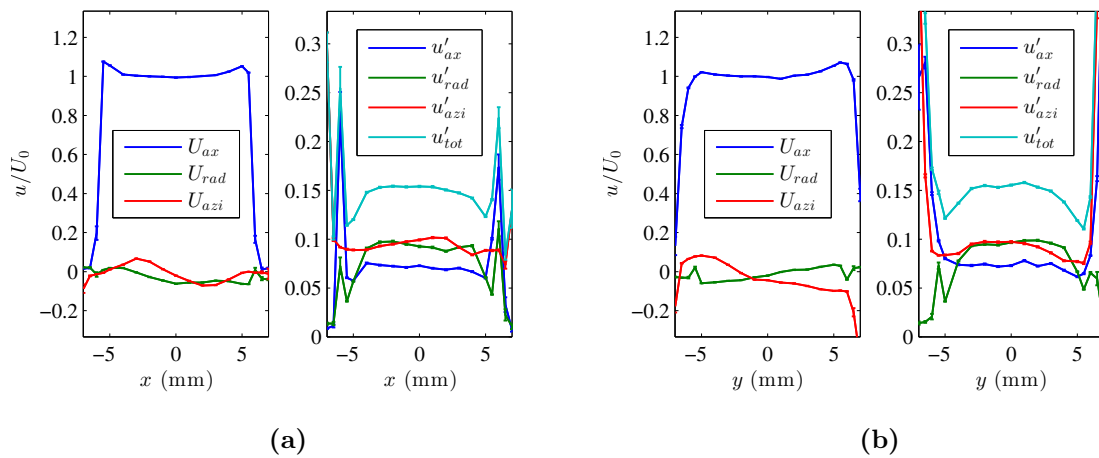


**Figure 106:** Mean and RMS velocity profiles for the 12 mm burner at  $p = 1$  atm,  $T = 300$  K,  $U_0 = 50$  m/s,  $BR = 81\%$  for the (a)  $x$  and (b)  $y$  traverses.

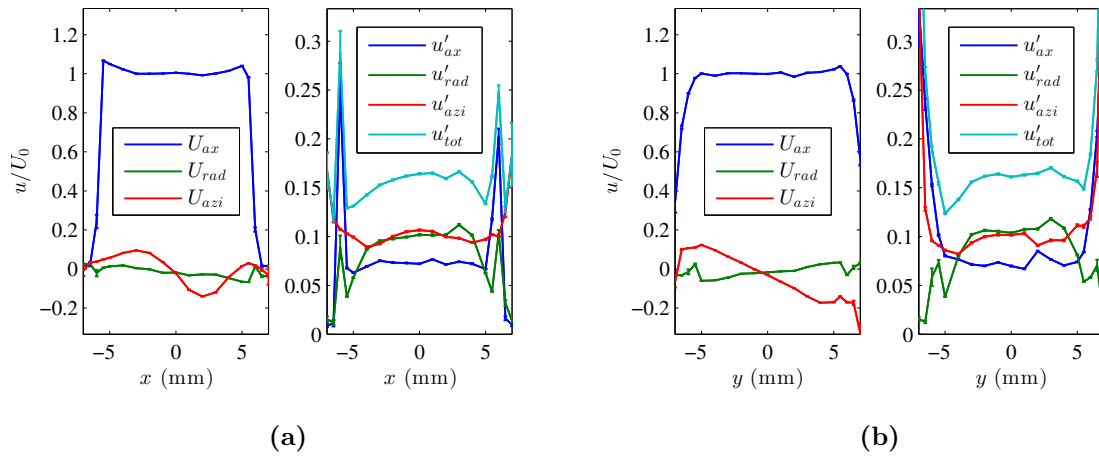


**Figure 107:** Mean and RMS velocity profiles for the 12 mm burner at  $p = 1$  atm,  $T = 300$  K,  $U_0 = 50$  m/s,  $BR = 85\%$  for the (a)  $x$  and (b)  $y$  traverses.

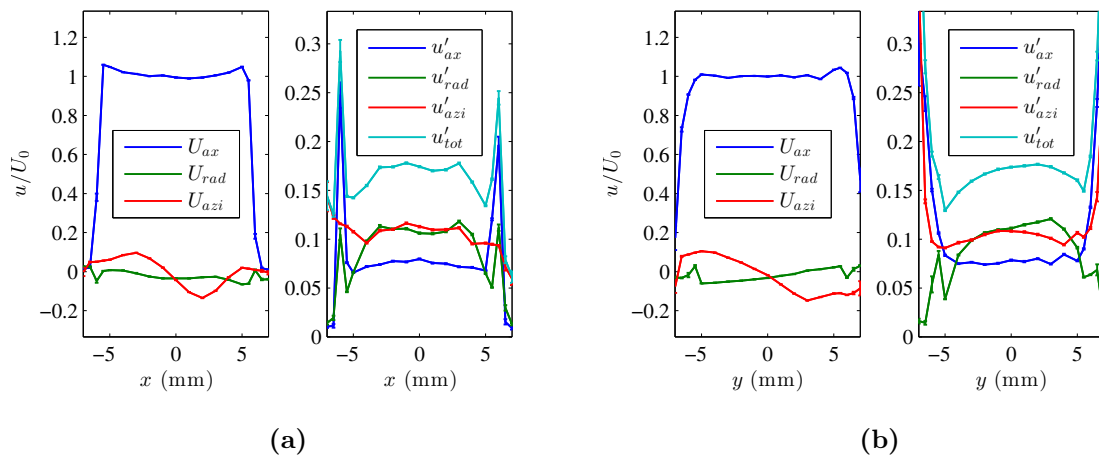


**Figure 108:** Mean and RMS velocity profiles for the 12 mm burner at  $p = 1$  atm,  $T = 300$  K,  $U_0 = 50$  m/s,  $BR = 87\%$  for the (a)  $x$  and (b)  $y$  traverses.

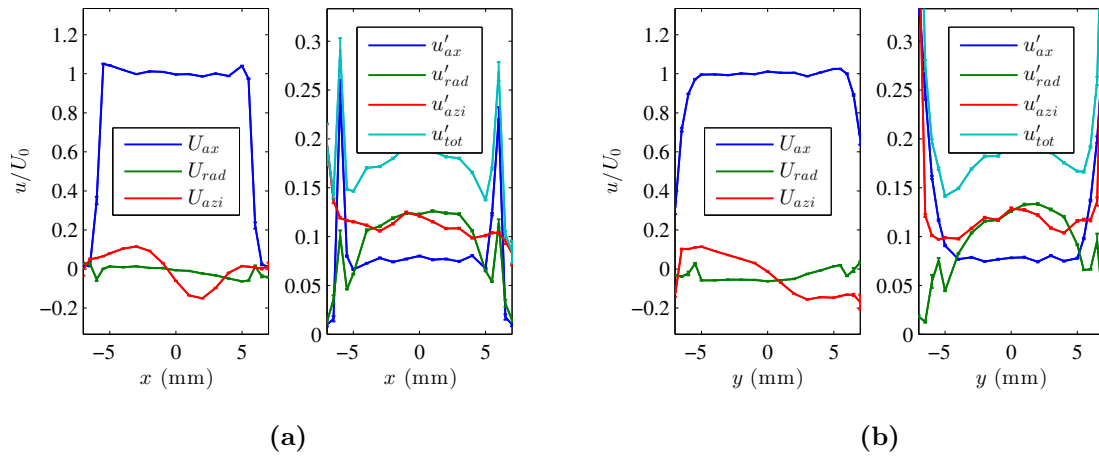


**Figure 109:** Mean and RMS velocity profiles for the 12 mm burner at  $p = 1$  atm,  $T = 300$  K,  $U_0 = 50$  m/s,  $BR = 89\%$  for the (a)  $x$  and (b)  $y$  traverses.

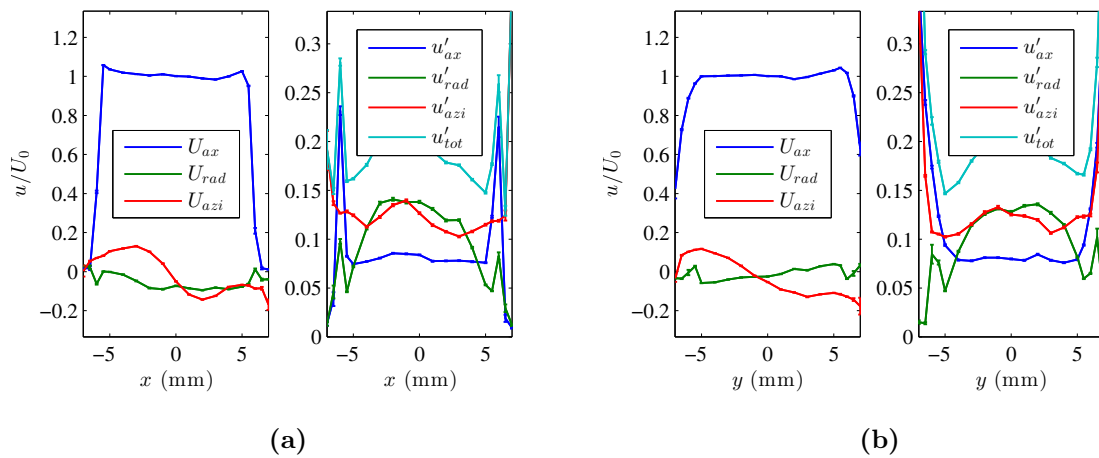


**Figure 110:** Mean and RMS velocity profiles for the 12 mm burner at  $p = 1$  atm,  $T = 300$  K,  $U_0 = 50$  m/s,  $BR = 91\%$  for the (a)  $x$  and (b)  $y$  traverses.

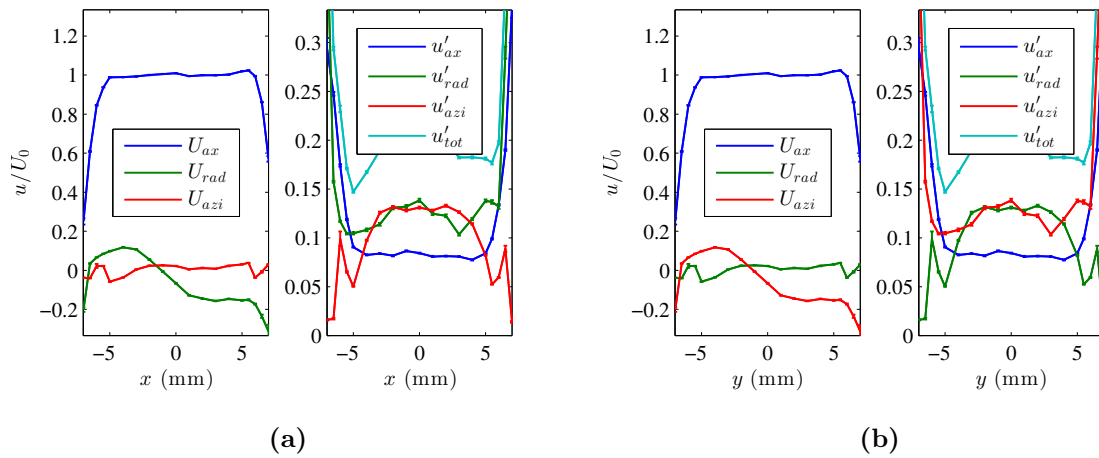


**Figure 111:** Mean and RMS velocity profiles for the 12 mm burner at  $p = 1$  atm,  $T = 300$  K,  $U_0 = 50$  m/s,  $BR = 93\%$  for the (a)  $x$  and (b)  $y$  traverses.

### B.1.2 5 atm

This section presents mean and RMS velocity profiles for the 12 mm burner at a pressure of 5 atm.

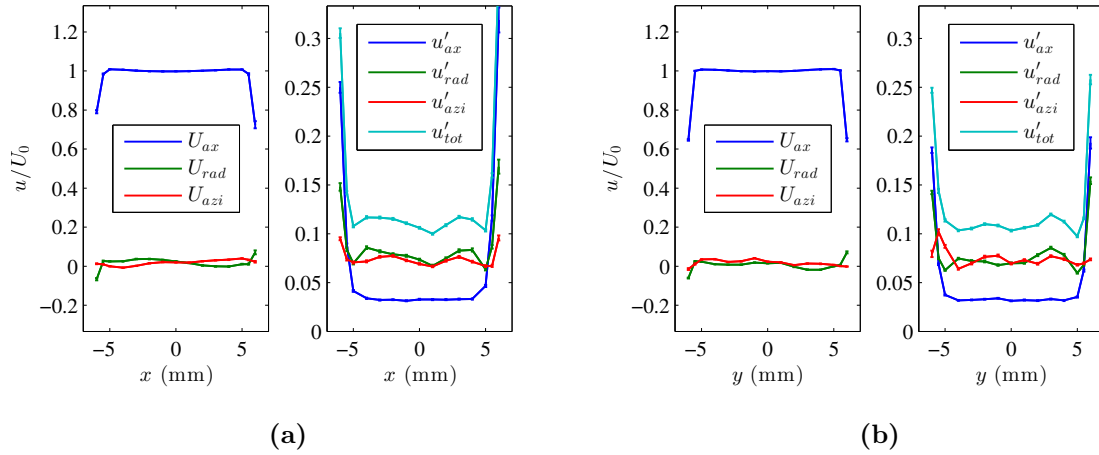


**Figure 112:** Mean and RMS velocity profiles for the 12 mm burner at  $p = 5$  atm,  $T = 300$  K,  $U_0 = 10$  m/s,  $BR = 69\%$  for the (a)  $x$  and (b)  $y$  traverses.

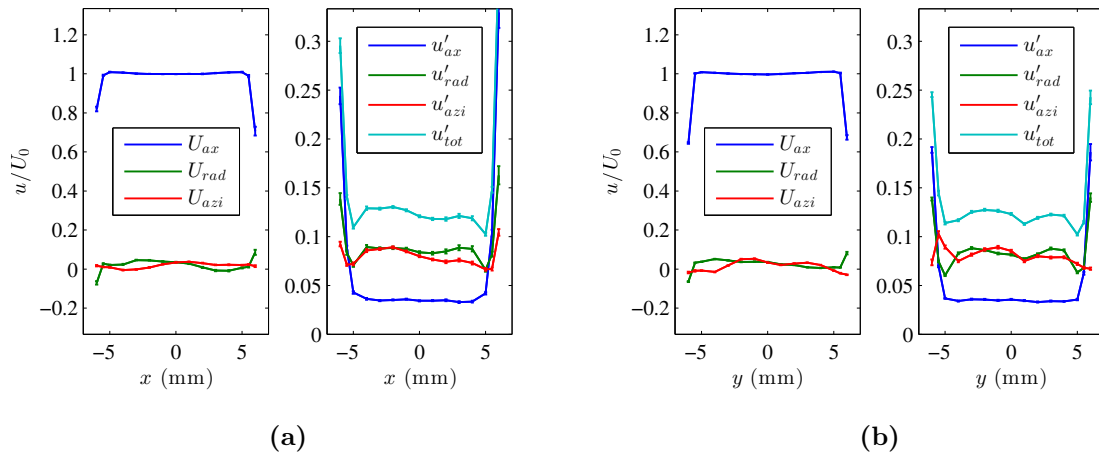


**Figure 113:** Mean and RMS velocity profiles for the 12 mm burner at  $p = 5$  atm,  $T = 300$  K,  $U_0 = 10$  m/s,  $BR = 75\%$  for the (a)  $x$  and (b)  $y$  traverses.

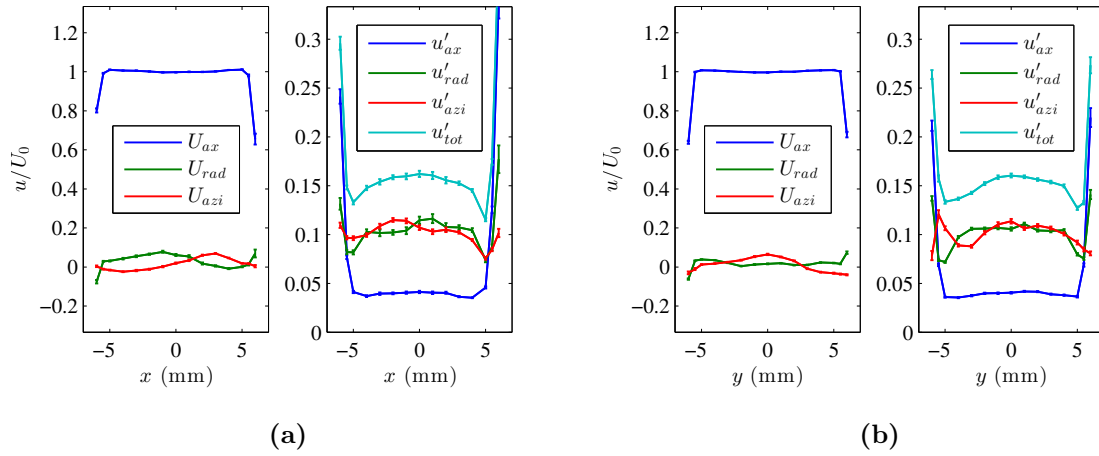


**Figure 114:** Mean and RMS velocity profiles for the 12 mm burner at  $p = 5$  atm,  $T = 300$  K,  $U_0 = 10$  m/s,  $BR = 81\%$  for the (a)  $x$  and (b)  $y$  traverses.

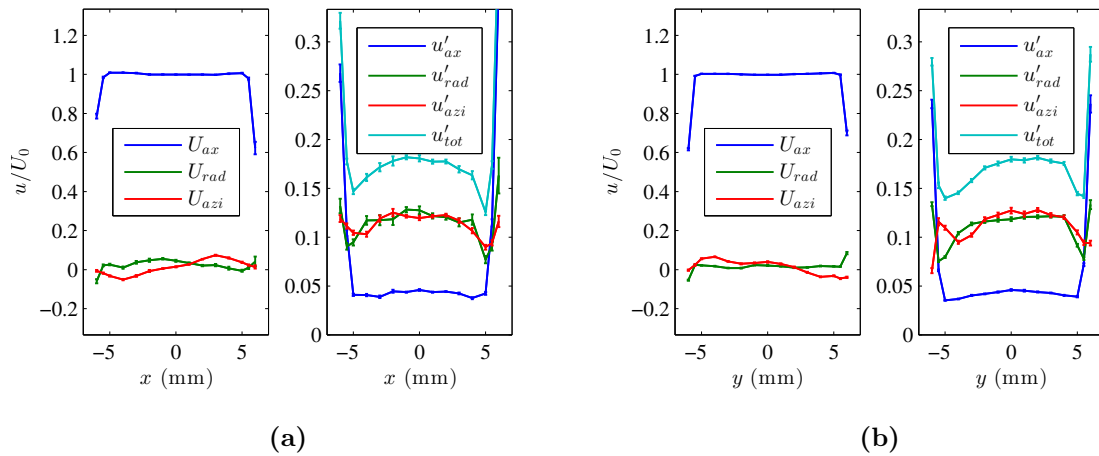


**Figure 115:** Mean and RMS velocity profiles for the 12 mm burner at  $p = 5$  atm,  $T = 300$  K,  $U_0 = 10$  m/s,  $BR = 87\%$  for the (a)  $x$  and (b)  $y$  traverses.

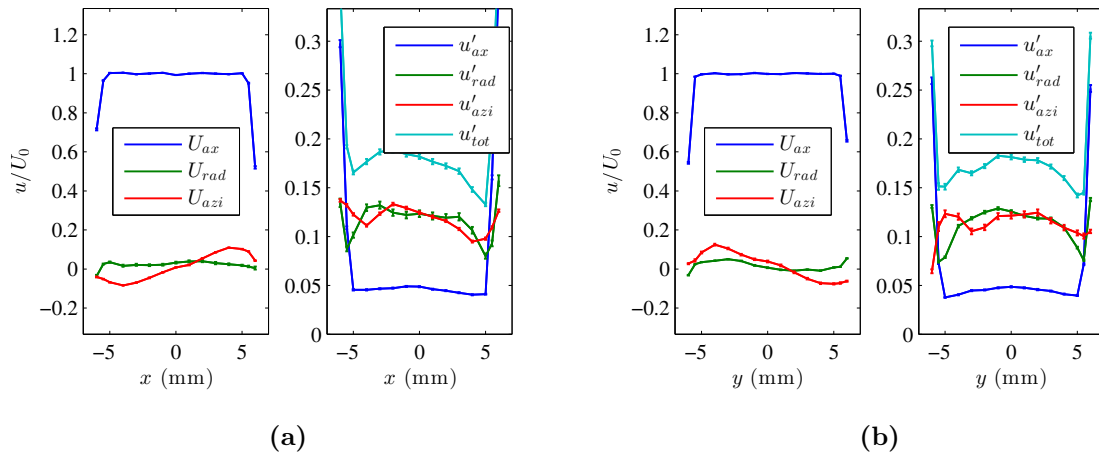


**Figure 116:** Mean and RMS velocity profiles for the 12 mm burner at  $p = 5$  atm,  $T = 300$  K,  $U_0 = 10$  m/s,  $BR = 93\%$  for the (a)  $x$  and (b)  $y$  traverses.

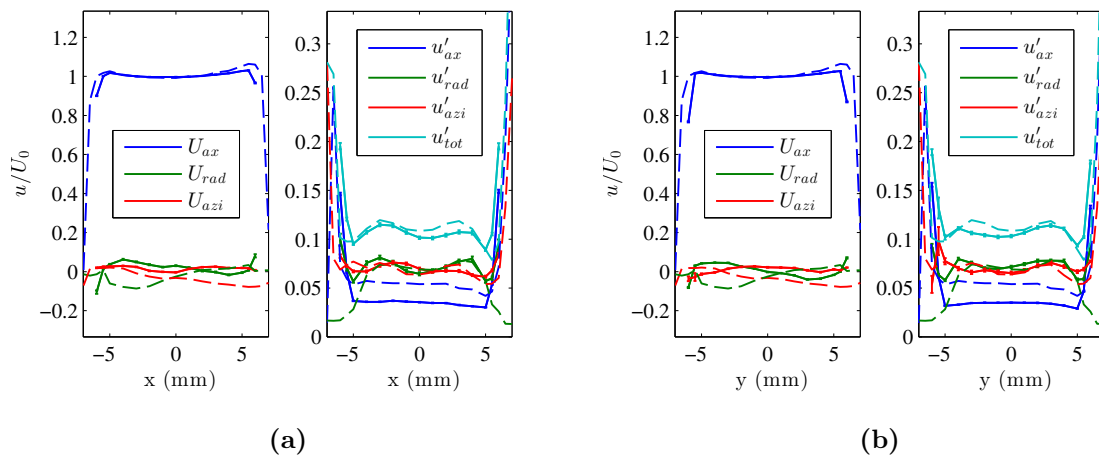


**Figure 117:** Mean and RMS velocity profiles for the 12 mm burner at  $p = 5$  atm,  $T = 300$  K,  $U_0 = 30$  m/s,  $BR = 69\%$  for the (a)  $x$  and (b)  $y$  traverses.

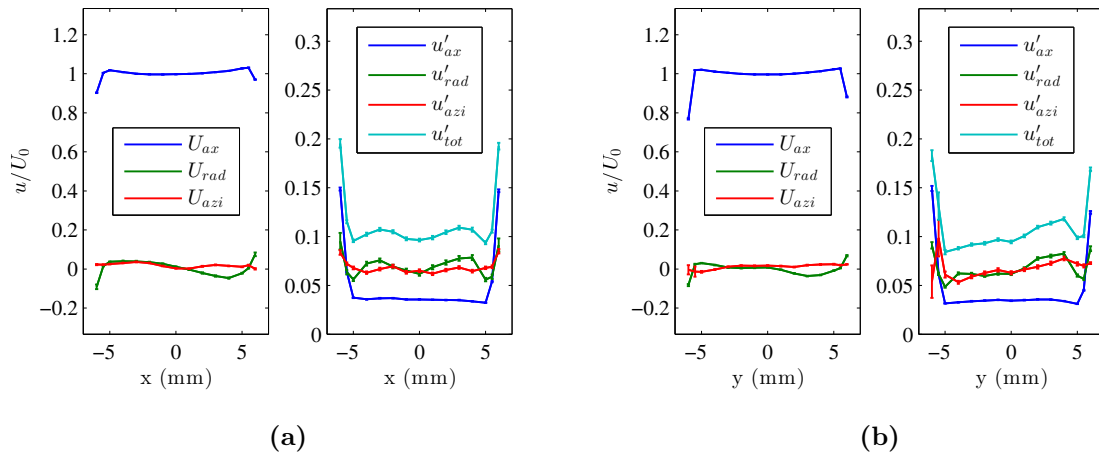


**Figure 118:** Mean and RMS velocity profiles for the 12 mm burner at  $p = 5$  atm,  $T = 300$  K,  $U_0 = 30$  m/s,  $BR = 75\%$  for the (a)  $x$  and (b)  $y$  traverses.

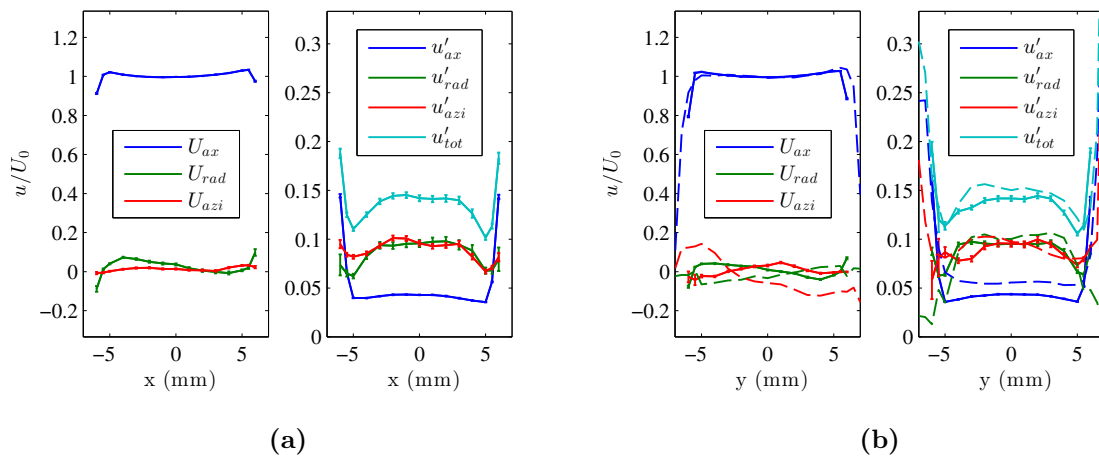


**Figure 119:** Mean and RMS velocity profiles for the 12 mm burner at  $p = 5$  atm,  $T = 300$  K,  $U_0 = 30$  m/s,  $BR = 81\%$  for the (a)  $x$  and (b)  $y$  traverses.

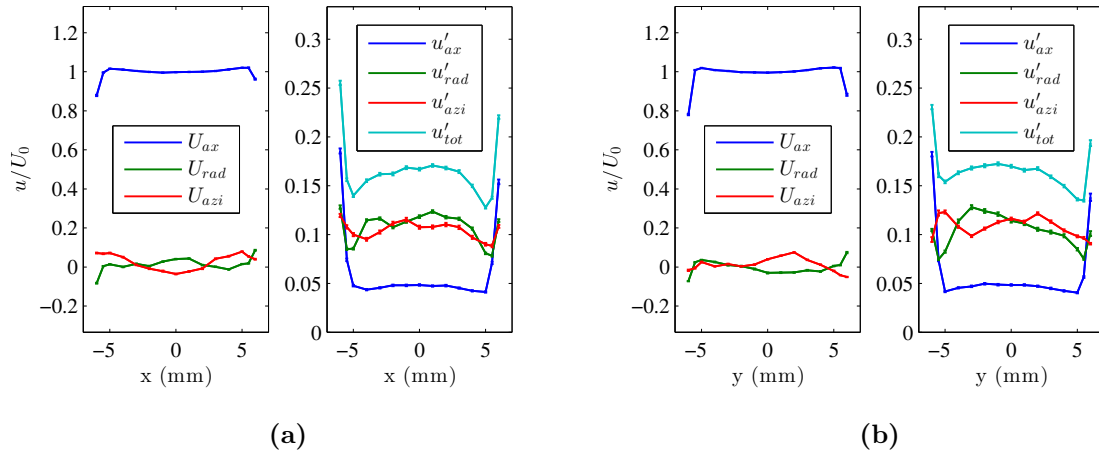


**Figure 120:** Mean and RMS velocity profiles for the 12 mm burner at  $p = 5$  atm,  $T = 300$  K,  $U_0 = 30$  m/s,  $BR = 87\%$  for the (a)  $x$  and (b)  $y$  traverses.

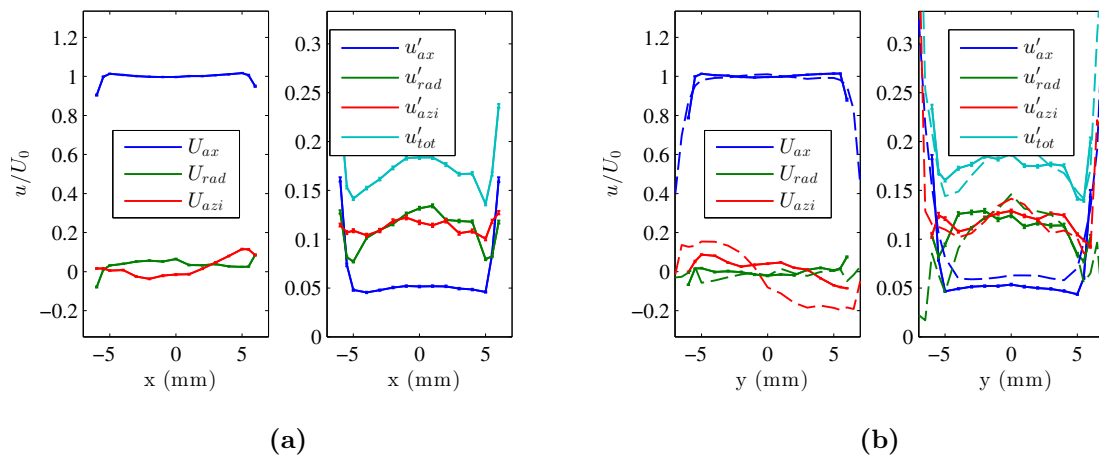


**Figure 121:** Mean and RMS velocity profiles for the 12 mm burner at  $p = 5$  atm,  $T = 300$  K,  $U_0 = 30$  m/s,  $BR = 93\%$  for the (a)  $x$  and (b)  $y$  traverses.

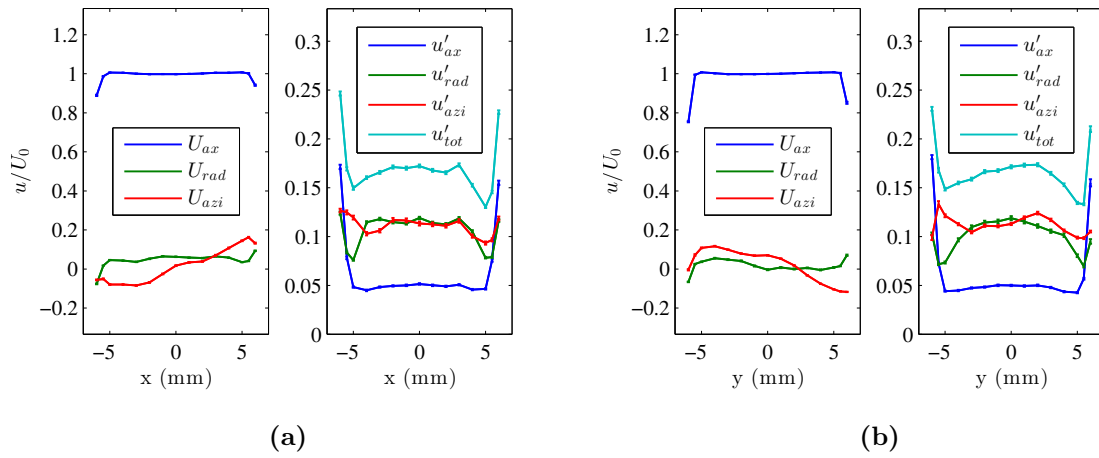


**Figure 122:** Mean and RMS velocity profiles for the 12 mm burner at  $p = 5$  atm,  $T = 300$  K,  $U_0 = 30$  m/s,  $BR = 95\%$  for the (a)  $x$  and (b)  $y$  traverses.

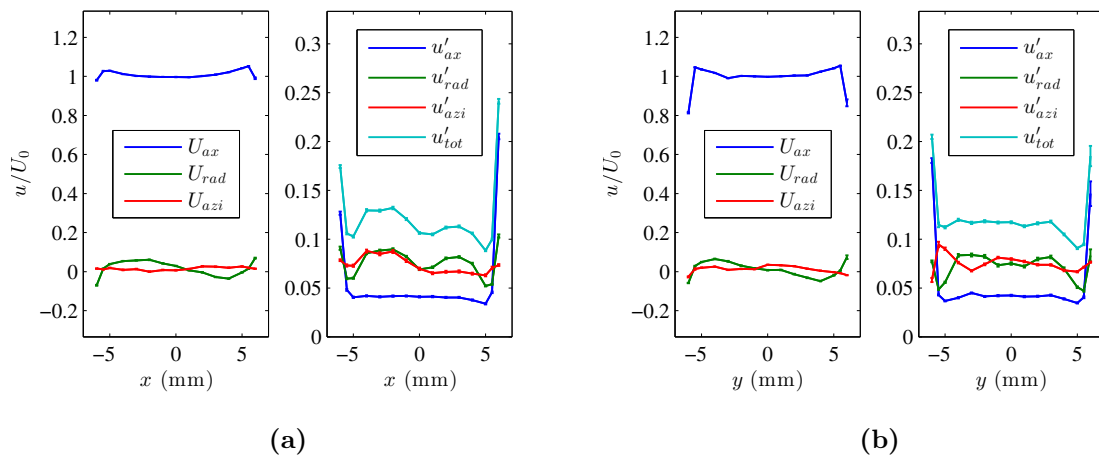


**Figure 123:** Mean and RMS velocity profiles for the 12 mm burner at  $p = 5$  atm,  $T = 300$  K,  $U_0 = 50$  m/s,  $BR = 69\%$  for the (a)  $x$  and (b)  $y$  traverses.

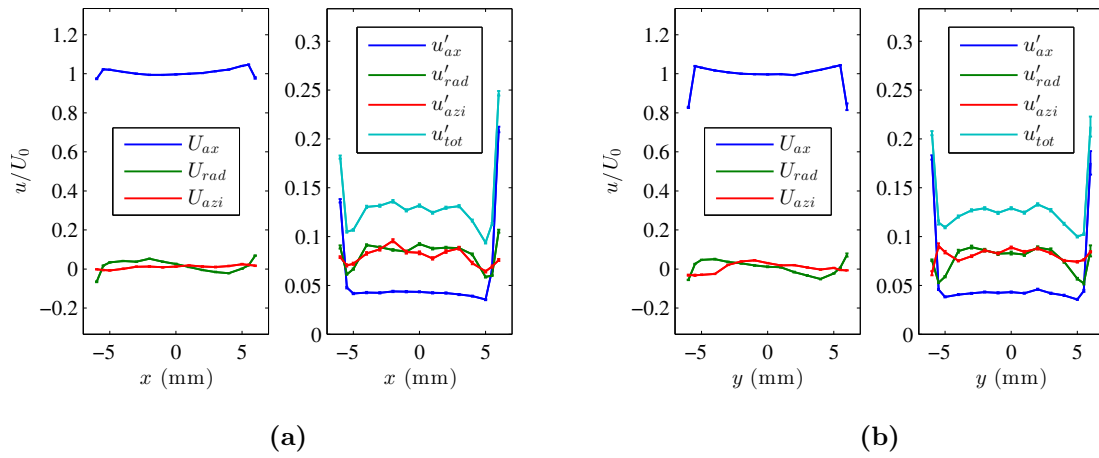


**Figure 124:** Mean and RMS velocity profiles for the 12 mm burner at  $p = 5$  atm,  $T = 300$  K,  $U_0 = 50$  m/s,  $BR = 75\%$  for the (a)  $x$  and (b)  $y$  traverses.

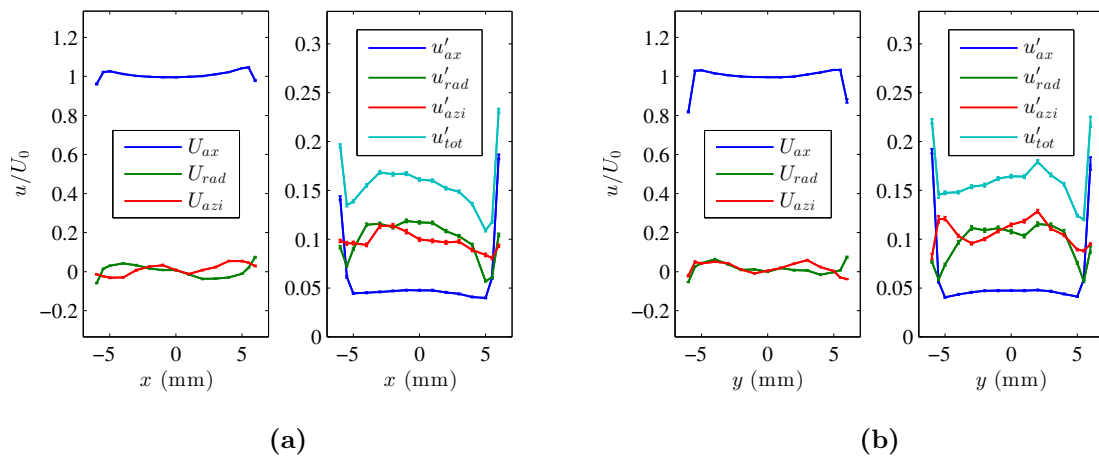


**Figure 125:** Mean and RMS velocity profiles for the 12 mm burner at  $p = 5$  atm,  $T = 300$  K,  $U_0 = 50$  m/s,  $BR = 81\%$  for the (a)  $x$  and (b)  $y$  traverses.

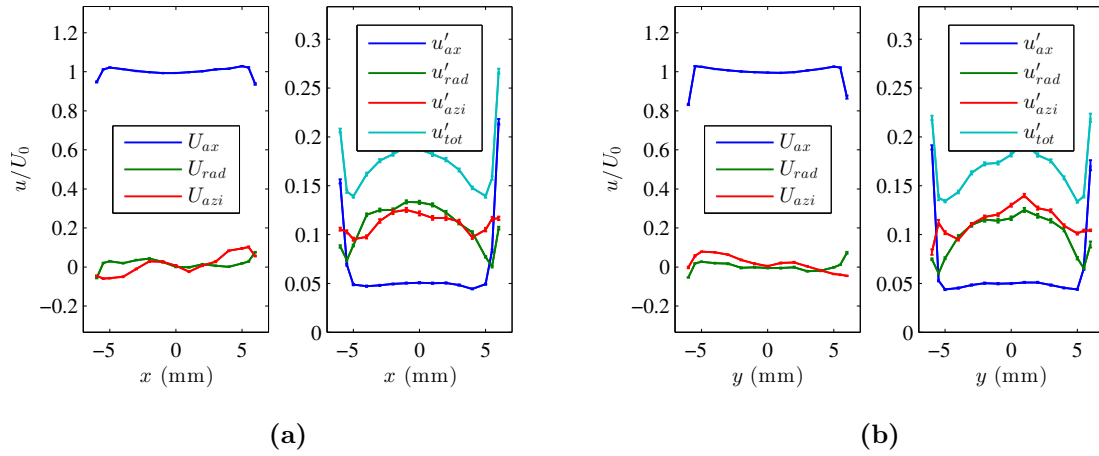


**Figure 126:** Mean and RMS velocity profiles for the 12 mm burner at  $p = 5$  atm,  $T = 300$  K,  $U_0 = 50$  m/s,  $BR = 87\%$  for the (a)  $x$  and (b)  $y$  traverses.

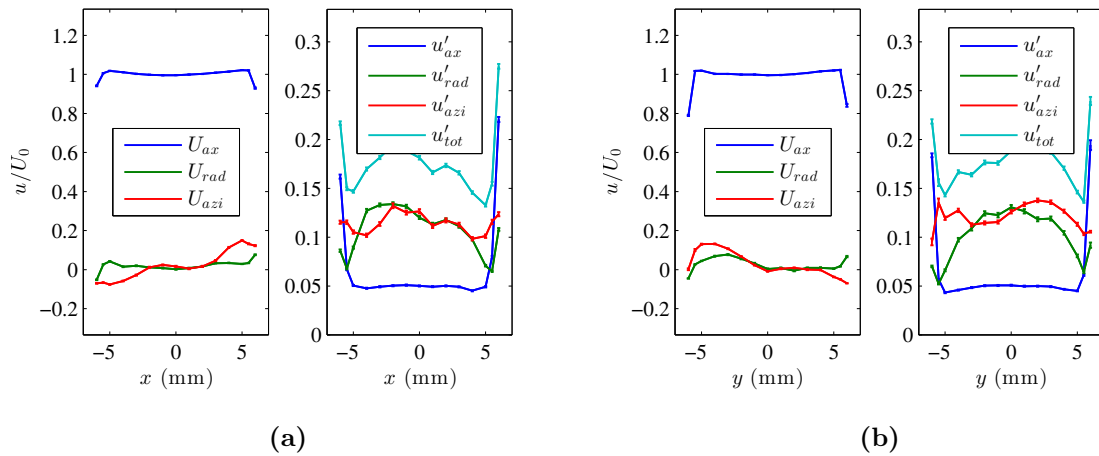


**Figure 127:** Mean and RMS velocity profiles for the 12 mm burner at  $p = 5$  atm,  $T = 300$  K,  $U_0 = 50$  m/s,  $BR = 93\%$  for the (a)  $x$  and (b)  $y$  traverses.

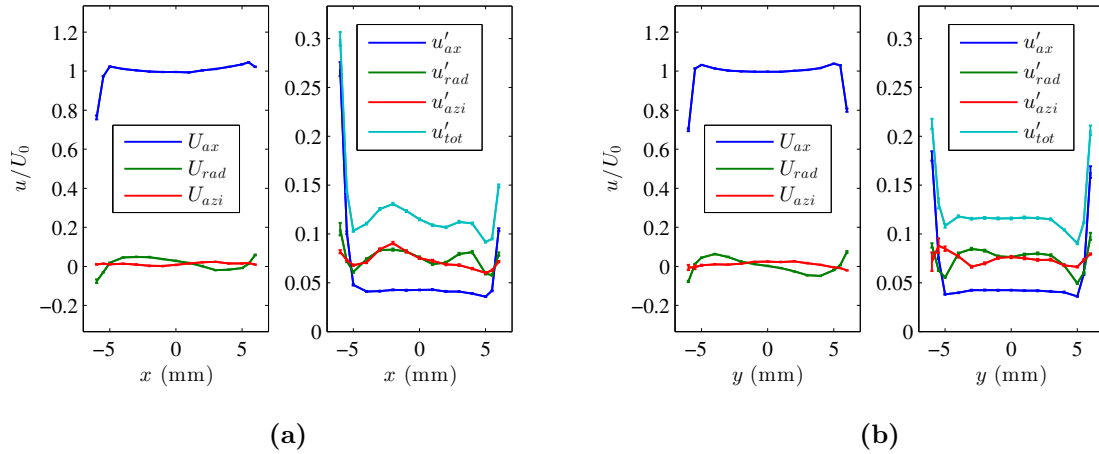


**Figure 128:** Mean and RMS velocity profiles for the 12 mm burner at  $p = 5$  atm,  $T = 427$  K,  $U_0 = 50$  m/s,  $BR = 69\%$  for the (a)  $x$  and (b)  $y$  traverses.

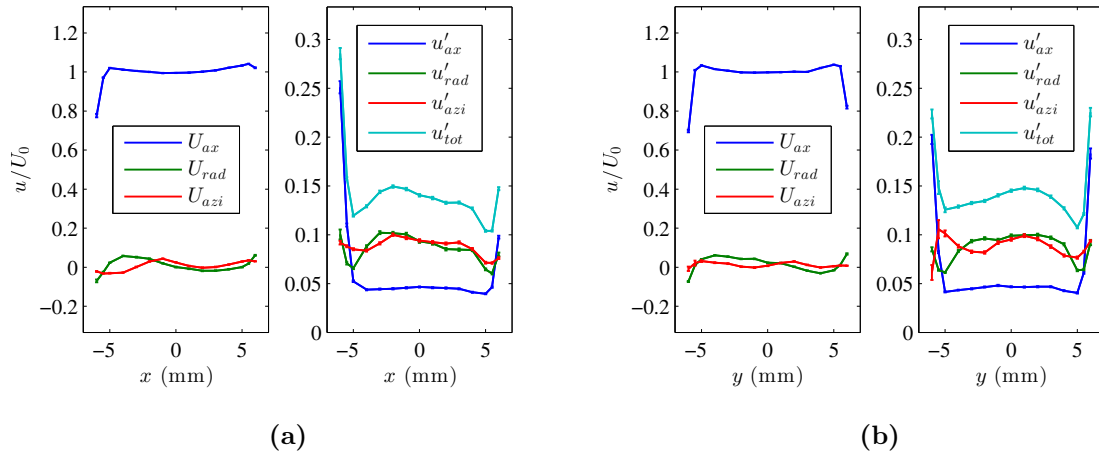


**Figure 129:** Mean and RMS velocity profiles for the 12 mm burner at  $p = 5$  atm,  $T = 427$  K,  $U_0 = 50$  m/s,  $BR = 81\%$  for the (a)  $x$  and (b)  $y$  traverses.

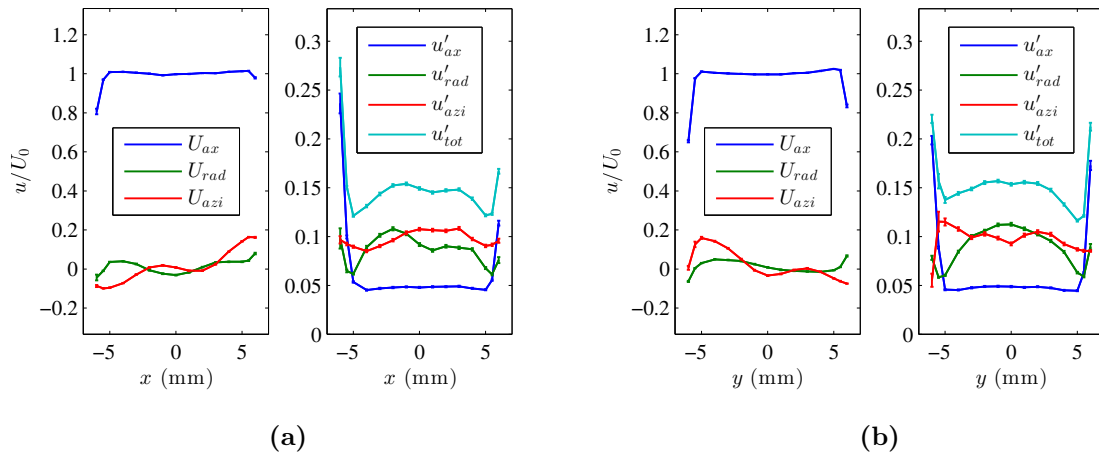


**Figure 130:** Mean and RMS velocity profiles for the 12 mm burner at  $p = 5$  atm,  $T = 427$  K,  $U_0 = 50$  m/s,  $BR = 93\%$  for the (a)  $x$  and (b)  $y$  traverses.

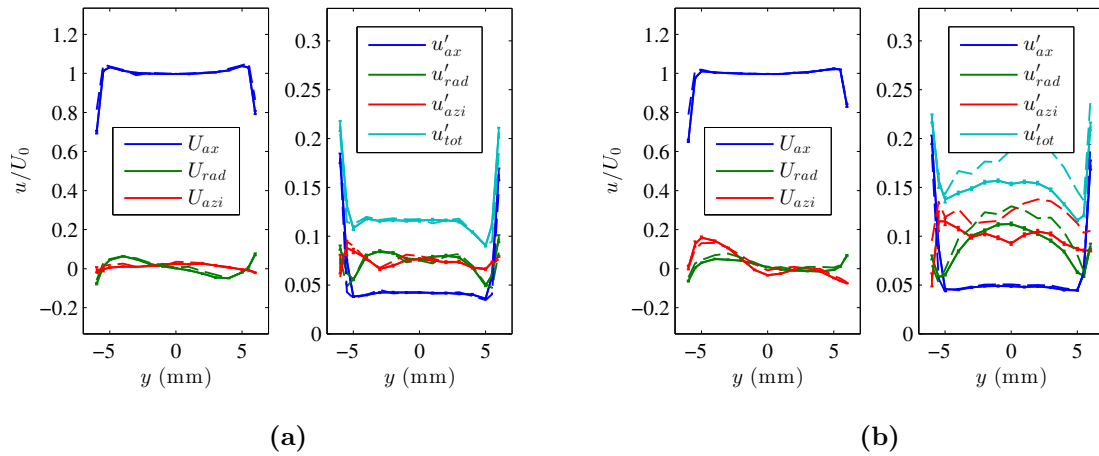


**Figure 131:** Mean and RMS velocity profiles for the 12 mm burner at  $p = 5$  atm,  $U_0 = 50$  m/s, for  $T = 427$  K (solid lines) and  $T = 300$  K (dashed lines) at (a)  $BR = 69\%$  and (b)  $BR = 93\%$ .

### B.1.3 10 atm

This section presents mean and RMS velocity profiles for the 12 mm burner at a pressure of 10 atm.

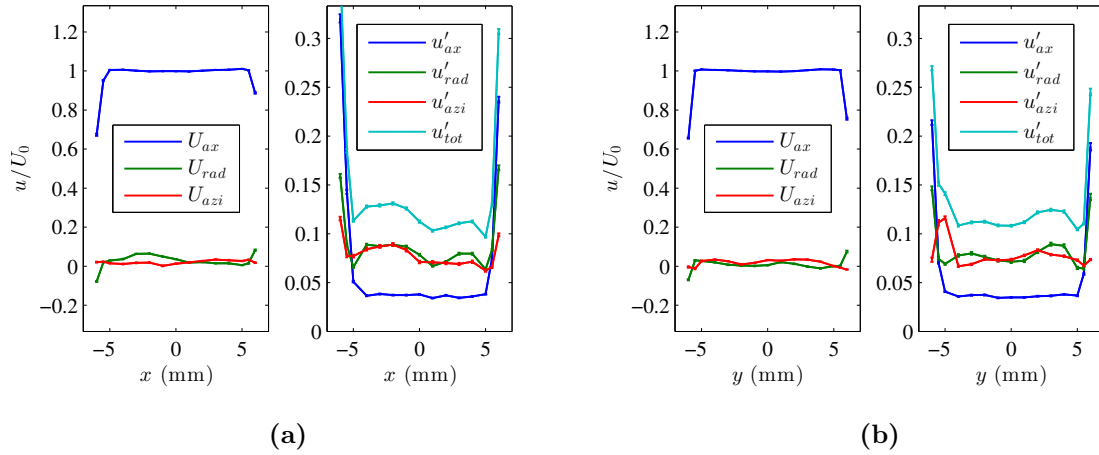


**Figure 132:** Mean and RMS velocity profiles for the 12 mm burner at  $p = 10$  atm,  $T = 300$  K,  $U_0 = 10$  m/s,  $BR = 69\%$  for the (a)  $x$  and (b)  $y$  traverses.

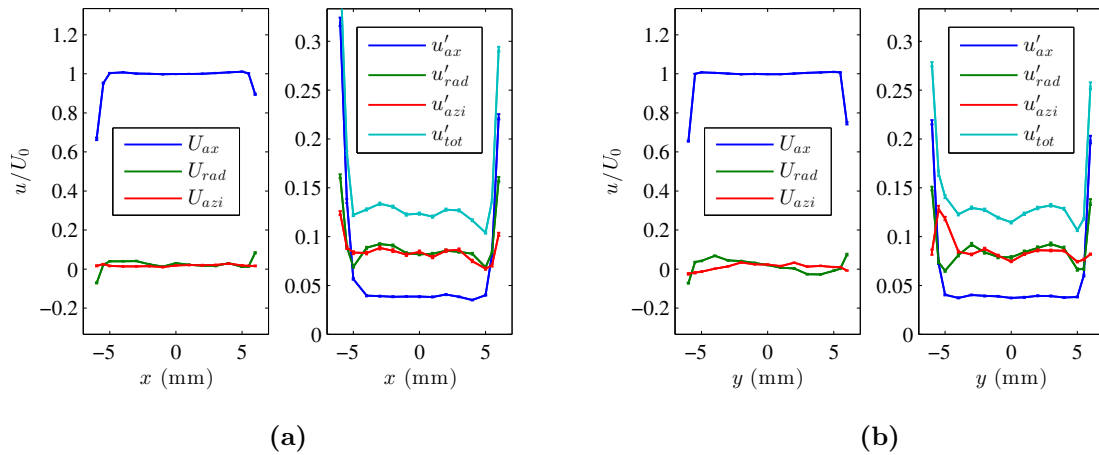


**Figure 133:** Mean and RMS velocity profiles for the 12 mm burner at  $p = 10$  atm,  $T = 300$  K,  $U_0 = 10$  m/s,  $BR = 75\%$  for the (a)  $x$  and (b)  $y$  traverses.

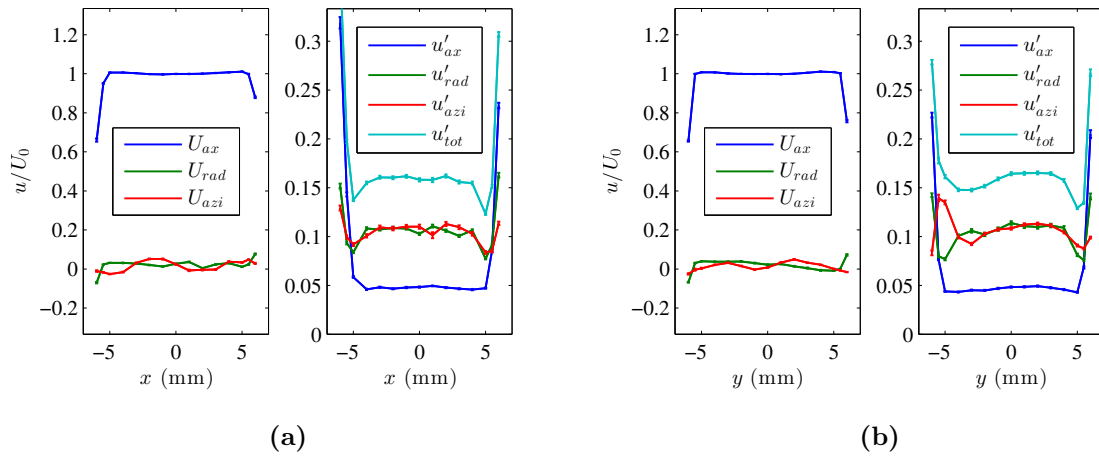


**Figure 134:** Mean and RMS velocity profiles for the 12 mm burner at  $p = 10$  atm,  $T = 300$  K,  $U_0 = 10$  m/s,  $BR = 81\%$  for the (a)  $x$  and (b)  $y$  traverses.

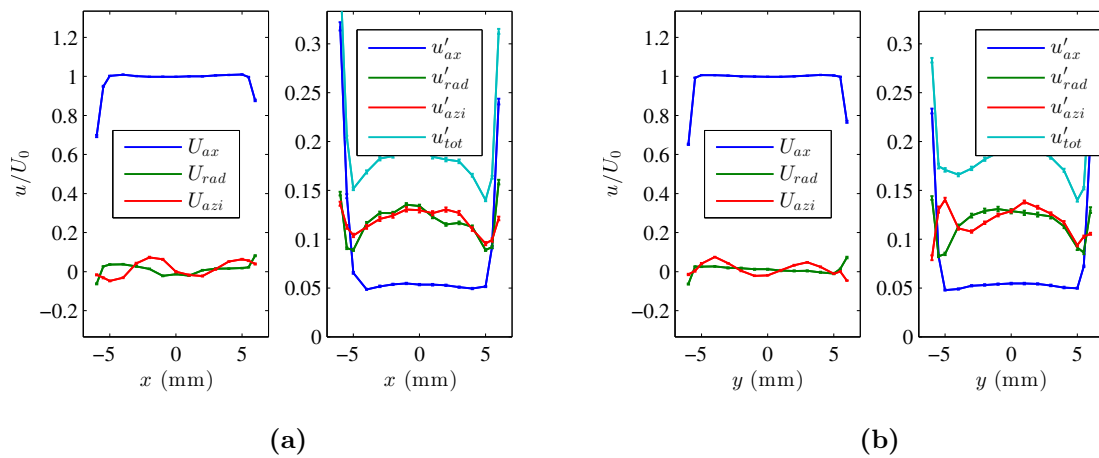


**Figure 135:** Mean and RMS velocity profiles for the 12 mm burner at  $p = 10$  atm,  $T = 300$  K,  $U_0 = 10$  m/s,  $BR = 87\%$  for the (a)  $x$  and (b)  $y$  traverses.

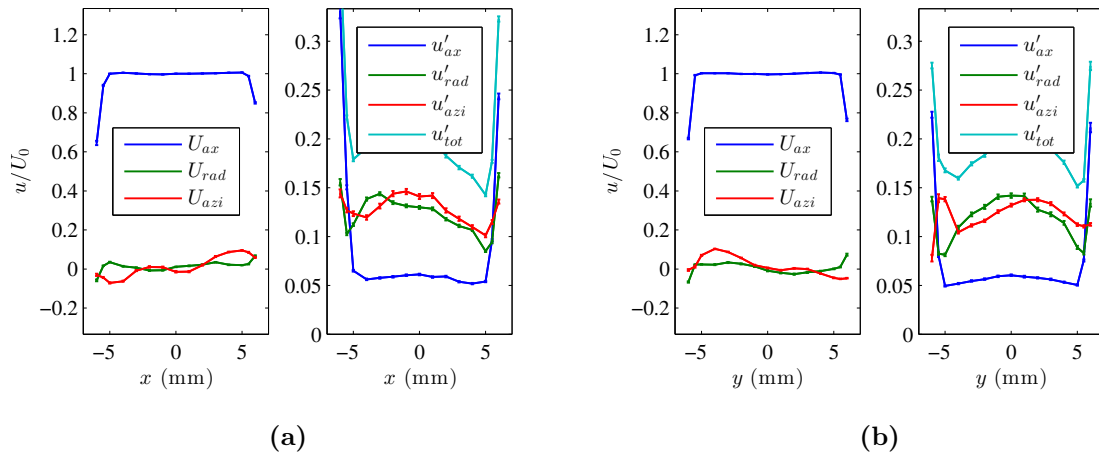


**Figure 136:** Mean and RMS velocity profiles for the 12 mm burner at  $p = 10$  atm,  $T = 300$  K,  $U_0 = 10$  m/s,  $BR = 93\%$  for the (a)  $x$  and (b)  $y$  traverses.

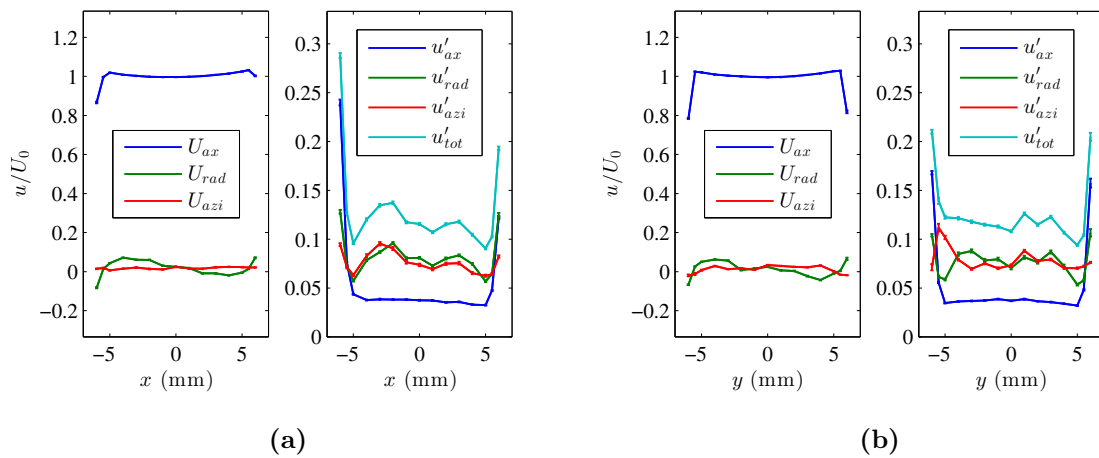


**Figure 137:** Mean and RMS velocity profiles for the 12 mm burner at  $p = 10$  atm,  $T = 300$  K,  $U_0 = 27$  m/s,  $BR = 69\%$  for the (a)  $x$  and (b)  $y$  traverses.

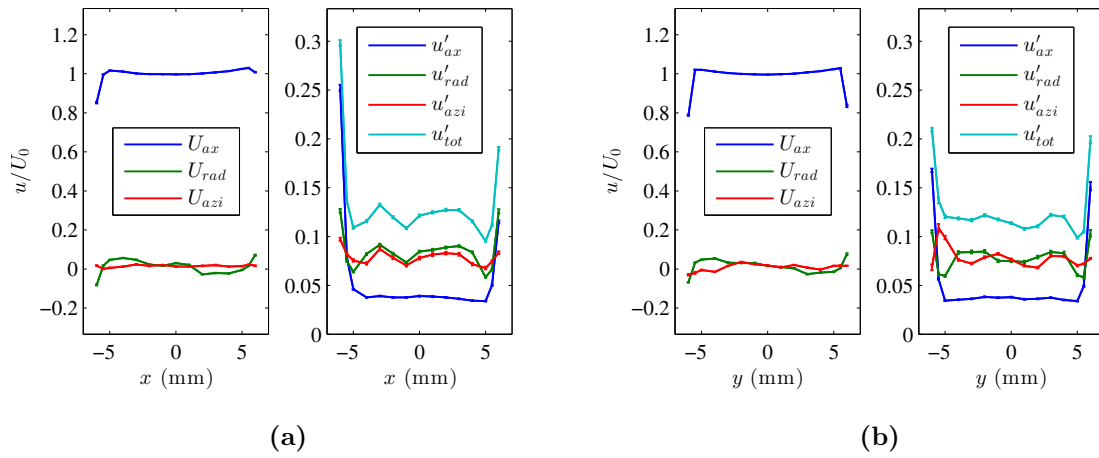


**Figure 138:** Mean and RMS velocity profiles for the 12 mm burner at  $p = 10$  atm,  $T = 300$  K,  $U_0 = 27$  m/s,  $BR = 75\%$  for the (a)  $x$  and (b)  $y$  traverses.

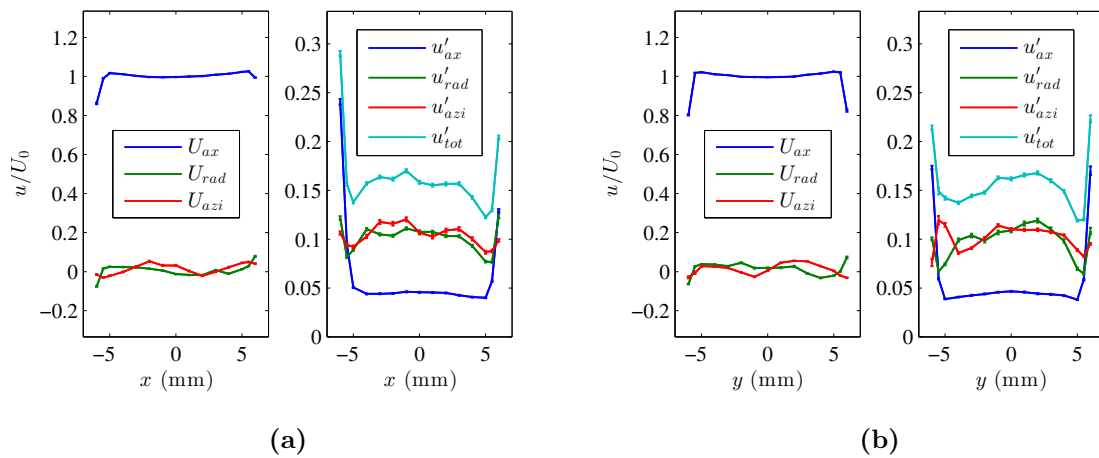


**Figure 139:** Mean and RMS velocity profiles for the 12 mm burner at  $p = 10$  atm,  $T = 300$  K,  $U_0 = 27$  m/s,  $BR = 81\%$  for the (a)  $x$  and (b)  $y$  traverses.

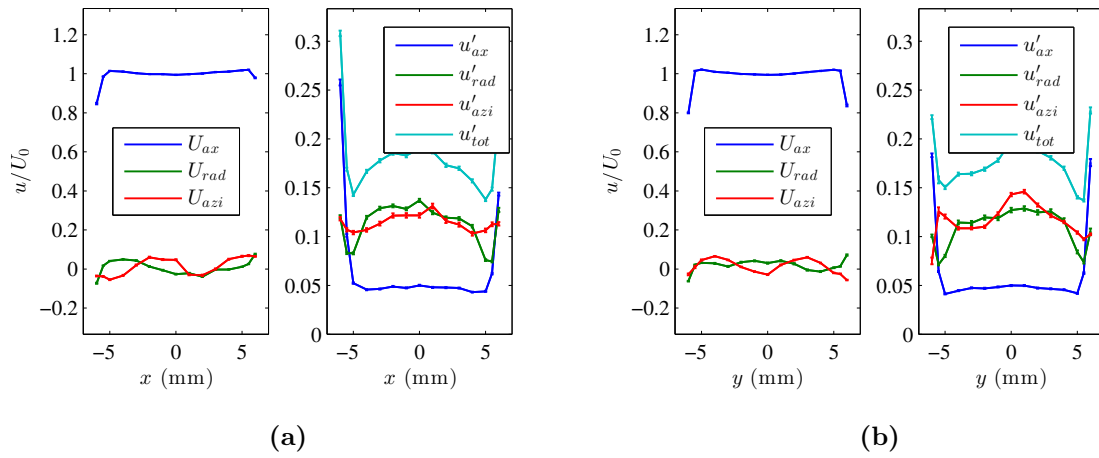


**Figure 140:** Mean and RMS velocity profiles for the 12 mm burner at  $p = 10$  atm,  $T = 300$  K,  $U_0 = 27$  m/s,  $BR = 87\%$  for the (a)  $x$  and (b)  $y$  traverses.

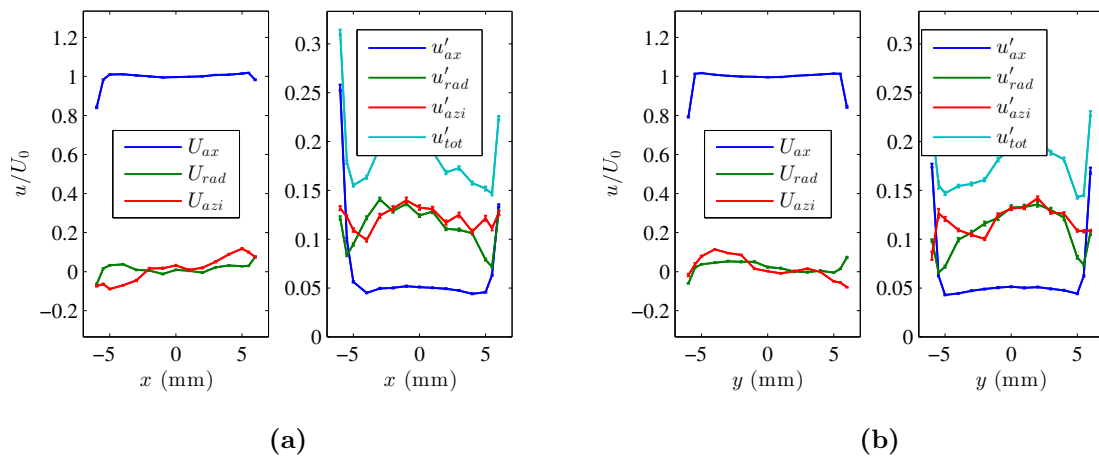


**Figure 141:** Mean and RMS velocity profiles for the 12 mm burner at  $p = 10$  atm,  $T = 300$  K,  $U_0 = 27$  m/s,  $BR = 93\%$  for the (a)  $x$  and (b)  $y$  traverses.

### B.1.4 20 atm

This section presents mean and RMS velocity profiles for the 12 mm burner at a pressure of 20 atm.

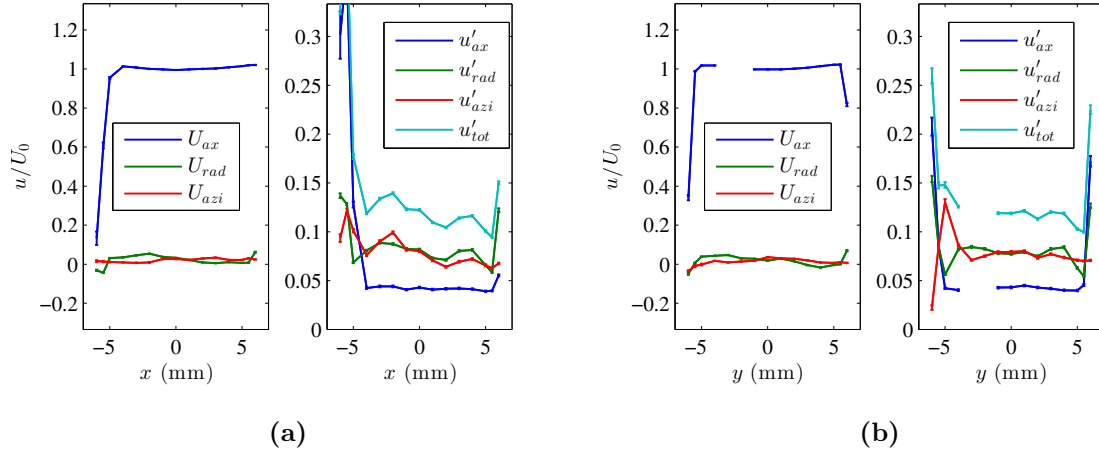


**Figure 142:** Mean and RMS velocity profiles for the 12 mm burner at  $p = 20$  atm,  $T = 300$  K,  $U_0 = 10$  m/s,  $BR = 69\%$  for the (a)  $x$  and (b)  $y$  traverses.

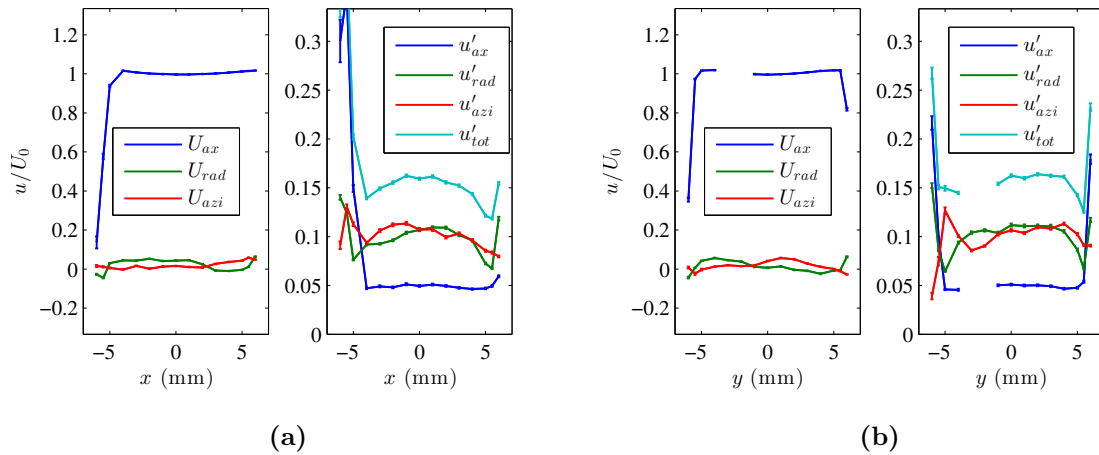


**Figure 143:** Mean and RMS velocity profiles for the 12 mm burner at  $p = 20$  atm,  $T = 300$  K,  $U_0 = 10$  m/s,  $BR = 81\%$  for the (a)  $x$  and (b)  $y$  traverses.

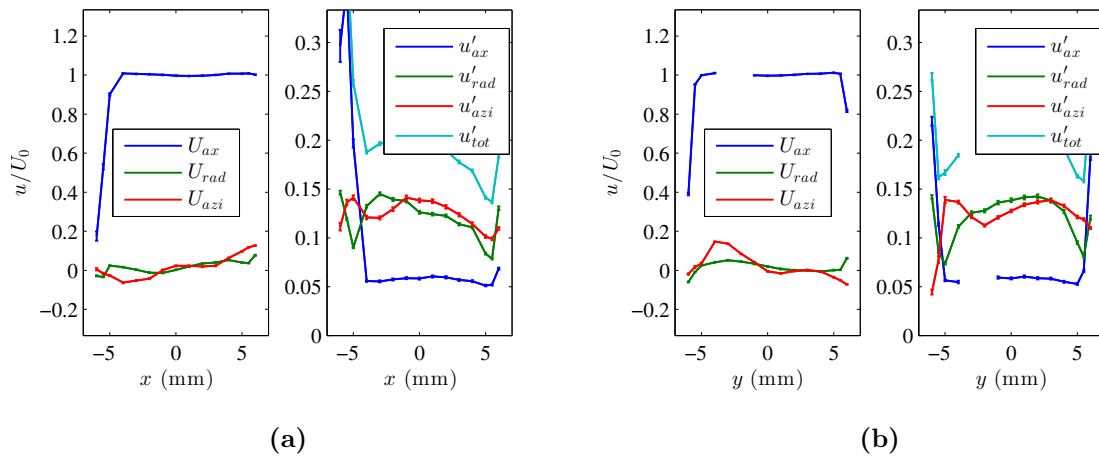


**Figure 144:** Mean and RMS velocity profiles for the 12 mm burner at  $p = 20$  atm,  $T = 300$  K,  $U_0 = 10$  m/s,  $BR = 93\%$  for the (a)  $x$  and (b)  $y$  traverses.

## B.2 20 mm Burner

### B.2.1 1 atm

This section presents mean and RMS velocity profiles for the 20 mm burner at a pressure of 1 atm.

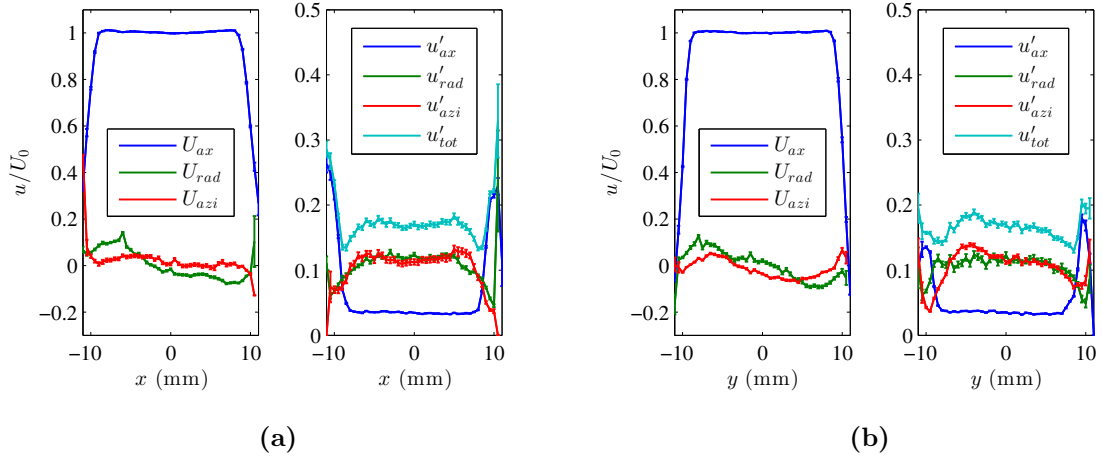


**Figure 145:** Mean and RMS velocity profiles for the 20 mm burner at  $p = 1$  atm,  $T = 300$  K,  $U_0 = 4$  m/s,  $BR = 69\%$  for the (a)  $x$  and (b)  $y$  traverses.

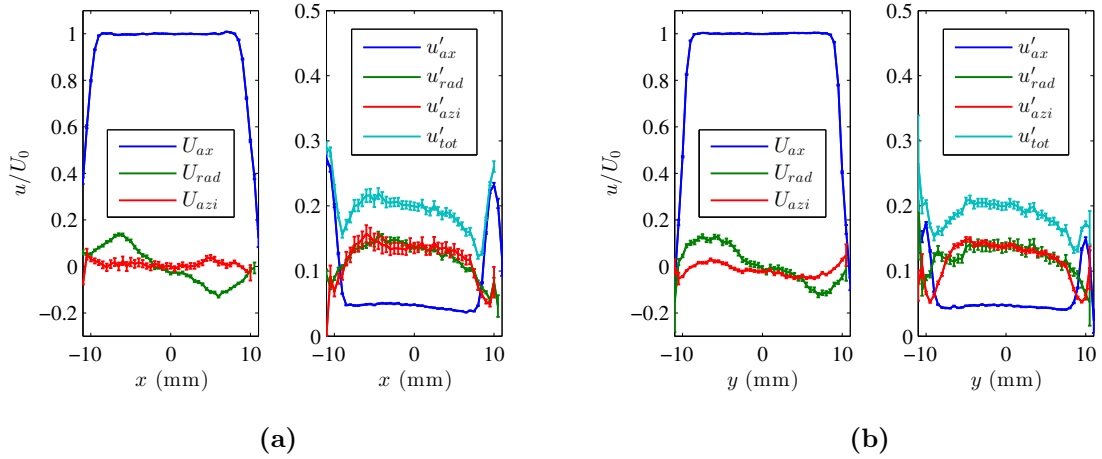


**Figure 146:** Mean and RMS velocity profiles for the 20 mm burner at  $p = 1$  atm,  $T = 300$  K,  $U_0 = 4$  m/s,  $BR = 73\%$  for the (a)  $x$  and (b)  $y$  traverses.

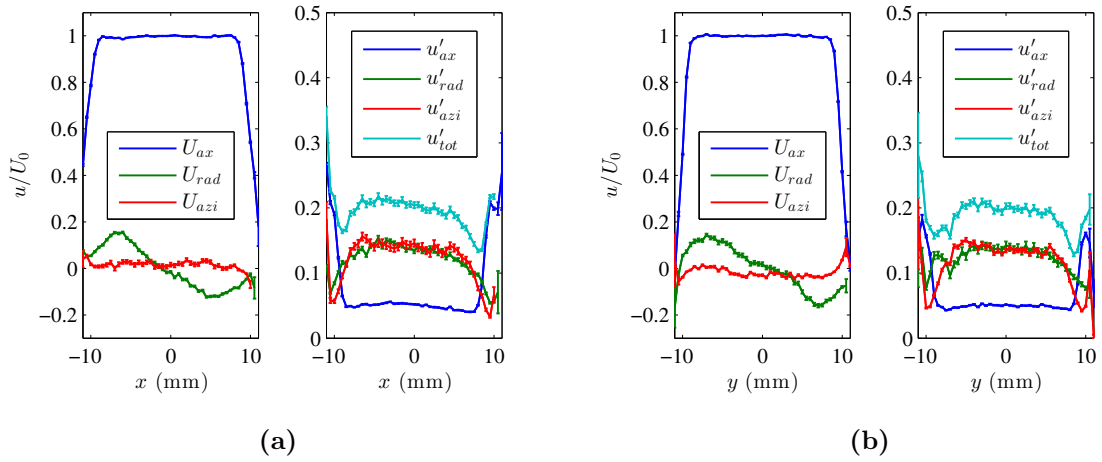


**Figure 147:** Mean and RMS velocity profiles for the 20 mm burner at  $p = 1$  atm,  $T = 300$  K,  $U_0 = 4$  m/s,  $BR = 75\%$  for the (a)  $x$  and (b)  $y$  traverses.

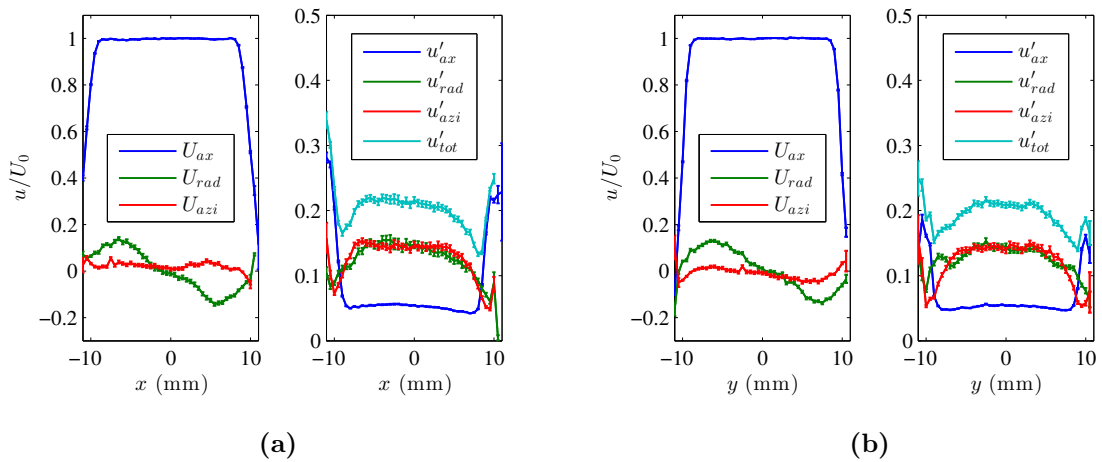


**Figure 148:** Mean and RMS velocity profiles for the 20 mm burner at  $p = 1$  atm,  $T = 300$  K,  $U_0 = 4$  m/s,  $BR = 77\%$  for the (a)  $x$  and (b)  $y$  traverses.

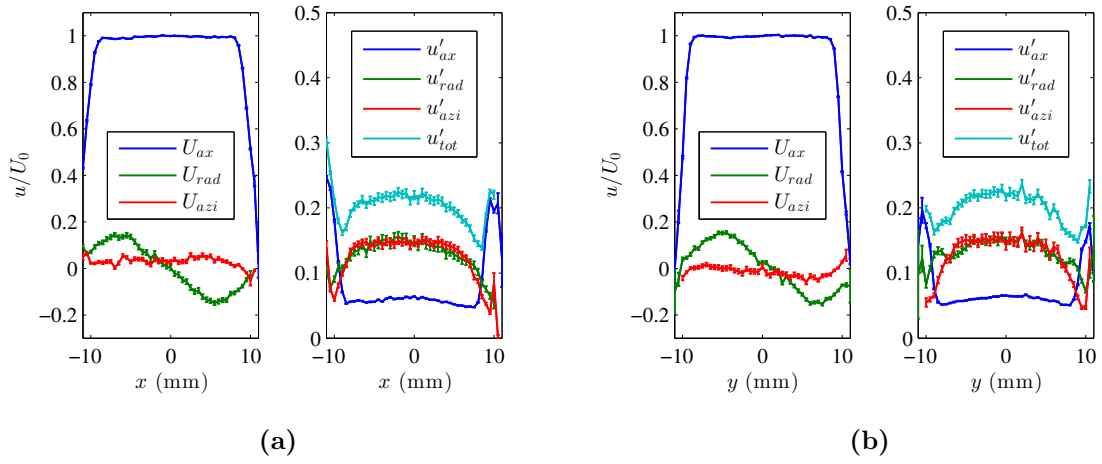


**Figure 149:** Mean and RMS velocity profiles for the 20 mm burner at  $p = 1$  atm,  $T = 300$  K,  $U_0 = 4$  m/s,  $BR = 81\%$  for the (a)  $x$  and (b)  $y$  traverses.

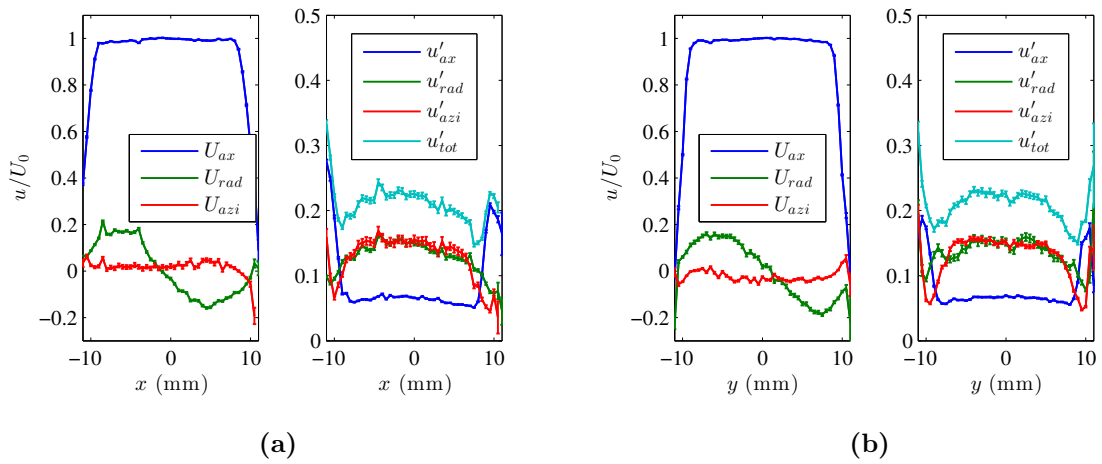


**Figure 150:** Mean and RMS velocity profiles for the 20 mm burner at  $p = 1$  atm,  $T = 300$  K,  $U_0 = 4$  m/s,  $BR = 83\%$  for the (a)  $x$  and (b)  $y$  traverses.

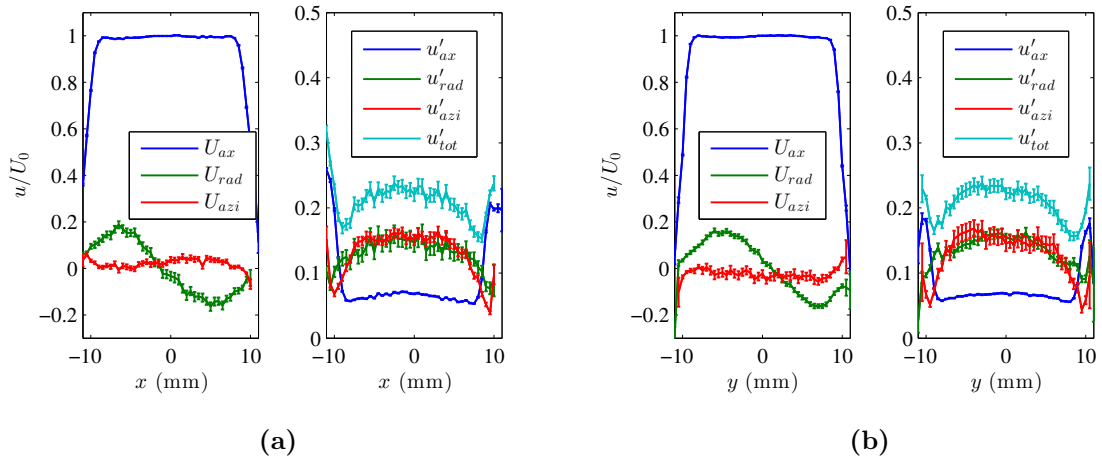


**Figure 151:** Mean and RMS velocity profiles for the 20 mm burner at  $p = 1$  atm,  $T = 300$  K,  $U_0 = 4$  m/s,  $BR = 85\%$  for the (a)  $x$  and (b)  $y$  traverses.

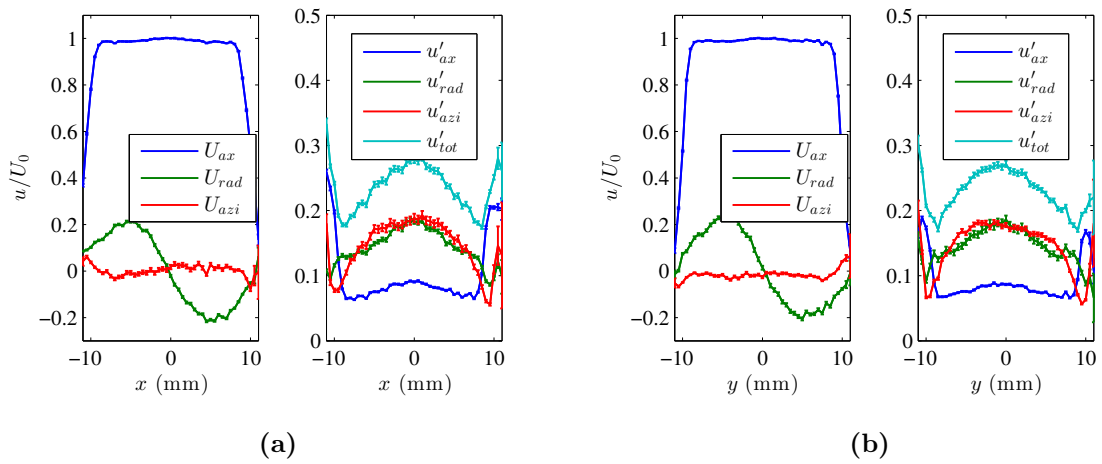


**Figure 152:** Mean and RMS velocity profiles for the 20 mm burner at  $p = 1$  atm,  $T = 300$  K,  $U_0 = 4$  m/s,  $BR = 89\%$  for the (a)  $x$  and (b)  $y$  traverses.

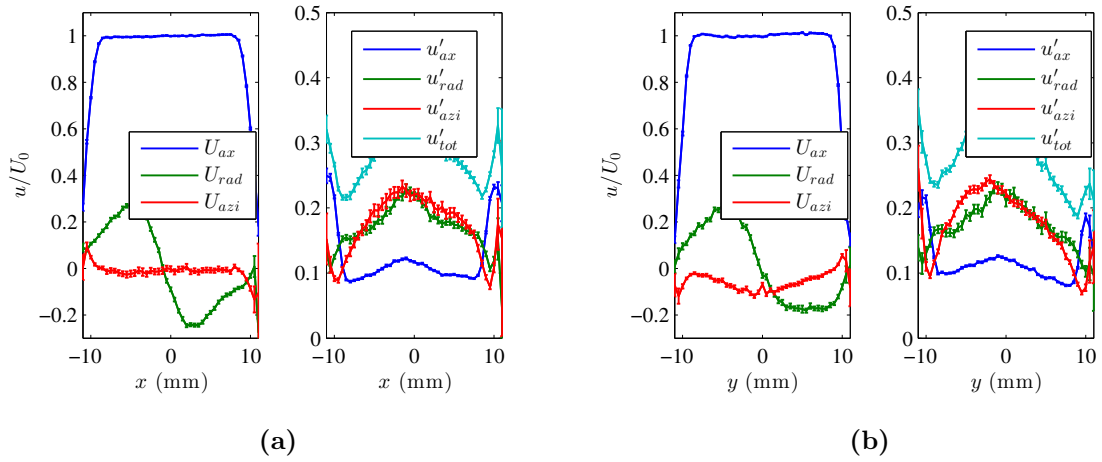


**Figure 153:** Mean and RMS velocity profiles for the 20 mm burner at  $p = 1$  atm,  $T = 300$  K,  $U_0 = 4$  m/s,  $BR = 91\%$  for the (a)  $x$  and (b)  $y$  traverses.

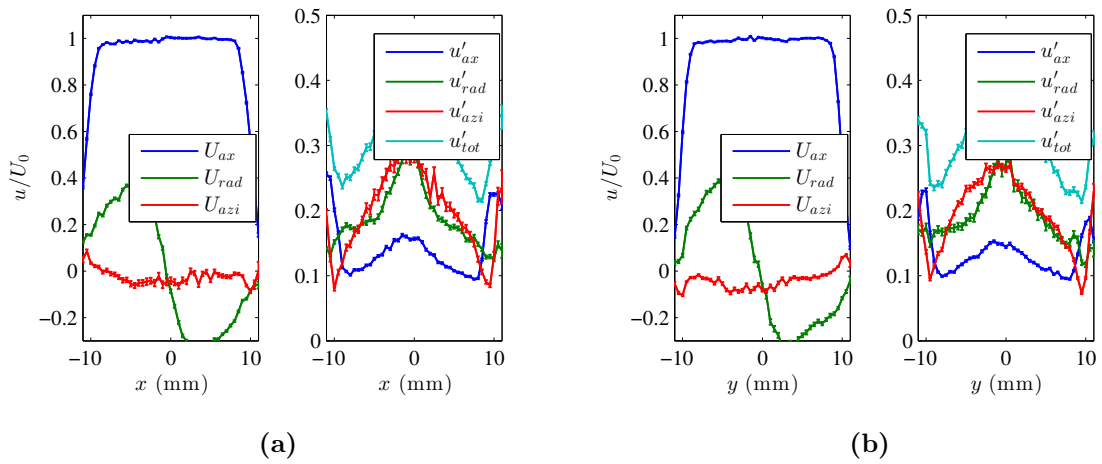


**Figure 154:** Mean and RMS velocity profiles for the 20 mm burner at  $p = 1$  atm,  $T = 300$  K,  $U_0 = 4$  m/s,  $BR = 93\%$  for the (a)  $x$  and (b)  $y$  traverses.

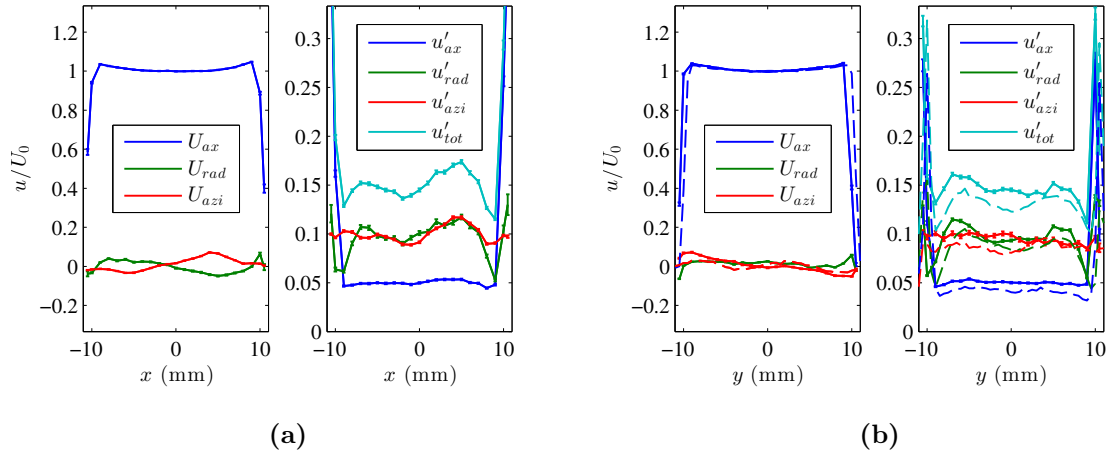


**Figure 155:** Mean and RMS velocity profiles for the 20 mm burner at  $p = 1$  atm,  $T = 300$  K,  $U_0 = 30$  m/s,  $BR = 69\%$  for the (a)  $x$  and (b)  $y$  traverses.

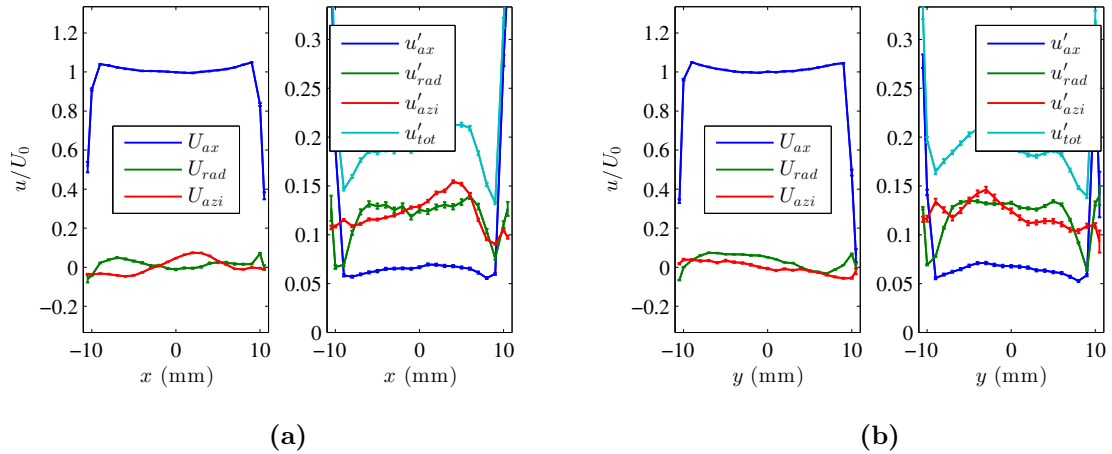


**Figure 156:** Mean and RMS velocity profiles for the 20 mm burner at  $p = 1$  atm,  $T = 300$  K,  $U_0 = 30$  m/s,  $BR = 75\%$  for the (a)  $x$  and (b)  $y$  traverses.

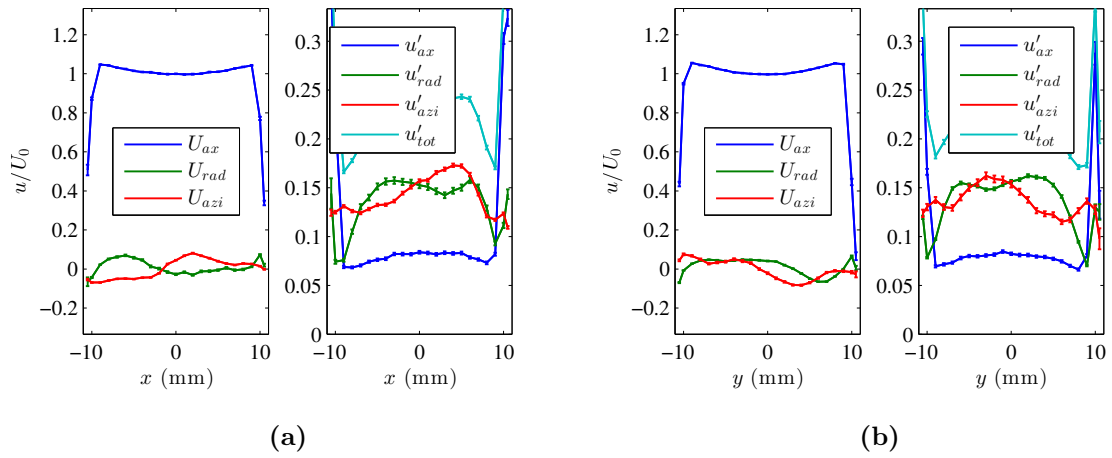


**Figure 157:** Mean and RMS velocity profiles for the 20 mm burner at  $p = 1$  atm,  $T = 300$  K,  $U_0 = 30$  m/s,  $BR = 81\%$  for the (a)  $x$  and (b)  $y$  traverses.

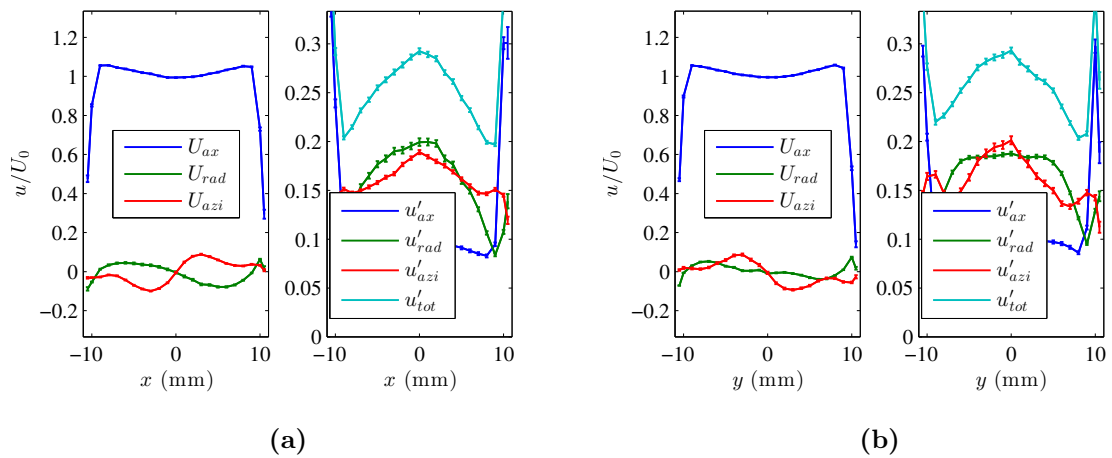


**Figure 158:** Mean and RMS velocity profiles for the 20 mm burner at  $p = 1$  atm,  $T = 300$  K,  $U_0 = 30$  m/s,  $BR = 87\%$  for the (a)  $x$  and (b)  $y$  traverses.

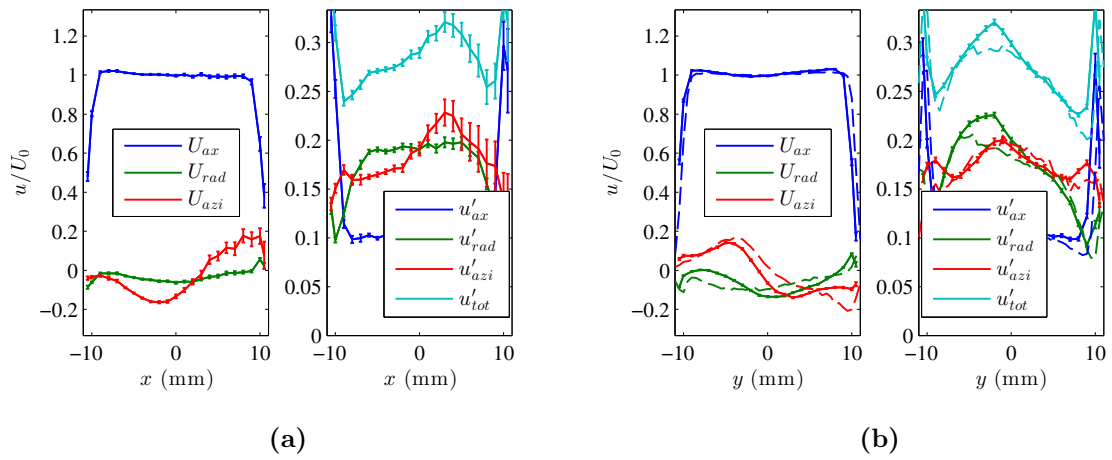


**Figure 159:** Mean and RMS velocity profiles for the 20 mm burner at  $p = 1$  atm,  $T = 300$  K,  $U_0 = 30$  m/s,  $BR = 93\%$  for the (a)  $x$  and (b)  $y$  traverses.

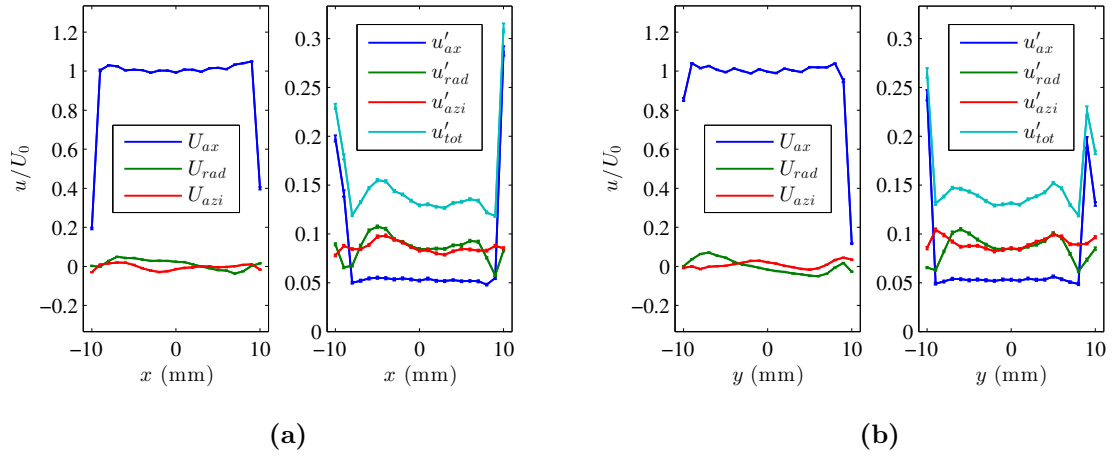


**Figure 160:** Mean and RMS velocity profiles for the 20 mm burner at  $p = 1$  atm,  $T = 300$  K,  $U_0 = 50$  m/s,  $BR = 69\%$  for the (a)  $x$  and (b)  $y$  traverses.

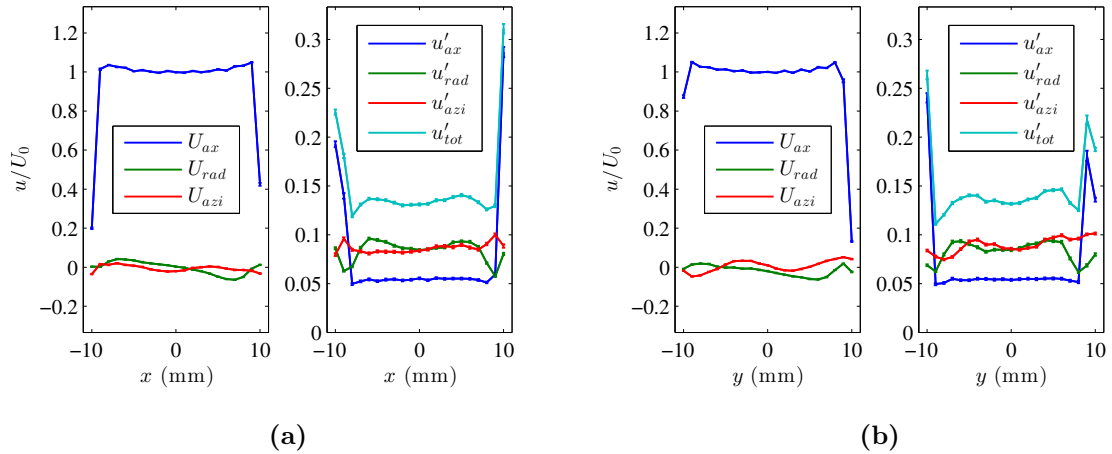


**Figure 161:** Mean and RMS velocity profiles for the 20 mm burner at  $p = 1$  atm,  $T = 300$  K,  $U_0 = 50$  m/s,  $BR = 75\%$  for the (a)  $x$  and (b)  $y$  traverses.

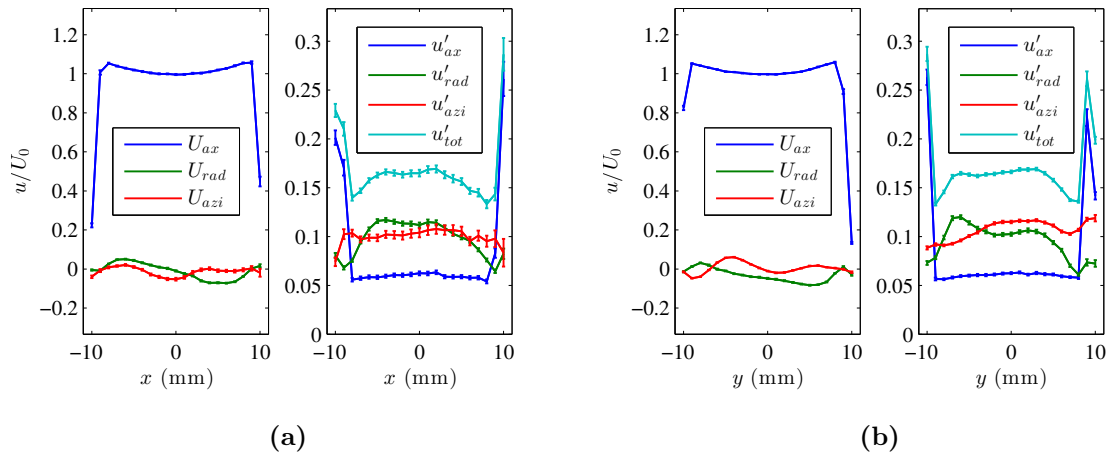


**Figure 162:** Mean and RMS velocity profiles for the 20 mm burner at  $p = 1$  atm,  $T = 300$  K,  $U_0 = 50$  m/s,  $BR = 81\%$  for the (a)  $x$  and (b)  $y$  traverses.

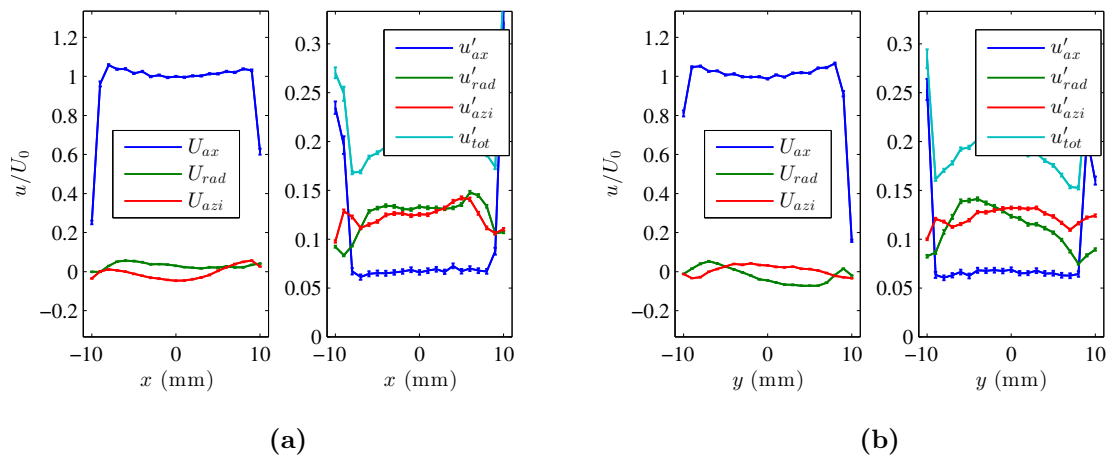


**Figure 163:** Mean and RMS velocity profiles for the 20 mm burner at  $p = 1$  atm,  $T = 300$  K,  $U_0 = 50$  m/s,  $BR = 87\%$  for the (a)  $x$  and (b)  $y$  traverses.

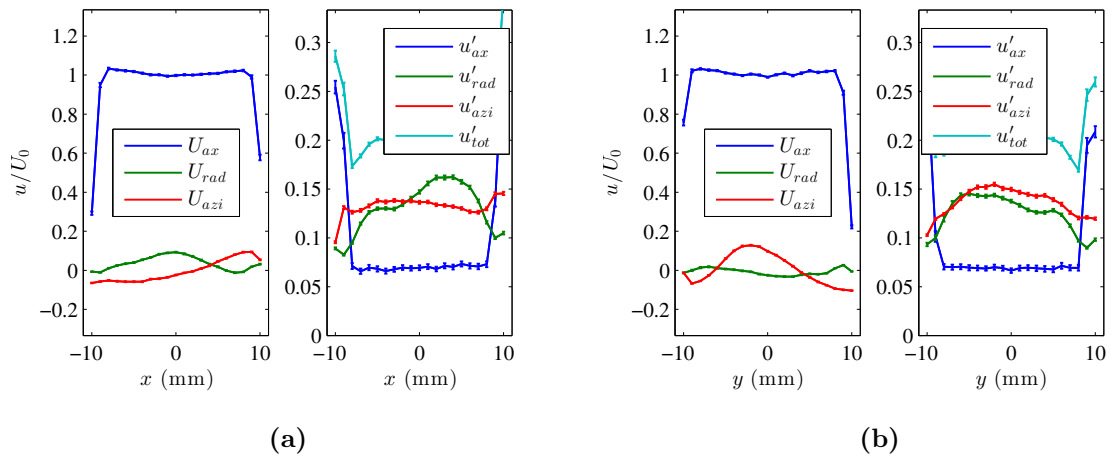


**Figure 164:** Mean and RMS velocity profiles for the 20 mm burner at  $p = 1$  atm,  $T = 300$  K,  $U_0 = 50$  m/s,  $BR = 93\%$  for the (a)  $x$  and (b)  $y$  traverses.

### B.2.2 5 atm

This section presents mean and RMS velocity profiles for the 20 mm burner at a pressure of 5 atm.

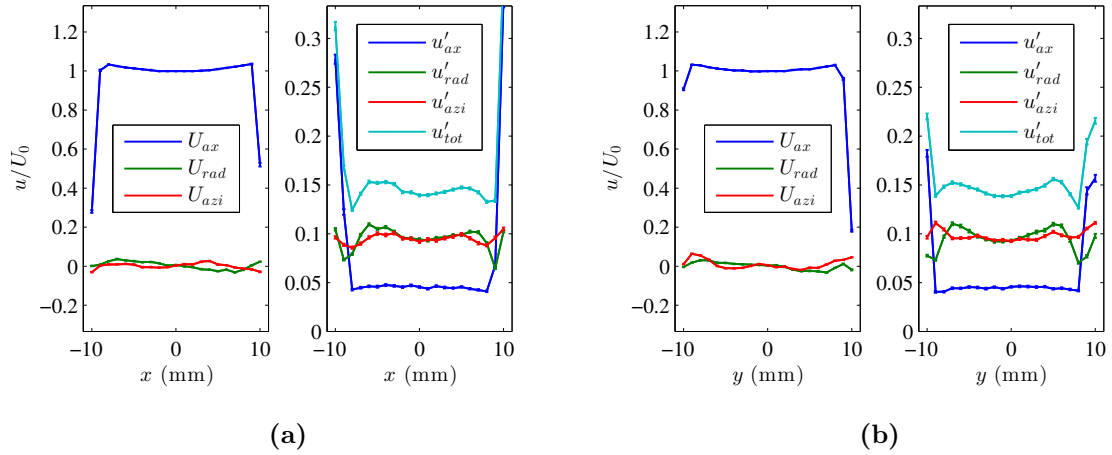


**Figure 165:** Mean and RMS velocity profiles for the 20 mm burner at  $p = 5$  atm,  $T = 339$  K,  $U_0 = 50$  m/s,  $BR = 69\%$  for the (a)  $x$  and (b)  $y$  traverses.

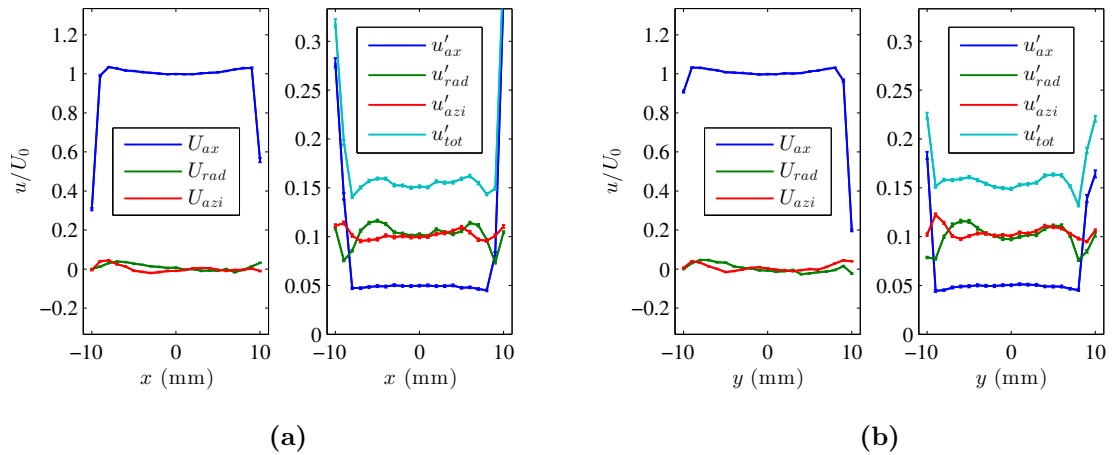


**Figure 166:** Mean and RMS velocity profiles for the 20 mm burner at  $p = 5$  atm,  $T = 339$  K,  $U_0 = 50$  m/s,  $BR = 75\%$  for the (a)  $x$  and (b)  $y$  traverses.

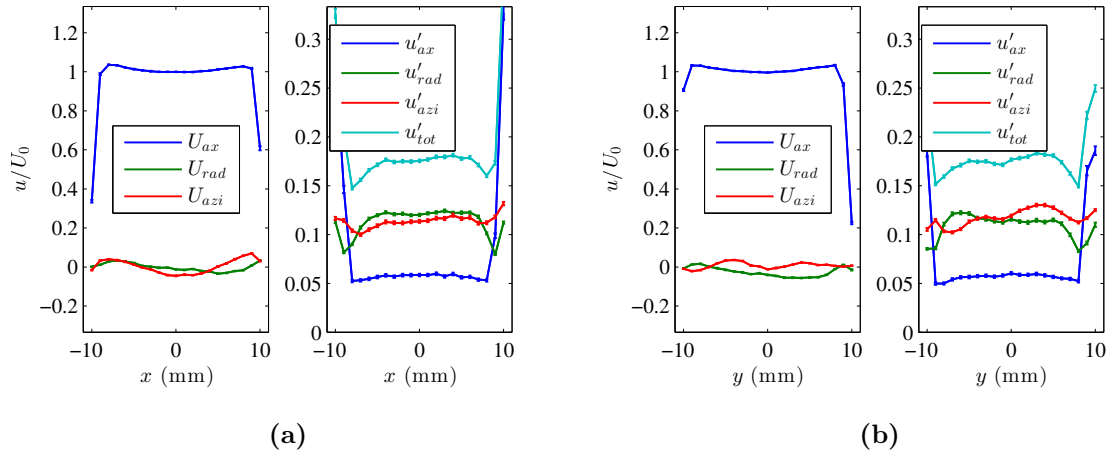


**Figure 167:** Mean and RMS velocity profiles for the 20 mm burner at  $p = 5$  atm,  $T = 339$  K,  $U_0 = 50$  m/s,  $BR = 81\%$  for the (a)  $x$  and (b)  $y$  traverses.

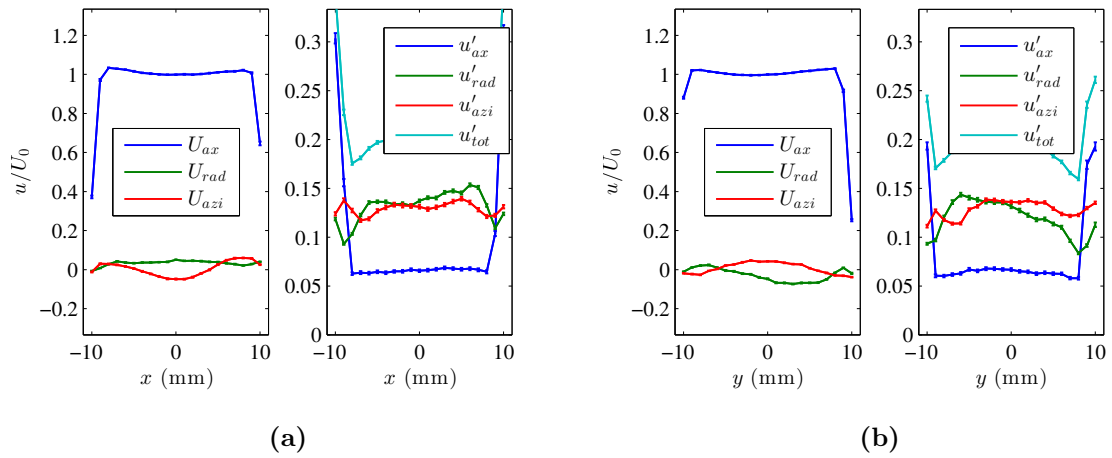


**Figure 168:** Mean and RMS velocity profiles for the 20 mm burner at  $p = 5$  atm,  $T = 339$  K,  $U_0 = 50$  m/s,  $BR = 87\%$  for the (a)  $x$  and (b)  $y$  traverses.

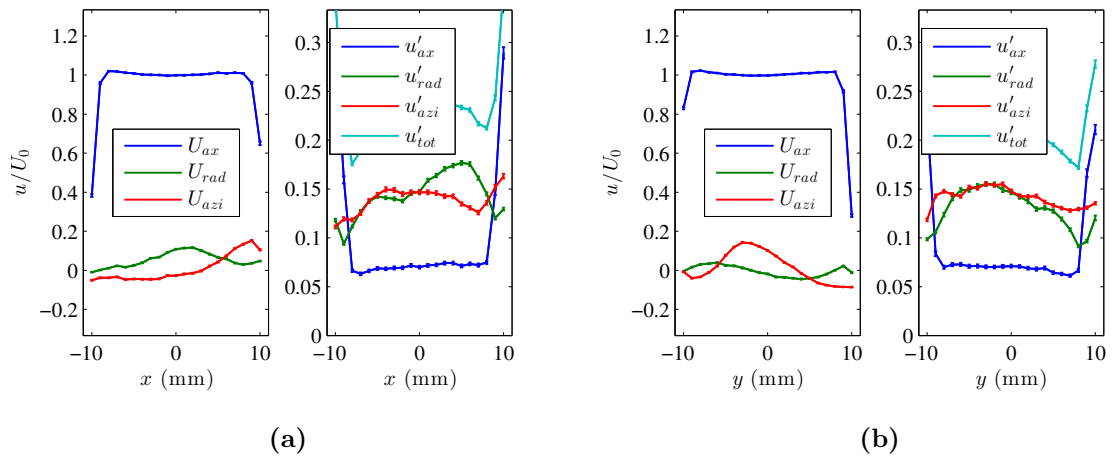


**Figure 169:** Mean and RMS velocity profiles for the 20 mm burner at  $p = 5$  atm,  $T = 339$  K,  $U_0 = 50$  m/s,  $BR = 93\%$  for the (a)  $x$  and (b)  $y$  traverses.

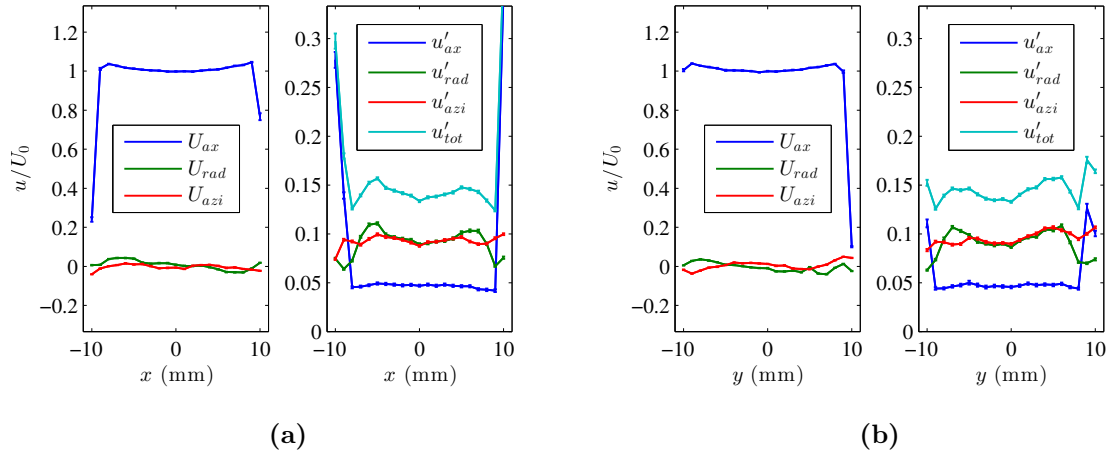


**Figure 170:** Mean and RMS velocity profiles for the 20 mm burner at  $p = 5$  atm,  $T = 515$  K,  $U_0 = 50$  m/s,  $BR = 69\%$  for the (a)  $x$  and (b)  $y$  traverses.

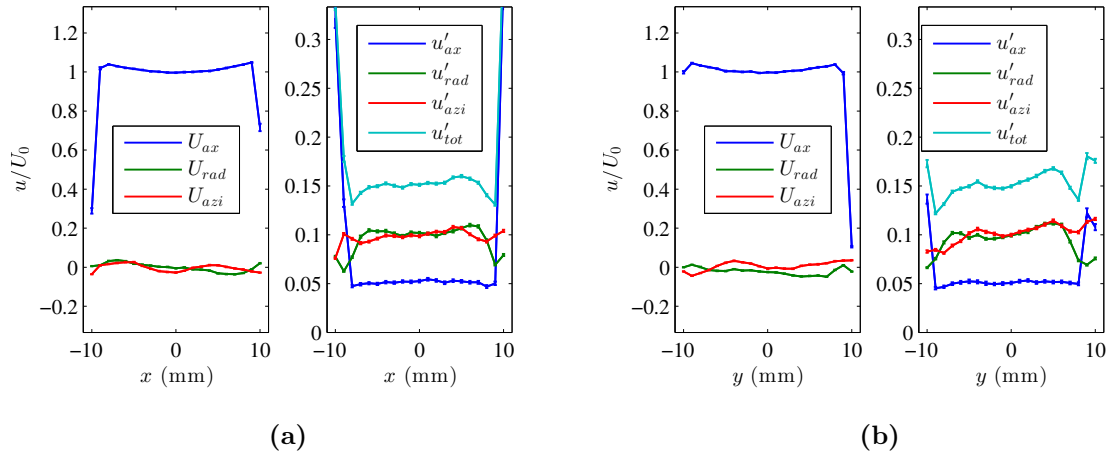


**Figure 171:** Mean and RMS velocity profiles for the 20 mm burner at  $p = 5$  atm,  $T = 515$  K,  $U_0 = 50$  m/s,  $BR = 75\%$  for the (a)  $x$  and (b)  $y$  traverses.

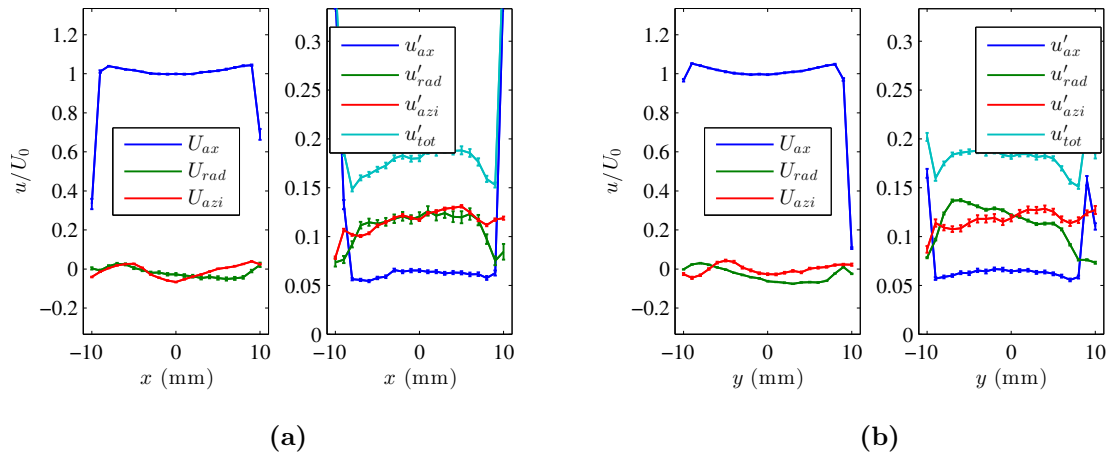


**Figure 172:** Mean and RMS velocity profiles for the 20 mm burner at  $p = 5$  atm,  $T = 515$  K,  $U_0 = 50$  m/s,  $BR = 81\%$  for the (a)  $x$  and (b)  $y$  traverses.

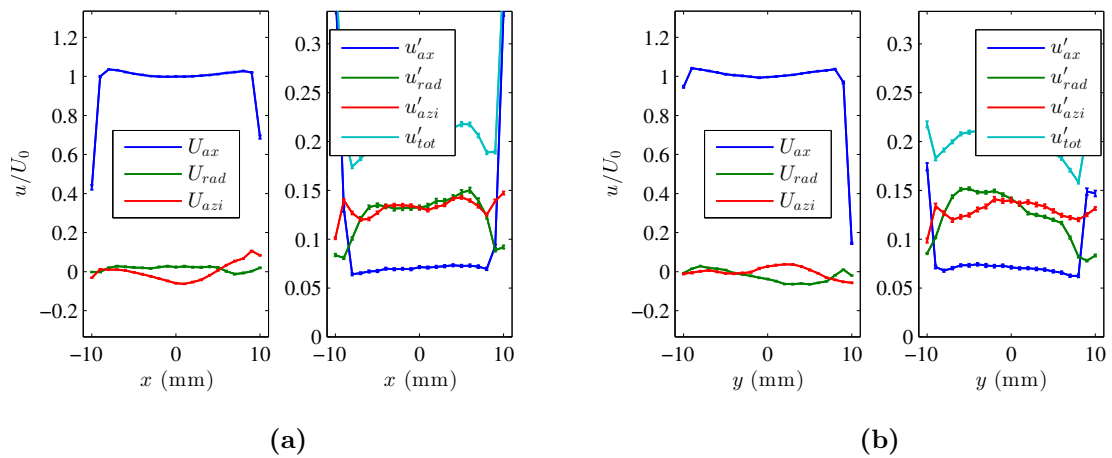


**Figure 173:** Mean and RMS velocity profiles for the 20 mm burner at  $p = 5$  atm,  $T = 515$  K,  $U_0 = 50$  m/s,  $BR = 87\%$  for the (a)  $x$  and (b)  $y$  traverses.

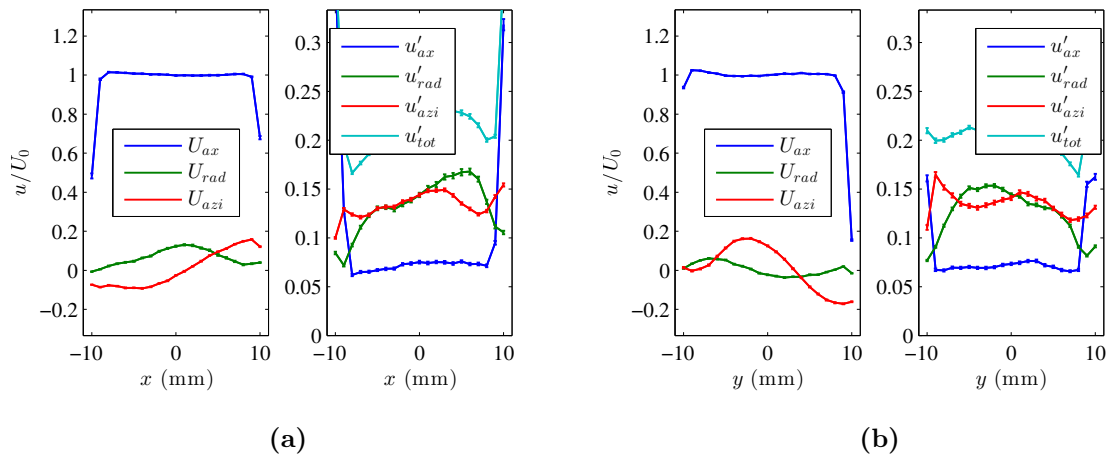


**Figure 174:** Mean and RMS velocity profiles for the 20 mm burner at  $p = 5$  atm,  $T = 515$  K,  $U_0 = 50$  m/s,  $BR = 93\%$  for the (a)  $x$  and (b)  $y$  traverses.

### B.2.3 10 atm

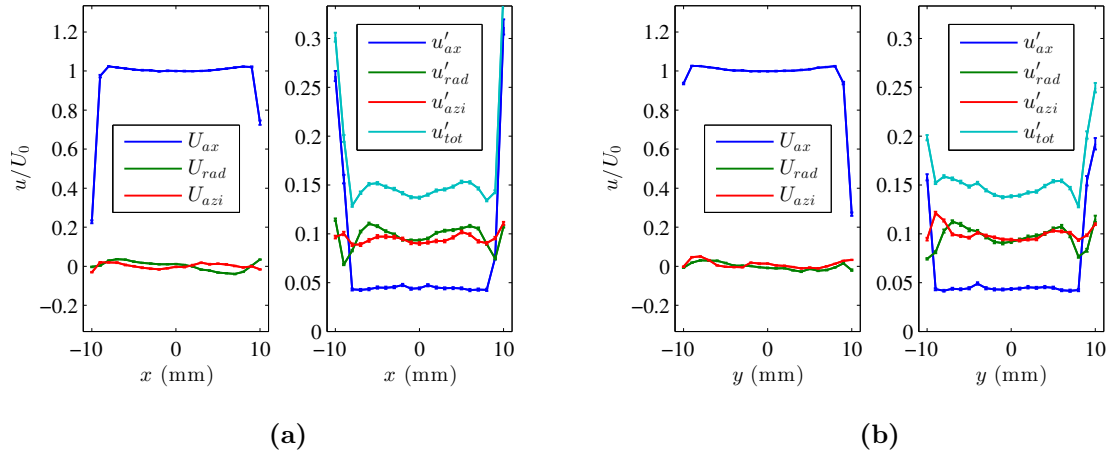


**Figure 175:** Mean and RMS velocity profiles for the 20 mm burner at  $p = 10$  atm,  $T = 330$  K,  $U_0 = 50$  m/s,  $BR = 69\%$  for the (a)  $x$  and (b)  $y$  traverses.

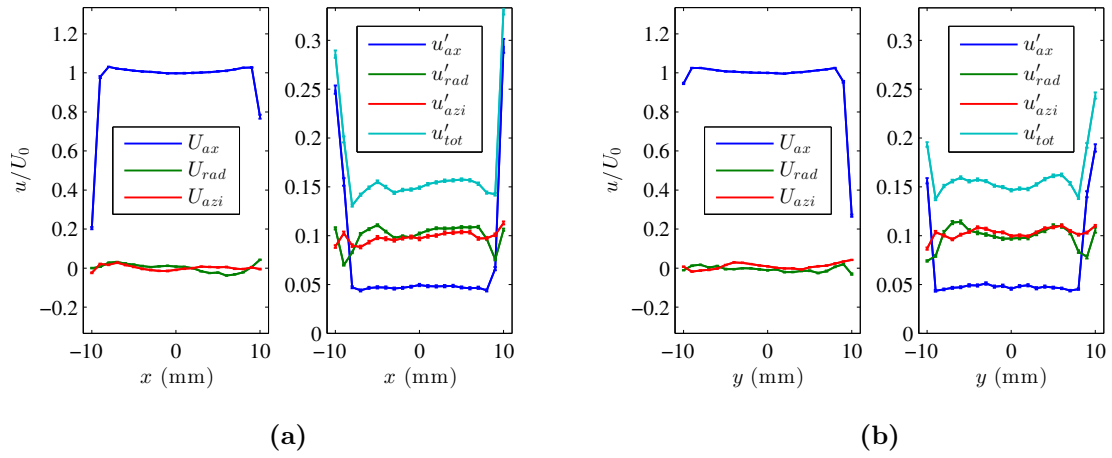


**Figure 176:** Mean and RMS velocity profiles for the 20 mm burner at  $p = 10$  atm,  $T = 330$  K,  $U_0 = 50$  m/s,  $BR = 75\%$  for the (a)  $x$  and (b)  $y$  traverses.

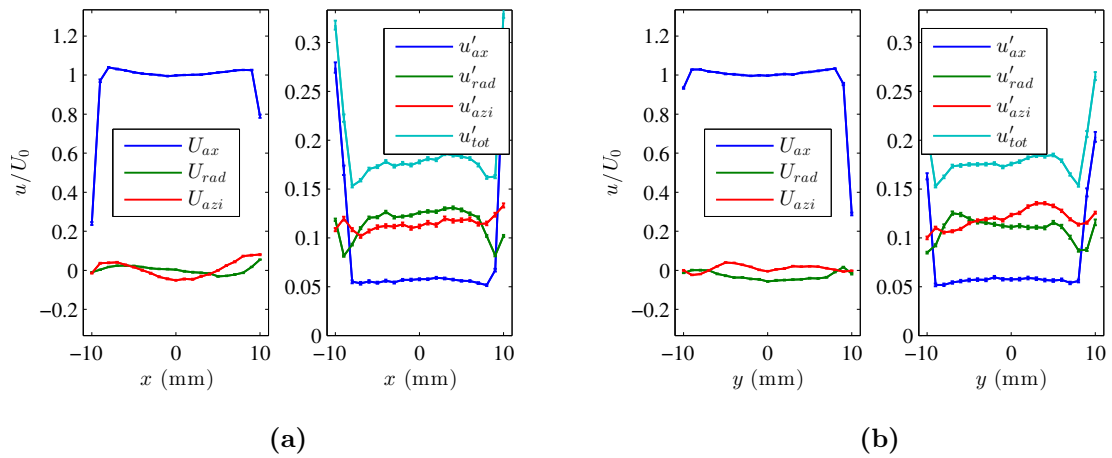


**Figure 177:** Mean and RMS velocity profiles for the 20 mm burner at  $p = 10$  atm,  $T = 330$  K,  $U_0 = 50$  m/s,  $BR = 81\%$  for the (a)  $x$  and (b)  $y$  traverses.

## REFERENCES

- [1] ABDEL-GAYED, R. G., AL-KHISHALI, K. J., and BRADLEY, D., “Turbulent burning velocities and flame straining in explosions,” *Proceedings of the Royal Society of London. Series A, Mathematical and Physical Sciences*, vol. 391, pp. 393–414, 1984.
- [2] AMATO, A., DAY, M., CHENG, R., BELL, J., and LIEUWEN, T., “Leading edge statistics of turbulent, lean, h<sub>2</sub>air flames,” *Proceedings of the Combustion Institute*, vol. 35, no. 2, pp. 1313 – 1320, 2015.
- [3] AMATO, A., DAY, M., CHENG, R., BELL, J., and LIEUWEN, T., “Leading point statistics of a turbulent, lean, h<sub>2</sub>-air flame,” Apr. 2012.
- [4] ANSELMO-FILHO, P., HOCHGREB, S., BARLOW, R. S., and CANT, R. S., “Experimental measurements of geometric properties of turbulent stratified flames,” *Proceedings of the Combustion Institute*, vol. 32, no. 2, pp. 1763–1770, 2009.
- [5] ASHURST, W. T. and SHEPHERD, I. G., “Flame front curvature distributions in a turbulent premixed flame zone,” *Combustion Science and Technology*, vol. 124, no. 1-6, pp. 115–144, 1997.
- [6] BAINES, W. and PETERSON, E., “An investigation of flow through screens,” *Trans. Am. Soc. Mech. Engrs*, vol. 73, no. 1, p. 467480, 1951.
- [7] BALLAL, D. R., “The structure of a premixed turbulent flame,” *Proceedings of the Royal Society of London. A. Mathematical and Physical Sciences*, vol. 367, no. 1730, pp. 353–380, 1979.
- [8] BALLAL, D. and LEFEBVRE, A., “The structure and propagation of turbulent flames,” *Proceedings of the Royal Society of London. A. Mathematical and Physical Sciences*, vol. 344, no. 1637, pp. 217–234, 1975.
- [9] BAYLEY, A., HARDALUPAS, Y., and TAYLOR, A., “Local curvature measurements of a lean, partially premixed swirl-stabilised flame,” *Experiments in Fluids*, vol. 52, no. 4, pp. 963–983, 2012.
- [10] BÉDAT, B. and CHENG, R. K., “Experimental study of premixed flames in intense isotropic turbulence,” *Combustion and Flame*, vol. 100, no. 3, pp. 485–494, 1995.
- [11] BOGER, M., VEYNANTE, D., BOUGHANEM, H., and TROUV, A., “Direct numerical simulation analysis of flame surface density concept for large eddy simulation of turbulent premixed combustion,” *Symposium (International) on Combustion*, vol. 27, no. 1, pp. 917–925, 1998.
- [12] BONALDO, A. and KELMAN, J. B., “Experimental annular stratified flames characterisation stabilised by weak swirl,” *Combustion and Flame*, vol. 156, no. 4, pp. 750–762, 2009.

- [13] BORGHI, R., "On the structure and morphology of turbulent premixed flames," *Recent advances in the aerospace sciences(A 85-47304 23-31)*. New York, Plenum Press, 1985, pp. 117–138, 1985.
- [14] BRADLEY, D., "How fast can we burn?," *Proceedings of the Combustion Institute*, vol. 24, no. 1, pp. 247–262, 1992.
- [15] BRADLEY, D., HAQ, M. Z., HICKS, R. A., KITAGAWA, T., LAWES, M., SHEPPARD, C. G. W., and WOOLLEY, R., "Turbulent burning velocity, burned gas distribution, and associated flame surface definition," *Combustion and Flame*, vol. 133, no. 4, pp. 415–430, 2003.
- [16] BRAY, K., "Studies of the turbulent burning velocity," *Proceedings of the Royal Society of London. Series A, Mathematical and Physical Sciences*, vol. 431, no. 1882, pp. 315–335, 1990.
- [17] BRUTSCHER, T., ZARZALIS, N., and BOCKHORN, H., "An experimentally based approach for the space-averaged laminar burning velocity used for modeling premixed turbulent combustion," *Proceedings of the Combustion Institute*, vol. 29, no. 2, pp. 1825–1832, 2002. doi: DOI:
- [18] BURKE, M., QIN, X., JU, Y., and DRYER, F., "Measurements of hydrogen syngas flame speeds at elevated pressures," in *5th US Combustion Meeting*, p. 14, 2007.
- [19] CANDEL, S. and POINSOT, T., "Flame stretch and the balance equation for the flame area," *Combustion Science and Technology*, vol. 70, no. 1, pp. 1–15, 1990.
- [20] CANT, R. S., POPE, S. B., and BRAY, K. N. C., "Modelling of flamelet surface-to-volume ratio in turbulent premixed combustion," in *Symposium (International) on Combustion*, vol. 23, pp. 809–815, Elsevier, 1991.
- [21] CHAKRABORTY, N. and CANT, R. S., "Effects of strain rate and curvature on surface density function transport in turbulent premixed flames in the thin reaction zones regime," *Physics of Fluids*, vol. 17, no. 6, p. 065108, 2005.
- [22] CHAKRABORTY, N. and CANT, R. S., "Influence of lewis number on curvature effects in turbulent premixed flame propagation in the thin reaction zones regime," *Physics of Fluids*, vol. 17, no. 10, p. 105105, 2005.
- [23] CHAKRABORTY, N. and CANT, R., "Influence of lewis number on strain rate effects in turbulent premixed flame propagation," *International Journal of Heat and Mass Transfer*, vol. 49, no. 1314, pp. 2158 – 2172, 2006.
- [24] CHAKRABORTY, N. and CANT, S., "Unsteady effects of strain rate and curvature on turbulent premixed flames in an inflow-outflow configuration," *Combustion and Flame*, vol. 137, no. 12, pp. 129–147, 2004.
- [25] CHAN, C. K., LAU, K. S., CHIN, W. K., and CHENG, R. K., "Freely propagating open premixed turbulent flames stabilized by swirl," *Symposium (International) on Combustion*, vol. 24, no. 1, pp. 511–518, 1992.

- [26] CHEN, Y.-C., KIM, M., HAN, J., YUN, S., and YOON, Y., “Analysis of flame surface normal and curvature measured in turbulent premixed stagnation-point flames with crossed-plane tomography,” *Proceedings of the Combustion Institute*, vol. 31, no. 1, pp. 1327–1335, 2007.
- [27] CHENG, R. K., “Velocity and scalar characteristics of premixed turbulent flames stabilized by weak swirl,” *Combustion and Flame*, vol. 101, no. 1-2, pp. 1–14, 1995.
- [28] CHENG, R. K., *Turbulent Combustion Properties of Premixed Syngas*, book section 5, pp. 129–168. CRC Press, 1 ed., 2009.
- [29] CHENG, R. K., FABLE, S. A., SCHMIDT, D., ARELLANO, L., and SMITH, K. O., “Development of a low swirl injector concept for gas turbines,” in *International Joint Power Conference*, 2001.
- [30] CHENG, R. K. and LITTLEJOHN, D., “Laboratory study of premixed h<sub>2</sub>-air and h<sub>2</sub>-n<sub>2</sub>-air flames in a low-swirl injector for ultralow emissions gas turbines,” *Journal of Engineering for Gas Turbines and Power*, vol. 130, no. 3, p. 031503, 2008.
- [31] CHENG, R. K., LITTLEJOHN, D., NAZEER, W. A., and SMITH, K. O., “Laboratory studies of the flow field characteristics of low-swirl injectors for adaptation to fuel-flexible turbines,” *Journal of Engineering for Gas Turbines and Power*, vol. 130, no. 2, p. 021501, 2008.
- [32] CHENG, R. K., LITTLEJOHN, D., STRAKEY, P. A., and SIDWELL, T., “Laboratory investigations of a low-swirl injector with h<sub>2</sub> and ch<sub>4</sub> at gas turbine conditions,” *Proceedings of the Combustion Institute*, vol. 32, no. 2, pp. 3001–3009, 2009.
- [33] CHENG, R. K., SHEPHERD, I. G., BÉDAT, B., and TALBOT, L., “Premixed turbulent flame structures in moderate and intense isotropic turbulence,” *Combustion Science & Technology*, vol. 174, no. 1, pp. 29–59, 2002.
- [34] CHENG, R. K., YEGIAN, D. T., MIYASATO, M. M., SAMUELSEN, G. S., BENSON, C. E., PELLIZZARI, R., and LOFTUS, P., “Scaling and development of low-swirl burners for low-emission furnaces and boilers,” *Proceedings of the Combustion Institute*, vol. 28, no. 1, pp. 1305–1313, 2000.
- [35] COHEN, J. M. and ANDERSON, T. J., “Experimental investigation of near-blowout instabilities in a lean, premixed step combustor,” in *34th AIAA Aerospace Sciences Meeting and Exhibit*, 1996.
- [36] COMTE-BELLOT, G. and CORRSIN, S., “The use of a contraction to improve the isotropy of grid-generated turbulence,” *Journal of Fluid Mechanics Digital Archive*, vol. 25, no. 04, pp. 657–682, 1966.
- [37] COPPOLA, G. and GOMEZ, A., “Experimental investigation on a turbulence generation system with high-blockage plates,” *Experimental Thermal and Fluid Science*, vol. 33, no. 7, pp. 1037–1048, 2009.
- [38] CORREA, S. M., “A review of NO<sub>x</sub> formation under gas-turbine combustion conditions,” *Combustion Science and Technology*, vol. 87, no. 1, pp. 329–362, 1993.

- [39] CRAVEN, P. and WAHBA, G., “Smoothing noisy data with spline functions,” *Numerische Mathematik*, vol. 31, no. 4, pp. 377–403, 1978.
- [40] DAMKÖHLER, G., “The effect of turbulence on the flame velocity in gas mixtures,” *Zeitschrift Electrochem*, vol. 46, pp. 601–626, 1940.
- [41] DANIELE, S., JANSOHN, P., MANTZARAS, J., and BOULOUCHOS, K., “Turbulent flame speed for syngas at gas turbine relevant conditions,” *Proceedings of the Combustion Institute*, vol. 33, no. 2, pp. 2937–2944, 2011.
- [42] DASCH, C., “One-dimensional tomography: a comparison of abel, onion-peeling, and filtered backprojection methods,” *Applied Optics*, vol. 31, no. 8, pp. 1146–1152, 1992.
- [43] DAVIS, S. G., JOSHI, A. V., WANG, H., and EGOLFOPOULOS, F., “An optimized kinetic model of h<sub>2</sub>/co combustion,” *Proceedings of the Combustion Institute*, vol. 30, no. 1, pp. 1283–1292, 2005.
- [44] DAY, M., TACHIBANA, S., BELL, J., LIJEWSKI, M., BECKNER, V., and CHENG, R. K., “A combined computational and experimental characterization of lean premixed turbulent low swirl laboratory flames: I. methane flames,” *Combustion and Flame*, vol. 159, no. 1, pp. 275–290, 2012.
- [45] DE BOOR, C., *A Practical guide to splines*, vol. 27 of *Applied Mathematical Sciences*. New York: Springer-Verlag, 1978.
- [46] DE GOEY, L. P. H., PLESSING, T., HERMANN, R. T. E., and PETERS, N., “Analysis of the flame thickness of turbulent flamelets in the thin reaction zones regime,” *Proceedings of the Combustion Institute*, vol. 30, no. 1, pp. 859–866, 2005.
- [47] D’ERRICO, J., “inpaint\_nans.” MATLAB Central File Exchange: <http://www.mathworks.com/matlabcentral/fileexchange/4551-inpaint-nans>, February 2004. Retrieved Mar 21, 2013.
- [48] DONBAR, J. M., DRISCOLL, J. F., and CARTER, C. D., “Strain rates measured along the wrinkled flame contour within turbulent non-premixed jet flames,” *Combustion and Flame*, vol. 125, no. 4, pp. 1239–1257, 2001.
- [49] Dr.-Ing. Ritter Apparatebau GmbH & Co KG, Coloniastr. 19-23, D-44892 Bochum, Germany, *Ritter Gas Meters*.
- [50] DRISCOLL, J. F., “Turbulent premixed combustion: Flamelet structure and its effect on turbulent burning velocities,” *Progress in Energy and Combustion Science*, vol. 34, no. 1, pp. 91–134, 2008.
- [51] DUCLOS, J. M., VEYNANTE, D., and POINSOT, T., “A comparison of flamelet models for premixed turbulent combustion,” *Combustion and Flame*, vol. 95, no. 12, pp. 101–117, 1993.
- [52] EGOLFOPOULOS, F., “Geometric and radiation effects on steady and unsteady strained laminar flames,” *Proceedings of the Combustion Institute*, vol. 25, no. 1, pp. 1375–1381, 1994.

- [53] FILATYEV, S. A., DRISCOLL, J. F., CARTER, C. D., and DONBAR, J. M., “Measured properties of turbulent premixed flames for model assessment, including burning velocities, stretch rates, and surface densities,” *Combustion and Flame*, vol. 141, no. 1-2, pp. 1–21, 2005.
- [54] GASHI, S., HULT, J., JENKINS, K. W., CHAKRABORTY, N., CANT, S., and KAMINSKI, C. F., “Curvature and wrinkling of premixed flame kernels—comparisons of oh plif and dns data,” *Proceedings of the Combustion Institute*, vol. 30, no. 1, pp. 809–817, 2005.
- [55] GLASSMAN, I. and YETTER, R., *Combustion*. Burlington: Academic Press, 4th ed., 2008.
- [56] GOULDIN, F. and CHENG, R. K., “International workshop on premixed turbulent flames,” 2006.
- [57] HAKBERG, B. and GOSMAN, A. D., “Analytical determination of turbulent flame speed from combustion models,” *Symposium (International) on Combustion*, vol. 20, no. 1, pp. 225–232, 1985.
- [58] HAQ, M., SHEPPARD, C., WOOLLEY, R., GREENHALGH, D., and LOCKETT, R., “Wrinkling and curvature of laminar and turbulent premixed flames,” *Combustion and Flame*, vol. 131, no. 1-2, pp. 1–15, 2002.
- [59] HAWKES, E. R. and CANT, R. S., “A flame surface density approach to large-eddy simulation of premixed turbulent combustion,” *Proceedings of the Combustion Institute*, vol. 28, no. 1, pp. 51–58, 2000.
- [60] HAWKES, E. R., SANKARAN, R., and CHEN, J. H., “Estimates of the three-dimensional flame surface density and every term in its transport equation from two-dimensional measurements,” *Proceedings of the Combustion Institute*, vol. 33, no. 1, pp. 1447–1454, 2011.
- [61] HAWORTH, D. C. and POINSOT, T. J., “Numerical simulations of lewis number effects in turbulent premixed flames,” *Journal of Fluid Mechanics*, vol. 244, pp. 405–436, 1992.
- [62] IM, H. G. and CHEN, J. H., “Effects of flow transients on the burning velocity of laminar hydrogen/air premixed flames,” *Proceedings of the Combustion Institute*, vol. 28, no. 2, pp. 1833–1840, 2000.
- [63] JENKINS, K. W. and CANT, R. S., “Curvature effects on flame kernels in a turbulent environment,” *Proceedings of the Combustion Institute*, vol. 29, no. 2, pp. 2023–2029, 2002.
- [64] KARPOV, V. P., LIPATNIKOV, A. N., and ZIMONT, V. L., *Flame curvature as a determinant of preferential diffusion effects in premixed turbulent combustion*, vol. 173, pp. 235–250. Reston, VA: AIAA, 1997.
- [65] KARPOV, V. P. and SEVERIN, E. S., “Effects of molecular-transport coefficients on the rate of turbulent combustion,” *Combustion, Explosion and Shock Waves*, vol. 16, no. 1, pp. 41–46, 1980.

- [66] KEE, R., GRGAR, J., SMOOKE, M., and MILLER, J., “Premix: a fortran program for modeling steady laminar one-dimensional premixed flames,” Report SAND85-8240, Sandia National Laboratories, 1983.
- [67] KEE, R. J., MILLER, J. A., EVANS, G. H., and DIXON-LEWIS, G., “A computational model of the structure and extinction of strained, opposed flow, premixed methane-air flames,” *Proceedings of the Combustion Institute*, vol. 22, no. 1, pp. 1479–1494, 1989.
- [68] KERL, J., LAWN, C., and BEYRAU, F., “Three-dimensional flame displacement speed and flame front curvature measurements using quad-plane piv,” *Combustion and Flame*, no. 0, 2013.
- [69] KIDO, H., NAKAHARA, M., HASHIMOTO, J., and BARAT, D., “Turbulent burning velocities of two-component fuel mixtures of methane, propane and hydrogen,” *JSME International Journal Series B Fluids and Thermal Engineering*, vol. 45, no. 2, pp. 355–362, 2002.
- [70] KIDO, H., NAKAHARA, M., NAKASHIMA, K., and HASHIMOTO, J., “Influence of local flame displacement velocity on turbulent burning velocity,” *Proceedings of the Combustion Institute*, vol. 29, no. 2, pp. 1855–1861, 2002.
- [71] KIM, S. H. and PITSCH, H., “Scalar gradient and small-scale structure in turbulent premixed combustion,” *Physics of Fluids*, vol. 19, no. 11, 2007.
- [72] KITAGAWA, T., NAKAHARA, T., MARUYAMA, K., KADO, K., HAYAKAWA, A., and KOBAYASHI, S., “Turbulent burning velocity of hydrogen-air premixed propagating flames at elevated pressures,” *International Journal of Hydrogen Energy*, vol. 33, no. 20, pp. 5842–5849, 2008.
- [73] KOBAYASHI, H., TAMURA, T., MARUTA, K., NIIOKA, T., and WILLIAMS, F. A., “Burning velocity of turbulent premixed flames in a high-pressure environment,” *Proceedings of the Combustion Institute*, vol. 26, no. 1, pp. 389–396, 1996.
- [74] KOLMOGOROV, A., PETROVSKII, I., and PISKUNOV, N., “A study of the equation of diffusion with increase in the quantity of matter, and its application to a biological problem,” *Bjul. Moskovskogo Gos. Univ.*, vol. 1, no. 7, pp. 1–26, 1937.
- [75] KORTSCHIK, C., PLESSING, T., and PETERS, N., “Laser optical investigation of turbulent transport of temperature ahead of the preheat zone in a premixed flame,” *Combustion and Flame*, vol. 136, no. 1-2, pp. 43–50, 2004.
- [76] KOSTIUK, L., SHEPHERD, I., and BRAY, K., “Experimental study of premixed turbulent combustion in opposed streams. part ii: spatial structure of flames,” *Combustion and Flame*, vol. 118, no. 1-2, pp. 129–139, 1999.
- [77] KOUTMOS, P. and MCGUIRK, J. J., “Isothermal flow in a gas turbine combustor a benchmark experimental study,” *Experiments in Fluids*, vol. 7, no. 5, pp. 344–354, 1989.
- [78] KUZNETSOV, V. R. and SABEL’NIKOV, V. A., *Turbulent Combustion of a Homogeneous Mixture*, book section 6, pp. 235–251. New York, Washington, Philadelphia, London: Hemisphere Publishing Corporation, 1st ed., 1990.

- [79] LAW, C. K., *Combustion Physics*. New York: Cambridge University Press, 2006.
- [80] LAWSON, N. J. and WU, J., “Three-dimensional particle image velocimetry: experimental error analysis of a digital angular stereoscopic system,” *Measurement Science and Technology*, vol. 8, no. 12, p. 1455, 1997.
- [81] LEE, T., LEE, J., NYE, D., and SANTAVICCA, D., “Local response and surface properties of premixed flames during interactions with krmm vortex streets,” *Combustion and Flame*, vol. 94, no. 1-2, pp. 146–160, 1993.
- [82] LEE, T., NORTH, G., and SANTAVICCA, D., “Curvature and orientation statistics of turbulent premixed flame fronts,” *Combustion Science and Technology*, vol. 84, no. 1, pp. 121–132, 1992.
- [83] LEE, T., NORTH, G., and SANTAVICCA, D., “Surface properties of turbulent premixed propane/air flames at various lewis numbers,” *Combustion and Flame*, vol. 93, no. 4, pp. 445–456, 1993.
- [84] LIAO, S. Y., JIANG, D. M., GAO, J., and HUANG, Z. H., “Measurements of markstein numbers and laminar burning velocities for natural gasair mixtures,” *Energy & Fuels*, vol. 18, no. 2, pp. 316–326, 2003. doi:.
- [85] LIEUWEN, T., MCDONELL, V., PETERSEN, E., and SANTAVICCA, D., “Fuel flexibility influences on premixed combustor blowout, flashback, autoignition, and stability,” *Journal of Engineering for Gas Turbines and Power*, vol. 130, pp. 011506–1–011506–10, 2008.
- [86] LIEUWEN, T. C. and YANG, V., *Combustion Instabilities in Gas Turbine Engines: Operational Experience, Fundamental Mechanisms, and Modeling*, vol. 210. American Institute of Aeronautics and Astronautics, 2005.
- [87] LIPATNIKOV, A. N. and CHOMIAK, J., “Turbulent flame speed and thickness: phenomenology, evaluation, and application in multi-dimensional simulations,” *Progress in Energy and Combustion Science*, vol. 28, no. 1, pp. 1–74, 2002.
- [88] LIPATNIKOV, A. N. and CHOMIAK, J., “Molecular transport effects on turbulent flame propagation and structure,” *Progress in Energy and Combustion Science*, vol. 31, no. 1, pp. 1–73, 2005.
- [89] LITTLEJOHN, D. and CHENG, R. K., “Fuel effects on a low-swirl injector for lean premixed gas turbines,” *Proceedings of the Combustion Institute*, vol. 31, no. 2, pp. 3155–3162, 2007.
- [90] LITTLEJOHN, D., CHENG, R. K., NOBLE, D. R., and LIEUWEN, T., “Laboratory investigations of low-swirl injectors operating with syngases,” *Journal of Engineering for Gas Turbines and Power*, vol. 132, no. 1, pp. 011502–1–011502–8, 2010.
- [91] MAKITA, H., “Realization of a large-scale turbulence field in a small wind tunnel,” *Fluid Dynamics Research*, vol. 8, no. 1-4, pp. 53–64, 1991.
- [92] MAYO JR, W. T., “A discussion of limitations and extentions of power spectrum estimation with burst-counter ldv systems,” in *International Workshop on Laser Velocimetry*, vol. 1, pp. 90–101, 1974.

- [93] MEI, R., “Velocity fidelity of flow tracer particles,” *Experiments in Fluids*, vol. 22, no. 1, pp. 1–13, 1996.
- [94] MELLING, A., “Tracer particles and seeding for particle image velocimetry,” *MEASUREMENT SCIENCE AND TECHNOLOGY*, vol. 8, no. 12, p. 1406, 1997.
- [95] MYDLARSKI, L. and WARHAFT, Z., “On the onset of high-reynolds-number grid-generated wind tunnel turbulence,” *Journal of Fluid Mechanics*, vol. 320, no. -1, pp. 331–368, 1996.
- [96] MYDLARSKI, L. and WARHAFT, Z., “Passive scalar statistics in high-péclet-number grid turbulence,” *Journal of Fluid Mechanics*, vol. 358, no. -1, pp. 135–175, 1998.
- [97] NAKAHARA, M. and KIDO, H., “Study on the turbulent burning velocity of hydrogen mixtures including hydrocarbons,” *AIAA Journal*, vol. 46, no. 7, pp. 1569–1575, 2008.
- [98] NAZEER, W. A., SMITH, K. O., SHEPPARD, P., CHENG, R. K., and LITTLEJOHN, D., “Full scale testing of a low swirl fuel injector concept for ultra-low nox gas turbine combustion systems,” *ASME Turbo Expo 2006: Power for Land, Sea and Air*, 2006.
- [99] NOGENMYR, K. J., FUREBY, C., BAI, X. S., PETERSSON, P., COLLIN, R., and LINNE, M., “Large eddy simulation and laser diagnostic studies on a low swirl stratified premixed flame,” *Combustion and Flame*, vol. 156, no. 1, pp. 25–36, 2009.
- [100] NOGENMYR, K. J., PETERSSON, P., BAI, X. S., FUREBY, C., COLLIN, R., LANTZ, A., LINNE, M., and ALDN, M., “Structure and stabilization mechanism of a stratified premixed low swirl flame,” *Proceedings of the Combustion Institute*, vol. 33, no. 1, pp. 1567–1574, 2011.
- [101] NOGENMYR, K. J., PETERSSON, P., BAI, X. S., NAUERT, A., OLOFSSON, J., BRACKMAN, C., SEYFRIED, H., ZETTERBERG, J., LI, Z. S., RICHTER, M., DREIZLER, A., LINNE, M., and ALDN, M., “Large eddy simulation and experiments of stratified lean premixed methane/air turbulent flames,” *Proceedings of the Combustion Institute*, vol. 31, no. 1, pp. 1467–1475, 2007.
- [102] OTSU, N., “A threshold selection method from gray-level histograms,” *IEEE Transactions On Systems, Man, And Cybernetics*, vol. 9, no. 1, pp. 62–66, 1979.
- [103] PEIYONG, W., HU, S., WEHRMEYER, J., and PITZ, R., “Stretch and curvature effects on flames,” 2004.
- [104] PETERS, N., “Laminar flamelet concepts in turbulent combustion,” *Proceedings of the Combustion Institute*, vol. 21, no. 1, pp. 1231–1250, 1988.
- [105] PETERS, N., “The turbulent burning velocity for large-scale and small-scale turbulence,” *Journal of Fluid Mechanics*, vol. 384, pp. 107–132, 1999.
- [106] PETERS, N., *Turbulent Combustion*. Cambridge Monographs on Mechanics, Cambridge: Cambridge University Press, 2000.
- [107] PETERSSON, P., OLOFSSON, J., BRACKMAN, C., SEYFRIED, H., ZETTERBERG, J., RICHTER, M., ALDN, M., LINNE, M. A., CHENG, R. K., NAUERT, A., GEYER, D., and DREIZLER, A., “Simultaneous piv/oh-plif, Rayleigh thermometry/oh-plif and

- stereo piv measurements in a low-swirl flame,” *Appl. Opt.*, vol. 46, no. 19, pp. 3928–3936, 2007.
- [108] PFADLER, S., BEYRAU, F., and LEIPERTZ, A., “Flame front detection and characterization using conditioned particle image velocimetry (CPiv),” *Opt. Express*, vol. 15, no. 23, pp. 15444–15456, 2007.
- [109] PLESSING, T., KORTSCHIK, C., PETERS, N., MANSOUR, M. S., and CHENG, R. K., “Measurements of the turbulent burning velocity and the structure of premixed flames on a low-swirl burner,” *Proceedings of the Combustion Institute*, vol. 28, no. 1, pp. 359–366, 2000.
- [110] POINSOT, T. and VEYNANTE, D., *Theoretical and Numerical Combustion*. Philadelphia: RT Edwards, Inc., 2005.
- [111] PRANDTL, L., *Herstellung einwandfreier Luftströme (Windkanäle)*. Akademische Verlagsgesellschaft MBH, 1932.
- [112] RENOU, B., BOUKHALFA, A., PUECHBERTY, D., and TRINIT, M., “Effects of stretch on the local structure of preely propagating premixed low-turbulent flames with various lewis numbers,” *Symposium (International) on Combustion*, vol. 27, no. 1, pp. 841–847, 1998.
- [113] SHAVIT, U. and CHIGIER, N., “Development and evaluation of a new turbulence generator for atomization research,” *Experiments in Fluids*, vol. 20, no. 4, pp. 291–301, 1996.
- [114] SHEPHERD, I. G., BOURGUIGNON, E., MICHOU, Y., and GKALP, I., “The burning rate in turbulent bunsen flames,” *Symposium (International) on Combustion*, vol. 27, no. 1, pp. 909–916, 1998.
- [115] SHEPHERD, I. G., CHENG, R. K., PLESSING, T., KORTSCHIK, C., and PETERS, N., “Premixed flame front structure in intense turbulence,” *Proceedings of the Combustion Institute*, vol. 29, no. 2, pp. 1833–1840, 2002.
- [116] SHEPHERD, I. and ASHURST, W., “Flame front geometry in premixed turbulent flames,” in *Symposium (International) on Combustion*, vol. 24, pp. 485–491, Elsevier, 1992.
- [117] SHIMURA, M., UEDA, T., CHOI, G.-M., TANAHASHI, M., and MIYAUCHI, T., “Simultaneous dual-plane ch plif, single-plane oh plif and dual-plane stereoscopic piv measurements in methane-air turbulent premixed flames,” *Proceedings of the Combustion Institute*, vol. 33, no. 1, pp. 775–782, 2011.
- [118] SMALLWOOD, G. J., GLDER, . L., SNELLING, D. R., DESCHAMPS, B. M., and GKALP, I., “Characterization of flame front surfaces in turbulent premixed methane/air combustion,” *Combustion and Flame*, vol. 101, no. 4, pp. 461–470, 1995.
- [119] SMITH, G. P., GOLDEN, D. M., FRENKLACH, M., MORIARTY, N. W., EITENEER, B., GOLDENBERG, M., BOWMAN, C. T., HANSON, R. K., SONG, S., GARDINER JR, W. C., LISSIANSKI, V. V., and QIN, Z., “Gri-mech 3.0.”

- [120] SOIKA, A., DINKELACKER, F., and LEIPERTZ, A., “Pressure influence on the flame front curvature of turbulent premixed flames: comparison between experiment and theory,” *Combustion and Flame*, vol. 132, no. 3, pp. 451–462, 2003.
- [121] STEINBERG, A. and DRISCOLL, J., “Straining and wrinkling processes during turbulence-premixed flame interaction measured using temporally-resolved diagnostics,” *Combustion and Flame*, 2009.
- [122] SUNG, C. J., LAW, C. K., and AXELBAUM, R. L., “Thermophoretic effects on seeding particles in ldv measurements of flames,” *Combustion Science and Technology*, vol. 99, no. 1-3, pp. 119–132, 1994.
- [123] TAYLOR, G., “Turbulence in a contracting stream,” *ZAMM-Journal of Applied Mathematics and Mechanics/Zeitschrift für Angewandte Mathematik und Mechanik*, vol. 15, no. 1-2, pp. 91–96, 1935.
- [124] TEMME, J. SKIBA, A. W. T. D. J., “Premixed turbulent combustion in high reynolds number regimes - of thickened flamelet and distributed reactions,” in *8th U.S. National Combustion Meeting*, 2013.
- [125] TENNEKES, H. and LUMLEY, J., *A first course in turbulence*. The MIT press, 1972.
- [126] THOLE, K., BOGARD, D., and WHAN-TONG, J., “Generating high freestream turbulence levels,” *Experiments in Fluids*, vol. 17, no. 6, pp. 375–380, 1994.
- [127] TROPEA, C., YARIN, A. L., and FOSS, J. F., *Springer handbook of experimental fluid mechanics*, vol. 1. Springer Science & Business Media, 2007.
- [128] TRUNK, P. J., BOXX, I., HEEGER, C., MEIER, W., BHM, B., and DREIZLER, A., “Premixed flame propagation in turbulent flow by means of stereoscopic piv and dual-plane oh-plif at sustained kHz repetition rates,” *Proceedings of the Combustion Institute*, vol. 34, no. 2, pp. 3565–3572, 2013.
- [129] TSENG, L.-K., ISMAIL, M., and FAETH, G. M., “Laminar burning velocities and markstein numbers of hydrocarbonair flames,” *Combustion and Flame*, vol. 95, no. 4, pp. 410–426, 1993.
- [130] TUMMERS, M. J. and PASSCHIER, D. M., “Spectral estimation using a variable window and the slotting technique with local normalization,” *Measurement Science and Technology*, vol. 7, pp. 1541–1546, 1996.
- [131] TURNS, S. R., *An Introduction to Combustion*. New York: McGraw-Hill, 1996.
- [132] VENKATESWARAN, P., MARSHALL, A., SEITZMAN, J., and LIEUWEN, T., “Pressure and fuel effects on turbulent consumption speeds of h<sub>2</sub>/co blends,” *Proceedings of the Combustion Institute*, vol. 34, no. 1, pp. 1527–1535, 2013.
- [133] VENKATESWARAN, P., MARSHALL, A., SHIN, D. H., NOBLE, D., SEITZMAN, J., and LIEUWEN, T., “Measurements and analysis of turbulent consumption speeds of h<sub>2</sub>/co mixtures,” *Combustion and Flame*, vol. 158, no. 8, pp. 1602–1614, 2011.
- [134] VENKATESWARAN, P., *Measurements and Modeling of Turbulent Consumption Speeds of Syngas Fuel Blends*. PhD thesis, Georgia Institute of Technology, May 2013.

- [135] VIDETO, B. D. and SANTAVICCA, D. A., “A turbulent flow system for studying turbulent combustion processes,” *Combustion Science and Technology*, vol. 76, no. 1, pp. 159–164, 1991.
- [136] WILLIAMS, F. A., “Criteria for existence of wrinkled laminar flame structure of turbulent premixed flames,” *Combustion and Flame*, vol. 26, pp. 269–270, 1976. doi: DOI.
- [137] WILLIAMS, F. A., *Combustion Theory*. Combustion Science and Engineering Series, Menlo Park: Benjamin/Cummings Publishing Company, 2nd ed., 1985.
- [138] WON, S. H., WINDOM, B., JIANG, B., and JU, Y., “The role of low temperature fuel chemistry on turbulent flame combustion propagation,” *Combustion and Flame*, vol. 161, no. 2, pp. 475–483, 2014.
- [139] WU, C. and LAW, C., “On the determination of laminar flame speeds from stretched flames,” *Proceedings of the Combustion Institute*, vol. 20, no. 1, pp. 1941–1949, 1985.
- [140] WU, M. S., KWON, S., DRISCOLL, J. F., and FAETH, G. M., “Turbulent premixed hydrogen/air flames at high reynolds numbers,” *Combustion Science and Technology*, vol. 73, no. 1, pp. 327–350, 1990.
- [141] YUEN, F. T. C. and GLDER, M. L., “Turbulent premixed flame front dynamics and implications for limits of flamelet hypothesis,” *Proceedings of the Combustion Institute*, vol. 34, no. 1, pp. 1393–1400, 2013.
- [142] YUEN, F. T. and GÜLDER, O. L., “Investigation of dynamics of lean turbulent premixed flames by Rayleigh imaging,” *AIAA journal*, vol. 47, no. 12, pp. 2964–2973, 2009.
- [143] ZEL'DOVICH, Y. B. and FRANK-KAMENETSKII, D. A., *Turbulent and Heterogeneous Combustion*. Moscow: Moscow Institute of Mechanical Engineering, 1947.